Computational Fluid Dynamics analysis of photobioreactors: a numerical model to assess the effects of light-dark cycles on Haematococcus pluvialis and Chlorella…

Giannelli Luca

(Degree)
博士（工学）

(Date of Degree)
2014-09-25

(Date of Publication)
2016-09-25

(Resource Type)
doctoral thesis

(Report Number)
甲第6221号

(URL)
https://hdl.handle.net/20.500.14094/D1006221

Doctoral Dissertation

Computational Fluid Dynamics analysis of photobioreactors: a numerical model to assess the effects of light-dark cycles on *Haematococcus pluvialis* and *Chlorella sorokiniana* cultures

Luca Giannelli

Graduate School of Engineering

Kobe University

July 2014

For Sayo,

she that came and changed my life.

Table of Contents

List of abbreviations

ALR	Air Lift Reactor
AST	Astaxanthin concentration
BCR	Bubble Column Reactor
CSV	Comma Separated Value
DNS	Direct Numerical Solution
GMO	Genetically Modified Organisms
IA	Image Analysis
LCE	Light Conversion Efficiency
$MSIM$	Molina Standard Inorganic Medium
NPQ	Non Photochemical Quenching
OER	Oxygen Evolution Rate
OF	OpenFOAM
PAR	Photosynthetic Active Radiation
PSI	Photosystem I
$PSII$	Photosystem II
$RANS$	Reynolds Averaged Navier-Stokes
ROS	Reactive Oxygen Species
VOF	Volumes Of Fluids

Roman symbols

Symbol	***Description***	***Units***
A	Cross section of the flow in the cascade reactor	m^2
A_C	Continuous light area	px
A_{DC}	Downcomer cross section	m^2
A_F	Flashing light area	px
A_{PBR}	PBR total area	px

A_R	Riser cross section	m^2
C_i	Numerical tracer concentration (L for liquid, G for Gas)	$kg \cdot m^{-3}$
C_i^*	Numerical tracer concentration at equilibrium (L for liquid, G for Gas)	$kg \cdot m^{-3}$
CHL	Total chlorophyll concentration	$mg \cdot l^{-1}$
$\mathfrak{D}$	Diffusion coefficient	$m^2 \cdot s^{-1}$
D	Duty cycle	
d_B	Bubble diameter	m
d_i	Draft tube inner diameter	mm
D_i	Reactor inner diameter	mm
d_n	Nozzle diameter	mm
d_o	Draft tube outer diameter	mm
DW	Dry weight	$g \cdot l^{-1}$
$Eö$	Eötvös number	$(g \cdot (\rho_L - \rho_G) \cdot d_B^2 \cdot \sigma^{-1})$
f_v	Surface tension	$N \cdot m^{-2}$
g	Gravitational acceleration constant	$m \cdot s^{-2}$
H	Henry's constant	
h_{apron}	Draft tube bottom clearance	mm
h_{DT}	Draft tube height	mm
M	Morton number	$g \cdot \mu_L^4 \cdot (\rho_L - \rho_G) \cdot \rho_L^{-2} \cdot \sigma^{-3}$
N_a	Avogadro's Number	mol^{-1}
n_i	moles of the i species	mol
$\dot{n}_{LG}$	diffusion flux in the liquid/gas sytsem	$mol \cdot s^{-1}$
OER	Oxygen Evolution Rate	$\mu mol\, O_2 \cdot (\mu g\, CHL)^{-1} \cdot h^{-1}$
p	Pressure	$N \cdot m^{-2}$
P	Wetted perimeter	m
PFD	Photon Flux Density	$\mu mol \cdot m^{-2} \cdot s^{-1}$
$r.u.$	Relative units	
R_H	Hydraulic Radius	m
s	Culture layer thickness	m
t	Residence time	s
t_d	Dark time	ms
t_f	Flashing time	ms
U_i	Fluid velocity (along the i axis when specified)	$m \cdot s^{-1}$
x	Lateral position coordinate/axis	m
y	Depth position coordinate/axis	m
z	Vertical position coordinate/axis	m

Greek symbols

Symbol	***Description***	***Units***
α	Partition coefficient	
$\Delta\tilde{H}_{comb,i}$	Specific enthalpy of combustion of the i species	$kJ \cdot mol^{-1}$
λ	Wave length	nm
μ_i	Dynamic viscosity (L for liquid, G for Gas if present)	$Pa \cdot s$
ν	Wave frequency	s^{-1}
ν_i	Kinematic viscosity (L for liquid, G for Gas)	$m^2 \cdot s^{-1}$
ρ_i	Fluid density (L for liquid, G for Gas if present))	$kg \cdot m^{-3}$
σ	Surface tension	$N \cdot m^{-1}$
φ	Flux through the cell faces	$m \cdot s^{-1}$
ϕ	Flashing light frequency	s^{-1}

Part 1

Introduction

1.1 Background

It is a widespread and accepted fact that Earth as we know it nowadays originated a relatively small time ago, from a geological point of view. To be precise, the first animals (sponges, jellyfishes) started to roam the oceans of the primordial terraqueous globe roughly $8 \cdot 10^6$ years ago while for the migration of life out of the water and the rise of the first dinosaurs, then mammals, another $4 \cdot 10^6$ years had to pass. Not to mention the advent of the first humans which happened only 2 millions years ago. However, all these living species could not have existed without the so called "oxygenic photosynthesis", a complex physico-chemical reaction carried out by primordial cyanobacteria, which is supposed to have appeared some time around $2.5 \cdot 10^9$ years ago (Rasmussen et al., 2008). Ever since then, oxygenic photosynthesis represents the most important process supporting life on Earth, being it the one and only way that living organisms have to harness the sole energy source entering the system "Earth" from outer space: the solar light. In other words, photosynthesis plays a central role in the accumulation of biomass on Earth, by fixing inorganic carbon from the atmosphere, i.e. CO_2, using solar light as energy while simultaneously supporting all the heterotrophic life forms, by releasing oxygen as a by-product of the process. The total power deriving from solar light irradiation received by the Earth amounts to 174 PW of which only the 70% is able to reach ground and to be absorbed (122 PW), while the remaining is reflected back to space by the clouds. Of the absorbed radiation only the 0.077% is captured and successfully converted into viable biomass through photosynthesis (Miyamoto, 1997), a process that thus proves to be highly energy-inefficient. Nevertheless, the energy scale we are referring to still represents roughly 30 times the total energy produced for human consumption on planet Earth in one year, 96 EJ in 2011 (U.S. Energy Information Administration, 2013), and should therefore in theory suffice for the

total energetic self-sufficiency of the world human population. However, as for the year 2011, 91.2 EJ of said energy are still produced by non-renewable sources (crude oil, natural gas, nuclear and coal), with an optimistic provision of an increase from 10 to 13% of the energy generated by renewable sources for the years up to 2040, especially biofuels (U.S. Energy Information Administration, 2013). This outlook of the global energy usage pattern calls for a complete restructuring of the whole system where renewable sources will quickly take place of non-renewable ones in an attempt to achieve a more sustainable interaction between humanity and our host planet. This is the so-called "green revolution", a process that started to take place all over the world, with huge amounts of capitals slowly shifting towards the investigation of new energy sources that could possibly be renewed indefinitely. As stated by the U.S. Energy Information Administration (2013), despite being a huge producer of bioethanol (obtained from the bio-conversion of corn and sorghum) (Nuffield Council on Bioethics, 2011), the US are planning to move towards an even larger biofuel production in the coming 20 years. This is the direct consequence of crude oil price increase, along with a sort of preparation to fuel shortages that can be easily foreseen in the close future. However, said bioethanol production from corn is blamed as the responsible of both the price increase of corn (and similar crops) for human consumption and the increase of land exploitation, in terms of water usage and pollution by by the use/employment of agriculture pharmaceuticals (Nuffield Council on Bioethics, 2011). Furthermore, GMOs are the best candidates for high yield productions, leading to the utterly controversial debate on their ethical use in agriculture. All this being said, its is clear that this kind of approach may not lead to a complete solution to fossil energy shortage, despite it being a first step towards the right direction.

A promising and smart solution to this problem may be represented by biofuels extracted from raw algal biomass. Because of their relatively simple metabolism,

microalgae are said to be able to fix up to a hundred times the amount of CO_2 that plants and other terrestrial photosynthetic organisms can normally fix in their leaves and fibrous tissues, but with an obviously higher turnover speed (Falkowski and Raven, 2007). This difference easily translates into an analogous scale reduction in the hypothetical plant footprint for achieving the same biomass revenue, together with the fact that said production facilities could be established on land that is not suitable for other crops without any interference on the prizes of vegetables destined to human consumption. Not to mention the fact that a faster turnover is beneficial on the productivity/operational time factor of the plant (i.e. the overall efficiency). For these reasons, in the last 10 years numerous big company names operating in the energy field (Exxon Mobil, Royal Dutch Shell and ENI) have started various pilot plants to try and exploit these benefits on a semi-industrial scale[1]. Even so, with the apparent sole exception of the Japanese company Denso[2], the other research groups did not achieve any substantial result, apart from the commendable effort of investigating an innovative renewable energy source; as a consequence the technology has been deemed as "still unprofitable" and the projects abandoned. The main reason of this investment debacle resides in the low light-to-biomass conversion efficiency characterizing algae, a peculiarity which is really difficult to handle both for physical reasons (light distribution) and chemical constraints (nutrient distribution). In this work we wanted to address this issue, as we believe that it deserves an in-depth analysis before an industrial scale exploitation could be possible. However, to be able to give an answer to the many open questions in this filed, we believe that a deep knowledge of three apparently unrelated fields is required, and for this reason, up to the present day this route was left unexplored. To understand the connection

[1]DOE/Lawrence Berkeley National Laboratory (2010, November 3). Algae for biofuels: Moving from promise to reality, but how fast?. Science Daily. Retrieved December 7, 2013, from http://www.sciencedaily.com/releases/2010/11/101102131110.htm

[2]Denso Corporation, Tokyo Motor Show 2011 presentation, Retrieved December 7, 2013, from http://www.denso.co.jp/ja/news/event/tokyomotorshow/2011/booth/pdf/biofuel.pdf

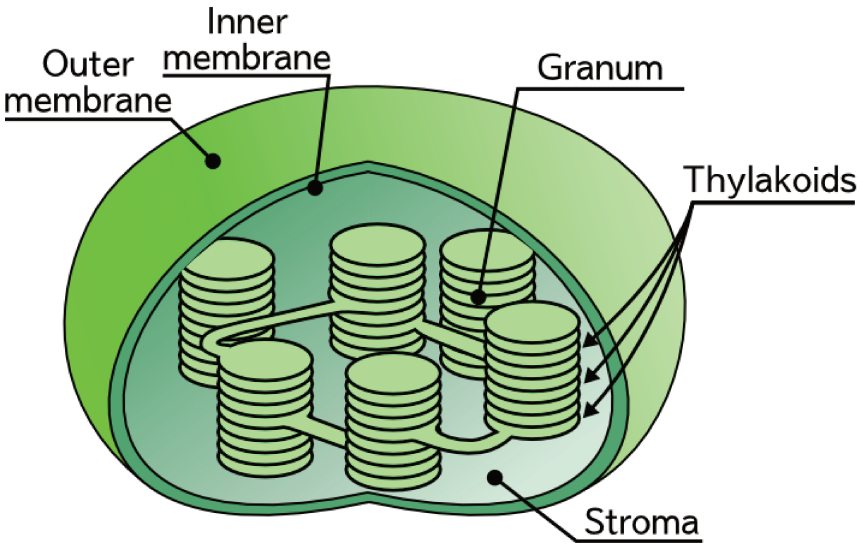

Figure 1.2.1: Graphic representation of a chloroplast.

between said fields which become the vary foundation of this work, an introduction to the following is required: 1) inner workings of the photosynthetic reaction, 2) basic photobioreactor design principles and 3) data analysis with computational fluid dynamics software. Further information related to the algae strain used is in the Materials and Methods section.

1.2 Photosynthesis

1.2.1 The photosynthetic apparatus

As any other chemical nutrient, light has to be absorbed in order to be processed in the metabolism by the photosynthetic organism. This task is carried out by highly specialized organelles called *chloroplasts* (Figure 1.2.1). The chloroplast is the part of the photosynthetic cell that contributes to all the light-related reactions: it contains, in fact, all the light-capturing pigments, the electron carriers and the carbon-fixating enzymes. As shown in Fig. 1.2.1, the chloroplast contains a vast number of sack shaped membranes called *thylakoids,* which in turn show the tendency to stack one over the other forming a sort of fibrous matrix, the so called

grana. Each thylakoid in the chloroplast represents one small fraction of the light-harvesting antenna of the microorganism constituted by the pigments located on the thylakoid membrane itself, where light-dependent reactions actually take place. The inside of the sack itself, called *lumen*, contains instead some of the proteins involved in the photosynthesis and represents the site where water is actually oxidized, producing gaseous oxygen. In green algae the thylakoids seem to be grouping in grana constituted by three or more units, but the actual number is strongly dependent on the species and illumination conditions (Kirk, 2011). The last part of the chloroplast is the *stroma,* the liquid filling the organelle in which the grana are floating. This fluid represents an important component of the chloroplast as it is the place where chloroplast ribosomes and DNA are located but, more importantly, the carbon fixation (i.e. the Calvin-Benson cycle) happens due to the high concentrations of Rubisco protein (Grzebyk et al., 2003). In addition to the carbon fixation, it is inside the chloroplast stroma that inorganic nutrients like NO_2^- and SO_4^{2-} get reduced to ammonium/amino acids, and organic sulfide compounds, respectively (Falkowski and Raven, 2007).

1.2.2 The photosynthetic reaction

The term "photosynthesis" refers to that group of reactions which convert light energy, CO_2, H_2O and inorganic nutrients in highly reduced organic compounds (starch, lipids, etc.), along with ATP and $NADPH_2$, i.e. the building blocks for the base cellular metabolism, and the energy needed to assemble them. First of all let us concentrate on the actual portion of photosynthesis that relies on constant light input for its completion: *the light reactions*.

The main light-driven reaction is the water-splitting (oxidation) process realized by using 8 photons to convert NADP in $NADPH_2$ and ADP into ATP and ultimately

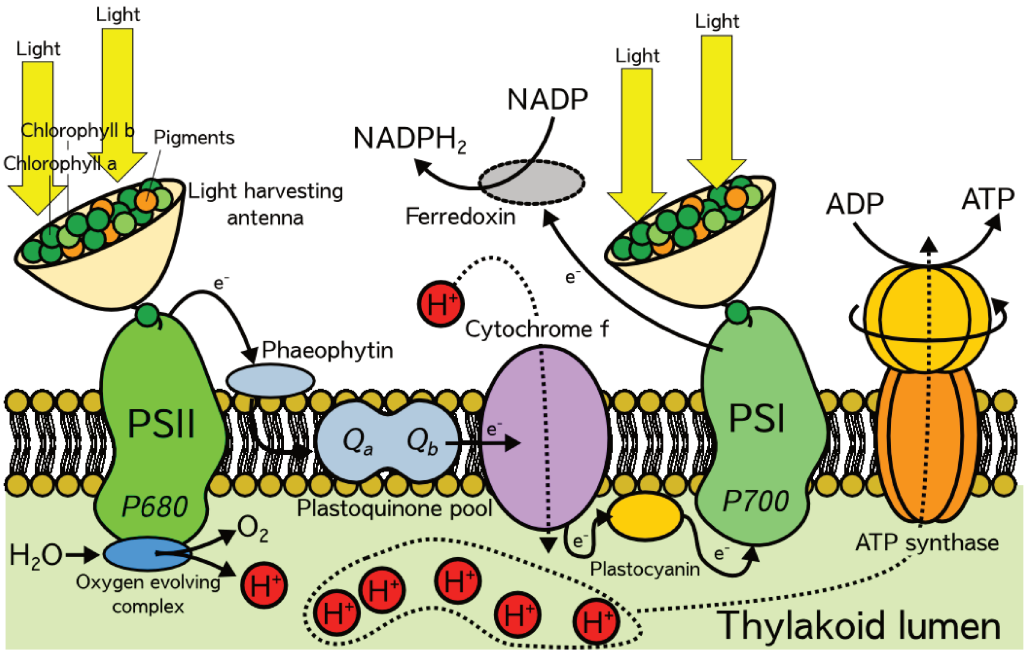

Figure 1.2.2: Simplified photosynthetic electron transport chain scheme. Starting from the water molecule (bottom left) the electron flow is represented by the straight arrows up to its final destination, the Ferredoxin enzyme. Dotted lines represent H^+ions molar flows between the lumen and the stroma.

produce one O_2 molecule. The reaction is summarized like this:

$$\begin{array}{c} 2\,H_2O + 2\,NADP \xrightarrow{\sim 8 \cdot h\nu} O_2 + 2\,NADPH_2 \\ 4\,ADP + 4\,P_i \longrightarrow 4\,ATP \end{array} \tag{1.2.1}$$

As depicted in 1.2.1, the light reaction seems to proceed as a smooth transition between NADP and its reduced form mediated by light energy, which is clearly different from what is actually going on inside the chloroplast: the reaction is instead split over a series of sequential intermediate reactions which take place on the thylakoid membrane. A simplification of the overall reaction sequence, known as the "*photosynthetic transport chain*" can be seen in Figure 1.2.2. First of all, the reaction is now believed to be split among two functional molecule groups called Photosystem I (PSI) and Photosystem II (PSII) where two different light harvesting antennae absorb incident light at slightly different wavelengths namely, 680 nm

and 700 nm for the PSII and PSI respectively. As Fig. 1.2.2 clearly shows, PSII is responsible for the water splitting inside the thylakoid lumen thanks to the *oxygen evolving complex* which represents the site where the electrons are extracted thanks to the light-excited P680 unit. Among this reaction, two H^+ ions are produced which are the main responsible of the lowering of pH inside the thylakoid lumen during active photosynthesis. The excitation of the P680 unit is necessary to carry the electron to an higher energy level (thanks to the absorbed light energy) to initiate the subsequent reactions in a sort of energy cascade, back to the non-excited state. This cascade takes place between the Phaeophytin, Plastoquinone pool (PQ pool), Cytochrome f ending on the Plastocyanin. Now it is worth noting that during these series of passages, H^+ ions are transferred with two different methods: a static electron transfer and a dynamic electron transfer. To be precise, while Phaeophytin and Cytochrome f are molecular complexes linked to the thylakoid membrane and unable to move, both the PQ pool and the Plastocyanin have to shuttle back and forth to transfer the electrons. This phenomena happens on concentration gradients like any analogous process in the cell thus requiring more time than the contiguous ones and ending up being the bottleneck of the whole system. To be precise, the slowest turnover is that of the PQ pool which is reportedly in the time scale of the 100 ms (Falkowski and Raven, 2007). During the electron transfer step between the PQ pool and the Cytochrome f, an H^+ ion is actively transferred from the stroma to the thylakoid lumen, contributing further to the pH gradient across the membrane. The last molecule on this partial chain, plastocyanin, plays with the PSI the same role as the oxygen evolving complex with PSII, by shuttling the electron to the P700 reaction center when it is excited by the absorbed light energy. In an similar way to PSII chain reactions, PSI electron is transferred forward towards lower energy molecules up to its final destination, Ferredoxin, where NADP is converted in $NADPH_2$ by hydrogen reduction. The last step which must be highlighted

is that represented by the conversion of ADP in ATP which reportedly happen simultaneously to the light-dependent reactions (1.2.1) despite not being intrinsically light-driven by itself. This conversion takes place thanks to the trans-membrane protein ATP synthase. Said protein is able to shuttle H^+ ions from the inside of the thylakoid to the stroma, converting the potential difference into stored energy by converting ADP into ATP.

All this being said,it is clear that photosynthetic microorganisms are thus able to conduct an oxidation reaction (water splitting) to obtain as a final result, the reduction of ionic hydrogen, using photons as the sole source of reducing power and in addiction, to have an excess of stored energy (ATP) to be used in the dark phase of the cell metabolism. There has been a long debate around the exact number of photons used in this process: according to Warburg and Negelein (1928), only 4 photons where used to produce on O_2 molecule however data obtained from a later research (Emerson and Lewis, 1941) shown that on an average between 8 and 12 is a more reasonable number. In this work this second value has been used in the equations/calculations (more on this in section 1.2.4).

The only part that have been left unexplained is that regarding the light harvesting antennae, represented in Fig. 1.2.2 as oriented dishes mounted on the top part of each photosystem. This kind of representation is obviously a simplification to clarify the meaning of said antennae; in reality, photosynthetic pigments are packed around the reaction center (P680/P700) forming a globular cluster made by an intricate structure of both photosynthetic pigments and accessory proteins. As briefly indicated in Fig. 1.2.2, in photosynthetic organisms, at least two kind of pigments are present (Kirk, 2011):

- *Chlorophylls*: organo-metallic pigments in the family of porphyrins, that represent the vegetal equivalent of an hemoglobin molecule with Mg^{2+} in substi-

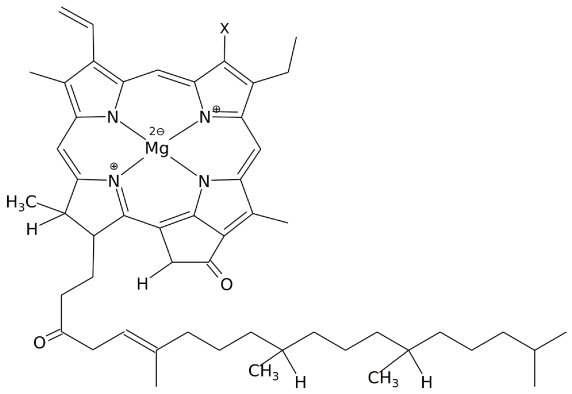

Figure 1.2.3: Chlorophyll molecule structure. The fundamental structure is the same between both chlorophyll a and b whit the only difference that the X radical becomes a CH_3 in the former and a CHO in the latter.

tution of Fe^{2+} atoms.

- *Carotenoids:* isoprenoid pigments with a length of about C_{40}. Despite the linear and relatively simple structure, they can absorb photons thanks to the multiple resonant double bonds spread along the chain.

There are many different kinds of chlorophylls (CHL) in nature: *a*, *b* (see the structure in Figure 1.2.3), *c1*, *c2* and *d* but the main components of the light harvesting complex of the vast majority of photosynthetic organisms are the first two: *a* and *b*. To be more precise, under normal natural conditions CHL *a* represents, on an average, the 80% of the total chlorophyll content representing the main photosynthetic pigment. CHLs are able to absorb certain wavelengths to emit back other frequencies through fluorescence (with lower energy) and are thus able to transfer said energy to the final reaction center (both in PSI and PSII). The reaction center itself is constituted by a CHL *a* coupled with a specialized protein, so we can conclude that in the last place, photosynthesis is conducted by CHL *a*. For this reason all the other pigments, being them CHLs or carotenoids, are generally referred at as "accessory pigments", as their main role is that of photosynthesis coadjuvants. However, researchers reported that in the total number of CHL molecules in a cell, only an extremely small percentage of reaction centers are found, namely about 1 for

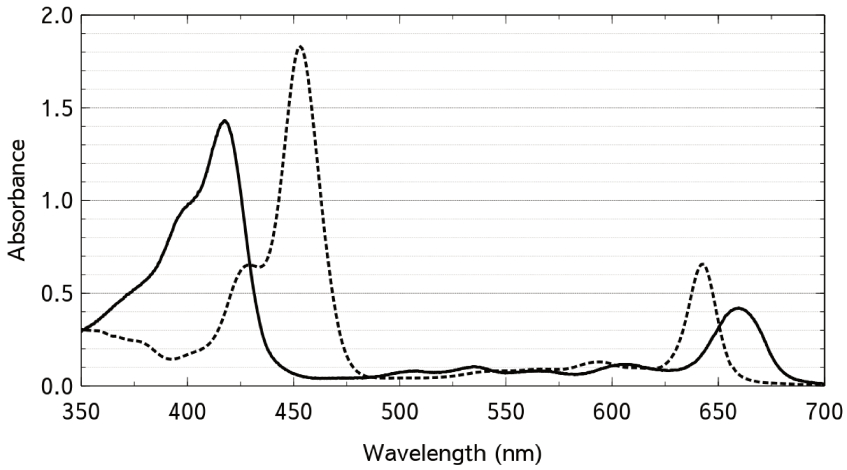

Figure 1.2.4: Absorption spectra of chlorophyll a (solid line) and b (dashed line) in methanol (after Dixon et al. (2005))

every 500 molecules (Emerson and Arnold, 1932; Rabinowitch and Govindjee, 1969). With this premise, a question arises: what is the role of the other pigments? Since the number of reaction centers is so small to be almost negligible in the antenna, one should expect two possibilities: 1) extremely low light conversion efficiencies or 2) extremely low chlorophyll content per cell. Evidently, both these conclusions are wrong as LCE up to 10% can be obtained (in ideal conditions) and CHL represent up to the $3 \sim 5\%$ of biomass weight: it has to be concluded that all the pigments in the antenna complex actually cooperate in the photon capturing process. The mechanism involved in the process is the one postulated by Förster (Knox, 2011), the so-called "*inductive resonance transfer system*". In this mechanism, chlorophylls (an to a minor extent carotenoids) are able to transfer the absorbed energy to each other in a redundant scheme where the last chlorophyll of the chain, probably a reaction center, will en-route the electron in the photosynthetic transport chain. This is possible thanks to the peculiar absorption/fluorescent emission properties of chlorophyll a and b (Figure 1.2.4). CHL a is able to absorb energy around 425 nm and 660 nm and similar values can be seen for CHL b; the absorbed photons can be emitted back through fluorescence which takes place around 625 nm, thus pho-

tons can be translated between CHL molecules by this series of absorption/emission steps. Absorption spectra of CHL a and b are slightly different, ensuring a wider overall absorption span; moreover, thanks to the presence of carotenoids which absorb in an even lower wavelength, microalgae are able to absorb and convert energy in the whole visible range. The only exception are the radiations in the green region ($500 \sim 600$nm) where an almost zero absorption is seen (hence the green color).

After the production of reducing power by means of the light reactions, the photosynthetic process is completed by its dark phase which can be summarized with the equation:

$$\mathrm{CO_2} + 2\,\mathrm{NADPH_2} \longrightarrow \mathrm{CH_2O} + \mathrm{H_2O} + 2\,\mathrm{NADP} \qquad 3\,\mathrm{ATP} \longrightarrow 3\,\mathrm{ADP} + 3\,\mathrm{P_i} \tag{1.2.2}$$

As indicated by the equation 1.2.2, the reducing power produced by the light reactions (1.2.1) is redirected towards the production of carbohydrates, the base of biological chemistry, through the Calvin-Benson cycle. The main objective of this work was directed towards the increase of light conversion efficiency, hence a detailed explanation of this complex part is beyond the scope of the dissertation. For a complete review refer to Martin and Schnarrenberger (1997). Anyway, light and dark reactions when conducted simultaneously overlap, resulting in this global energy/mass balance:

$$\mathrm{CO_2} + 2\,\mathrm{H_2O} \xrightarrow{\sim 8 \cdot h\nu} \mathrm{CH_2O} + \mathrm{H_2O} + \mathrm{O_2} \tag{1.2.3}$$

This is the formulation used for the light conversion efficiency (LCE) calculations.

1.2.3 The role of photosynthetic pigments

In the previous section a general description of the photosynthetic system and a first introduction to the role of photosynthetic pigments (CHLs or carotenoids) in the light reactions have been given. Nonetheless, apart from the secondary role they have in the inductive resonance system, all the accessory pigments play a primary role which is the very reason for their synthesis.

Chlorophylls

As already pointed out, one of the main roles of CHL b in the photosynthesis is that of augmenting the absorption spectrum of the light-harvesting apparatus. Its presence in large quantities can be therefore used as an indicator of cell metabolism. It is little known, however, that the ratio between CHL a and b can be used to assess whether a cell is receiving enough light for its metabolism and can consequently be used as a parameter to assess the onset of photolimiting conditions (Dale and Causton, 1992; Gratani et al., 1998). The reason for this effect, more than the increased absorption spectra, may reside in the positive influence that CHL b has in the transfer of light energy by fluorescence emission (Thorne and Boardman, 1971). It must be noted that some research points towards the fact that the CHL a/b ratio seems to be dependent on the incident light wavelength composition (Borodin, 2008), but the conclusions are not correct when considered from a light transfer point of view. It appears in fact evident from the absorption and fluorescence emission spectra (Dixon et al., 2005) that absorbed photons can be quenched to a longer wavelength, namely 645 nm, where CHL a can absorb them. The effects of light measured by Borodin (2008) where those of highly photolimited cultures due to the different turnover speeds in PSI and PSII (Kirk, 2011) that led to a redistribution of the antenna composition. Thus, the effect is on the photosystem turnover and not on the CHL synthesis pathways which respond directly to a perceived light depriva-

tion. We also tried to replicate this apparent light composition-dependent behavior in non-photolimited cultures of *Haematococcus pluvialis,* but without any appreciable result (data not shown). In addition, CHL b seems to be highly efficient in transferring the light absorbed by carotenoids (which absorb efficiently in ultraviolet wavelengths) to CHL a as demonstrated by Thorne and Boardman (1971). These two simultaneous contributions have an addictive effect on the increase of captured light energy and it seems thus natural for CHL b concentration to represent an important indicator of cellular photosynthesis.

Carotenoids

Carotenoids play an important role in the cell metabolism as, in addition to their limited light capturing capabilities, they act as photosystem protection molecules (Mimuro and Katoh, 1991). The mechanism with which they are able to protect the photosystems, despite being still quite uncertain, is related to their strong antioxidant activity which is also the reason why they are used in cosmetic and nutraceutical applications (Spolaore et al., 2006). It is in fact well known (Demmig-Adams and Adams, 2002) that carotenoids can intercept the highly instable Reactive Oxygen Species (ROS) which are formed together with the excitation of CHLs by three mechanisms: CHLs triplet state quenching, super-oxide and singlet oxygen quenching (Mimuro and Katoh, 1991). Whatever the quenching mechanism, the light energy absorbed by the CHLs is passed directly to carotenoids which can accept singlet state electrons because of the high number of resonant double bonds in their chain structure; upon absorption, energy is dissipated as heat that represents a big part of that phenomenon which has become known as the "non photochemical quenching" (NPQ) (Baker, 2008). This parameter is one of the most used in the determination of light-induced physiological stress together with other fluorescence related parameters (Fv/Fm, φ, etc (Baker, 2008)) however, due to the lack

of specialized measuring equipment (PAM fluorometer), we had to rely only on the CHL/Car ratio as a stress indicator; to be precise, the lower the ratio, the higher the perceived stress (Grobbelaar and Kurano, 2003; Solovchenko et al., 2009).

1.2.4 Photosynthesis theoretical efficiency

According to Eq. 1.2.3, the photosynthetic process requires 8 quanta together with two H_2O molecules for each CO_2 molecule to produce one CH_2O. In reality, the final product of the photosynthesis is a glucose molecule which suggests that each "batch" of photosynthesis, to yield a viable glucose molecule has to use 6 times the quantities reported in Eq. 1.2.3. This means that the correct overall equation becomes:

$$6\,CO_2 + 12\,H_2O \xrightarrow{\sim 48 \cdot h\nu} C_6H_{12}O_6 + 6\,H_2O + 6\,O_2 \tag{1.2.4}$$

As for the energy balance involved in this process, if the equation is correct, it is trivial to calculate the amount of energy attained for each absorbed quantum or, more easily, the theoretical maximum LCE. For each glucose molecule and in the end for the overall process, we can say:

$$LCE_{max,t} = \frac{n_{glu} \cdot \Delta\tilde{H}_{comb,glu}}{\bar{E}_{phot} \cdot n_{phot}} \cdot 100 = \frac{1 \cdot 2805}{209 \cdot 48} \cdot 100 = 27.96\% \tag{1.2.5}$$

provided a glucose specific enthalpy of combustion of $\Delta\tilde{H}_{comb,glu} = 2805\ kJ \cdot mol^{-1}$ (Perry et al., 1999) and an average photon energy of $\bar{E}_{phot} = 209\ kJ \cdot mol^{-1}$. The calculation of the $\bar{E}_{phot}$ parameter is the result of the integration process of each local quantum energy content over the total solar light spectrum; this can be alternatively calculated by using wave frequencies (Eq. 1.2.6) or by wave lengths after taking care of substituting the integrand differential with the proper one (Eq.

1.2.7). Among the two equations, the latter is easier to visualize due to the diffused habit of referring to wavelengths more than frequencies and thus is reported with explicit wavelength values in the formula.

$$\bar{E}_{phot} = \int_{\nu_{min}}^{\nu_{max}} N_a \cdot h \cdot d\nu \tag{1.2.6}$$

$$\bar{E}_{phot} = \int_{2500}^{250} N_a \cdot h \cdot \frac{c}{\lambda^2} \cdot d\lambda \tag{1.2.7}$$

The wavelengths used in this calculation extend clearly beyond the boundaries of visible light or more precisely the photosynthetic active radiation (PAR) which only spans between 430 and 680 nm and only covers the 41% of the total solar radiation (Kirk, 2011). Following this, the maximum LCE attained by any photosynthetic organism will be only able to cover the 41% of the total, as only radiations included in the PAR are available. This leads to the maximum LCE on PAR which is:

$$LCE_{max,PAR} = LCE_{max,t} \cdot 0.41 = 11.46\% \tag{1.2.8}$$

These calculations show how, for any given photon in the PAR radiation, only about 11.5% can be converted into glucose, rendering the process extremely inefficient. However, this number taken by itself still does not take into account all the possible invalidating conditions. It is well known in fact that high intensity radiation has a "saturating" effect on the photosynthetic complex that has to be taken into account as algae are usually illuminated by high intensity solar light. A visual representation of the saturating effect can be observed in Figure 1.2.5 where a *Haematococcus pluvialis* Photosynthesis-Intensity curve (P-I curve) is represented. These curves are obtained by varying the incident light intensity on the culture and recording the outcomes by means of a photosynthesis-related characteristic param-

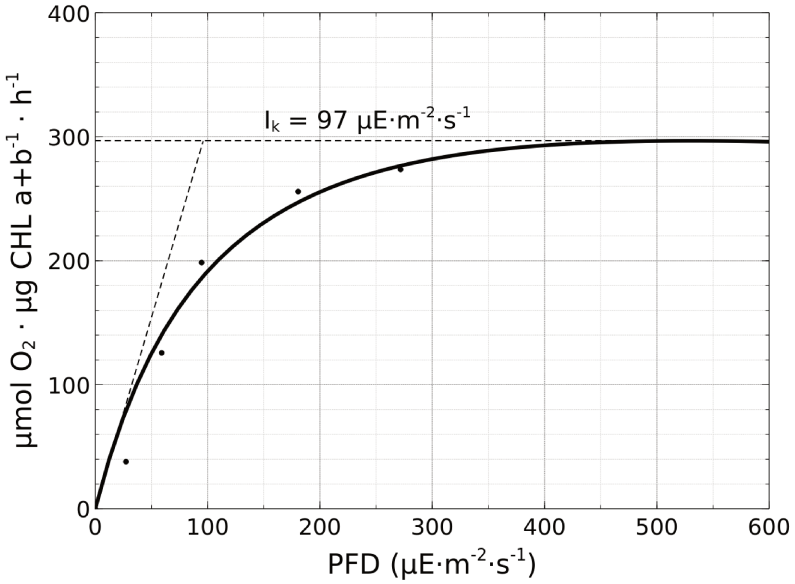

Figure 1.2.5: Photosynthetic activity curve of *Haematococcus pluvialis* NIES-144 measured at 27°C

eter, in this case the specific oxygen evolution rate (OER). In the first part of the P-I curve the OER response is perfectly linear up to 25 $\mu mol \cdot m^{-2} \cdot s^{-1}$ but such linearity is quickly lost when the curve starts to saturate up to a maximum level of approximately 300 $\mu mol\, O_2 \cdot (\mu g\, CHLa + b)^{-1} \cdot h^{-1}$. This behavior is thought to be dependent on two main phenomena: 1) the light induced damage of the D1 protein in the PSII complex (Han et al., 2000; Melis, 1999) and 2) an acceptor side inhibition where electrons are stuck downstream in the PQ pool step redox reactions (Vass et al., 1992). Especially in the latter, a non-destructive kind of inhibition is reported: the electrons which are physically unable to proceed down the photosynthetic electron transport chain act as a negative feedback on the PSII and ultimately, slow down the whole process. While both phenomena are thought to be interdependent (Melis, 1999) they are both reversible even if recovery from the first one is remarkably slower (up to 12 h) when compared to the latter which can be reversed just by lowering the illumination intensity below the saturation.

The contribution of the light saturation effect in the reduction of LCE under

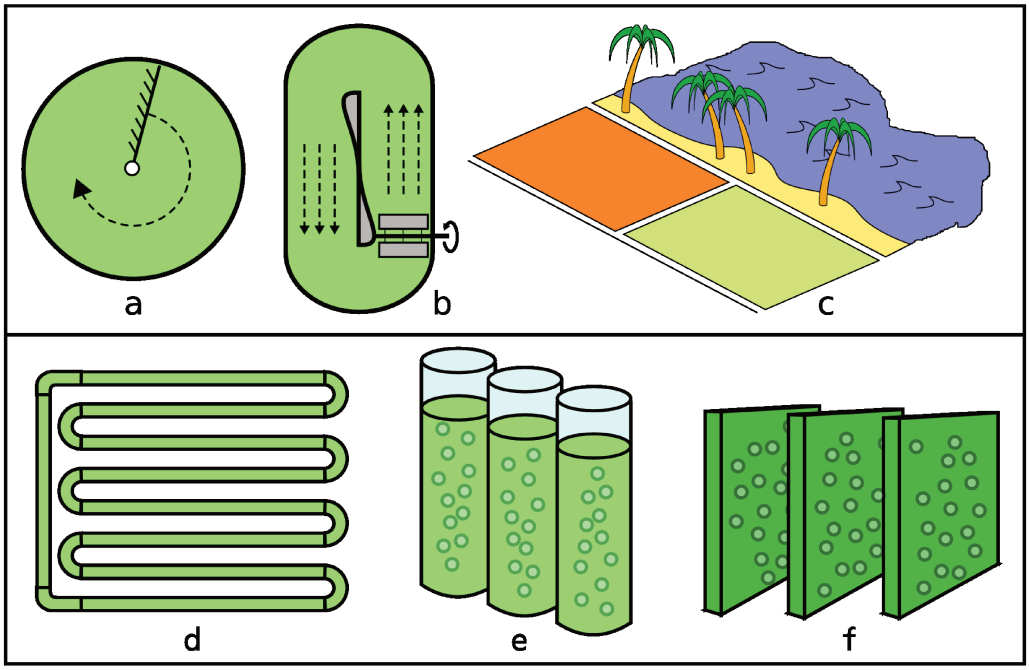

Figure 1.3.1: Examples of open pond (top) and PBRs (bottom) configurations. a) Circular open pond (*Chlorella vulgaris*); b) Raceway pond (*Spirulina platensis*); c) Coastal natural/artificial lagoons (*Dunaliella salina*); d) Tubular PBR (*Haematococcus pluvialis*, *Dunaliella s.*, *Chlorella v.*); e) Vertical cylindrical bubble column, air-lift or annular PBRs (Phytoplankton cultivation); f) Flat panel PBRs (*Tetraselmis s.*, *Nannochloropsis g.*)

high light conditions, is extremely difficult to assess as it is dependent on the time of the day, weather conditions and the season. However, there is a wide spread consensus that during the most harsh summer days with solar PFD reaching for its top (over 2000 $\mu mol \cdot m^{-2} \cdot s^{-1}$), an average of 3 to 6% LCE is recorded in high density cultivation systems (Van Oorschot, 1955; Miyamoto, 1997). For all these considerations, the maximum attainable LCE in natural conditions never rises above the 6% (in overcast sky conditions) and mostly will lie around the 3% in full sun light. It is thus evident the need for an improved PBR design being able to efficiently utilize high PFD values while keeping high productivity and scalability.

1.3 Photobioreactors

1.3.1 Classification of photobioreactors

One of the major tasks that phycologists and bio-engineers have been continuously focusing on for years is the design of high efficiency photobioreactors (PBRs) to achieve an economic conversion of zero-cost sources of light and CO_2 to produce various added value products (Borowitzka, 1999; Goldman, 2000; Spolaore et al., 2006). Despite such efforts the most widely used PBR for commercial scale production still remains the "open pond" system which therefore deserves a small elucidation. Various pond design have been investigated (Becker, 1994) (Fig. 1.3.1-top) but they all share the same weak points to some extent (Tredici, 2004):

- Turbulence in the reactor is strongly related to the culture cross section: culture thickness should never lower below 15 cm to avoid uncontrolled sedimentation and lack of oxygenation. Even in the most favorable conditions, open ponds cannot be considered highly turbulent systems (except for the area around the paddle wheel).

- Low culture density: due to the self shading phenomenon (more on this in Section 1.3.3), cultures in open ponds are strongly photolimited and therefore, the deeper the pond, the lower the achievable culture concentration. As a consequence of the previous point, even the shallowest ponds have pretty low densities (around 0.6 $g \cdot l^{-1}$) with deeper ponds becoming even more photolimited.

- Low surface to volume (S/V) ratio: with over-abundant illumination conditions (like in outdoor PBRs) reactors with high S/V ratios are favored for algae growth as higher concentrations can be achieved. Open ponds represent the opposite situation where the highest possible S/V ratio is regulated by the

culture thickness:

$$\left(\frac{S}{V}\right)_{max} = \frac{1}{0.15\ cm} = 6.67\ m^{-1} \tag{1.3.1}$$

- Contamination risk: as an open air system, the culture is subjected to contamination and even in very selective culturing conditions it is still at risk of being overrun by other exogenous algae or protozoa.

The reason why these reactors are still adopted resides mainly in their ease of operation and the price per square meter of occupied land which is, at least, one degree of magnitude lower than that of any closed PBR also rendering the biomass cheaper (cost between 9~17 €·kg^{-1}).

To address these drawbacks, closed PBRs have been devised to be the most controllable environment possible to allow for the production of added-value chemicals with a high degree of purity deriving from culture reliability/repeatability. Several reactor configurations (Fig. 1.3.1-bottom) for various applications have been proposed (Goldman, 2000; Posten, 2009; Pulz, 2001; Tredici, 2004) and they are all characterized by the efforts spent on the following aspects:

- Culture purity: as many products for the health/beauty and nutraceutical markets may be produced with algae, it is really important to have a completely pure culture. In some algae-based food companies, purity is only achieved as a trade off by selective environmental conditions coupled with constant quality check (Belay, 2008) but in the case of more fine products, a completely pure and axenic culture is imperative.

- High culture concentration: a higher culture concentration results in lower harvesting costs which are thought to amount at least to the 20~30% of the total production cost (Molina-Grima et al., 2004). Achieving the highest biomass concentration is actually the most difficult challenge in PBR design as it represents the final result of different design solutions.

- Land usage optimization: Algae as a photosynthetic crop compete for light and land utilization with those crops intended for human consumption. In a sustainable future scenario, this competition should be reduced as much as possible. For this reason, almost all the PBRs with very few exceptions are devised as vertical structures to exploit the utilized land to the fullest potential (see Fig. 1.3.1 for some examples). Vertical reactor arrangement permits the achievement of ultra-high S/V ratios, as high as 20 to 13 times those of standard ponds (Giannelli and Torzillo, 2012; Richmond and Zhang, 2001).

- Culture turbulence: Like any other chemical engineering application, it is quite evident that an increased turbulence inside the PBR can promote any mass transfer related phenomenon therefore increasing the overall productivity. In algal biotechnology however, more than nutrient deficiencies, culture inability to harvest enough light is the main cause for lowered productivities. For this reason, light distribution and culture turbulence correlation deserve an in-depth investigation.

1.3.2 Flashing light

All the introductory explanations reported up to this point always took into consideration one main aspect of the photosynthetic reaction: it is naturally conducted under continuous light. It is trivial to understand the reason why this assumption was so obvious as solar light was the only light source available during the evolution and it is evidently continuous. For this reason, except for day/night cycles and small diurnal light intensity variations, photosynthesis has always been a purely continuous phenomenon. However, in 1953 Kok discovered that illuminating *Chlorella pyrenoidosa* cultures with artificial flashing light could lead to an increase in LCE,

opening the road for a completely new technique to approach microalgal cultivation. Kok (1953), verified in fact that, by providing intermittent illumination with a proper duty cycle equal to 18% and regulating the flashing light duration, up to 7.5 times higher LCEs could be attained by the culture when compared to continuous light.

$$\begin{cases} D = t_f \cdot \varphi = 5.5^{-1} \\ (t_f + t_d)/t_f = 5.5 \end{cases} \tag{1.3.2}$$

As shown in Eq. 1.3.2, a fixed duty cycle (D) with different flashing time (t_f) duration only means that the same amount of light for each second is distributed to the culture with a different pattern; despite this fact, cultures show the ability to react in a different way to variegated illumination patterns leading many researchers to think that a physiological light-related phenomenon was involved in this beneficial response (Grobbelaar et al., 1992; Thomas and Gibson, 1990).

According to the literature, the photosynthetic activity loss (expressed as an F_v/F_m decrease) is ascribable to either the PSII light reaction centers closure or to the heavy reduced state of the Q_a (Rabinowitch and Govindjee, 1969; Šetlík et al., 1990; Vass et al., 1992; Vonshak and Torzillo, 2004). In this conditions, flashing light could be seen as a way to relief such reducing power excess on the PQ pool due to the mechanism simplified in Fig. 1.3.2. As reported by the aforementioned figure, both continuous light and flashing light cultures in the very initial cultivation stage (a_1 and b_1 respectively) show the very same behavior: absorbed light is converted into an electron moving through the photosynthetic transport chain towards the PQ pool where it is furthermore transported as a reductant of the primary electron acceptor, the Qa. In Fig. 1.3.2, an ideal light-dark duration of 100 ms has been chosen to clearly represents the difference between the two illumination conditions as it is reportedly the PQ pool turnover duration (Falkowski and Raven, 2007). While in

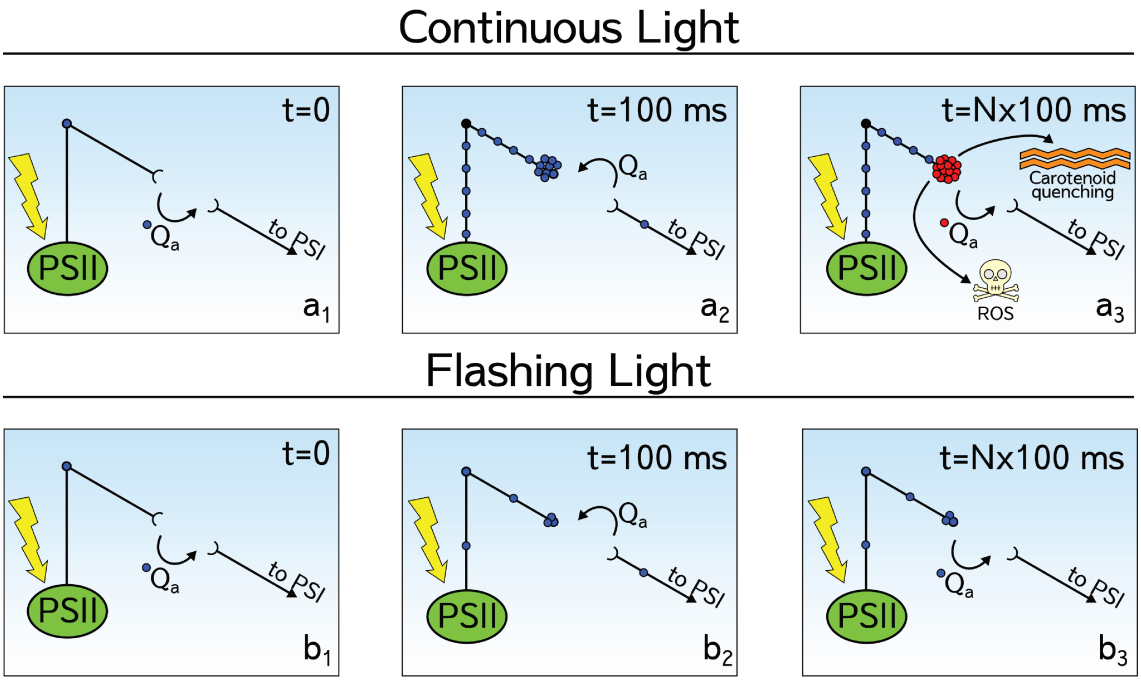

Figure 1.3.2: Schematic representation of the continuous light driven photo-inhibition system as compared to to an ideal flashing light regime. Continuous light photo-inhibition is represented by the upper panels (a_i) and flashing light is represented by the bottom panels (b_i). The flashing light interval adopted is that reported as the average PQ pool turnover duration (Falkowski and Raven, 2007).

Fig. 1.3.2b_2 the culture was kept in the dark for the whole 100 ms, in the corresonding continuous light panel (a_2) it kept absorbing photons up to a point where a continuous wave of electrons (blue dots) started to accumulate above the PQ pool. The increased number of electrons in Fig. 1.3.2a_2 is just a schematic representation of the increased degree of reduction showed by the Qa when exposed to excessive levels of illumination, as described by Šetlík et al. (1990). Eventually, after a time long enough to completely saturate the Qa binding site (Fig. 1.3.2a_3, the accumulated redox potential needs to be quenched by heat generating reactions (NPQ) involving either the accessory carotenoids or the over-abundant oxygen molecules surrounding the PSII. This latter set of reactions conduces to an uncontrolled and copious production of ROS which act as a growth inhibitor by practically destroying all the carotenoids and proteins in the light harvesting complex. On the other hand, if the light is properly flashed for the overall culture duration, the dark phase

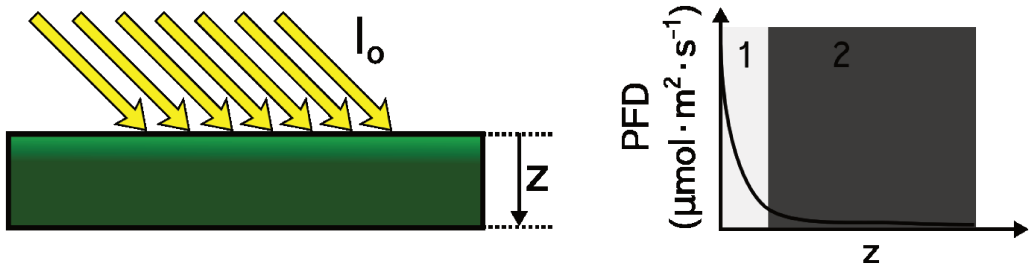

Figure 1.3.3: Culture mutual shading representation. Left: Schematic representation, Right: Typical light attenuation curve. In this example, the incident light I_o is quickly absorbed by the first culture layer (1) becoming thus insufficient for the underlying culture bulk (2). The ratio between 1 and 2 is thought to be roughly equal to 1/9 in sufficiently dense cultures (Torzillo G., personal communication).

becomes an energy-exhaustion process and a sort of steady-state degree of reduction is established on the PQ pool, dramatically lowering the oxidative stress in the cell and ultimately increasing the overall LCE of the culture (Fig. 1.3.2b_3).

Flashing light effect represents for these many reasons an interesting phenomenon which deserves to be investigated further; moreover, being able to include this as a feature in the PBR design process it could significantly increase culture productivity.

1.3.3 Implementing flashing light in photobioreactors

As already stated in section 1.3.1, PBRs are designed to allow a significantly higher biomass concentration to increase the volumetric yield thus lowering the overall production cost and land footprint. However, in such dense cultures, light intensity is drastically lowered by absorption and self shading in the first few centimeters of culture (Acién Fernandez et al., 1997; Garcìa-Malea et al., 2006) leading to an highly photolimited culture, that is the exact opposite problem than that shown by open ponds. In such a scenario the culture can be imagined as divided in two photic zones: 1) the external layer, highly illuminated by direct solar radiation and 2) the inner layer, poorly illuminated by the effect of culture mutual shading (see Fig. 1.3.3).

It has always been common belief that if one could displace the culture from on

photic zone to the other with the proper speed, i.e. a recurring 1-2-1-2... recirculation pattern, an increase in the overall culture productivity could be achieved (Kok, 1953). The concept itself was quite straightforward but the time scale required for flashing light to cause a substantial LCE increase always represented a major engineering problem due to the complicated design needed to attain sufficiently high fluid velocities and the increase in the needed energy to sustain them over the whole culture duration.

The easiest solution for this problem was to increase culture turbulence. The pioneering study from Richmond and Vonshak (1978) in mass cultivation of Spirulina platensis introduced the first consistent evidence supporting this theory. They reported in fact a 66% increase in culture productivity just by doubling the speed of the paddle wheel albeit the small size of the pond (1 m^2) may be considered a major component of this effect which can be difficult to reproduce in large scale ponds. Many articles have been subsequently presented in literature which report increased mixing as a key factor to attain a better illumination inside the PBRs (Carlozzi and Torzillo, 1996; Gobbelaar, 1994; Janssen et al., 2000; Muller-Feuga et al., 2003; Ugwu and Aoyagi, 2011) but the connection between better mixing and better productivity was in many cases still indicated as a possible responsible of the production increase without any quantitative correlation or model except Reynolds number measurements. Only in the last decade a deeper analysis of the effect of fluid pattern on light-dark cycles and therefore on LCE has started to attract interest and numerous studies have been conducted to try and elucidate this dependence. (Giannelli et al., 2009; Merchuk et al., 2007; Pruvost et al., 2006, 2008; Wu and Merchuk, 2004; Wu et al., 2009). Said studies reflected different kind of approaches, from the pure application of mathematical models (Merchuk et al., 2007; Wu and Merchuk, 2004) and fluid dynamics simulations (Pruvost et al., 2008; Wu et al., 2009) for designing the PBR to the empirical correlation of an optimized impeller

with the increase in culture productivity (Giannelli et al., 2009; Pruvost et al., 2006). However, despite all the papers being focused on the effects of the fluid dynamics on the culture productivity they failed in providing a reliable method to assess the effects of light-dark cycles "prior" to reactor construction and certainly provided very limited results tightly bonded with the investigated geometry. Nevertheless, all these studies provided a sound foundation for the development of this work by providing enough insights in the subject:

1. It is of critical importance to have a model, being it mathematical or physical, to correlate culture growth with the increase of the LCE.

2. Computational Fluid Dynamics can dramatically speed-up the determination of fluid patterns as generated by the PBR geometry.

3. Practical correlation between mathematical and physical models can lower both human and machine computational costs by "smoothing edges", rendering the process fast and sufficiently accurate (maximum efficiency).

4. Generalization of the results is still lacking in the field of PBR design and would be a very much appreciated characteristic of any new approach.

1.4 Computational Fluid Dynamics

Computational Fluid Dynamics (CFD) is the science that permits to simulate the fluid behavior in any particular condition starting from characteristic founding equations. This technique has been used on a broad array of applications ranging from the air motion on aerofoils, molding of fluid plastics and up to the study of blood flow in the veins (Marden Marshall and Bakker, 2004). CFD has been also extensively used in chemical applications, especially in the field of fluid mixing which is a branch of chemical engineering closely related to PBR design; for that reason, some

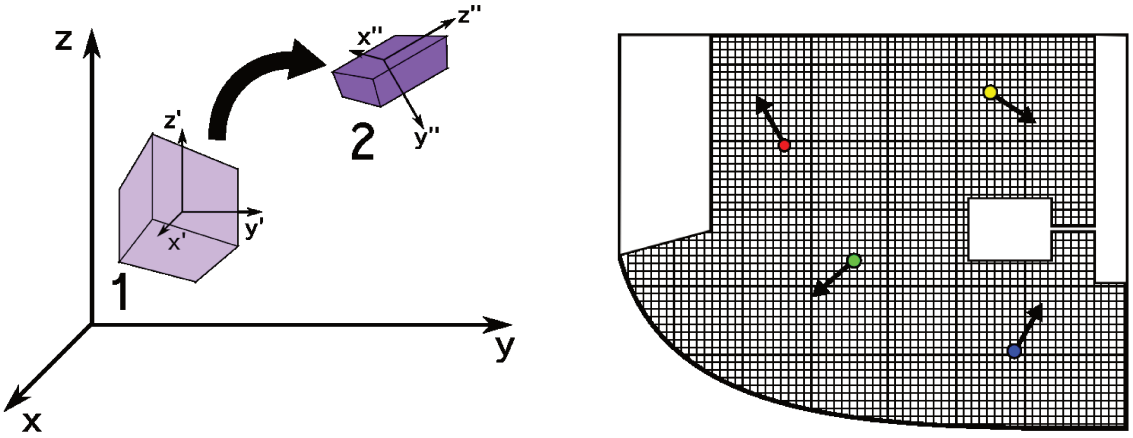

(a) (b)

Figure 1.4.1: Schematic representation of a CFD set-up. (a) The reference elementary fluid packet during its motion inside the simulation domain; (b) A characteristic mesh domain representing one half of a stirred reactor with a Rushton turbine. The points in the mesh represent some arbitrary control volumes whose fluid velocity vector and different properties (colors) are shown to attain an easier visualization.

attempts of CFD-aided PBR design have been reported in literature (Bitog et al., 2011; Pruvost et al., 2006, 2008; Wu et al., 2009; Xu et al., 2012).

1.4.1 Conservation equations

The motion of a small fluid portion inside a flowing continuum may be subjected to two different kind of distortion (Marden Marshall and Bakker, 2004) (Fig. 1.4.1a): translation and/or rotation, where the center of mass of the fluid element is displaced in a new point (from (x_1, y_1, z_1) to (x_2, y_2, z_2)) while probably rotating around an arbitrary point (axis system shift from (x', y', z') to (x'', y'', z'')); deformation, where the shape and volume of the fluid packet are modified on the effect of gravity, pressure or shear forces (shape and color change from point 1 to point 2). To represent such arbitrarily small but finite fluid volume, a suitable computational domain have to be created. In CFD simulations in fact, like any other finite-element analysis process, highly complex NLPDE are discretized in space to match the small variations on a multi-dimensional grid called *"mesh"* where the reactor geometry is simplified by an appropriate number of finite volumes (Fig. 1.4.1b). As shown in

the figure, each finite volume is characterized by a set of properties (defined for each different application) which can be calculated from the equations and stored in the so called "result files" from where the appropriate data analysis is conducted.

As all model in physics, CFD simulations rely on a set of founding equations which are directly derived from mass conservation and momentum conservation with the proper simplifications to render them easy to solve, especially in highly complicated fluid regimes where turbulence is involved. Anyway, the fundamental equations required by any CFD calculation are:

- the continuity equation
- the momentum equation

1.4.1.1 The continuity equation.

The so called *continuity equation* represents the overall mass balance on an arbitrary control volume. It is easy to figure out how many different fluxes may enter or leave said volume but we may always be able to further subdivide the control volume up to the point where each face of the control volume is interested by one flux and we can represent them as in Fig. 1.4.2.

To satisfy the mass conservation principle, the total flux on the control volume must be zero:

$$\begin{aligned}\rho \cdot (U_{x,in} - U_{x,out}) \cdot \Delta y \cdot \Delta z + \rho \cdot (U_{y,in} - U_{y,out}) \cdot \Delta x \cdot \Delta z + \\ + \rho \cdot (U_{z,in} - U_{z,out}) \cdot \Delta x \cdot \Delta y = 0\end{aligned} \tag{1.4.1}$$

which is the mass balance over the control volume $\Delta x \cdot \Delta y \cdot \Delta z$, where ρ is the fluid density and U_i is the local velocity component along the $i-th$ axis. Dividing Eq. 1.4.1 for said volume and expressing the resulting equation for an arbitrary

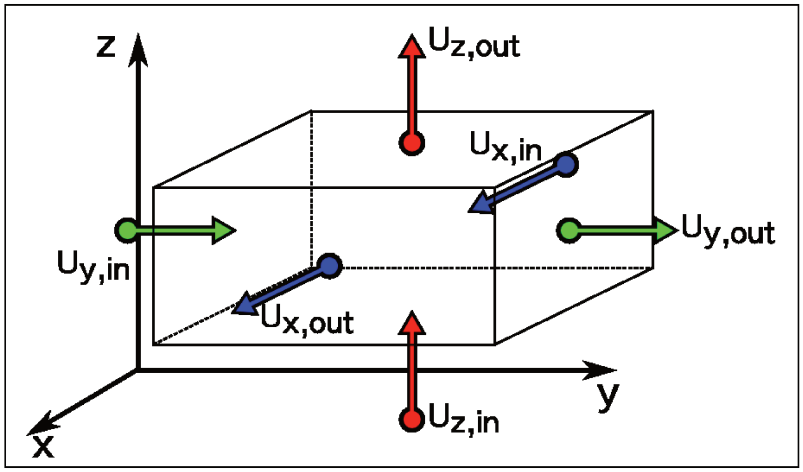

Figure 1.4.2: Visual representation of the flux balance on a control volume. $U_{i,in/out}$ is the i-th component of the local vectorial velocity respectively entering or leaving the control volume. The fluxes have been represented with different colors for each axis direction.

small volume leads to the familiar formula:

$$\rho \cdot \frac{\partial U_x}{\partial x} + \rho \frac{\partial U_y}{\partial y} + \rho \frac{\partial U_z}{\partial z} = \rho \nabla U = 0 \tag{1.4.2}$$

To be precise, the formulation reported in Eq. 1.4.2 is only valid in the case of an incompressible Newtonian fluid while, the general correlation where the density is a space-time variable is:

$$\frac{\partial \rho}{\partial t} + \nabla \rho U = 0 \tag{1.4.3}$$

1.4.1.2 The momentum equation.

The momentum conservation represents the balance of all the forces acting on the control volume:

$$\begin{array}{ccccccc} \frac{\partial \rho \bar{U}}{\partial t} & + \nabla \rho \varphi \cdot \bar{U} & = -\nabla p & + \nabla \mu \nabla \bar{U} & + \rho \cdot \overline{g} + & \overline{f_v} \\ \uparrow & \uparrow & \uparrow & \uparrow & \uparrow & \uparrow \\ a & b & c & d & e & f \end{array} \tag{1.4.4}$$

where:

a: time derivative of the momentum

b: momentum variation due to convection (φ = sum of fluxes on the control volume (as in Eq. 1.4.1))

c: pressure gradient

d: momentum variation due to viscous strains

e: gravitational force

f: surface tension

This set of three equations are also known as the *Navier-Stokes equations*; they are solved to obtain a space-dependent (as in steady state flows) or space-time dependent field for each of the variables, the most representative being the local fluid velocity.

1.4.2 The simplified Navier-Stokes equations

The direct numerical solution (DNS) of the conservation equations is an overwhelmingly difficult computational problem, especially as a consequence of the fact that ultra-fine resolutions are needed in order to have a proper solution (Rusche, 2002). Equations 1.4.3 and 1.4.4 are in fact "scale independent" which means that, the finer the mesh used in the simulation gets, the finer the resolution of the partial derivatives becomes. DNS may be thus interesting for the determination of the exact solution in small scale laminar problems while relevant fluid regimes are, however, either turbulent or extremely turbulent, meaning that DNS solutions may become so long to be practically unfeasible. For this reason, Navier-Stokes equations usually undergo an (almost) mandatory set of further manipulations to render them able to tackle turbulent flows in a reasonable time span. Said manipulation is the *Reynolds averaging* process where the local fluid velocity is decomposed in an equilibrium component and a fluctuating one. The terms in Eq. 1.4.4 including the fluctuating component get averaged to zero (if the time is long enough) leaving only those

terms where the two velocities appear as a product, i.e. those originating from the convective term (Eq. 1.4.4-b):

$$\frac{\partial \rho \bar{U}}{\partial t} + \nabla \rho \varphi \cdot \bar{U} = -\nabla p + \nabla \mu \nabla \bar{U} + \rho \cdot \overline{g} + \overline{f_v} - \nabla \rho \cdot \overline{u_i' \cdot u_j'} \tag{1.4.5}$$

This is the set of the three Reynolds Averaged Navier-Stokes (RANS) equations. During the averaging process however, the fluctuating velocity is introduced as a new variable in the problem which needs to be correlated to the other with new equations in order to have a solvable problem. This is done by the use of the "turbulence models", additional sets of instructions where turbulence is approximated with the following models to be less computation intensive while retaining an acceptable amount of approximation. The algorithm used in this work (*interFoam*) only uses the DNS or the k-ϵ model selectable by a runtime switch, thus a detailed description of the inner workings of each model is behind the scope of this work. Please refer to Marden Marshall and Bakker (2004) for further details. The principal categories are:

- k-ϵ model: robust and stable has been validated against many different reactor configurations. It is the less resource intensive.
- RSM model: the Reynolds Stress Model adds 6 equations to be solved together with the RANS and it thus represents the most resource intensive model immediately after the DNS. On modern computer clusters it can be run with reasonable simulation times.
- LES: the Large Eddy Simulation is the model where large and small turbulence eddies are separated and the simulation is solved only by taking into account the formers while assuming that small eddies will probably have a geometry independent behavior.

Even after the introduction of said models, this kind of calculations maintain relatively high requirements, especially in locally dense meshes, therefore high-end computers are a mandatory requirement. For example, while a 100 seconds simulation in sufficiently dense 2D meshes of a square reactor can be solved with an ordinary multi-core CPU in about one week, the same mesh in 3D would require up to 2 months. It is easy to imagine how long it may take to solve the complex problem of weather simulations that, in fact, require for the software to be executed on cluster computers to have a solution in a reasonably short time.

1.4.3 Multiphase flow

The study of models for a multiphase flow originated as an answer for the great number of industrial applications dealing with more than one phase and because virtually all industrial applications respond to that definition, such models are of vital importance to the chemical engineer. Despite the fact that more general applications have been developed, the "*two-phase flow*" application is by far the most used and diffused one. Moreover a broad variety of two-phase flows may establish in different appliances: liquid-liquid, liquid-gas, liquid-solid and all the other combinations of separated and dispersed regimes (Ishii and Hibiki, 2011; Perry et al., 1999). For this reason, the task of solving this kind of problem with the aid of CFD is of crucial importance. The *two-phase flow* problem is solved by adopting either one of the following approaches:

1. the discrete Dispersed Phase Element (DPE) theory (Rusche, 2002) where the two phases are treated as completely separated phase with different properties and different equations and the DPE is tracked as a Lagrangian object. This is known as an Euler-Lagrange model.

2. the two-fluid model (Hill, 1998) where the two phases are considered perfectly

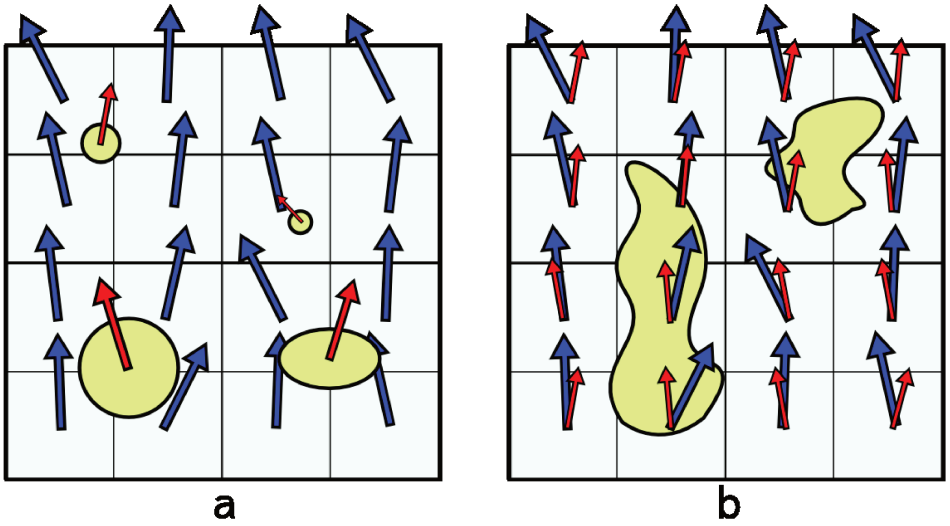

Figure 1.4.3: Two-phase flow solver representation: a) Euler-Lagrangian model (discrete DPE model), b) Euler-Euler model (two-fluids model). Blue vectors indicate the continuous fluid velocity and the red vectors indicate the dispersed phase velocity.

intepenetrating each other as two simultaneous continuum phases. Each phase is then weighted out from the combined continuum by using a partition coefficient (usually indicated as α or γ).

A schematic representation of these two models can be seen in Fig. 1.4.3. The fundamental difference between the two is that, in the first one, the DPE is treated as a completely separated phase (as in reality) where the Lagrangian form of the RANS is solved using the DPE properties and the continuous phase is solved in respect to an inertial axis system (in this case the same used by the mesh). In Euler-Euler simulations both phases are solved against the same axis system (the mesh). This can be clearly seen in Fig. 1.4.3a as each velocity vector of the DPE is centered on the DPE itself while the the continuous phase vectors are centered in the cell centers. This kind of solution is ideal to separate the phases when mass transfer or phase transition calculations are needed as the properties of each phase can be specified separately. As one of the aims for this work was to create a CFD based method to analyze some fundamental PBR parameters as the mixing time or the mass transfer capabilities, we decided to focus only on the Euler-Lagrange

approach even if it represents the most computational intensive solution between the two.

1.4.3.1 Free surface methodologies.

The main characteristic of the DPE model is represented by the physical separation between the two fluids which, in the two-fluids method, is only attained with a partition coefficient. This big difference prompts for a specific resolution algorithm able to calculate an interface between the fluids (where the discontinuity originates) and to track it throughout the simulation. Three different kind of algorithms are known for being able to do this kind of calculation; 1) Surface tracking with the aid of marker particles, 2) Moving mesh that adapts to the fluid shape and 3) Volume tracking with the aid of a surface compressing algorithm. In this work, only the last category of simulation software has been explored by using a solver based on the Volume of Fluid (VOF) algorithm reported for the first time by Hirt and Nichols in 1981.

1.4.4 Simulation software

Various commercial programs including the algorithms to solve two-phase flow problems are available; the only problem in these kind of solvers is the closed source nature of the code itself. Many industrial applications rely on them for the scale-up of numerous plant equipment basically accepting the intrinsic code as an established standard. On the other hand, the application of CFD in a research environment prompts for the need to modify the code to add or remove unneeded features which is something that simply cannot be attained with closed source software. Many research groups then are involved in the creation of original solvers which may or may not attain "universal" results, with the limited risk of generating non repeatable simulations. To completely avoid to build a new solver *from scratch* and to

attain the most general solution possible, we opted for the open source CFD code called OpenFOAM[3]. As reported on the homepage, this software has a wide user base on a broad array of different scientific branches, from chemical to mechanical engineering; moreover, being open source, the solvers can be modified to suit one's needs without making major changes on the consolidated solvers thus requiring less additional validation work. A part of this work has been possible only thanks to this very characteristic together with the author's stubbornness, while it would be near to impossible if a commercial code was used.

In the Materials and Methods section, the use of this code for simulation solving and data processing will be analyzed in depth, however, the technological aspects of the simulation running, source coding and data analysis scripting have been reported in Appendices II and III as a sort of "*how-to*" with the aim of helping in spreading this excellent software.

1.5 Aim of the work

In this work the vexed question about the effect of light-dark cycles on culture productivity have been discussed in depth. It has been at least sixty years since the first inferences about the effects of flashing light on outdoor culture productivity were formulated and yet, no definitive answer was given to the questions "why" and "how" said flashing light influences algal cultures. While many other research groups have tried to explain the flashing light effect through turbulence measures, in this work a numerical parroach was used to tackle the problem. The final aim of the work was to find a correlation between the photosynthetic light conversion efficiency increase and the mixing induced flashing light by using CFD as the connection to allow the future PBR design experts to rely on a powerful computational tool; a tool that

[3]Visit the homepage at www.openfoam.org/ for the free downloadable packages

does not require money and is free to be adapted to any possible PBR geometry. For this reason an open source CFD software was used to be able to follow the culture motion inside the reactor and to assess whether a probable mixing induced flashing light effect could be expected or not. The basic idea was to inject numerical "particles" in the fluid flow to study their motion in the light gradient. Doing so it becomes really easy to determine the magnitude of the PFD variation as sensed by an hypothetic cell moving in the coordinate system integral to the particle itself (i.e. moving in respect to the rest of the reactor). With this system, a time-PFD correlation could be calculated for each reactor position allowing for the location of those reactor regions undergoing a fast swirling motion which could be responsible for an increase in reactor productivity.

After verifying the feasibility of this approach, all the findings were used to create a numerical model to predict the effect of mixing induced flashing light on culture growth. To accomplish this task, two well established PBR geometries, namely the Bubble Column Reactor (BCR) and the Air-Lift Reactor (ALR) were considered as a bench test application for the model as they are characterized by the same overall geometry with just some small changes (the draft tube). It was common belief that ALR is characterized by a better overall productivity when compared to an equivalent BCR because of the recurring light-dark phases originated from fluid revolving around the draft tube. Such an important statement have always remained in the realm of suppositions, in needs for a rigorous validation to be finally accepted. Said validation was carried out by means of the new CFD approach with promising results.

Efforts were also concentrated on the application of the new model on different PBR configurations, namely two cascade PBRs characterized by different fluid flow regimes: the standard flat cascade PBR design was used as a control in the comparison with a wavy bottom cascade PBR. In the latter, strong culture recirculation in

the troughs was correlated to the flashing light effect by means of the aforementioned CFD model. Simultaneously, effects of mass transfer and light regime on culture productivity were investigated to further validate the applicability of the new method under completely different conditions. This work serves thus as a proof of concept of an innovative, economic, fast and reliable photobioreactor design approach.

Part 2

Materials and Methods

2.1 Strains and culture conditions

Two different microalgae have been used to test the CFD model against the broadest array of microorganisms possible. To achieve such a goal would have required us to explore thousands of different microorganisms, rendering the study an highly complex task. We thus aimed for two widely used microalgae to have substantial literature available for the discussion of our results yet selecting two strains characterized by completely different characteristics. With this decision we tried to attain a direct comparison between different organisms uncoupling each other's physical differences by using our CFD model to properly design a new photobioreactor (PBR). The strains used in this work are (see Fig. 2.1.1 for micro-graphs):

- *Haematococcus pluvialis*
- *Chlorella sorokiniana*

H. pluvialis is a green alga capable of producing large quantities of the carotenoid "astaxanthin", an high added value product (Boussiba and Vonshak, 1991). Unfor-

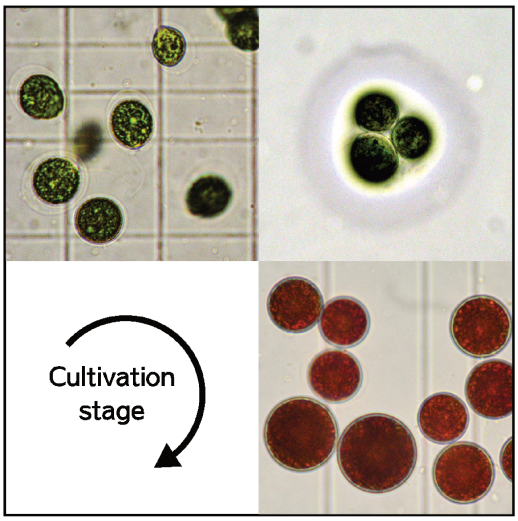

(a) Haematococcus pluvialis micro-graphs. Cultivation stages: 1) Green vegetative cell, 2) Palmelloid, 3) Red cyst

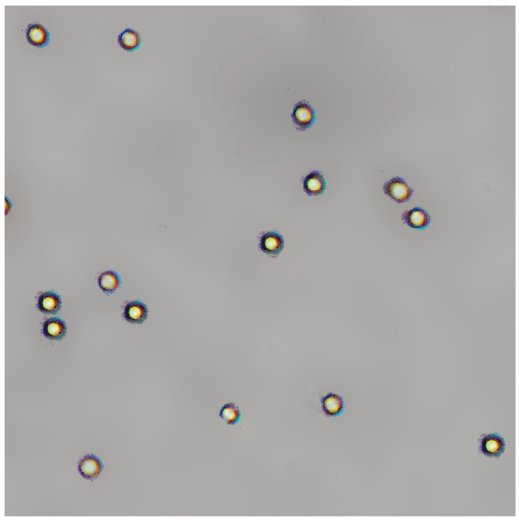

(b) *Chlorella sorokiniana* micro-graph

Figure 2.1.1: *Haematococcus* and *Chlorella* micro-graphs. Same magnification for all the pictures.

tunately, its characteristic growth rate is reportedly very low. Moreover, *H. pluvialis* low resistance to harsh environment changes (temperature, pH, light intensity, etc.) is well known and documented (Harker et al., 1996). On the contrary, *C. sorokiniana* is a fast growing alga able to accumulate more lipids than any other *Chlorella sp.* strain (Putri et al., 2011) and is thus on the list of the eligible candidates for a large scale algae-based oil/biofuel production facility. The higher growth rate is not the only difference between the two algae: *C. sorokiniana* is also able to withstand high shear stress conditions due to its small size, making it perfect for the cultivation in outdoor PBR where culture recirculation is often achieved by using high head centrifugal pumps.

With these differences in mind we proceeded to optimize the culture growth in both strains and in different PBRs while trying to use a CFD model to foresee the effects of geometry on the culture. The cultivation techniques for each alga are hereafter described in detail.

2.1.1 Haematococcus pluvialis

The *Haematococcus pluvialis* strain used in this study was the "*Haematococcus pluvialis* NIES-144" obtained from the Microbial Culture Collection of the National Institute for Environmental Studies (Ibaraki, Japan)[4]. The same strain is known under different names such as "*Haematococcus lacustris*" or "*Haematococcus pluvialis Flotow*" but they all seem to represent the same algal strain which is widespread around the world in temperate climate zones. This particular strain has been isolated in Hokkaido and it is believed to have an optimum cultivation temperature around $20°C$.

[4]The strain page on NIES web portal can be found here:http://mcc.nies.go.jp/strainList.do;jsessionid=58810378AA86CD45012C1A519DFE2D7A?strainId=142&strainNumberEn=NIES-144 (Retrieved April 30, 2014)

Figure 2.1.2: Slants and plates for the long time preservation of *Haematococcus pluvialis* on agarized C media.

2.1.1.1 Slant and plate storage.

Slant and plates for long term storage of the strain were maintained photoautotrophically on agarized inorganic C media, incubated at $20 \pm 0.1°C$ (MIR-153, Sanyo, Japan) as suggested by the culture collection page (Fig. 2.1.2). The composition of the C media is shown in Table 1.11 in Appendix I - Cultivation media. Light was supplied by means of a 18 W cool white fluorescent tube (FL20SS·ECW/18X, Panasonic, Japan) and the intensity was regulated to 10 $\mu mol \cdot m^{-2} \cdot s^{-1}$ by using white semi-transparent sheets. Being this an inorganic culture media it is indicated only for long time storage where almost no growth is desired. For short term storage plates or slants used as a "live" cell stock, 1.2 $g \cdot l^{-1}$ of CH_3COONa were added as a carbon source to support mixotrophic growth.

2.1.1.2 Seeding culture.

The first step in the inoculum scale-up process was the *seeding culture.* A fully growing culture of *H. pluvialis* was concentrated by centrifugation (K-5200, Kubota, Japan) and resuspended in C media up to a final concentration of $3.3 \cdot 10^5$ $cells \cdot ml^{-1}$

to be subdivided in 10 ml aliquots among the storing tubes. Seeding culture was prepared beforehand and was vertically stored in glass tubes (Fig. 2.1.3) maintained under the same conditions of slants and plates. No culture older than 1 month have been used in this study to ensure only the best vital cells were used for the growth experiments.

2.1.1.3 Inoculum scale-up.

Prior to the inoculation in the full scale PBR the culture was further scaled up in two steps. First, *H. pluvialis* cells were grown for four full days in unshaken Erlenmeyer flasks (Fig. 2.1.4a) on *Kobayashi basal medium*, an organic media where yeast extract is supplied to the culture for speeding up the growth (photoeterotrophic conditions). Culture concentration at the end of this step reached $6.5 \pm 0.3 \cdot 10^5$ $cells \cdot ml^{-1}$. Medium composition is shown in Table 1.12. The temperature was kept constant by means of a thermostatic bath (ZL-100, Taitec, Japan) and the light was again

Figure 2.1.3: *H. pluvialis* seeding culture

supplied by means of a 18 W cool white fluorescent tube (FL20SS·ECW/18X, Panasonic, Japan). Light intensity was measured with a quantum photometer (LI-250A, LI-COR, USA) equipped with a cosine corrected flat probe (LI-190, LI-COR, USA) and regulated to 70 $\mu mol \cdot m^{-2} \cdot s^{-1}$.

To achieve sufficient biomass quantities for the cultivation in the big PBR, the culture underwent a second scale-up step by using a small scale bubble column reactor (Fig. 2.1.4b) with a working volume of 200 ml (inner diameter 3.6 cm) sparged with a constant flow rate of 100 $ml \cdot min^{-1}$ (RK-1150, Kofloc, Japan) with a 95:5$^{v}/_{v}$ mixture of CO_2 enriched air. Culture temperature was left unchanged while light intensity was increased to 100 $\mu mol \cdot m^{-2} \cdot s^{-1}$ and supplied with a circular fluorescent tube to achieve a more even distribution. The cultivation media used in this step was the Molina Standard Inorganic Medium (MSIM). These last two measures were adopted to protect the culture from excessive light stress (by higher inoculum concentration) and the stress deriving by a sudden medium change in

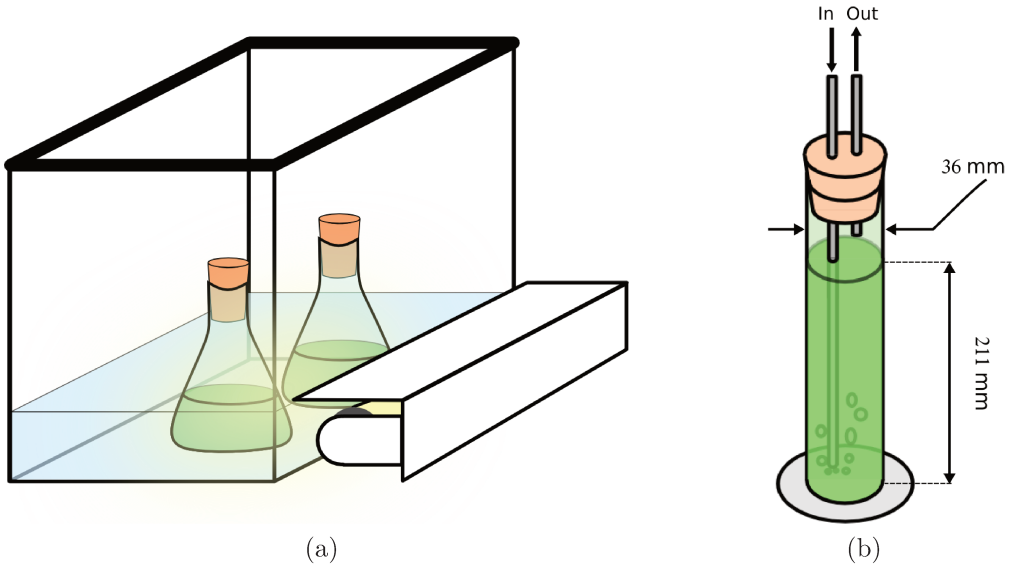

(a) (b)

Figure 2.1.4: Inoculum scale up steps: a) Erlenmeyer flask cultivation with Kobayashi basal medium; b) bubble column cultivation with MSIM medium. In the bubble column stage the light was evenly distributed on the culture by a circular fluorescent tube around the PBR.

the subsequent step. Again, after four full cultivation days the cell concentration reached $9.1 \pm 0.6 \cdot 10^5\ cells \cdot ml^{-1}$.

2.1.1.4 Main cultivation stage.

The main cultivation stage was carried out in the main PBR, a cylindrical 1 liter PBR that could be alternatively operated as a Bubble Column Reactor (BCR) or an Air Lift Reactor (ALR). This reactor, being quite versatile and representing one of the focal points of the whole investigation, deserves an apposite section and we will limit this description to the basilar cultivation conditions. See sections 2.3.1 and 2.3.2 for a detailed description of both configurations.

The culture medium used in this step was the MSIM whose composition is reported in detail in Table 1.13 in Appendix I - Cultivation media. Light intensity and temperature in this stage were kept exactly equal to those in the previous inoculum scale-up phase, while pH was kept constant around 7.4 with an automatic control system (EPC-2000, Eyela, Japan) which controlled the amount of CO_2 in the sparging gas mixture. Sparging flow rate was increased to 200 $ml \cdot min^{-1}$ (RK-1150, Kofloc, Japan) to accommodate for the increased PBR volume. During the growth stage, *H. pluvialis* cultures consume enormous amounts of nutrients, especially N and P which soon become limiting; to avoid the onset of astaxanthin accumulation nutrients were added back to the culture using the MSIM stock solutions after the determination of both N and P.

The main goal set for these experiments was the determination of the maximum growth rate and biomass productivity in correlation with the reactor geometry in *Haematococcus pluvialis* cultures and therefore astaxanthin induction and accumulation experiments have not been carried out in this kind of reactor albeit they may be considered the next step in the PBR optimization.

2.1.1.5 Experiments on temperature.

To evaluate the feasibility of a large scale *Haematococcus cultivation* for astaxanthin production, operation costs have been taken into account by investigating the effects of temperature on the algal growth. The weight of culture temperature control devices on the overall plant energy efficiency is quite relevant, we therefore decided to investigate the best cultivation conditions from an economic perspective. The experiments were carried out in the small scale 200 ml BCR usually used for inoculum scale up (section 2.1.4) by changing the temperature to $20°C$, $23.5°C$, $27°C$ and $30.5°C$ by means of a thermostatic bath (ZL-100, Taitec, Japan). The other cultivation conditions were maintained the same as in Section 2.1.4. For each temperature condition cells were harvested from the reactors after reaching the maximum achievable culture concentration and resuspended to a $1 \cdot 10^6$ $cells \cdot ml^{-1}$ concentration in the nitrogen deficient formulation of the inorganic media (MSIM-N). See the composition in Table 1.13. The temperatures investigated during the astaxanthin accumulation ($20°C$ and $27°C$) were chosen keeping in mind that: 1) the optimum

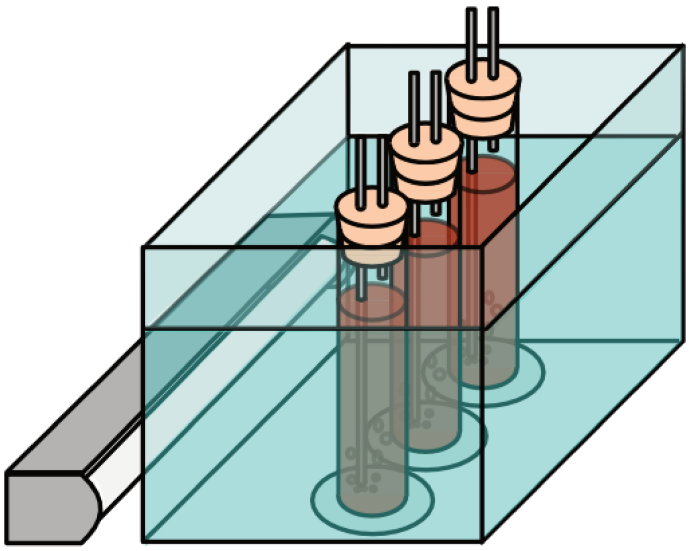

Figure 2.1.5: Astaxanthin induction experimental setup. Three replicates of the experiments where carried out simultaneously in the same thermostatic bath. Picture courtesy of Dr. Yamada Hiroyuki

temperature reported for the *H. pluvialis* NIES 144 strain is $20°C$ and 2) a temperature of $27°C$ seemed to be the proper choice for cost reduction if the reactor was to be operated year round in the Kobe area. Reactors arrangement is reported in Fig. 2.1.5.

2.1.2 Chlorella

The *Chlorella sorokiniana* strain used in this study was kindly provided from the algal collection of the Istituto per lo Studio degli Ecosistemi (ISE, Florence, Italy) by Dr. Torzillo Giuseppe. The strain was selected as it is addressed as the most oleaginous species of the Chlorella family, capable of producing 1.8 times more oil than *C. vulgaris* in the same cultivation conditions. Moreover, the higher growth rate makes it preferable even when compared with other oleaginous algal species (Putri et al., 2011), making it the ideal candidate for a large scale algae-based oil plant. The optimal temperature for this strain is reported to be $27°C$ and it has been kept constant throughout the experiments. This temperature has been deemed ideal for the cultivation in the Kobe area, as already stated in section 2.1.1.5.

2.1.2.1 Slant and plate storage.

C. sorokiniana slant and plates for long term storage were maintained photoautotrophically on agarized *MSIM* media (Table 1.13) with the addition of 1.2 $g \cdot l^{-1}$ CH_3COONa. Slants and plates were conserved in the same incubator used for *H. pluvialis* (Fig. 2.1.2): a light intensity of 10 $\mu mol \cdot m^{-2} \cdot s^{-1}$ was supplied with a 18 W cool white fluorescent tube (FL20SS·ECW/18X, Panasonic, Japan) and the incubation temperature was kept at $20 \pm 0.1°C$ (MIR-153, Sanyo, Japan) to ensure a longer conservation. *Chlorella s.* is a fast growing specimen and needs frequent renovation of the agarized supports to maintain an active growth. On the other hand, the strain is quite sturdy and resistant to outer stresses so that properly maintained

liquid cultures can be used as long as they remain axenic.

2.1.2.2 Inoculum scale-up.

Inoculum scale-up of *C. sorokiniana* cultures was carried out with an approach closer to established algal techniques if compared with what reported in section 2.1.1.3 (Lorenz et al., 2005). Cells were first moved from the plates to 100 ml Erlenmeyer flasks (working volume 50 ml) and subsequently the volume was further increased to 100 ml inside 200 ml Erlenmeyer flasks. The temperature in these steps was kept constant and equal to $27°C$ (MIR-153, Sanyo, Japan) and the flask shaken at 90 rpm in a rotary shaker (Taitec NR-2, Japan). The culture medium used in this step was the MSIM enriched by the addition of urea at the same concentration of Trebon medium (Table 1.14). This solution was adopted because urea can be used by Chlorella simultaneously as a carbon and nitrogen source but the resulting culture media remains still contamination resistant. Moreover, the medium used in the cascade PBR is based on urea as the main nutrient and an intermediate step between two different media can help to lower the sudden environment change.

To efficiently scale up the culture volume in preparation to the 4 liter PBR, two 200 ml BCRs were inoculated from the Erlenmeyer flasks and a constant flow rate of 100 $ml \cdot min^{-1}$ (RK-1150, Kofloc, Japan) with a 95:5$^{v}/_{v}$ mixture of CO_2 enriched air was supplied while culture temperature was left unchanged and light intensity increased to 100 $\mu mol \cdot m^{-2} \cdot s^{-1}$. The culture was carried out for about eight days that was the time needed to attain a total chlorophyll concentration (CHL) of 70 $mg \cdot l^{-1}$.

2.1.2.3 Main cultivation stage.

The alga was cultivated in an open thin-layer PBR, often referred to as “cascade photobioreactor” for its resemblance to a natural cascade stream. *Chlorella sorokini-*

ana was inoculated in full Trebon medium (Table 1.14) to a final concentration of 7 $mg \cdot l^{-1}$ and the pH was kept constant by the addition of 5 $ml \cdot l^{-1} \cdot min^{-1}$ of CO_2 through an aquarium sparging stone placed inside the culture reservoir. Temperature was regulated to $27 \pm 1°C$ by using an aquarium resistor (JET-36 Auto Heater, JAX corp., Japan) even though heating was only needed during the period from mid-autumn to the end of the winter.

The cascade PBR had adjustable inclination, flow rate and illumination and therefore, these cultivation conditions are better described in Section 2.3.3 together with the PBR itself.

2.2 Analytical Procedures

2.2.1 Biomass concentration

Culture concentration has been determined by two different approaches, the culture dry weight (DW) and the cell number. The approach based on the DW gives information on the total culture productivity while completely fails to address changes in culture population (cell number). This problem is not relevant in *C. sorokiniana* cultures where the cells never change shape or size but is of crucial importance in *H. pluvialis* cultivation. In this kind of alga in fact, when growth ceases leaving space for cyst formation, the number of cells does not increase but each cell gets larger and larger resulting in an increased DW. We therefore determined both parameters and, where needed, expressed sensitive data by using the ratio between the two, i.e. the weight of each single cell.

2.2.1.1 Dry Weight

Dry weight has been measured by filtering known volumes of culture on pre-weighted glass membrane filters (Whatman GF/C). The membranes were stored in the oven at $80°C$ overnight and weighted the next day until constant weight.

2.2.1.2 Cell number

The total cell number was measured with a Coulter counter (CDA-500, Sysmex, Japan). *Haematococcus* cells were big enough to be counted this way (15~25 μm) while Chlorella cells were too small and the measurement result was heavily influenced. We thus proceeded to the determination of a correlation factor between culture DW and cell number in *C. sorokiniana* cultures (Section XX).

2.2.2 Chlorophylls and carotenoids

Chlorophylls and total carotenoids have been measured with a spectrophotometer after 90% acetone extraction according to Lichtenthaler (1987). After a first centrifugation step to remove the culture media (5 min@2300g, K-5200, Kubota, Japan) the culture was resuspended in Falcon tubes with 1 ml of Acetone 90%$^{v}/_{v}$ and about 1 ml of glass beads were added. The Falcon tubes were attached to a dedicated Falcon Vortex and shaken for at least 10 minutes in a subdued light environment to avoid light degradation of the pigments. Subsequently, the proper amount of additional Acetone solution was added and the sample was centrifuged once again. The resulting supernatant was read at wavelengths of 450, 630, 645,663 and 750 νm with a spectrophotometer (Pharmaspec UV-1700, Shimadzu, Japan). Equations 2.2.1 have been used to calculate the total chlorophyll and carotenoid concentration.

$$
\begin{aligned}
CHL_A &= ((11.64 \cdot (\lambda_{663} - \lambda_{750})) - (2.16 \cdot (\lambda_{645} - \lambda_{750})) + (0.1 \cdot (\lambda_{630} - \lambda_{750}))) \cdot \frac{V_{solv}}{V_{sample}} \\
CHL_B &= ((-3.94 \cdot (\lambda_{663} - \lambda_{750})) - (2.16 \cdot (\lambda_{645} - \lambda_{750})) + (0.1 \cdot (\lambda_{630} - \lambda_{750}))) \cdot \frac{V_{solv}}{V_{sample}} \\
CAR &= \left(4.1 \cdot (\lambda_{450} - \lambda_{750}) - \left(0.0435 \cdot CHL_A \cdot \frac{V_{sample}}{V_{solv}}\right) - \left(0.367 \cdot CHL_B \cdot \frac{V_{sample}}{V_{solv}}\right)\right) \cdot \frac{V_{solv}}{V_{sample}}
\end{aligned}
\tag{2.2.1}
$$

2.2.3 Astaxanthin concentration

Astaxanthin is, strictly speaking, a carotenoid an thus it can be quantified by the same method used for CHLs and carotenoids. Said method (Lichtenthaler, 1987) suffers from a problem deriving by the low saturation concentration of the 450 νm ABS value which seems indeed calibrated for the low concentrations of accessory pigments present in normal vegetative conditions. Astaxanthin was therefore quantified spectrophotometrically according to Tolasa et al. (2005) but using acetone instead of n-hexane for the extraction. This change prompted for a new calibration which is reported in Fig. 2.2.1. The ABS was pretty linear up to 1 even if the last point is slightly below the interpolating line. We thus decided to set the maximum acceptable ABS for the samples to be 0.9. Interpolating line is shown in Equation 2.2.2.

$$
\begin{aligned}
[AST] &= 3.446 \cdot [ABS] + 2.3 \cdot 10^{-13} \\
R^2 &= 0.997
\end{aligned}
\tag{2.2.2}
$$

2.2.4 Nitrate concentration

Nitrate concentration was used mainly to maintain *H. pluvialis* cultures in nitrogen replete conditions to avoid astaxanthin accumulation. The concentration has been quantified either spectrophotometrically (Pharmaspec UV-1700, Shimadzu, Japan) or by using a portable membrane nitrate sensor (twinNO_3 B-343, Horiba, Japan), depending on the amount of culture sample available. This means that culture

samples from the 1 l PBR were always tested spectrophotometrically while the smaller culture aliquots from the 200 BCR reactors were analyzed with the portable sensor. Furthermore, we also verified that measurements on the same sample made with both methods shown an acceptable degree of agreement (data not shown).

The spectrophotometric determination was carried out according to Armstrong (1963). The culture sample was centrifuged to collect the culture media (5 min@2300g, K-5200, Kubota, Japan) and 150 μl were transferred in a 15 ml falcon tube. In the same tube, 100 μl of 1 M HCl were added and made up to a 5 ml volume with distilled water. Sample ABS was read at 220 νm against a distilled water blank and the concentration calculated by using Equation 2.2.3.

$$[NO_3^-] = 10.068 \cdot [ABS] - 0.561 \qquad R^2 = 0.996 \tag{2.2.3}$$

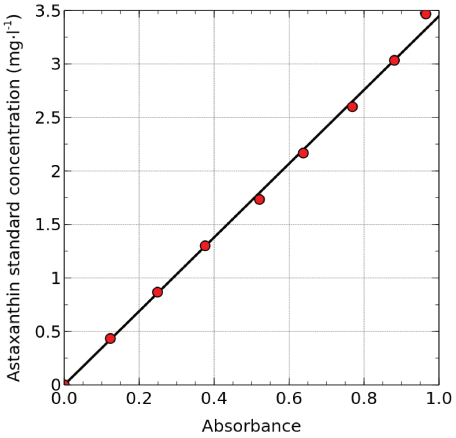

Figure 2.2.1: Calibration line for Astaxanthin extraction in 90% Acetone. Equation 2.2.2.

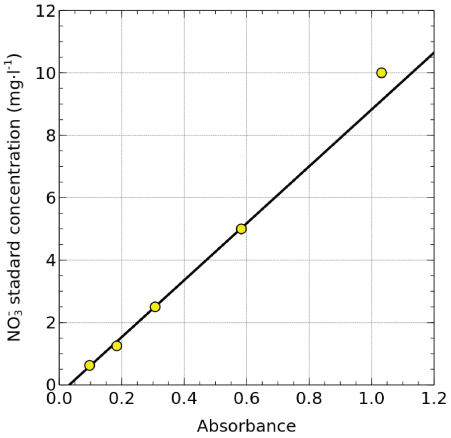

Figure 2.2.2: Calibration line for the determination of nitrate concentration. Equation 2.2.3.

2.2.5 Phosphate concentration

In *Chlorella sorokiniana* cultures, nitrogen was supplied both in the form of nitrates and urea so, due to the lack of a fast non specific determination method, the phosphate concentration was used a the reference parameter to keep the cultures in nutrient replete conditions (Doucha and Livansky, 2009). The measurements were performed according to the procedure described by Eibl and Lands (1969). The culture supernatant was collected after centrifugation and diluted 100 times with distilled water. A total of 8.1 ml of the diluted sample were collected in a 15 ml Falcon tube and 0.9 ml of ammonium molybdate solution (2.5 g of $(NH_4)_6Mo_7O_{24}{\cdot}4\,H_2O$ in 100 ml of H_2SO_4 6 N) were added together with 90 μl of Triton-X solution (1 g of Triton-X diluted to 100 ml with water). After exactly 20 min from the injection of the last reagent the ABS of each sample was read at 660 νm against a water blank. The resulting ABS value was used in Equation 2.2.3 to calculate the concentration of P in $mmol \cdot l^{-1}$.

$$[P] = (369.63 \cdot [ABS] - 3.0609) \cdot \frac{Dilution\,rate}{0.0081} \cdot 10^{-6} \tag{2.2.4}$$

2.2.6 Oxygen Evolution Rate

The OER was measured to quantify the photosynthetic efficiency of *H. pluvialis* under different temperature conditions. The sample collected from an exponentially growing culture was illuminated by red LED lights with variable intensity and the resulting OER was measured with an oxygen sensor (OE-8250M, Tda-Dkk, Japan) whose current transmitted across a 10 $k\Omega$ resistor was read on a digital multimeter (AD7461A, Advantest, Japan) according to Bonaventura and Meyers (1969). The temperature was kept constant throughout the whole experiment (20°C and 27°C) and the calibration of the electrode was carried out against oxygen/nitrogen mixtures

of known concentration.

2.2.7 Fluid velocity

Fluid velocity in particle tracking experiments was measured through high speed photography by recording a 240 fps video (EX-FH100, Casio, Japan) of almost neutrally buoyant alginate beads injected inside the PBR. The beads were 2 mm in diameter and were realized according to Moreno-Garrido (2008) by injecting the alginate in the polymerizing Ca^{2+} solution with a syringe needle. High speed videos have been then exported frame by frame and the speed of each bead have been analyzed manually through open source image analysis software (ImageJ[5] and Gimp[6]).

2.2.8 Conductivity measurements

The conductivity have been used as a reference parameter to quantify the mixing time in each reactor to differentiate the geometries and to validate simulation results. To measure the conductivity, a saturated NaCl tracer solution was added in the PBR and the time course of the solution conductivity was followed with a self-built probe. The probe was realized out of two aluminum rods (1 cm long) placed 1 cm apart for a total measuring cell surface of 1.256 cm^2. The digital multimeter (AD7461A, Advantest, Japan) connected to the probe was used for the data logging. The measuring was carried out by placing the probe 5 mm below the fluid surface in the exact center of the reactor in the PBR and the computational simulation domain.

[5]ImageJ home page: http://imagej.nih.gov/ij/
[6]The Gimp home page: http://www.gimp.org/

2.3 The photobioreactors

Three different PBRs have been used in this study in an effort to correlate the fluid dynamics achieved by different geometries with the light conversion efficiency of the microorganisms. The different PBR geometries adopted were:

- ➙ Bubble Column Reactor
- ➙ Air-Lift Reactor
- ➙ Cascade Reactor

The first two are well suited for this kind of comparison as they essentially consist of the same reactor and the operational shift from BCR to ALR is attained just by inserting a draft tube inside the BCR. The cascade PBR, on the contrary has been used until today in just one configuration where the channel bottom consisted in a simple flat plate. In this study a new shape variation for this reactor has been investigated to verify whether light-dark cycles could be capable of further increasing this PBR's productivity.

2.3.1 Bubble Column Reactor

The reactor consisted of a vertical cylindrical glass chamber with an open top and bottom hosting two metal parts realized in stainless steel. The total vertical length of the reactor chamber was 43 cm and its inner diameter 7.05 cm (Fig. 2.3.1). This cylindrical vessel also contains the thermostatic jacket where water is recirculated by a positive head thermostatic bath (Lauda RE206, LAUDA-Brinkmann LP, USA). The bottom plate hosted the gas sparging nozzles, four holes characterized by an inner diameter of 1 mm (d_n). The top plate was designed to be able to host various accessories like the pH probe (405-DPAS Sc-K85/225, Mettler-Toledo, Switzerland), accessory sampling ports and the exhaust gas outlet. These tree parts were joined

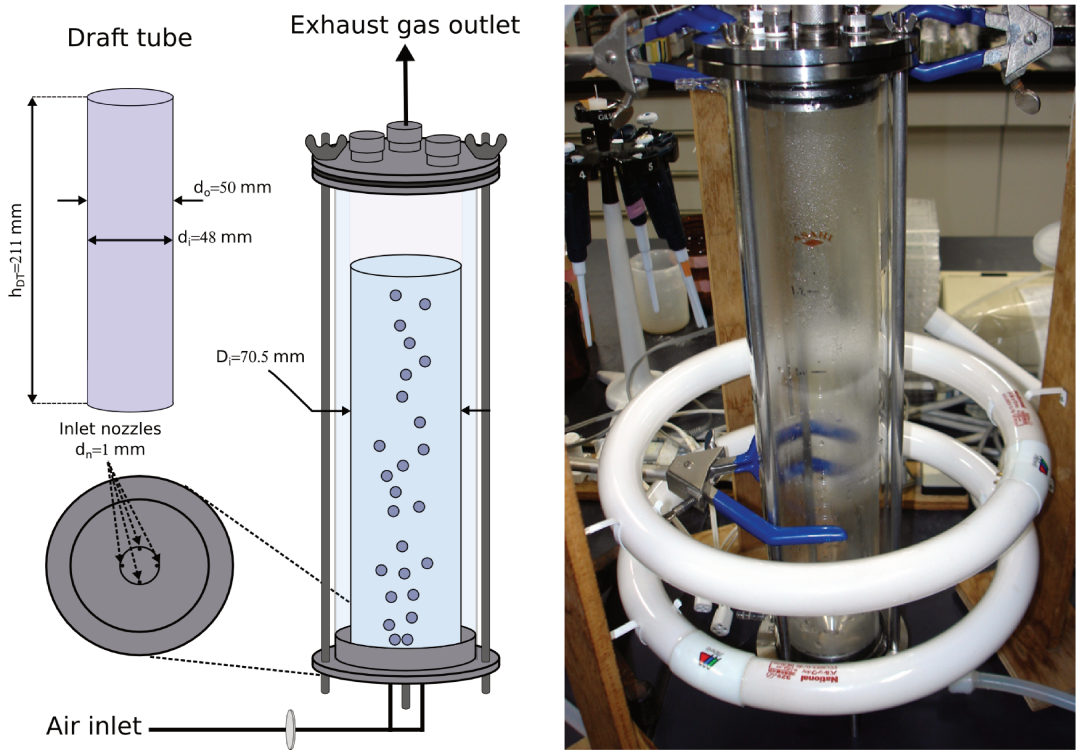

Figure 2.3.1: Bubble Column Reactor scheme: a) sketch of the main reactor components, including the draft-tube used in the ALR configuration; b) A picture of the empty BCR with the cultivation lights set-up and ready for inoculation.

together before autoclaving and assembled permanently with three vertical threaded studs. The junctions between the glass and the metal components were kept sealed with o-rings to avoid fluid leakage and to dramatically lower the risk of culture contamination.

The reactor was used under the cultivation conditions specified in section 2.1.1.4 and the overall experimental setup is schematically represented in Fig. 2.3.2.

2.3.2 Air-Lift Reactor

The Air-Lift reactor consisted in the very same components of the BCR with the only addition of a draft-tube that needed to be placed concentric to the glass vessel to achieve the desired configuration. The draft tube was made of glass and had the dimensions shown in Fig. 2.3.1 that are: height (h_{DT}) 211 mm, outer diameter (d_O)

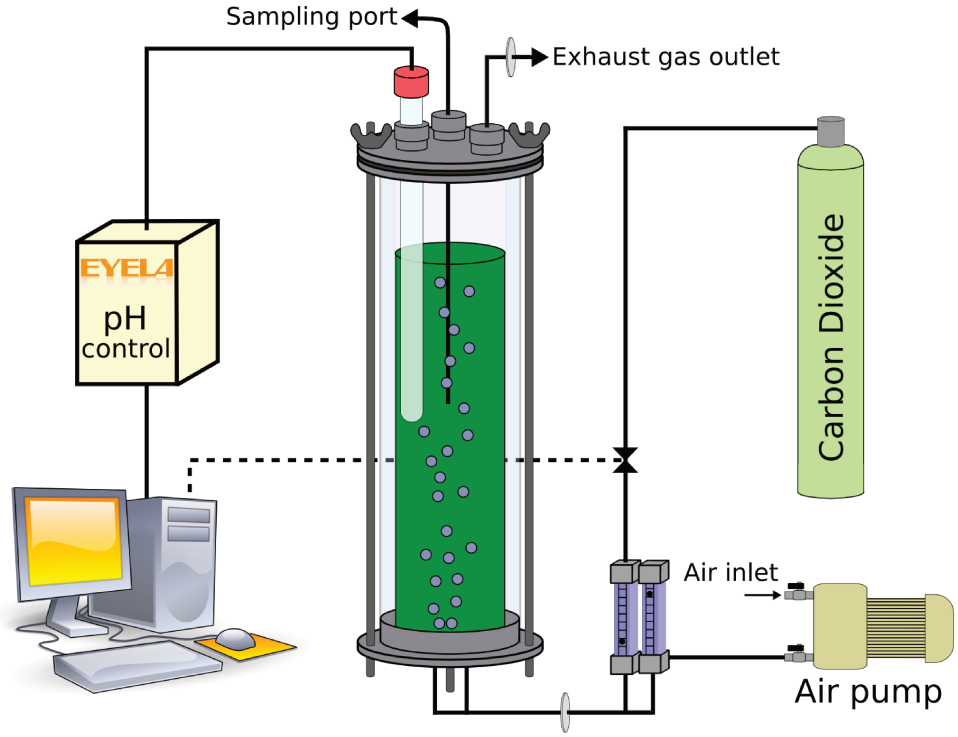

Figure 2.3.2: Bubble Column Reactor arranged for culture growth experiments.

50 mm, inner diameter (d_i) 48 mm. The tube was kept in place by four properly shaped supports that prevented it from tilting or going off-center. Compared with a basic BCR configuration, this element subdivides the PBR inner volumes into two separate sections:

- The riser: it represents the zone where the bubbles rise the fluid with their vertical buoyant motion. This zone can be alternatively referred to as *riser* or *draft-tube*. Culture flowing inside the riser is subjected to the lowest illumination.

- The downcomer: is the zone where the fluid is forced to lower towards the bottom of the PBR to maintain liquid continuity. Culture flowing in the downcomer is subjected to the highest values of PFD resulting in a probably photosaturated PSII.

As already explained in section 1.3.1, illumination in PBRs is of crucial importance and therefore for the design of an optimized PBR, the ratio between the downcomer area (A_{DC}) and the riser area (A_R) must be object of investigation. With the factory parameters here reported the ALR was characterized by an A_{DC}/A_R equal to 1.1, which means the speed of the culture in the riser is the same as that in the downcomer. During the optimization, various values of this ratio were investigated in the simulation but only the most promising one was constructed, leading to a modified draft-tube with the same overall length but with a smaller d_i =34 mm (d_O =3.6 mm) and A_{DC}/A_R=3.22. The new draft-tube was made of clear Plexiglas and was not autoclavable but needed to be adequately sterilized chemically (an diluted hydrochloride solution was used).

2.3.3 Cascade photobioreactor

The cascade PBR represents an optimum trade-off between open and closed PBRs with its high productivity and low costs (Doucha and Livansky, 2009). Three different kind of reactors have been used in this study: 1) flat bottom cascade, 2) wavy bottom cascade and 3) small scale model. All these reactors had the same overall configuration of the typical cascade PBR which has been in use in *Třeboň* (Czech Republic) since 1963 (Fig. 2.3.3a). This was a new small unit operated during the work from Masojidek and coworkers (2011). As shown in the picture, the reactor consisted of four main components:

1. *Culture reservoir*: the culture is collected in this tank as it overflows from the reactor itself. This is also the same tank used for overnight culture storage or during heavy rain days to avoid over-dilution from the rain. The tank volume must then be bigger than the whole culture volume. The cultivation unit reported in Fig. 2.3.3a was characterized by a volume of 170~227 liters.

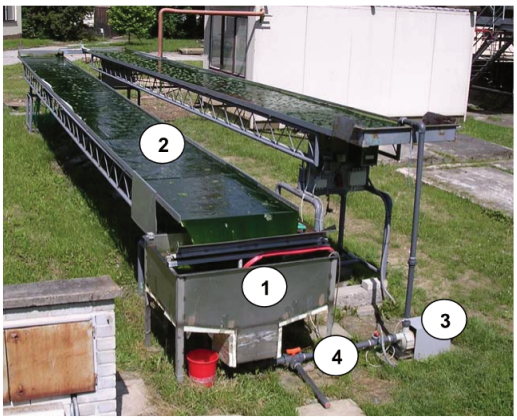

(a) Flat bottom cascade: 1) culture reservoir; 2) culture thin layer; 3) recirculation pump; 4) CO_2 supply

(b) Wavy bottom cascade PBR: the same elements of the flat bottom reactor are present but not highlighted here.

Figure 2.3.3: The two different arrangements of the cascade PBR

2. *Thin layer*: this represents the reactor itself where the culture flows over a series of interconnected glass plates sustained by a stainless steel scaffold. In the wavy bottomed version of the PBR the glass plates were substituted by a stainless steel wavy surface to increase the flashing light effect.

3. *Recirculation pump*: a standard centrifugal pump used to recirculate the pump from the bottom of the reactor to the to manifold. Algae are extremely sensitive to shear stress and tend to be disrupted by centrifugal pumps (Gudin and Chaumont, 1991; Jaouen et al., 1999; Leupold et al., 2013), especially on fragile strains lacking a cell wall. Amongst algae equipped with a sturdy cell wall, *Chlorella* proved to be quite resistant and its use have been therefore investigated.

4. *Carbon dioxide supply*: the supply system for inorganic carbon to sustain culture growth. CO_2 was supplied to the culture through an automatic pH control system or by hand.

All the three types of reactor were based on this layout but had different dimensions, mainly because of the fact that they were built separately by three different research

groups in three different locations (*Třeboň*, Florence and Kobe). Here follows a detailed description of each reactor dimensions.

2.3.3.1 Flat bottom cascade PBR

The reactor reported in Fig. 2.3.3a was characterized by a 24 m^2 surface and an operational culture volume of 180 l which could be, however, easily variated between 170 and 227 l. The reactor open channel was constituted by 12 glass plates (size $l \times w = 2\,m \times 1\,m$) for a total length of 24 m subdivided in two counter-sloped sections (slope $S_o = 0.017$) oriented to the south. Culture was distributed at the top of the PBR by a standard multi-hole manifold (same design in all units) and between the two sections by an horizontal connecting trough. The culture flow rate was kept at 0.027 $m^3 \cdot s^{-1}$ achieving a constant layer thickness (about 6 mm) and fluid velocity (U=0.5 $m \cdot s^{-1}$) throughout the whole reactor. Many stationary waves appeared in the proximity of the junctions between the plates and the walls which may contribute to some extent to the increase of the flashing light effect of this reactor and they have been therefore investigated.

2.3.3.2 Wavy bottom cascade PBR

The wavy bottom cascade PBR can be seen in Fig. 2.3.3b in its installation in the outdoor area of the ISE-CNR laboratories in Florence (Italy). This is the first wavy bottom PBR reported in literature (Torzillo et al., 2010) and has been specially designed by the PBR group of the ISE-CNR to achieve an increased and easily sustainable flashing light effect on the culture when compared on a flat bottom cascade. The effect is supposed to derive from the culture recirculation inside the troughs where a variable light intensity regime that may improve culture productivity is established.

This cultivation unit was slightly smaller than the one in *Třeboň* with a total

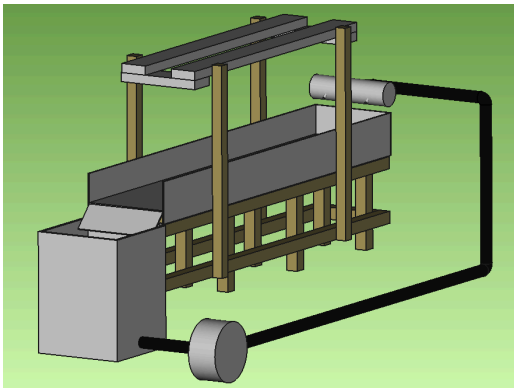

(a) Reactor CAD model used as the base of the project stage.

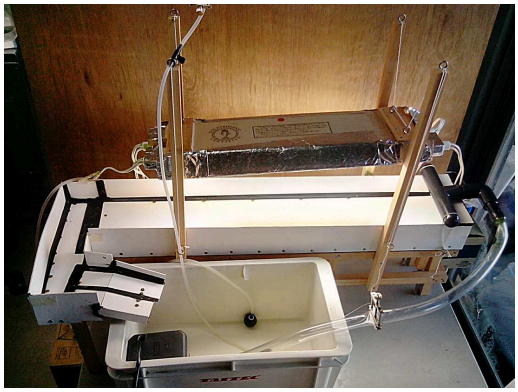

(b) Picture of the PBR after the construction. The project have been slightly variated to comply with the laboratory layout.

Figure 2.3.4: Small scale model of the cascade PBR.

illuminated surface of 5 m^2 arranged on a single slope section (size $l \times w = 5\,m \times 1\,m$) with an inclination ($S_o$) of 0.0873. The increased slope respect to the flat bottom PBR was needed to avoid culture sedimentation in the the troughs and was accounted for in culture speed calculations (see Results and Discussion). The total culture volume was 125 l and was kept constant by replacing evaporated water with deionized water.

2.3.3.3 Small scale model

To validate simulations results without recurring to the big cultivation units (physically placed in other countries) a small bench scale PBR was constructed in pinewood to exactly reproduce the characteristics of the bigger PBRs. The 3D sketch can be seen together with a picture in Fig. 2.3.4. The total volume of this cultivation unit could be variated from a minimum of 4 l to a maximum of 10 l but an increase in the total culture volume results in a loss in the S/V ratio of the reator, hence in the productivity, and we operated the reactor at a fixed 4 l volume. The slope of this reactor could be regulated through a bolt-nut system where the height of the inlet could be set up almost exactly up to $^1/_{10^{th}}$ of a mm by using a Vernier caliper.

Finally, the illuminated path in the sloped section was 70 cm long and 14 cm wide for a total illuminated surface of 0.1 m^2; this surface is indeed really small if compared to those of the other units (5 and 24 m^2) but we were intrested in establishing a relationship between the fluid dynamics of the reactor and the productivity and thus, provided that the channel is wide enough to neglect any border effect, virtually no difference in the fluid motion is recorded. This probably represents the strongest benefit for this kind of reactor: it is an almost linearly scalable structure, at least up to that point where the increased pumping stress does not impact negatively on the cultivation outcome.

2.4 Computational Fluid Dynamics

2.4.1 Simulation software

The computational fluid dynamics software used in this study was the open source suite OpenFOAM[7]. This software has a wide user base and a dedicated branch in the *cfd-online* forums[8] which proved to be a rich a lively source of information. As any open source project, different specialists from different scientific branches have developed many solutions which can be implemented in the code to make it suit one's needs. After intensively using this software four years we realized how important this kind of support is and strongly encourage the reader to try his first steps in the CFD word starting from there.

Regarding the solution procedure, all inner workings have been explained in Appendices II and III and therefore we report here the needed steps needed on order to run the simulation properly. This is the flow we followed for each computation case:

[7]Visit the homepage at www.openfoam.org/ for the free downloadable packages

[8]see all OpenFOAM related issue at the address http://www.cfd-online.com/Forums/openfoam/

➙ *Mesh generation*: the mesh for each case was created using the *blockMesh* software included in the OpenFOAM suite. Mesh size were expressed in meters and an average size of at least $1\,mm \times 1\,mm$ was used. For BCR and ALR simulations, a multi graded mesh was used to better represent the mesh area around the inlet (at least $0.5\,mm \times 0.5\,mm$).

➙ *Definition of fluid properties*: this step was needed to define Phase I and Phase II properties in the simulation config files. We decided to follow the standard notation in OpenFOAM where Phase I represents "water" and Phase II represents "air". With this configuration the partition coefficient α indicates *air* when 0 and *water* when 1.

⊖ Fluid properties (water):

⊕ Density $(\rho_L) = 1000\,kg \cdot m^{-3}$
⊕ Kinematic viscosity $(\nu_L) = 1 \cdot 10^{-6}\,m^2 \cdot s^{-1}$
⊕ Surface tension $(\sigma) = 0.07\,N \cdot m^{-1}$

⊖ Fluid properties (air):

⊕ Density $(\rho_L) = 1000\,kg \cdot m^{-3}$
⊕ Kinematic viscosity $(\nu_L) = 1 \cdot 10^{-6}\,m^2 \cdot s^{-1}$

➙ *Boundary conditions definition*: boundary conditions are defined to change inlet velocities and fluid partitioning inside the reactor. Each case was characterized by different boundary conditions therefore we specified them in each section of the Results and Discussion.

➙ *Simulation run*: the used solver was chosen between the stock VOF solver (*interFoam*) and the solvers developed by us for the tracer and mass transfer calculation experiments.

Simulation were run for a number of timesteps big enough to achieve a stable solution; both ALR/BCR and cascade reactors are characterized by locally transient fluid flows and thus with the term "stable solution" we indicated that regime where the time average of the measured fluid properties was reasonably constant.

2.4.2 Visualization software

Data visualization programs are those pieces of software capable of translating the mesh numerical data to a human-intilligible form where each parameter can be visualized, calculated and eventually exported. The software we used is the Paraview data visualization suite from Kitware[9] which is the one suggested from the OpenFOAM developing team. The open source nature of this software was indeed a powerful addition to our data manipulation software array. Numerous Python script have been developed and integrated in the Paraview software for data manipulation and, moreover, each simulation run involved numerous data analysis steps which in turn made heavy use of such software functions; for this reason, we decided to explain in deep detail each operation in Appendix III.

2.4.3 Fluid velocity

Fluid velocity is one of the fluid propertied directly calculated from the simulation results. However, in particle tracking experiments, local fluid velocities along the x and z axes were calculated for each particle by means of a Python script and the data saved as a Comma Separated Value (CSV) file. Furthermore, to represent the fluid streamlines, the fluid velocity field $\overline{U}$ was integrated with Runge-Kutta 4-5 algorithm of the Paraview filter "Streamlines" ($Filter \rightarrow Common \rightarrow Streamlines$).

[9]The software can be downloaded freely from the homepage: http://www.paraview.org/

2.4.4 Particle Tracking

As already explained in section 1.4.3, the VOF algorithm uses a Lagrangian approach for the solution of the dispersed phase. However, once the solution was achieved (from the solver) and saved in the case folder, it was converted in an Eulerian solution. This means that each cell is characterized by the local fluid properties expressed as an array originating in the center of the cell itself. This array is time dependent but the values always represent the properties of the fluid in the cell volume for a given time frame. It is evident that by using the raw data, no particle tracking could be ever possible (each particle/cell does not move). To solve this problem we used an elaborated chain of filters in Paraview to transform some cells in Lagrangian particles and to follow them during their motion in the reactor[10]. Starting from the case base file (.foam) we added one after the other the filters that allowed us to convert an Eulerian solution in a Lagrangian one. The toolchain is represented in Table 1.1.

1. the base case file: Paraview opens this file by default each time is run in a case directory.

2. Temporal Interpolator: ($Filter \rightarrow Temporal \rightarrow Temporal\,Interpolator$) the filter that permits a more coarse subdivision of the case solution. We used the same time as the simulation timestep to attain the most accurate solution possible

3. Particle Tracer: ($Filter \rightarrow Alphabetical \rightarrow Particle\,Tracer$) this is the filter that actually converts the Eulerian data into Lagrangian data creating one particle out of each selected cell and following it in each interpolated time step t. The position for the timestep $t+1$ are calculated basing on the fluid velocity

[10]This method was developed starting from a post on the cfd-online forum by the user 7islands: http://www.cfd-online.com/Forums/openfoam-paraview/82036-do-particle-tracking-paraview.html#post283475

Filter name	Source	Parameters
1) .foam	---	---
2) Temporal Intepolator	1	Time step= sim timestep
3) Particle Tracer	Source=1 Input=2	Reinjection= sim time
4) Particle Pathlines	3	Mask points= 4000 Track length= 200 Step distance= 0.005 IDChannel= ParticleID
5) Tube	4 (Pathlines)	Radius= 0.0005
6) Glyph	4 (Particles)	Type= Sphere Radius= 0.05 Scale mode= Scalar

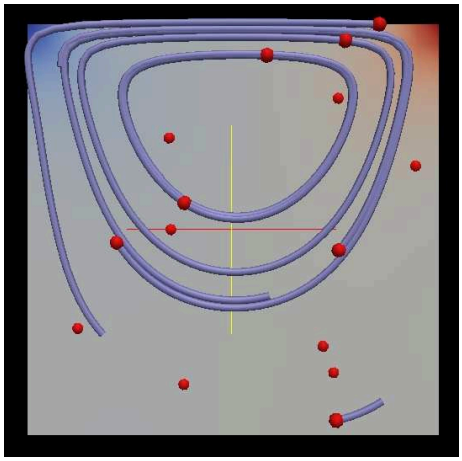

Table 1.1: Filter chain for the Lagrangian particle tracking in Paraview. The values reported here may be adjusted to fit a broader spectrum of different cases. A visualization of the result in a test mesh is also shown alongside the table

and its direction on the previous timestep. In this filter the input and source elements are different so the case file (1) is defined as the point source domain while the time interpolator filter (2) is selected for the calculation of the time variations.

4. Particle Pathlines: (*Filter* → *Alphabetical* → *Particle Pathlines*) for a nice visualization of each particle, the paprticle itself and the trail were generated by this filter. Moreover, this filter is the one that allows for the selection of a limited number of particles (maskpoints) and not the whole number of cells in the mesh.

5. Tube: (*Filter* → *Alphabetical* → *Tube*) the trail of each particle

6. Glyph: (*Filter* → *Common* → *Glyph*) the sphere representing the particle itself

The result of this procedure is a moving set of particles with various "ParticleID" each followed by its trail, as shown in the picture provided by Table 1.1. To extract each particle data as a function of time, the subcomponent "*particles*" in the Particle Pathlines filter was selected and all the timesteps data was saved with the "Save Data" command ($File\ Menu \rightarrow Save\,Data$). The result of this operation was a folder with one particle file for each time step, containing the values for each particle. We had therefore to elaborate a Python script to separate each particle and to save its data as a function of time in a CSV file. The script is reported in Appendix III.

2.4.5 Tracer concentration

The interFoam solver was modified to accommodate for an additional chemical species dissolved in the two-phase system. After this modification the additional tracer concentration (C) was available in the Paraview interface as a normal simulation parameter. To save its value either the Plot Over Line filter ($Filter \rightarrow Data\,Analysis \rightarrow Plot\,Over\,Line$) or the Probe Location filter ($Filter \rightarrow Data\,Analysis \rightarrow Probe\,Location$) were used. Results were saved as usual in a CSV file.

2.4.6 Shear stress

Shear stress has been measured starting from CFD measurements results only and has been expressed as an average of the shear stress of each cell in the mesh. The standard formula for shear stress is:

$$\tau = -\mu\nabla\overline{U} = -\mu \cdot \begin{bmatrix} \dfrac{\partial U_x}{\partial x} & \dfrac{1}{2}\left(\dfrac{\partial U_x}{\partial y} + \dfrac{\partial U_y}{\partial x}\right) & \dfrac{1}{2}\left(\dfrac{\partial U_x}{\partial z} + \dfrac{\partial U_z}{\partial x}\right) \\ \dfrac{1}{2}\left(\dfrac{\partial U_y}{\partial x} + \dfrac{\partial U_x}{\partial y}\right) & \dfrac{\partial U_y}{\partial y} & \dfrac{1}{2}\left(\dfrac{\partial U_y}{\partial z} + \dfrac{\partial U_z}{\partial y}\right) \\ \dfrac{1}{2}\left(\dfrac{\partial U_z}{\partial x} + \dfrac{\partial U_x}{\partial z}\right) & \dfrac{1}{2}\left(\dfrac{\partial U_z}{\partial y} + \dfrac{\partial U_y}{\partial z}\right) & \dfrac{\partial U_z}{\partial z} \end{bmatrix} \tag{2.4.1}$$

This formula has been coded into Paraview by means of the Python Calculator filter ($Filters \rightarrow Alphabetical \rightarrow Pyhton\,Calculator$). First of all, as the fluids are considered isotropic and with time-independent properties, we considered the viscosity μ as constant (not affected by the gradient) and we thus calculated the product between the local velocities and the viscosity ($0.001 * U$) and applied over the result the Gradient of Unstructured Dataset filter ($Filter \rightarrow Alphabet \rightarrow Gradient\,of\,Unstructured\,Dataset$). As the shear stress is represented by the tensor in Eq. 2.4.1, this filter produces a tensor made by 9 parameters named "Gradients_i" with $i = 0 \cdots 8$. It is well known that the magnitude of a tensor is given by:

$$||\mathbf{T}|| = \sqrt{\mathbf{T}{:}\mathbf{T}} = \sqrt{\sum_{i=0}^{8} T_i \cdot T_i}$$

so we coded this formula again with the Python calculator to attain the shear stress magnitude in each cell as a value (and not as a matrix). The Python expression is too long to be reported here but the basic structure was:

$$(Gradients\_0 * Gradients\_0 + \cdots + Gradients\_8 * Gradients\_8)\hat{}(1/2)$$

2.4.7 Culture layer thickness

In the VOF simulations, the partition coefficient (α) is used to identify the liquid and the gas phase; it is common practice to identify the interface between the two where $\alpha = 0.5$. We selected all the cells where this condition was met by using the contour filter ($Filter \rightarrow Common \rightarrow Contour$) and exported the results in a CSV file where we proceeded to calculate the average of the z value in each cell. This average, indicated with s represented the culture thickness in a cascade PBR while it was obviously not measured in the BCR/ALR experiments where the culture thickenss cannot even be defined.

2.4.8 Reynolds number

The Reynolds number have been manually calculated for the cascade reactors according to the formula:

$$Re = \frac{\rho_L \cdot U_x \cdot \left(\frac{L \cdot s}{L + 2 \cdot s}\right)}{\mu} \tag{2.4.2}$$

as explained in depth in Section 3.3.1. To calculate the value by means of CFD, the same equation was programmed in Paraview with the Python calculator filter ($Filters \rightarrow Alphabetical \rightarrow Pyhton\,Calculator$) by using the formula:

$$\begin{aligned} &alpha1 * (1000 * abs(U_X)/0.001 * (s/(2 * s + 1)))+ \\ &+(1 - alpha1) * (1 * abs(U_X)/0.00001 * (s/(2 * s + 1))) \end{aligned} \tag{2.4.3}$$

Please note that Equation 2.4.3 is in represented in the proper Python expression form and only the value of the film thickness (s) is required as the variable. Moreover, please note that this gives the average Re in the flow as the fluid velocity composition

is uses *as is* in the calculations, meaning that for the cells near the bottom, the U_x is practically zero.

2.4.9 Residence time

The residence time of a cell in the thin layer PBR has been calculated as the ratio between the abscissa of the examined mesh cell and the fluid velocity as attained from the simulation itself:

$$t = \frac{x(t)}{U_x}$$

$x(t)$ represents the position reached by the tracer at the time t.

2.4.10 Mass transfer coefficient

Mass transfer coefficient k_La was determined according to two different metodologies:

1. the gassing out method (Wise, 1951)
2. the Higbie penetration theory (Higbie, 1935)

Both methods have been strictly applied only to numerical simulation data and are explained in detail in the *Equations* section (3.4). We decided to use these two kinds of calculation separately to account for the defference in reactor geometry: in the flat bottom cascade PBR it is really easy to calculate the k_La while it is not so trivial for the wavy bottom cascade PBR. This problem required us to incorporate a new equation in the VOF solver to take into account the dissolved CO_2 to calculate the k_La with the gassing out method.

Part 3

Equations

3.1 Volume of Fluid equations

A brief description of the inner working characterizing the VOF method (Hirt and Nichols, 1981) was given in section 1.4.3. We report here in detail the equations used in this method and their description. The set of three equations needed as a minimun requirement for a VOF problem to be saturated are:

$$\frac{\partial \rho}{\partial t} + \nabla\varphi \cdot \rho + \nabla\mathfrak{D}\nabla\rho = 0 \tag{3.1.1}$$

$$\frac{\partial \rho \cdot \bar{U}}{\partial t} + \nabla\rho\varphi \cdot \bar{U} = -\nabla p + \nabla\mu\nabla\bar{U} + \rho \cdot g + f_v \tag{3.1.2}$$

$$\frac{\partial \alpha}{\partial t} + \bar{U} \cdot \nabla\alpha + \nabla\bar{U} \cdot \alpha(1-\alpha) = 0 \tag{3.1.3}$$

where:

- ρ fluid density
- φ sum of fluxes on the mesh cell. The flux on each mesh face is calculated as the ratio between the incoming fluid flow ($m^3 \cdot s$) and the surface of the cell (m^2) and thus φ has the same dimensions of a velocity ($m \cdot s^{-1}$)
- $\mathfrak{D}$ Diffusion coefficient (a.k.a. mass diffusivity coefficient)
- $\bar{U}$ Fluid velocity vector
- μ Dynamic viscosity
- f_V surface tension
- α phase partition coefficient

Equations 3.1.1 and 3.1.2 have been already described in the previous section. The last equation (Eq. 3.1.3) is known as the *indicator equation* or *alfa equation*. To understand the role of this equation in the VOF scheme we have to first explain how the variables and the properties are defined in this algorithm.

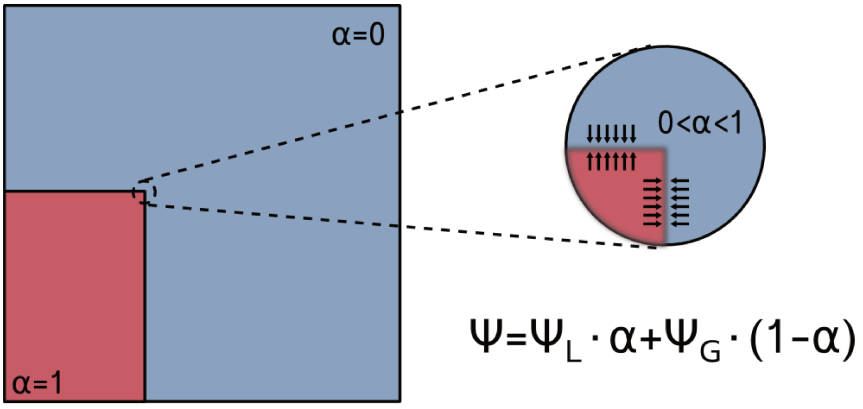

Figure 3.1.1: Multiphase boundary conditions for the "breaking of a dam" case (Hirt and Nichols, 1981)

The VOF is just the name of a surface methodology in the broader concept of the DPE model. In this model, the DPE have to distinguished from the continuous element by means of some function or equation as the computational domain is only one and each variable in the domain must have a unique definition. In this situation how could liquid and gas properties be defined simultaneously in the same mesh while not physically occupying the same mesh cell? This is accomplished by defining an additional dimensionless scalar field called phase partition coefficient or simply phase fraction and indicated by the symbol α. This coefficient is bounded between 1 and 0 by definition to alternatively describe the two phases. By using this scalar together with properly designed boundary conditions, one can define the properties for the liquid and the gas simultaneously and select them by using α as the weighting coefficient. Let's take the "breaking of a dam" example in Figure 3.1.1. The boundary conditions are here represented with different colors where red is the liquid ($\alpha = 1$) and blue is the gas ($\alpha = 0$) and a generic variable ψ (being it a physical property or an unknown) is defined as:

$$\psi = \psi_L \cdot \alpha + \psi_G \cdot (1 - \alpha)$$

The values of ψ_L and ψ_G are then defined separately in a configuration file as two distinct constants. In this configuration, when the VOF solver is initialized, the values for ψ are calculated in each cell according to this definition obtaining $\psi = \psi_L$ where $\alpha = 1$ and $\psi = \psi_G$ where $\alpha = 0$ as expected. As shown in the inset, wherever the value of α lies between the two extremes, the variation between the liquid and the gas is identified as a "physical" interface. It is common practice to assume that the interface is located where $\alpha = 0.5$. The alpha equation was designed with these constrains in mind as an additional conservation equation with a structure similar to the mass conservation equation (the first two terms on the left are the same as in Eq. 3.1.1). The additional term is an artificial surface compression introduced by Rusche (2002) to attain an interface as narrow as possible. The presence of the term $\alpha(1-\alpha)$ ensures that this surface compression is only active in the proximity of the surface itself (the gradient of α^2 is used) and it does not interfere with the calculations in the rest of the computational domain.

3.2 Adding a new equation

A lot of measurements carried out in this work, namely the mixing time calculations and the k_La determination, required the addition of a third component in the multi-phase system. While a n-phase VOF solver is available in the OF suite, none of the available programs were able to take into account the presence of a solute in either phase of the system. To calculate the mixing time of a reactor, the best practice is to inject a tracer in the liquid and to follow the time course of its concentration with a suitable measurements (see Brown et al. 2004 for the basics and Giannelli et al. 2009, Giannelli and Torzillo 2012 and Sanchez Miron et al. 2004 for PBR specific applications). For this reason, the simulation software must be capable of handling an additional solute in the system therefore we had to derive by ourselves a new

equation for this component starting from the basic conservation equation.

3.2.1 Non-volatile tracer

We wanted a new mass balance equation for a new solute in the system. The mass conservation equation expressed as a volumetric concentration is:

$$\frac{\partial C}{\partial t} + \nabla\varphi \cdot C + \nabla\mathfrak{D}\nabla C = 0 \tag{3.2.1}$$

As described in the previous section, due to the nature of the VOF model, in the mesh domain no actual separation exists between the two fluids but just a single continuum where gas and liquid are separated through the use of the α parameter. We thus used this definition to introduce the new solute in each phase by defining its concentration C:

$$C = \alpha \cdot C_L + (1-\alpha) \cdot C_G \quad \text{and} \quad \mathfrak{D} = \alpha \cdot \mathfrak{D}_L + (1-\alpha) \cdot \mathfrak{D}_G \tag{3.2.2}$$

We imagined it to be NaCl (we just needed a non-volatile solute) by setting its properties in the simulation but this choice does not affect the calculation at this stage. We made an important assumption: the jump between the liquid phase and the gas phase is a diffusion driven phenomenon where convection does not interfere. This is a perfectly reasonable assumption if the amount of liquid spraying and sputtering from the surface is negligible. Furthermore we wanted this model to obey to the diffusion theory from Fick where the tracer flux in the domain can be expressed as:

$$\dot{n}_L = \mathfrak{D}_L \nabla C_L \quad \text{and} \quad \dot{n}_G = \mathfrak{D}_G \nabla C_G \tag{3.2.3}$$

This must satisfy the mass conservation by assuming a constant flux throughout the

mesh, both in the liquid and the gas phases:

$$\nabla \dot{n}_{L,G} = \nabla \mathfrak{D}_L \nabla C_L = \nabla \mathfrak{D}_G \nabla C_G = 0 \tag{3.2.4}$$

At this point, as the tracer concentration in the gas phase C_G should be equal to zero we proceeded neglecting that term and then calculating the derivative of C:

$$\nabla C = \nabla \left(\alpha \cdot C_L\right) = \alpha \nabla C_L + C_L \nabla \alpha \tag{3.2.5}$$

To express this concentration in its final form as it appears in the diffusive term of the conservation equation (Eq. 3.2.1) we multiplied for the diffusion coefficient and applied again the gradient to attain the divergence of the tracer concentration:

$$\nabla \mathfrak{D}(\alpha \nabla C_L + C_L \nabla \alpha) = \alpha \nabla \cdot \mathfrak{D}_L \nabla C_L + \mathfrak{D}_L \nabla \alpha \nabla C_L + C_L \cdot \mathfrak{D}_L \cdot \nabla^2 \alpha + \nabla \mathfrak{D}_L C_L \nabla \alpha \tag{3.2.6}$$

This is the definition of the Fick law in the computational domain applied to the new solute concentration. Let us analyze this equation term-by-term.

- $\alpha \nabla \mathfrak{D}_L \nabla C_L$ this term is easily recognized as zero by analyzing Eq. 3.2.4.

- $\mathfrak{D}_L \nabla \alpha \nabla C_L$ According to the distribution theory (Haroun et al., 2010, 2012), the flux can be defined as$\nabla \alpha = -\dot{n}_{L,G}$ which means:

$$\mathfrak{D}_L \nabla \alpha \nabla C_L = -\mathfrak{D}_L \dot{n}_{L,G} \nabla C_L = -\dot{n}_{L,G}^2 \simeq 0$$

  This is only an approximation to simplify the calculations: this equation is added after the main loop and having to calculate the mixed divergence of an unknown (C_L) and an already solved field (α) requires another calculation

round which almost exactly doubles the solution time. Anyway, this is not a far fetched approximation as in the case of a non-volatile solute the flux at the interface is almost zero by definition. It is of course identically zero everywhere else.

➙ $C_L \cdot \mathfrak{D}_L \cdot \nabla^2\alpha$ Once again, $\nabla\alpha = -\dot{n}_{L,G}$ and $\nabla\dot{n}_{L,G} = 0$.

The last term of the equation is the only one that can be considered not null and represents the equilibrium concentration of the solute between the liquid and the gas phases. As the solute is non-volatile, this term represents a constrain where the "outgoing" solute flux is redirected to a zero gas concentration. With this term compiled in the solver the solute will remain in the liquid phase but without it, the solution would be entirely calculated with no interface at all, obviously leading to unrealistic results.

By adding back to the diffusion the convection an the time variation we obtain the complete mass conservation equation in:

$$\frac{\partial C}{\partial t} + \nabla\varphi \cdot C + \nabla\mathfrak{D}\nabla C = \nabla\mathfrak{D}_L C_L \nabla\alpha \tag{3.2.7}$$

which is the same conservation equation as that used by Haroun et al. (2010) but neglecting the phase change. This is the equation that have been included in the OpenFOAM code as a new solver, under the name of *alpha.tracer.interFoam* (see Appendix IV for the instructions to include the new equations in the code).

3.2.2 Volatile solute

The inclusion of this mass conservation equation was required for the determination of the k_La in the cascade PBRs. To measure the mass transfer coefficient between two phases, the actual phase change have to be modeled and implemented in Open-

FOAM. This follows exactly the work from Haroun and coworkers (2010). Briefly, given the same conditions of the previous point, this time the gas concentration can not be neglected as it represents a part of the solution. We therefore obtain:

$$\nabla C = \alpha \nabla C_L + (1-\alpha)\nabla C_G + (C_L - C_G)\,\nabla \alpha$$

and calculating the divergence we obtain:

$$\nabla \mathfrak{D} \nabla C = \alpha \nabla \mathfrak{D} \nabla C_L + (1-\alpha)\nabla \mathfrak{D} \nabla C_G + (\mathfrak{D} \nabla C_L - \mathfrak{D} \nabla C_G)\,\nabla \alpha + \nabla \mathfrak{D}\,(C_L - C_G)\,\nabla \alpha$$

which analyzed term-by-term:

- $\alpha \nabla \mathfrak{D} \nabla C_L = 0$ - as the flux is isotropic in the liquid phase by definition
- $(1-\alpha)\nabla \mathfrak{D} \nabla C_G = 0$ - for the same reason
- $(\mathfrak{D} \nabla C_L - \mathfrak{D} \nabla C_G)\,\nabla \alpha = 0$ - This time there is a phase change and the mass flux leaving on phase and entering the other must be equal in both phases, therefore $\mathfrak{D} \nabla C_L = \mathfrak{D} \nabla C_G$

The last term represents the phase transition condition for a volatile solute. Adding back the other terms of the mass conservation equation we obtain:

$$\frac{\partial C}{\partial t} + \nabla \varphi \cdot C + \nabla \mathfrak{D} \nabla C = \nabla \mathfrak{D}\,(C_L - C_G)\,\nabla \alpha$$

It is worth noting that in the case of $C_G = 0$ Equation 3.2.7 is obtained. If the correlation between the liquid concentration and the gas concentration is known, the term $C_L - C_G$ can be further calculated. In our case we used the Henry correlation and the final result is:

$$\frac{\partial C}{\partial t} + \nabla \varphi \cdot C + \nabla \mathfrak{D} \nabla C = \nabla \mathfrak{D} \left(\frac{1-H}{\alpha \cdot H + (1-\alpha)} \right) C \nabla \alpha \tag{3.2.8}$$

where H is the Henry constant for the solute (in our case, CO_2) which needs to be included in the properties file. This is the second equation that has been added in the OpenFOAM code under the name of *alpha.tracer.interFoam.phase* and was used to calculate the mass transfer coefficient in the cascade PBRs.

3.2.3 Chemical reaction

Measuring the mass transfer coefficient in a bioreactor is different from the determination of the same parameter in other standard unitary operations. The main reason is that inside a bioreactor there is a live organism consuming the species we want to measure (usually oxygen) invalidating any indirect measurement. The same thing happens in the PBRs where the CO_2 concentration is partly lost through evaporation a partly consumed by the culture. The consumption rate is proportional to the growth rate and the CO_2 mass balance requires a generative term.

A daily average CO_2 consumption rate can be calculated by the daily volumetric production (biomass based). For *Chlorella* sp. in a cascade reactor (Doucha and Livansky, 2006), a daily productivity of about 4000 $g \cdot m^{-3} \cdot d^{-1}$ was reported. According to Mandalam and Palsson (1998), 51.4% to 72.6% of *Chlorella vulgaris* biomass is made up by carbon, and thus in one day, an average of 2480 $g \cdot m^{-3} \cdot d^{-1}$ of carbon (C) are fixated in the biomass.

$$100 \cdot K_{CO_2} = \frac{2480 \left[\frac{g_C}{m^3 \cdot d}\right]}{3600 \left[\frac{s}{h}\right] \cdot 24 \left[\frac{h}{d}\right]} \cdot \frac{44}{12} = 1.052 \cdot 10^{-1} \left[\frac{g_{CO_2}}{m^3 \cdot s}\right]$$

This is the linear loss of carbon dioxide due to culture growth in the x direction (culture flow direction) per second. It is represented as $100 \cdot K_{CO_2}$ because this coefficient is subtracted explicitly from the equation on each time step which is 0.01 seconds and thus it needs to be homogeneous with the rest of the equation. This

does not represent an extremely elegant solution and we are still investigating how to include the time dependence in this term during the solution to avoid confusion and erroneous calculations. The mass conservation equations for a volatile solute in the presence of microbial growth is the written as:

$$\frac{\partial C}{\partial t} + \nabla\varphi \cdot C + \nabla\mathfrak{D}\nabla C - K_{CO_2} \cdot \begin{pmatrix} 1 \\ 0 \\ 0 \end{pmatrix} = \nabla\mathfrak{D}\left(\frac{1-H}{\alpha \cdot H + (1-\alpha)}\right) C\nabla\alpha \quad (3.2.9)$$

3.3 Equations for open channels

3.3.1 Reynolds number in open channels

The Reynolds number have been calculated for the cascade reactors according to the standard formula:

$$Re = \frac{\rho_L \cdot U_x \cdot R_H}{\mu}$$

where R_H is the hydraulic radius, measured by the ratio between the flow cross section (A) and the wetted perimeter (P) (Figure 3.3.1):

$$\begin{cases} A = L \cdot s \\ \\ P = L + 2 \cdot s \end{cases} \quad \Longrightarrow \quad R_H = \frac{A}{P} = \frac{L \cdot s}{L + 2 \cdot s}$$

where L is the channel width and s the culture layer thickness. With this considerations, the formula used to manually calculate the Reynolds number becomes:

$$Re = \frac{\rho_L \cdot U_x \cdot \left(\dfrac{L \cdot s}{L + 2 \cdot s}\right)}{\mu} \quad (3.3.1)$$

For the flow of incompressible fluids in open channels, a critical Re value of 1000

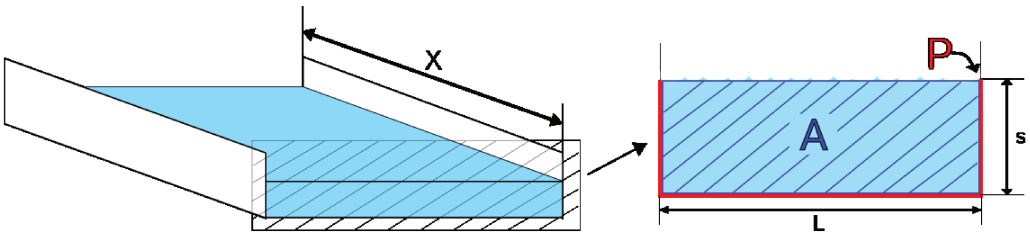

Figure 3.3.1: Characteristic dimensions of the cascade PBR: X, total lane length; L, lateral width; s, culture layer thickness; A, flow cross section; P, wetted perimeter.

is given (Janna, 2010), meaning that:

$$\begin{cases} \text{if } Re < 1000 \Rightarrow \text{laminar flow} \\ \text{if } Re > 1000 \Rightarrow \text{turbulent flow} \end{cases}$$

3.3.2 Laminar flow equation

The laminar flow in an open channel can be calculated by manually solving the balance of the forces acting on an elementary fluid packet. The base for the calculations is represented in Fig. 3.3.2 where the forces acting on the fluid packed, Pressure, gravity and shear stress are indicated. Writing the equilibrium condition along the x axis we obtain

$$\begin{aligned} \sum F_X = &-\tau \cdot dx \cdot dy + (\tau + d\tau)\, dx \cdot dy + \rho g dx \cdot dy \cdot dz \cdot \dot{sin}\theta \\ &+ P \cdot dy \cdot dz - \left(P + \frac{\partial P}{\partial x} \cdot dx\right) \cdot dy \cdot dz \quad = 0 \end{aligned}$$

which can be expressed for volume unit and simplified to obtain

$$\frac{d\tau}{dz} + \rho g \cdot sin\theta - \frac{\partial P}{\partial x} = 0 \tag{3.3.2}$$

The same can be done along the z axis to obtain:

$$\frac{\partial P}{\partial z} = \rho g \cdot cos\theta \tag{3.3.3}$$

The equations 3.3.2 and 3.3.3 when integrated against the boundary conditions (see

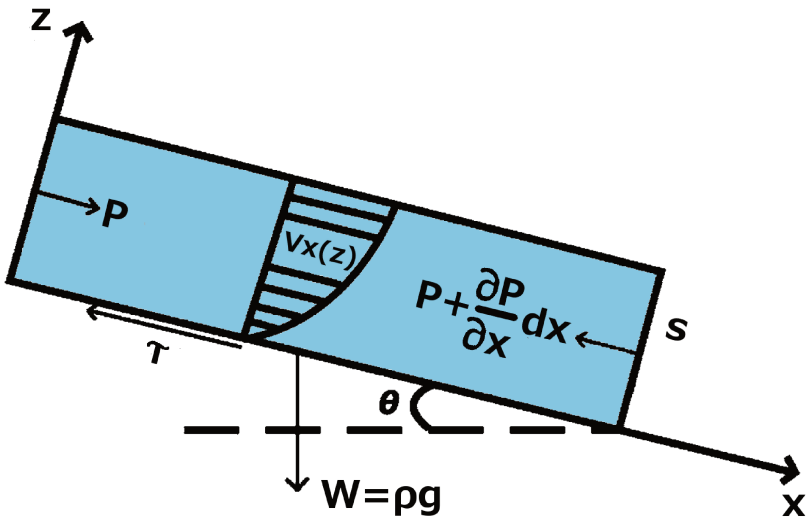

Figure 3.3.2: Elementary fluid packet lying on the inclined surface of the cascade PBR. Only x and z axis are shown while forces acting in the y axis have been neglected. (Picture adapted from Masojidek et al. (2011))

Janna (2010) for the complete dissertation) yelds the expression of the fluid velocity for the laminar flow in a tilted flat open channel used in this study.

$$U_{x,max} = \frac{\rho g}{\mu} \cdot \frac{s^2}{2} \cdot sin\theta \tag{3.3.4}$$

3.3.3 Turbulent flow equation

The equation for the turbulent flow starts from the same hypothesis of the previous section with the only difference that the shear stress is expressed in this case as a function of the wet perimeter (like in closed pipes). The expression is:

$$\tau_w = \rho g \frac{A}{P} sin\theta = \rho g R_H sin\theta$$

where the shear stress can be expressed as a function of a friction factor:

$$\tau_w = \frac{f}{4} \cdot \frac{\rho U^2}{2}$$

which combined with the previous equation and solved for the fluid velocity yields:

$$U = \sqrt{\frac{8g}{f} \cdot R_H \cdot sin\theta} \tag{3.3.5}$$

This is the so called "Chezy equation" which is the starting point used by Manning to derive his formula. Manning noticed by thorough experimentation that the friction factor f was a function of the hydraulic radius:

$$\sqrt{\frac{8g}{f}} = \frac{1}{n} (R_H)^{1/6}$$

which he then used to modify the Chezy equation (3.3.5) into his famous equation:

$$Q = A \cdot U = A \cdot \frac{R_h^{2/3} \cdot S_o^{1/2}}{n} \tag{3.3.6}$$

3.4 Mass transfer equations

3.4.1 Gassing out method

The determination of the interphase mass transfer coefficient $K_L a$ in a bioreactor is a complex task as highly dynamic gas equilibria are involved. Usually this kind of measurement is conducted using the so called "static gassing out method" (Wise, 1951) where a nitrogen scrubbed liquid is sparged with air until constant O_2 concentration is achieved (Figure 3.4.1). As the mass transfer phenomenon is essentially dependent on the reactor's shape and the sparging characteristic, the process can be applied in the reverse direction (gassing in) obtaining the very same results for the $K_L a$ (with negative sign), if the same gas is used and the same sparging conditions can be replicated exactly.

During this kind of determination, the dissolved concentration $C_L(t)$ rises with

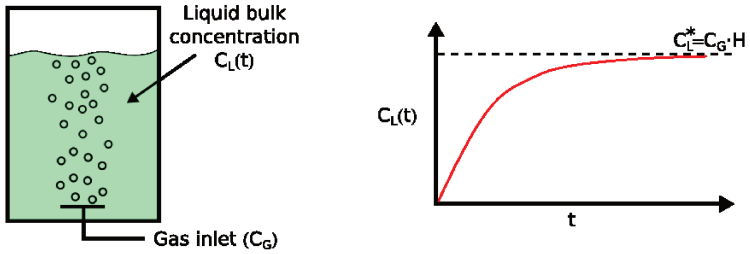

Figure 3.4.1: Schematic representation of the static gassing out method. $C_L(t)$=Liquid bulk concentration, C_G=Gas inlet concentration, C_L^*=Liquid/Gas equilibrium concentration (calculated with the Henry's constant)

the typical saturation curve pattern, where the final achieved concentration is of course the equilibrium concentration (C_L^*) of the particular involved gas with its concentration in the gas phase. The mass transfer equation governing this process is:

$$\frac{dC_L(t)}{dt} = K_L \cdot a \cdot (C_L^* - C_L(t))$$

where K_L is the mass transfer coefficient, a is the Liquid/Gas interface area and C_L^* is the equilibrium concentration in the liquid phase. The value can either be calculated as a function of the gas concentration (using Henry's law, $C_L^* = H \cdot C_G$) or taken directly from the time plot as the final (almost) constant value where time variations in liquid concentration are negligible.

The gas dissolution in the liquid (hence its concentration) is limited by the driving force ($C_L^* - C_L(t)$), which also explains why the concentration rises steeply in the first few seconds (high driving force) and then the slope rapidly lowers to the saturation (low driving force). If we reorganize the equation by separating the variables:

$$dC_L(t) = K_L \cdot a \cdot (C_L^* - C_L(t)) \cdot dt \tag{3.4.1}$$

and then integrate it on the experiment span, we obtain:

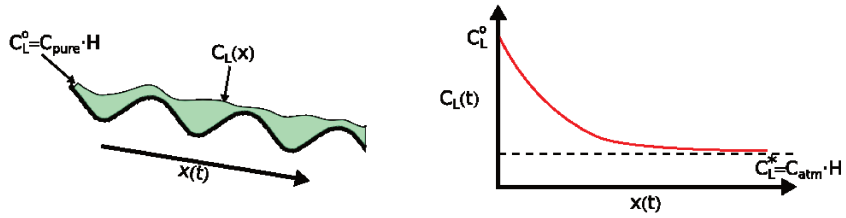

Figure 3.4.2: Schematic representation of the static gassing in method applied to the wavy bottomed PBR. C_L^o=Equilibrium concentration with pure CO_2, $C_L(x)$=concentration as a function of the linear position, $x(t)$=linear position as a function of time. A wavy bottom cascade is represented but the same principle applies to the flat bottom cascade PBR.

$$\int_0^{C_L(t)} \frac{dC_L(t)}{C_L^* - C_L(t)} = K_L \cdot a \cdot \int_0^t dt$$

$$ln(C_L^* - C_L(t)) = -K_L \cdot a \cdot t - lnC_L^* \tag{3.4.2}$$

The integrated formula in Eq. 3.4.2 shows that the logarithm of the driving force is linear when plotted against time and, more important, that the slope slope of the function represents the mass transfer coefficient.

In the case of a sloped cascade PBR the principle is exactly the same as that used in stirred reactors and fermenters with the difference that the concentration distribution is not a function of time but, conversely a function of the position of the fluid element along the reactor linear coordinate (Figure 3.4.2). For this reason, with this kind of system, each portion of the PBR can be considered to be in a steady state, where its gas concentration stays constant during the overall experiment conditions, provided that no variation in the inlet concentration is recorded. To measure the mass transfer coefficient in this configuration a change in the way of data collection must be accounted for.

The gassing out method cannot be applied in this situation as changing the inlet concentration with time up to saturation will cause a change in the concentration of each point along the PBR length which will become both time and space dependent.

In such an assumption, equation 3.4.1 will become a NLPDE that cannot be easily solved by analytical methods. On the contrary, the gassing in method can be used by flushing the reactor with CO_2 saturated water and following the evolution of its concentration along the reactor x axis. We already seen how in microalgal cultures we may need to include the CO_2 consumed by the microorganism; this can be written with the overall balance:

$$\frac{dC_{CO_2}}{dt} = -K_{CO_2} + K_L a \cdot (C^*_{L,CO_2} - C_{L,CO_2}(t)) \tag{3.4.3}$$

This time dependence has to be calculated as a function of the sampling position due to the nature of the cascade PBR. The integration of this equation leads to the same results of the previous case with the only difference that in this case the presence of microorganisms inside the system has been taken into account through the generation term. Integrating Eq. 3.4.3 with the generation term will be difficult but rearranging it as shown by Eq. 3.4.4 will create a linear dependence between two terms with the slope that, once again, represents a function of the $K_L a$ parameter.

$$-\frac{1}{K_{L\cdot} \cdot a}\left(\frac{dC_{CO_2}}{dt} + \dot{n}_{g,CO_2}\right) + Constant = C_{L,CO_2} \tag{3.4.4}$$

By plotting this equation against simulation results we verified that the generation term does not affect the solution which can be safely carried out by using Eq. 3.4.2 even in the presence of the growing culture.

3.4.2 Higbie theory

Higbie predicted in 1935 that the local mass transfer coefficient k_L is a square root function of the time of exposure to the mass exchange:

$$k_L = 1.13 \cdot \sqrt{\frac{\mathfrak{D}}{t}}$$

This equation can be easily used to calculate the mass transfer coefficient on the cascade PBRs when the simulation data is availe. The exposure time is, in fact, the time required for the fluid to travel a length x with a fluid velocity of U_x which are parameters that can be simply retrieved by the simulation results. We obtain therefore:

$$k_L = 1.13 \cdot \sqrt{\frac{\mathfrak{D}}{\frac{1}{U_x} \cdot x(t)}}$$

As we are interested in expressing the mass transfer as $k_L a$, multiplying this equation for the specific volumetric area a (the ratio between the exchange area and the reactor volume) the local $k_L a$ values can be calculated:

$$k_L a = 1.13 \cdot \sqrt{\frac{\mathfrak{D}}{\frac{1}{U_x} \cdot x(t)}} \cdot a = 1.13 \cdot \sqrt{\frac{\mathfrak{D}}{\frac{1}{U_x} \cdot x(t)}} \cdot \frac{X \cdot L}{X \cdot L \cdot s} = \frac{1.13}{s} \cdot \sqrt{\frac{\mathfrak{D}}{\frac{1}{U_x} \cdot x(t)}} \quad (3.4.5)$$

When local velocity data are available, local values for the mass transfer coefficient can be easily calculated, moreover, in the Higbie model there is no dependence on the measured concentration but only fluid dynamic parameters are used (U_x , s and x). In this way, the Higbie model was used to validate the $k_L a$ measurements carried out with the simulation software.

Part 4

Results and Discussion I: Bubble Column and Air-Lift comparison

4.1 Simulation setup

The setup process for the creation of a functioning case includes three fundamental steps:

- ➙ the mesh generation
- ➙ the selection of the discretization schemes
- ➙ the selection of proper boundary conditions

Each step is of crucial importance in the sense that, the smaller error at this stage may lead to a completely unrealistic simulation and one would realize that only after months of work. For this very reason, a lot of time-consuming testing have been carried out in the experimental stage but we don't report it here for brevity. The mesh cell size was especially complicated as a consequence of the cylindrical nature of the PBRs used in this section and required an enormous amount of trial and error even when the proper settings were easily attained by simple mathematical calculations. Moreover, the highly experimental nature of the simulation software left us with a good degree of freedom in regard to the selection of the meshing software. This only added further entropy to the initial set-up "chaotic phase". For these very reasons, only the most important, final and functioning settings are specified hereafter and may be adopted as a good first approach configuration.

4.1.1 Mesh generation

4.1.1.1 3D test run

As a first approach to the problem we attempted to discretize the reactor in the form of a suitable three dimensional mesh with a good degree of fitness with the actual geometry. It is common knowledge that the number of cells constituting a

mesh represents the degree of "fitness" of the mesh itself which directly reflects in the simulation results. As an ideal condition, an infinite number of cells represents the best fit, being the discretized form that nearly approaches the continuum. This is especially true in the case of non-square geometries where curves have to be approximated by an adequate amount of small squares. The direct solution of such a domain is clearly impossible due to the extremely high computational cost required by the multiphase DNS solving algorithms and an optimum mesh size must thus be investigated.

The reactor geometry has been modeled in this step with the Salome platform[11] and subsequently meshed using Netgen[12] to obtain a model consisting of a characteristic number of tetragonal cells depending on the chosen meshing strategy. The usage of this software suite is not reported in detail as it was only used to create the first 3D mesh and soon abandoned. We investigated many arrangements of cells size/cell distribution by varying the software parameters and we ended up with two meshes:

- *Uniform mesh*: The whole mesh has been calculated through the standard Netgen algorithm refining the result by specifying the mesh *finesse* and the maximum cell size. The mesh portion surrounding the inlets was rendered automatically.

- *Composite mesh*: The mesh was decomposed in sub-meshes where different Netgen parameters were imposed to achieve an uniform cell size distribution. In addition to the inner volume mesh, the PBR outside (the cylinder) the inlet and the otlet were modeled with secondary meshes (cell size 0.003 m) obtaining an uniform 0.003 m cell throughout all the reactor volume.

[11] http://www.salome-platform.org/
[12] http://www.hpfem.jku.at/netgen/

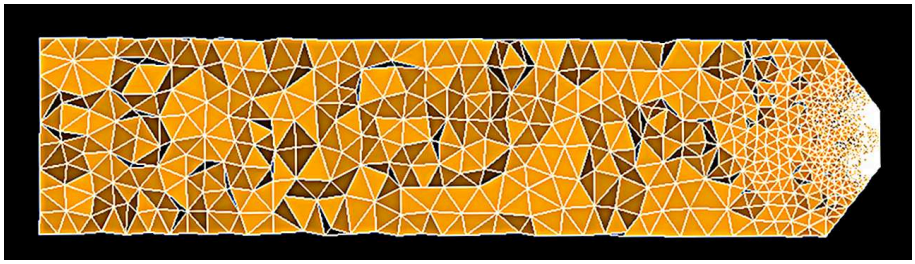

(a) Mesh parameters: Max cell size, 0.03 m, Finesse, *very fine*.

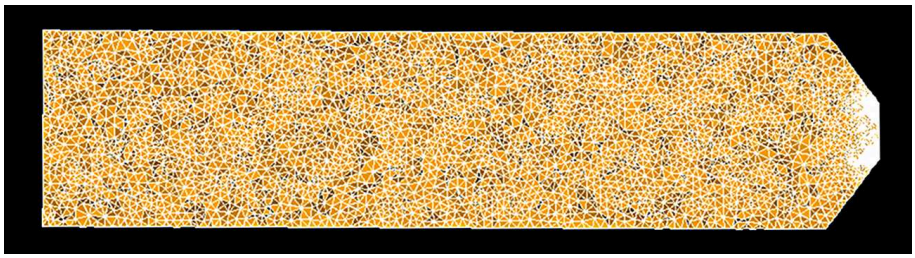

(b) Mesh parameters: Max cell size, 0.003 m, Finesse, *very fine* - Sub-mesh parameters: Max cell size, 0.003 m, Finesse, *very fine* (Netgen 2D algo).

Figure 4.1.1: Differences between a uniform mesh (a) and a composite mesh (b)

As depicted in Figure 4.1.1a and 4.1.1b, the mesh around the inlet area (rightmost end) was exactly the same in both cases while the global cell number grown four folds (135399 cells against 438548 cells). With these results, we carried out a comparison simulation run (data not shown) where we were able to verify that:

1. In our case a composite, ultra-fine mesh is required to properly define the interface between the liquid and the gas.

2. 3D meshes for DNS multiphase solutions are too computational-intensive and require overly long calculation times: the composite mesh required 1 day for 1 simulation second on a 4 core i7 Intel processor.

3. The presence of a small circular gas nozzle ($d_n = 1\,mm$) requires a multigraded mesh with a proper size set around the nozzle itself.

As the figures show, even the finest mesh still seems too harsh to properly represent small bubbles, the size being too big. A maximum size of 0.001 m was probably necessary but the amount of calculation required by such a mesh was way over the

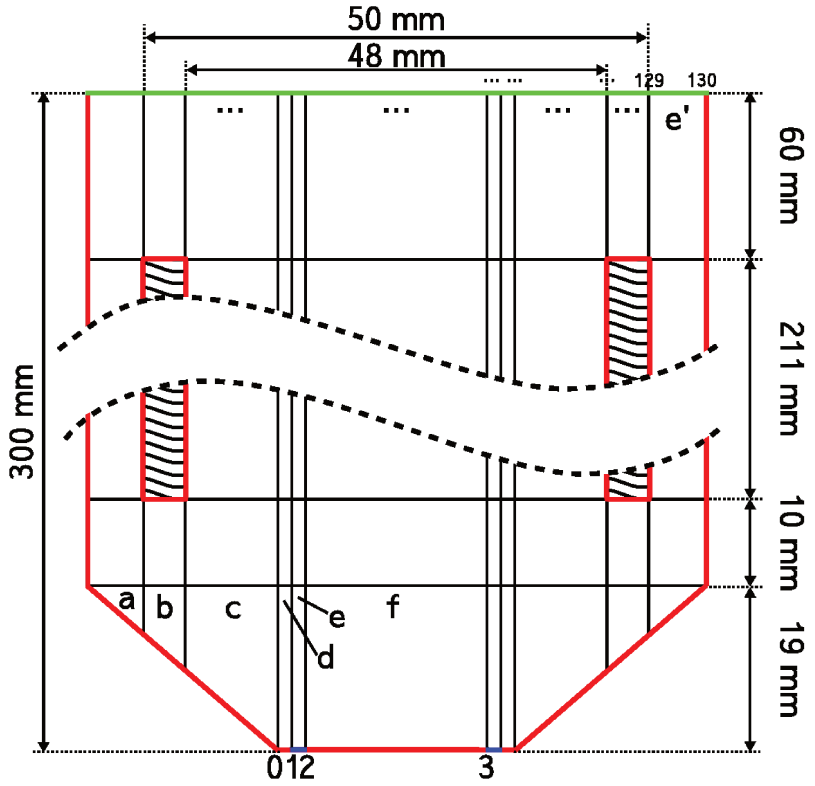

Figure 4.1.2: Two dimensional mesh sketch with dimesions (mm). The black lines only represent fictitious inner divisions in the reactor while colored lines represent the actual boundaries: red=Walls, blue=Inlet, green=Outlet.

maximum capabilities of our hardware. We therefore abandoned this approach and carried on these three hardly learned lessons on the next approach.

4.1.1.2 Functioning case

After the numerous failed attempts with 3D meshes we realized that, given the limited calculation power available, a bi-dimensional domain would be the only feasible approach to avoid changing the algorithm to a lighter one. We then proceeded to the transposition of the scheme in Figure 4.1.2 in the native OpenFOAM format, the blockMesh. The scheme had the very same dimensions of the real PBR: a thin slice including two nozzles placed in the exact center of the reactor was selected and converted to the OpenFOAM mesh file as explained in detail in Appendix II. The dimensions reported in Fig. 4.1.2 are those adopted in the first stage of the

study (prior to the draft tube optimization) and thus are the same reported in the Materials and Methods section (2.3.2). Due to the small size of the inlet nozzles, the mesh was multi-graded allowing for cell sizes that ranged from 0.5 to 1 mm. The resultant total number of cells was around 22,000, which was a higher cell density than that used with good results by Horvath et al. (2009). Moreover, given that the average bubble size was 4 mm, or slightly larger, this cell size was considered a good trade-off between computation time and simulation resolution and was able to accurately represent the liquid/gas interface on the bubbles in the liquid domain by means of the interface capturing algorithm.

4.1.2 Boundary conditions

The boundary conditions represents the physical constrains needed for the solution of the Navier-Stokes equations and each of the settings in the boundary conditions files specifically converts in the value of the constants used in the integration steps. Setting an inlet velocity will result in setting the values for the fluid velocity while setting the property of the walls results in setting the amount of shear stress the fluid will undergo in the walls proximity, etc etc.

In our case, the boundaries shown in Fig. 4.1.2 were defined in the solver according to the following rules. A set of three variables needing a boundary layer condition definition were used in the simulation and therefore we report them one by one hereafter.

- Fluid velocity - $\overline{U} = (U_x, U_y, U_z)$

  - Inlet:

    ```
    type fixedValue;
    value uniform (0 0 0.0424);
    ```

    (calculated form the sparging flow rate and the nozzle cross section)

- ⊖ Outlet:

  `type pressureInletOutletVelocity;`

  `value uniform (0 0 0);`

- ⊖ Walls:

  `type fixedValue;`

  `value uniform (0 0 0);`

  (the fluid velocity on the walls is zero by definition)

➙ Pressure field - p

- ⊖ Inlet:

  `type buoyantPressure;`

  `value uniform 0;`

  (the pressure is calculated by the Stevin Law)

- ⊖ Outlet:

  type totalPressure;

  p0 uniform 0;

  U U;

  phi phi;

  rho rho;

  psi none;

  gamma 1;

  value uniform 0;

- ⊖ Walls:

  `type buoyantPressure;`

  `value uniform 0;`

➙ Partition coefficient - $alpha1$

- Inlet:

  ```
  type fixedValue;
  value uniform 0;
  ```

  (strictly equal to 0, meaning pure gas)

- Outlet:

  ```
  type inletOutlet;
  inletValue uniform 0;
  value uniform 0;
  ```

  (the interface is left open to mass flowing outward or inward)

- Walls:

  ```
  type constantAlphaContactAngle;
  theta0 0;
  limit none;
  value uniform 0;
  ```

  (walls with perfect wettability)

- A further initialization of alpha1 was needed to define the portion of the PBR containing the liquid. We set liquid up to an height of 25 cm (total volume, 1 l).

The simulations for the BCR and ALR configurations have been carried out always using these boundary conditions that moreover, where the same in both reactors.

A side note on the calculation of the gas flow velocity at the inlet in the case of a bi-dimensional mesh. The nozzle system adopted in the ALR and BCR reactors was a four point discontinuous gas bubbling system; in the case of a completely meshed PBR, the fluid velocity at each nozzle can be easily calculated but in the case of a two dimensional mesh the problem of identifying the proper flow rate is not trivial. As shown in Fig. 4.1.3, the bottom part of the reactor is characterized by a circular

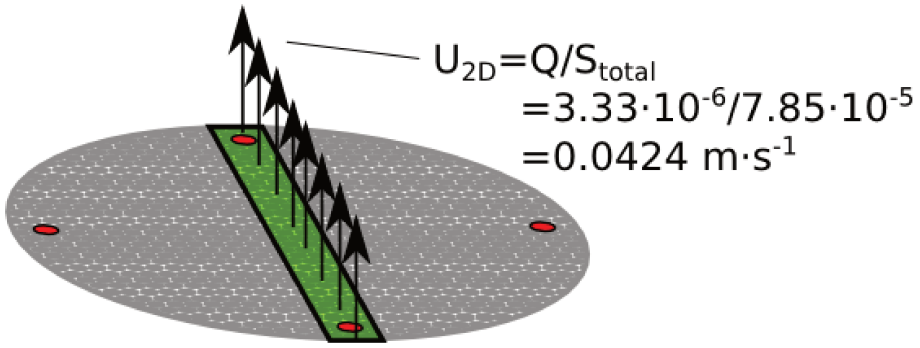

Figure 4.1.3: Simplified inlet gas velocity calculation

steel plate with four holes, each bubbling one fourth of the total flow rate. It was easy to calculate the average inlet velocity referred to the total bottom cross section ad adapt it to the new configuration. In this way, the two dimensional reactor sheet was sparged with the same amount of air even if it was actually containing the half of the total sparging capacity of the reactor. This simplification probably created some problems especially in the ab-initio conditions of the BCR which were completely off when compared with those reported by Horvath and coworkers (2009). To avoid this kind of influence, the minimum simulation time adopted was 100 s which was supposed to be long enough to attain a reasonably stable solution.

4.2 Simulation validation

4.2.1 Fluid regime in the BCR

The results of the fluid flow simulations in the BCR configuration, are presented in Figure 4.2.1. The results are depicted by means of the fluid velocity distribution in the whole domain (left half of the reactor) and the distribution of the partition coefficient (superimposed on the right half). Together with the simulated fluid flow, the visualization of a dye tracing experiment in the real PBR is presented in Fig. 4.2.1-inset.

The BCR showed the onset of four big swirling flows occupying almost all the

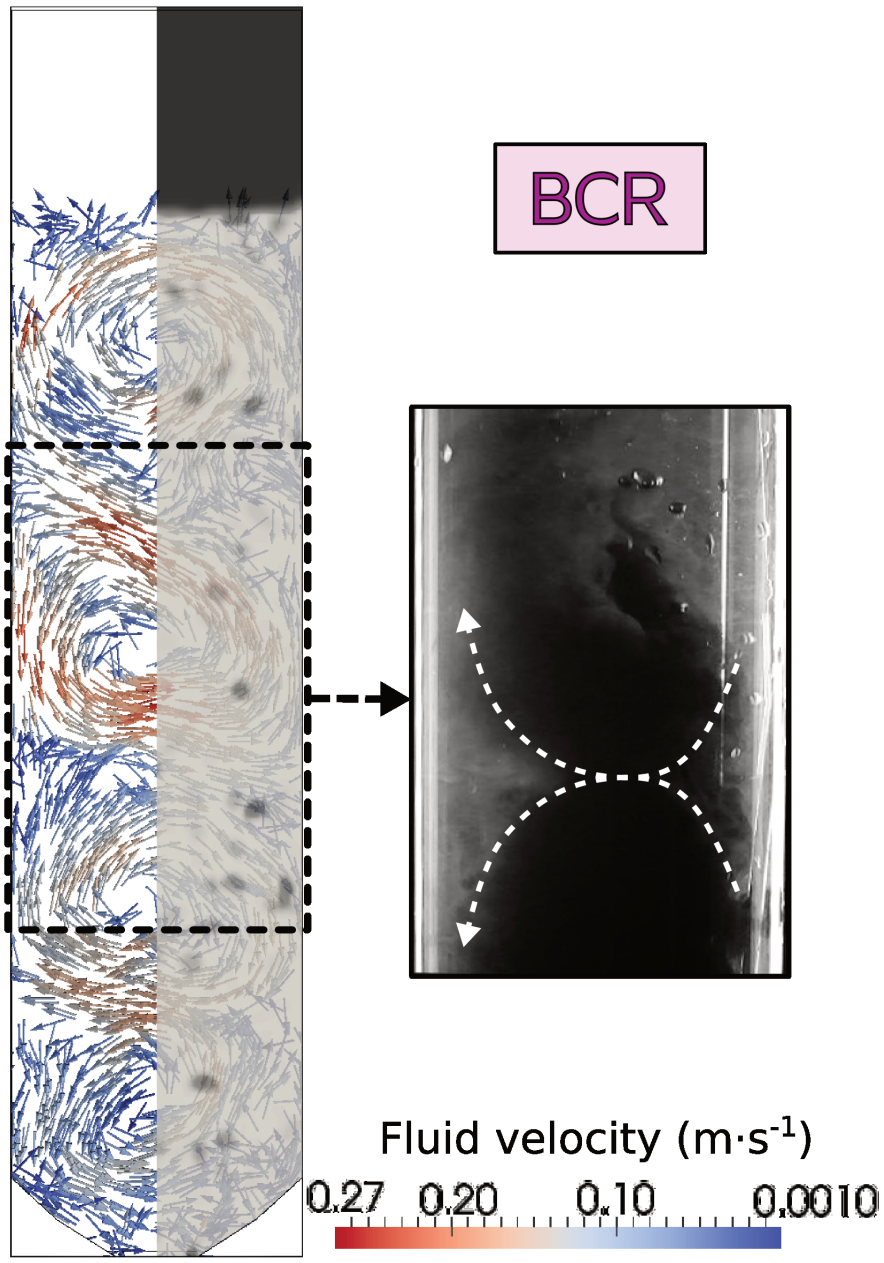

Figure 4.2.1: Fluid velocity vector distribution in the bubble column reactor. On the right half of the reactor, the gray-scale map of the partition coefficient α is represented (black fir the gas, gray for the fluid). *Inset*: one frame extracted from a high speed video from dye tracing experiments. The whirling flows are highlighted by the arrows.

PBR cross section. Each flow was rotating in the opposite direction of the neighboring ones because of the shear forces exerted by the rising bubbles. The presence of these whirling structures can be explained by watching at the lateral displacement of the rising bubbles. By using two characteristic dimensionless numbers typical for the multiphase flows, Eö (Eötvös number) and M (Morton number) the type of bubbles which originate in the reactor can be assessed. For this liquid/gas system the values are:

$$Eö = (\rho_L - \rho_G)\frac{g \cdot d_{bubble}^2}{\sigma} = 2.24 \tag{4.2.1}$$

$$M = (\rho_L - \rho_G)\frac{g \cdot \mu_L^4}{\sigma \cdot \rho_L^2} = 2.63 \cdot 10^{-11} \tag{4.2.2}$$

These values are completely geometry-independent being calculated directly from the fluid properties. The only indirect dependence is hidden in the d_{bubble} parameter which has been found to be a function of the gas flow rate when the nozzle size is fixed (Shen, 1994). This is due to the complicate phenomenon of bubble coagulation which affects all the BCRs above a given inlet flow rate. In our case the flow rate was always kept constant and therefore the calculated values for Eö and M have been treated as constants. According to Krishna and Van Baten (2001), the multiphase flow characterized by these two values is the "wobbling bubble". The experimental observation of both the simulation and the real reactor shown a good correspondence with this conclusion. The rising swarm of bubbles was free to move sideways thanks to the lack of the draft tube and we believe this lateral wide motion was the responsible for the onset of the whirling flows. Moreover, being the fluid motion quite chaotic, the rising flow was counterbalanced by an equivalent, inter-penetrating descending flow which coexisted with the rising one. This random nature could not be observed by the bare means of fluid velocity vector fields and it was first observed by a dye tracing empirical observation (Fig. 4.2.1-inset).

4.2.2 Fluid regime in the ALR

The ALR configuration is presented in Figure 4.2.2 by using the same parameters reported in the BCR (Fig. 4.2.1). The fluid flow observed in the PBR looks well represented by the solved equations: a steady rising motion inside the draft tube is accompanied by a descending flow in the downcomers. This perfectly fits with the ideal fluid circulation always observed in this kind of reactor and represents a first qualitative proof of the goodness of the simulation solution. Moreover, as can be seen from the right half of the reactor, the bubbles (black spots inside the gray fluid) remained confined inside the draft tube which then limited the lateral motion when compared to the BCR. Again, the calculated values for Eö and M are the same as those in the BCR and the swarm of bubbles obtained in these fluids should be of the "wobbling" type. Due to their strong lateral motion, wobbling bubbles rising inside the draft tube shown a characteristic S shaped rising pattern. This unfortunately cannot be visualized by the vectorial fluid velocity distribution in Fig. 4.2.2 due to the Eulerian simulation of the continuous phase. Nevertheless, by visualizing the fluid velocity with the "Streamlines" filter in paraview, a proper visualization can be attained (Figure 4.2.3). Moreover, the effect of this S shaped rising flow could be seen and even recorded on high speed video during the dye tracing experiments. A frame is shown in Fig. 4.2.2-inset. The dye was deliberately injected on the left side of the reactor to visually highlight the fluid segregation happening inside the draft tube:high speed rising bubble exert a strong drag force on the surrounding fluid when rising. On the other hand, the fluid set in motion by the bubbles creates a sort of rising stream following the S shaped bubbles trail. The fluid inside the pockets is set in rotation by the shear forces but the mass transfer between the two fluid portions is extremely limited. All these concepts can be seen in Fig. 4.2.2-inset where, in fact, the dye blackened out all the left side of the reactor without penetrating the small

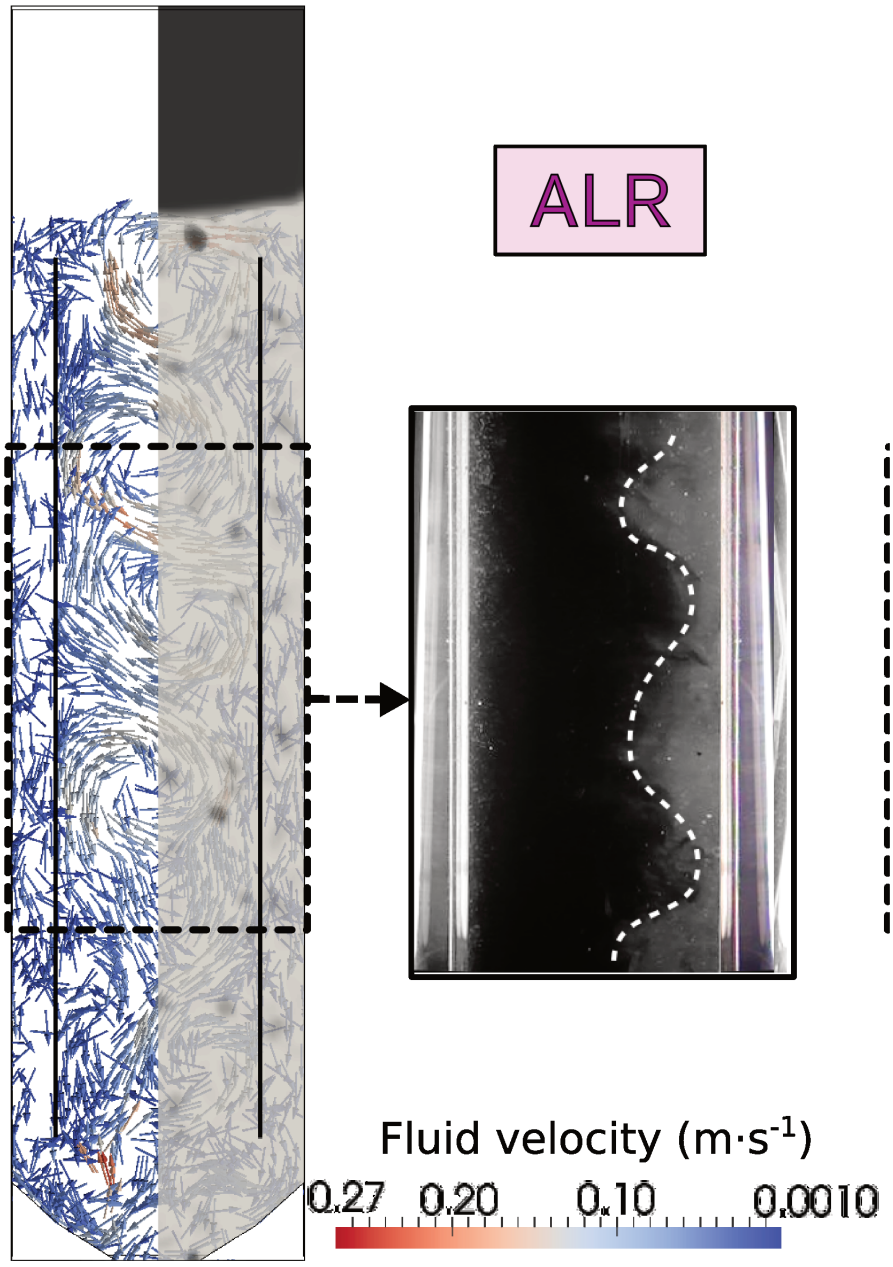

Figure 4.2.2: Fluid velocity vector distribution in the air-lift reactor. On the right half of the reactor, the gray-scale map of the partition coefficient α is represented (black for the gas, gray for the fluid). *Inset*: one frame extracted from a high speed video from dye tracing experiments. Notice the evident entrainment of the clear fluid inside the small high-frequency whirling flows.

swirling fluid pockets on the right. This flow is further explained and visualized in section 4.2.3 when the particle tracking experiments are shown. While the situation in the downcomer is highly dynamic and the number is always changing, about five turbulent whirling flows can be identified inside the draft tube (not present in the downcomers) which lead to think of a strong mixing-induced flashing light effect is established in this part of the reactor.

Regarding the solution and its qualitative consistency with real fluid motion inside the reactor, we found that both geometries were pretty well represented by numerical data. The only point which deserves to be further explained was regarding the ab-initio conditions: while the ALR calculations were able to initialize with any special adjustment of the calculations, the BCR needed way more time to converge

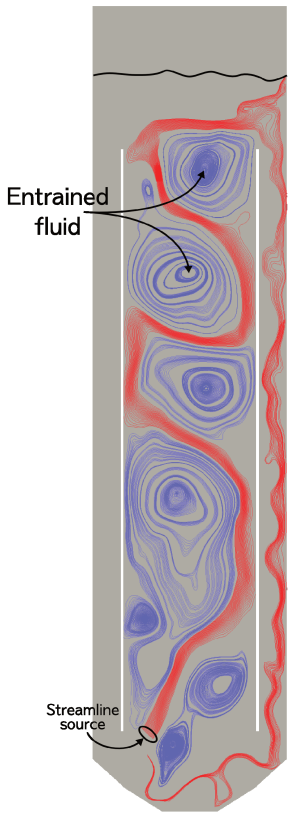

Figure 4.2.3: Fluid velocity streamlines in the ALR. The S shaped rising flow is highlighted in red while the entrained fluid is depicted in blue. Streamlines do not give information on the actual direction of the particles in the fluid but give a good representation of the most probable trajectory. For this reason they have not been used for the flashing time determination.

to a stable solution. Bubbles entering the simulation domain during the first seconds seemed to struggle in their ascending movement due to the undisturbed (i.e. stagnant) liquid layers above. Once this fluid "wall" was broken, the simulation was able to run undisturbed. This behavior is surprisingly not in accordance with the results shown by Horvath et al. (2009) where ab-initio solutions where almost perfectly aligned with those attained by a commercial software and the results of experiments. The parameter responsible for this discrepancy observed in the same numerical code may be either attributed to: 1) the fluid velocity calculations for the 2D mesh or 2) the differences between the inlet flow rates. This second option may be the most influent among the candidates provided that in our case the inlet velocity was almost 500 times lower (96 $l \cdot min^{-1}$ calculated from the superficial velocity against 0.200 $l \cdot min^{-1}$). This represents a big difference in the boundary conditions with a visible direct impact on simulation results, especially for initial time configurations. At higher flow rates the swarm of bubbles rising towards the top can displace the static fluid easily when compared to the feeble bubbles released by a way lower inlet flow rate. For this reason, especially for BCR simulations, at least 100 s of calculated time have been recorded before any further calculation took place.

4.2.3 Particle velocity

After the completion of both simulation calculations, the data has been processed using the visualization software Paraview to isolate pseudo-particles inside the fluid domain and to track their motion as a function of time to obtain a visual the trace of the trajectory along with the fluid velocity in each time step for each particle. Using this data a comparison with real scale motion patterns can be easily achieved. As Paraview does not come with a specific filter to carry out particle tracking, a

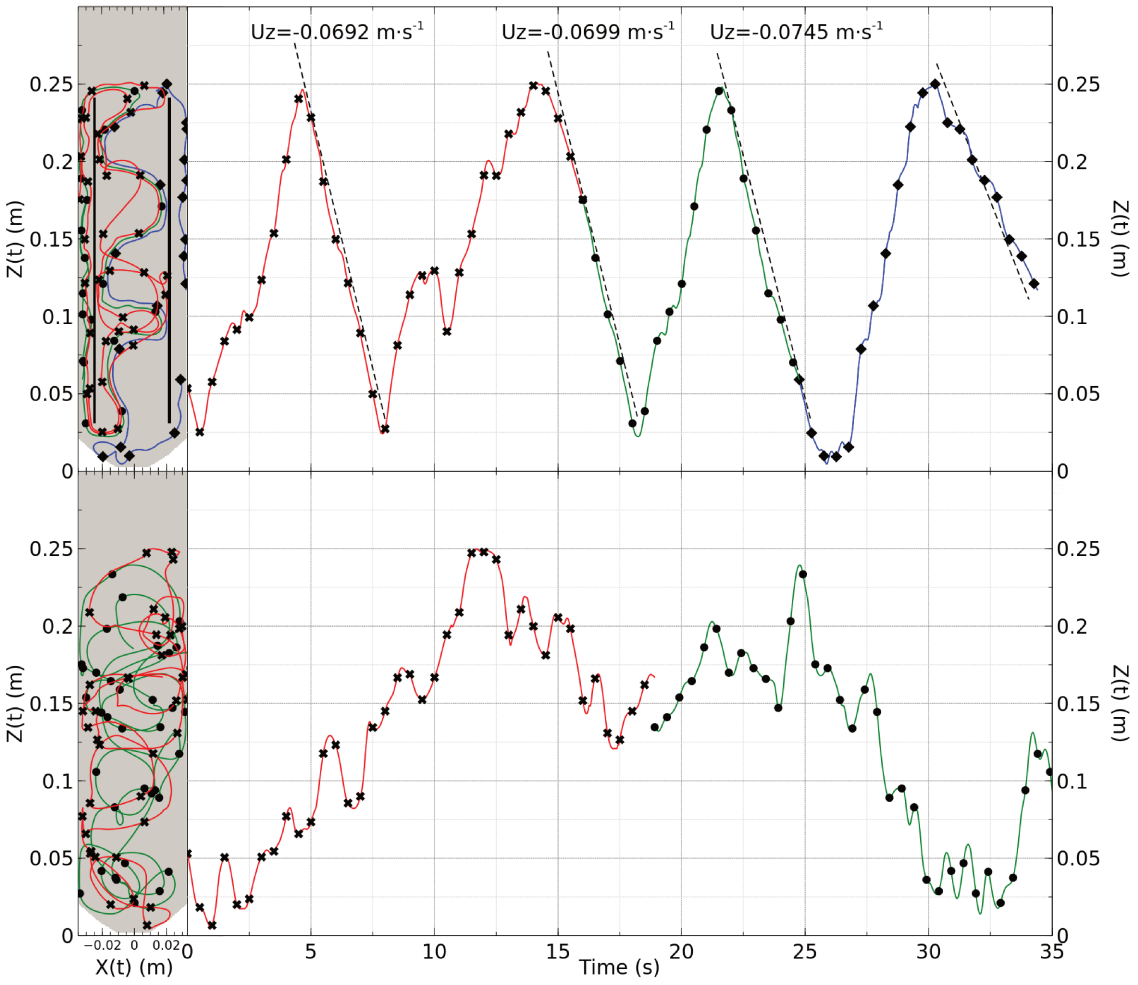

Figure 4.2.4: Lagrangian particle tracking in the air-lift reactor (top) and the bubble column reactor (bottom). The motion along the z direction of various particles is presented in the right plots while in the right panels, the (x, z) motion inside the reactor is shown.

dedicated work-flow has been created using a series of specific filters which worked together to create the particles and then follow their movement in the simulation (see section 2.4.4 for the filter list). The results are shown in Figure 4.2.4. The main panels (on right), represent the position's time course of a small swarm of particles, followed by using the (x, z, t) data attained through the numerical simulation with Paraview and rearranged by a Python script written by us. The sub-panels on the left report only the position as a (x, z) function (no time dependence). Data represented in this way show the trail of each particle in the reactor.

Following the pseudo-particles depicted in Figure 4.2.4, the basic flow charac-

teristics explained in the previous section can be verified easily. In the ALR the particles were moving around the draft tube with a regular circulation speed which was also easily measured, especially inside the downcomers (interpolant lines shown together with their slope in the plot). The left panel shows instead the behavior of each particle by means of the real motion trails attained during the calculations; it is this panel where the peculiar S shaped rising flow is highlighted in a clear intelligible way and represented the starting point for our innovative flashing light measuring technique. Comparing this panel for the two different configurations the differences become even more evident: while the ALR showed a well ordered motion, the BCR was chaotic and random even if the particles where moving in circles, unfortunately with a slow speed to be influenced by the mixing induced flashing light effect.

In a somewhat regular fluid flow like that shown by the ALR, the determination of fluid velocities can be carried out easily inside the real reactor too, without needing complex equipment (like particle image velocimetry apparatus). We thus measured the fluid velocity in the downcomers by high speed photography and image analysis to validate the numerical results. The results of the measurements are shown in Table 1.2 and the IA experimental setup is reported in Figure 4.2.5. To attain a significant fluid velocity average, up to six alginate particles with different form factor and size have been filmed and followed in IA: the results have been compared with those measured in Figure 4.2.4 to validate them. The average fluid velocity measured with each method, 0.0725 $m \cdot s^{-1}$ for with IA and 0.0712 $m \cdot s^{-1}$ for the simulation, were similar and only a 2% deviation was recorded. We thus concluded that the simulation results were in good agreement with the real fluid velocities in the real reactor, at least when the ALR configuration was concerned. Moreover, the self-made Lagrangian particle tracking based on Paraview and Python proved to be able to supply reliable fluid velocities to be used in the determination of the mixing induced flashing light efficiency.

Particle ID	$U_z\,(m \cdot s^{-1})$	
	Experiment	Numerical
1	0.0767	0.0692
2	0.0656	0.0699
3	0.0661	0.0745
4	0.0735	-
5	0.0770	-
6	0.0760	-
Average	0.0725	0.0712

Table 1.2: Velocity data for six alginate particles compared with numerical calculations

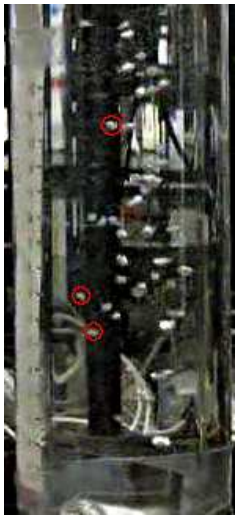

Figure 4.2.5: Frame of the high speed video used for the determination of the fluid velocity. Three particles are highlighted. The reference measure for IA can be seen on the left side .

4.2.4 Mixing time

As a more advanced comparison between the simulation result and the PBR data, we used the mixing time of both configurations measured by means of a numerical approach (OpenFOAM) and a conductivity measurement in the PBR. The numerical determination was carried out by injecting a virtual NaCl tracer in the simulation and by solving the additional mass balance equation added to the *interFoam* solver (see section 3.2.1 for the equation). The results were then analyzed according to section 2.4.5 and plotted against time. The results for both configurations are shown in Figure 4.2.6. After the trace injection, an initial lag in the conductivity measurement was recorded. This is a well known phenomenon, called "response time", which gives a rough indication of the time needed for the the tracer to reach the probe. was recorded. Both measuring methods seemed to be in good agreement: in the BCR the conductivity recorded the first variation after 2 s and the simulation data started to rise steeply after 3.01 s while in the ALR a perfect superposition

was attained with a sensing time of 1.85 s. There indeed was a slight difference in this initial behavior for the BCR, but that can be attributed mainly to the different measuring system. In fact, after 3.5 s, the conductivity data showed a good agreement with the simulated solution. The plot section between the response time and the flattening-out section (up to 20 s) showed how OpenFOAM simulation was able to represent the variations in conductivity, dynamically rising and lowering as a still non-homogeneous tracer was approaching the probe. On the contrary, the physical probe data seemed to be somewhat slower and probably a short time-averaged value was recorded. Nonetheless, both traces overlapped well until the point at which perfect mixing (99.5%) was achieved. The mixing time for the BCR was 58.74 s. In this case, we were able to compare the mixing time attained in our BCR with that measured by Sanchez Miron et al. (2004) with good results, as a similar inlet velocity and similar reactor geometries were used. This was an additional validation of both the simulation and conductivity data.

In the ALR, physical NaCl data seemed to be able to reproduce the initial conductivity rise but the typical ALR's concentration overshoot (Sanchez Miron et al., 2004) did not appear in the conductivity experiments. It has been reported how the tracer injection velocity could affect the mixing time determination (Brown et al., 2004), it is therefore our opinion that this discrepancy between the conductivity and the CFD data could be attributed to this phenomenon. The NaCl tracer, in fact, being injected with a high velocity required for the pulse-response methodology, likely undergoes a first "jet mixing" phase and it further gets diluted by the surrounding well mixed region. Fluid behavior attained by jet mixing experiments is well known for its deviation from the numerical results the almost always overestimate the concentration (for a clear example refer to Marek et al. (2006)). This behavior is better highlighted in the ALR where the tracer "blob" after the injection is entrapped by the rising flow in the draft tube where, on the contrary, in a BCR the lateral motion

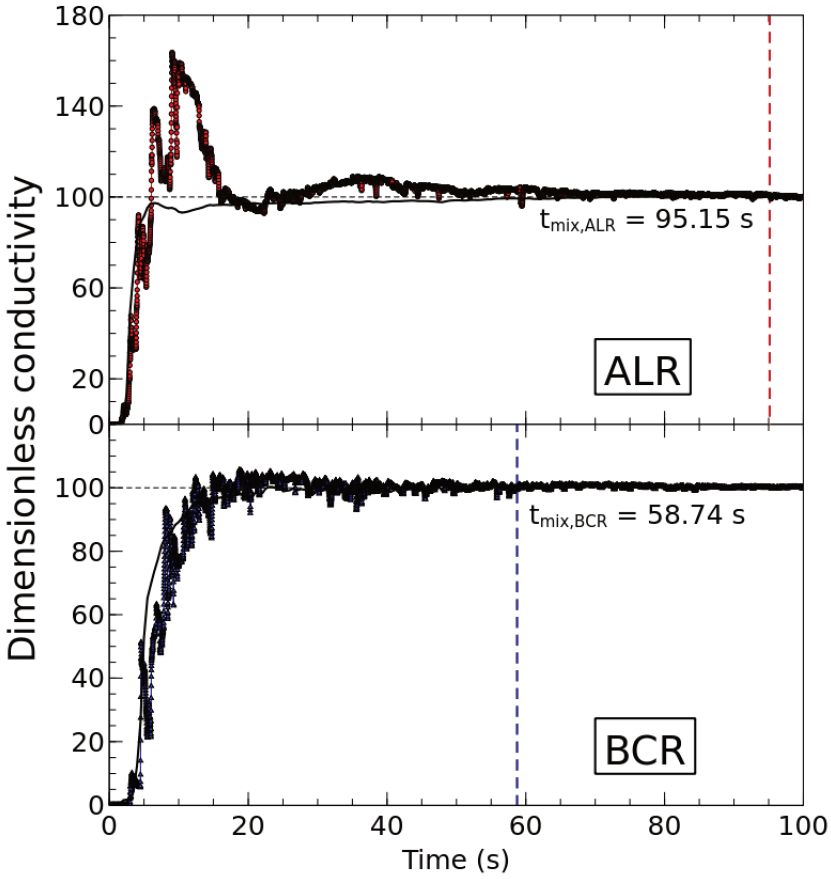

Figure 4.2.6: Mixing time determination in the air-lift reactor (top) and bubble column reactor (bottom) represented by means of dimensionless conductivity time variations after tracer injection. Point data: numerical results from the modified *interFoam*; Continuous line: NaCl conductivity.

is prevailing, somewhat diluting this effect. Moreover, the fluid/tracer entrainment in the swirling pockets in the draft tube can be seen as an additional contribution to this phenomenon. Nonetheless, for longer time scale variations towards the end of the experiments, both measured and simulated data overlapped perfectly and allowed us to determine a mixing time for the ALR equal to 95.15 s. The mixing time for ALRs is strongly correlated to reactor geometry (Chisti et al., 1988) by the means of numerous parameters (the draft tube to reactor cross-section ratio, the sampling position, the injection point, etc.), which render this measurement unsuitable for comparisons between different configurations. Comparing the mixing time achieved for our configuration and operational conditions with data from Sanchez Miron et al.

(2004) we verified that the difference between the values was in the order of 10 to 20 s. These differences may be ascribable to the different geometries of the reactors.

It has been proven that, in geometries characterized by high mixing-dependent fluid entrainment, more than the total mixing time value, the response time could better fit for mixing efficiency comparisons (Giannelli et al., 2009). In this BCR-ALR comparison, the ALR proved more responsive to punctual fluid property fluctuations, making it likely more reactive on a light harvesting point of view. A cell entrained in a vortex subjected to flashing light may be considered an instantaneous "property fluctuation" which will be better dispersed in the fluid bulk in the ALR reactor. A better excited cell dispersion entails a better culture replacement in the swirling flows which ends up in an increased PBR efficiency. It was our aim to prove this statement by means of local particle tracking measurements.

4.3 Flashing light conversion efficiency

4.3.1 Culture growth

To lay down a model able to predict any flashing light effect on the culture by means of mathematical calculations, the foundation to be consolidated before any other is the relationship between the flashing time and the increase in culture Light Conversion Efficiency (LCE). To achieve this basilar relationship we carried out growth experiments with *H. pluvialis* under flashing light conditions. As reported by Kok (1953) the optimal duty cycle for increased productivity in mixed PBRs is 18% and we decided to stick to the same pattern. Moreover, the same flashing time (t_f) values were adopted in the growth experiments for direct comparison, namely 3, 6, 30, 60, 100 ms together, of course, with the continuous light conditions. The results of the smallest and longest t_f are shown in Figure 4.3.1. The flashing time showing

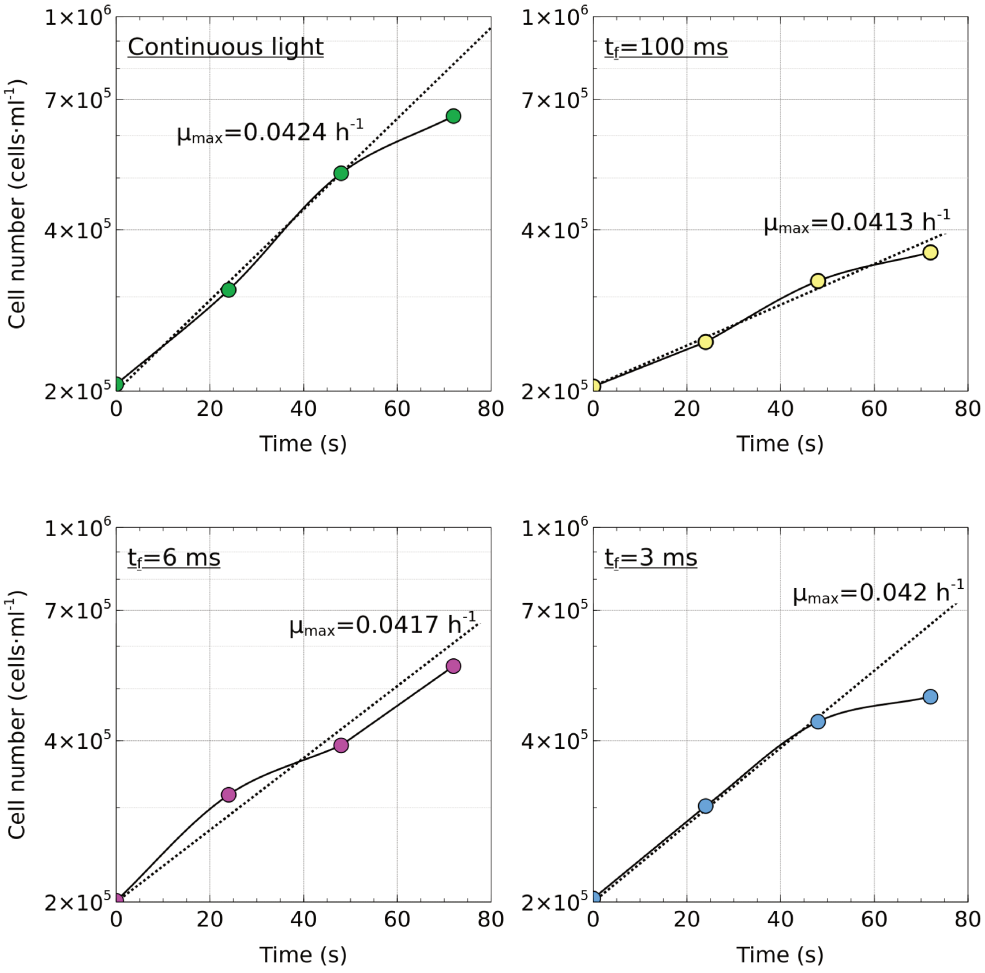

Figure 4.3.1: Growth curves of Haematococcus pluvialis cultures under different flashing light conditions: *upper-left*, continuous light; *upper-right*, $t_f = 100\,ms$; *lower-left*, $t_f = 6\,ms$; *lower-right* $t_f = 3\,ms$. The cell number is reported on a logarithmic scale and the interpolating lines (slope μ_{max}) for each growth curve are overlaid in each panel.

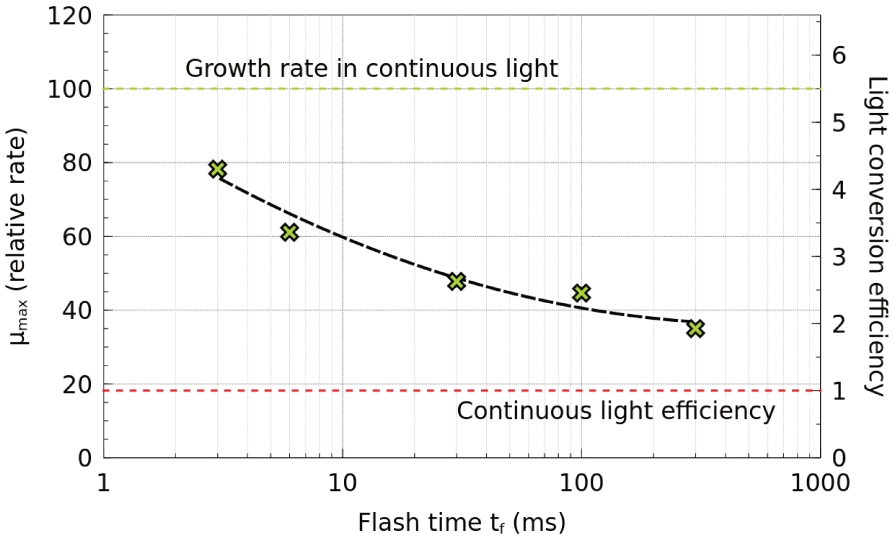

Figure 4.3.2: Dependence of the culture growth rate on the flashing time duration (t_f). Relative comparison of the growth rate (left axis) and the resultant increase in the calculated light conversion efficiency (right axis) are shown. As a reference, continuous light parameters are highlighted by the corresponding dashed lines.

the fastest growth were those in continuous light where a maximum growth rate μ_{max} of 0.0424 h^{-1} was attained. This result was not surprising as low light conditions as those adopted in these experiments are non saturating and no light-dependent inhibitory effect was expected. On the contrary a t_f=100 ms showed a lower growth rate (μ_{max}=0.0413 h^{-1}) as a confirm that, the slower the flashing light the less the increase in LCE attained. The faster t_f adopted in these experiments, 3 ms and 6 ms, reported in Fig. 4.3.1 shown a μ_{max} similar to that attained in the continuous light experiments (μ_{max}=0.042 h^{-1} and μ_{max}=0.0417 h^{-1} respectively).

4.3.2 LCE calculations

The growth rates measured with the experiments shown in Fig. 4.3.1 were converted to a relative scale (calculated between the maximum and minimum μ_{max}) and reported (in log scale) against the corresponding t_f duration, to attain a plot analogous to that published by Kok (1953). The results are shown in Figure 4.3.2.

On the y axis on the right of the plot, the estimated LCE values for each flashing

light condition are reported. These values are of course relative to the LCE attained in the continuous light conditions (LCE=1). For a flashing time of $t_f = 3\ ms$, an integration with continuous light of 78% was attained. This was the shortest flashing time used as we limited these to the same values adopted by Kok (1953). However, while *Chlorella pyrenoidosa* in that publication, in correspondence to the same flashing time showed 93% integration, *H. pluvialis* proved to be less efficient in the utilization of flashing light. The discrepancies with *C. pyrenoidosa* data were progressively lower as the flashing time was increased and, for t_f between 100 and 300 ms, they practically disappeared. This can be seen as an indication that, whatever alga is used inside the PBR, the expected integration to a mixing-induced flashing light may be the same for all strains.

The same data series may be simultaneously read on the right axis where the calculated relative light conversion efficiency is shown. The values were calculated by dividing the relative μ_{max} by the duty cycle (D). In this way, the attained growth rates under different light regimes can be compared in terms of successfully converted energy against absorbed energy. In other words, where continuous light is, obviously, continuously absorbed, flashing light alternates light and dark periods by a factor equal to D; no matter how many times the duty cycle is repeated in one second, the same amount of light is given to the culture, because the present study provided 180 ms of total illuminated time for each second. Using the same amount of light, but distributing it through different t_f, different light conversion efficiencies can be calculated. In these experiments the maximum efficiency achieved corresponded to the maximum integration point (t_f=3 ms) where a remarkable 4.3-fold increase was recorded. Even low integration points, namely 100 and 300 ms, were characterized by efficiency increases on the order of about 2-fold. These low integration points are particularly those falling in the flashing light time-scale attained by fluid dynamics (Giannelli et al., 2009; Grobbelaar, 1989), and, thus, being able to predict their

effect and to ponder them in the global reactor energy balances could allow for an *a priori* determination of the best PBR configuration.

4.4 Flashing light measurement through CFD

Before carrying out any growth experiments in the 1 liter PBR, we tried to elaborate a simple model to connect CFD measurements with productivity data. We compiled a simplified flow scheme of said model in Figure 4.4.1. The model we wanted to obtain from CFD results was intended for use in correlating particle motion data to an approximate flashing time measurement, namely the same t_f as determined in the previous section (section 4.3). With such flashing light values an approximate value for the local LCE inside those PBR regions with a high swirling flow could be possibly calculated therefore attaining a numerical measurement for the LCE increase inside the different PBRs. This kind of approach would be close to impossible without the aid of CFD and thus represents the biggest advantage over traditional PBR design techniques: with this technique, just by using numerical data, a good approximation of the real reactor behavior can be obtained.

As we pointed out in the previous sections, the culture grown inside an ALR is subjected to the entrainment in the pockets arising in the draft tube due to the S shape of the rising bubble swarm. We thus decided to concentrate on these zones and to determine the fluid rotation speed by means of the numerical particle tracking. In this way we were able to predict to which extent cells were illuminated by mixing-induced flashing light and to calculate the efficiency. The exact procedure depicted in Fig. 4.4.1 was:

1. Set up a functioning simulation for the ALR and BCR (as explained in section 4.1).

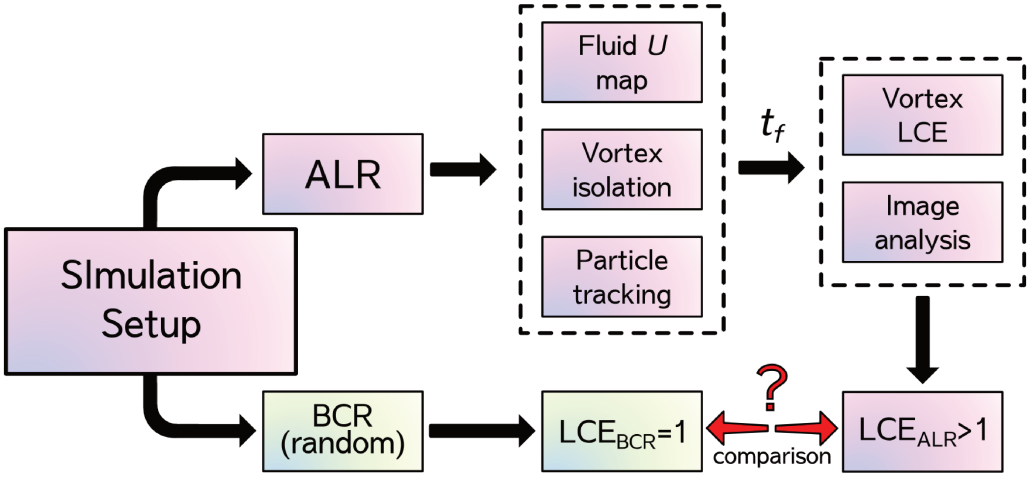

Figure 4.4.1: Flow scheme representing the adopted model for the calculation of the increased light conversion efficiency. The flow steps enclosed in the dashed lines represent these two phases: 1) the determination of t_f and 2) the surface averaging to attain the overall PBR light conversion efficiency.

2. Generation of a suitable visualization of the $\overline{U}$ distribution in the reactor after enough time was passed from the start.

3. Isolation of the swirling flows localized in the pockets.

4. Lagrangian particle tracking of those areas isolated in point 3 by using the same technique reported before (section 4.2.3).

5. Calculation of the expected local LCE in the vortexes.

6. Calculation of the averaged LCE in the whole PBR through IA.

As the point number 1 in the list have been already discussed in depth, only a thorough description starting from point 2 will be given. The point number 2 of this procedure is further illustrated in Figure 4.4.2 where the fluid velocity distribution of a generic time step in the simulation is represented in a black and white shaded color-map (a). This is the same representation of those used in Figs. 4.2.2 and 4.2.1 with the only difference that here the magnitude of the vector is represented on the color-map and the vector itself is not represented. High-velocity swirling regions can be clearly seen and thus easily isolated from the rest of the mesh by using the

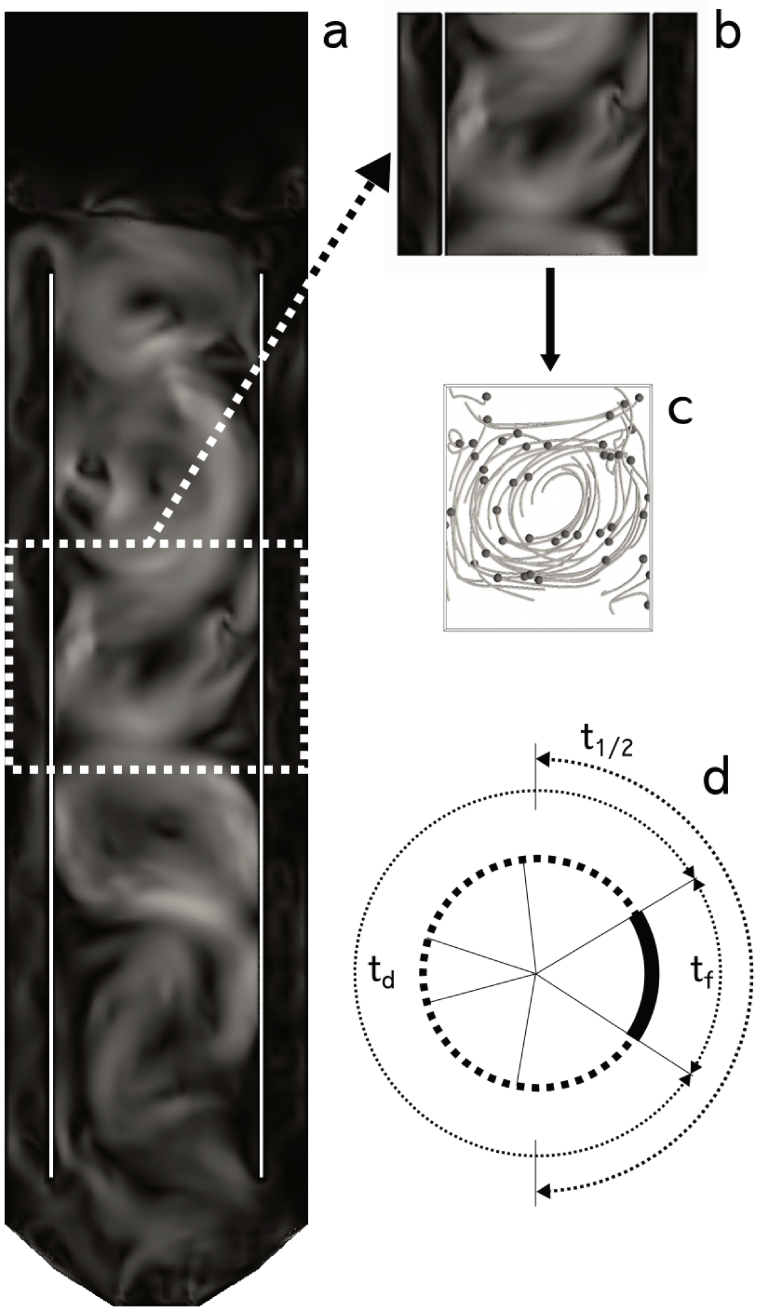

Figure 4.4.2: Scheme of the flashing time determination by means of Lagrangian particle tracking. Highly swirling fluid portions (b) were isolated from the fluid velocity color-map section (a) and particle tracking was used for creating a (t, x, z) plot for each particle (c). The simplified calculation (d) was then executed on the measured frequency data.

Clip filter in Paraview (Fig. 4.4.2b). The swirling regions isolated in this way were not those macroscopic circular regions inside the draft tube but those highlighted in Figure 4.4.3, i.e. the pockets already described in section 4.2.2. Lagrangian particle tracking (inset c) was used in each isolated PBR portion to attain a temporal function of each position coordinate by means of a Python script, which ultimately led to the creation of a (t, x, z) plot for each particle. By analyzing the maximum lateral displacement for each particle, we were able to calculate an average value for what we defined as the "half-time" (indicated with $t_{1/2}$). This parameter represents the time that each particle requires in order to complete half a rotation inside the vortex and its strong correlation with the flashing time is evident. By looking at the particle motion in video (data not shown) we predicted a semi-rigid rotation for the vortex and was easy to imagine how inner cells and outer cells would be subjected to the same half-time but with different fluid velocities. Moreover, in sufficiently dense cultures (chlorophyll concentration higher than 12 $mg \cdot l^{-1}$) a sufficient gradient in light intensity between the light and dark phase of the circle can be expected. In 24 $mg \cdot l^{-1}$ cultures of Chlamydomonas reinhardtii at the same culture depth, the difference between the light intensity on the illuminated face and the culture bulk can reach 4-fold (Giannelli et al., 2009). It was therefore evident how the cells entrained in the swirling flows were effectively subjected to a sustained mixing induced flashing light effect. To corroborate this hypothesis, we calculated the average absorbed light intensity on a swarm of seven different particles set in rotation by the fluid inside one of these swirling flows (Figure 4.4.4). The particles where randomly selected to represent different illumination data for various radii. Light intensity for a medium-high density culture (80 $mg \cdot l^{-1}$ of total chlorophylls) has been calculated according to the Lambert-Beer absorption theory with a modified absorption constant specific for *H. pluvialis* cultures (Garcìa-Malea et al., 2006), see Eq. 4.4.1.

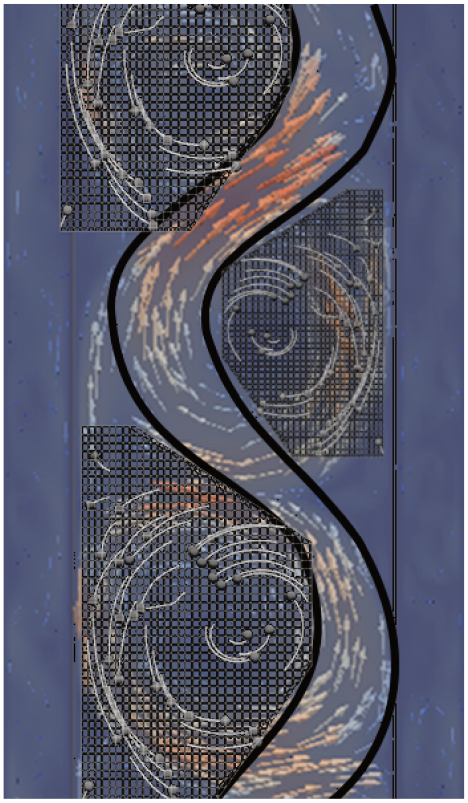

Figure 4.4.3: Highlight of the regions where high frequency culture recirculation is attained. As the particles in the image clearly point out, the fluid motion inside these regions is perfectly circular and an overall circulation frequency can be calculated.

$$\begin{cases} PFD(t) = e^{-x(t)\cdot K\cdot DW} \\ \\ K = 0.086 + 0.0065 \cdot CHL \\ DW = 1\,g \cdot l^{-1} \quad CHL = 80\,mg \cdot l^{-1} \end{cases} \tag{4.4.1}$$

This was the function used to record the light intensity changes to which cells are subjected (Fig. 4.4.4) and shows how different particles starting in different radial positions actually move around the vortex center roughly with the same angular speed. Between the maximum and minimum illumination positions an average $t_{1/2}$ of 0.348 s is obtained which was almost identical to that calculated by the simulation. Looking at these results we assumed that the complete light/dark cycle could simply be sharply divided into separate dark and light phases characterized by t_d and t_f, respectively. Since data collected in the flashing light growth curves could be used directly only under those illumination conditions reported in Eq. 1.3.2, we adopted

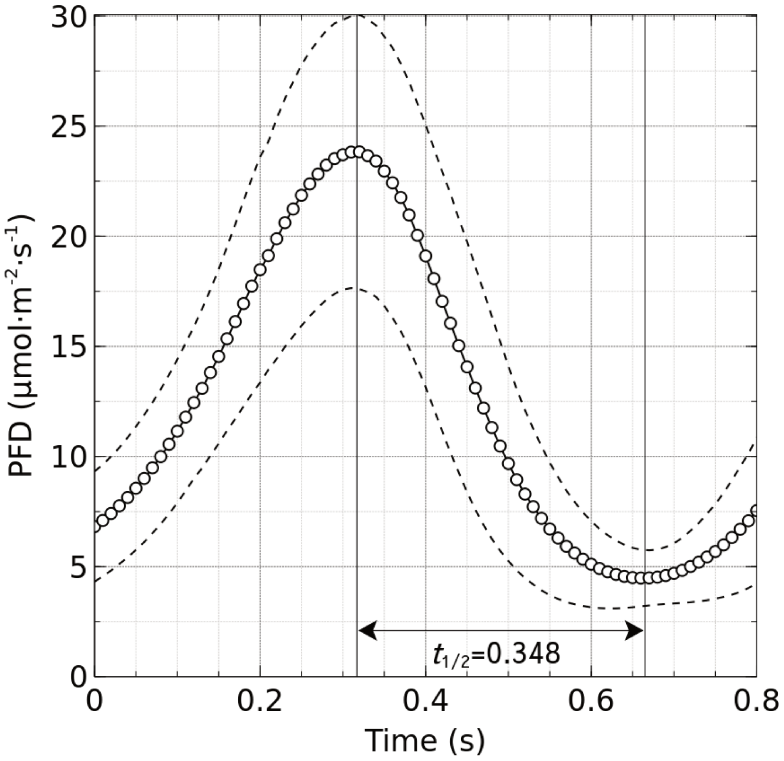

Figure 4.4.4: Time course of the average absorbed light energy by cells entrained in the swirling flows. Standard deviation is represented with the dashed lines. Particles have been selected to start at the same position inside the vortex but with different radial coordinate.

the same ratio in the calculation of t_f starting from the half-time $t_{1/2}$ (Eq. 4.4.2 for the calculations and Fig. 4.4.2d for a graphical representation).

$$t_f = t_{1/2} \cdot \frac{2}{5.5} \tag{4.4.2}$$

The value of t_f obtained this way was then used to calculate an approximate value for the increase in LCE by the flashing light effect using the plot shown in Fig. 4.3.2. With an average $t_{1/2}$ of 349 ms, according to the simplified calculation with Eq. 4.4.2, the average flashing time to which cells in the ALR were subjected was 126 ms, which corresponded to a 2.09-fold increase in local LCE. This increase was obviously limited to those zones undergoing high-frequency PFD variations and equal to 1 everywhere else due to the seemingly continuous light characteristic of

a random mixing. For this reason, IA was used to precisely assess the amount of reactor volume subjected to the flashing light effect and to calculate a weighted average value for the overall LCE of the PBR, according to the following equation:

$$\eta_{PBR} = \frac{A_F}{A_{PBR}} \cdot \eta_F + \frac{A_C}{A_{PBR}} \cdot 1 \tag{4.4.3}$$

where A_F and A_C represent the area of the PBR subjected to flashing light and that subjected to continuous light, respectively, and A_{PBR} is the total area. Again, with the term "continuous light," we indicate the portion of the PBR where random fluid motion did not permit a sustained mixing- induced flashing light effect. The LCE in flashing light conditions (η_F) is by definition greater than that of continuous light (Fig. 4.3.2), and, as a consequence, no matter how small the increase in LCE, a PBR with highly swirling regions will have a greater LCE than a perfectly random one. Using the values measured above, the resultant LCE increase that was calculated using this method for the ALR after the area weighting was 1.28-fold. Seen this result on the base assumptions of this model, this LCE increase meant that by comparing the BCR with the ALR under the experimental conditions simulated with OpenFOAM, the expected increase in algal productivity, in terms of dry cell weight or μ_{max}, should be close to this calculated value.

It is evident from the data reported in Figure 4.3.2 that shorter t_f can further increase the PBR productivity. It is however well known that faster flashing times are impossible to achieve in large scale PBR where the typical flashing time almost always exceed the limit of 100 ms (Giannelli et al., 2009; Grobbelaar, 1989). For this reason, an optimal t_f must be selected for each PBR configuration. For example, in the case of an ALR, the effect of the draft tube geometry is evident in the perspective of what shown in Fig 4.4.2: a faster S- shaped rising flow can generate a set of swirling fluid portions moving with an even faster frequency while a longer

draft tube may increase the amount of culture entrained in active swirling zones. In this situation, an increase in the cell damage generated by the harsh environmental conditions may however limit the growth of the more sensitive organisms and thus, an additional check of the feasibility of new designs must be taken into account.

4.5 Model validation

The comparison between the two different reactor configurations, BCR and ALR, can be used as a tool to verify the applicability of the LCE prediction model in full scale reactors. Once again, in this work the BCR is seen as the model reactor for a perfectly random fluid flow coupled with a continuous illumination regime where the cells do not routinely undergo mixing induced light-dark cycles. On the contrary, the ordered fluid flow attained in the ALR may be seen as a quantified example of LCE increased by mixing induced light dark cycles, where culture motion is harnessed despite the continuous light to attain a partial increase in culture productivity. To verify whether the model was able to suggest reasonable results, *H. pluvialis* cells have been cultivated inside the different geometries starting from the same inoculum culture and grown until the maximum biomass concentration was achieved. Of course, at least three repetitions have been carried out for each geometry.

4.5.1 BCR to ALR comparison: Dry weight

The results are shown in Figure 4.5.1b. Both geometries showed a similar behavior with the BCR being slightly lower for the whole duration of the experiments. The final reactor productivities, expressed as the total maximum DW attained were $1.933 \pm 0.15\ g \cdot l^{-1}$ and $1.508 \pm 0.11\ g \cdot l^{-1}$ in the ALR and BCR respectively. The increase in productivity, amounting to 1.282 times, almost coincides with that predicted with the light-dark cycles model where a 1.28 fold increase in ALR light

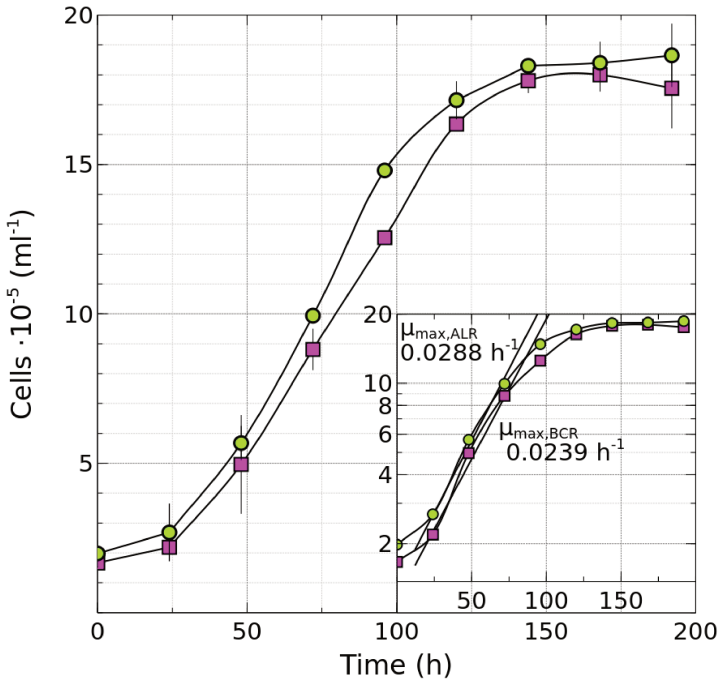

(a) Cell number time course. The logarithmic plot used for the μ_{max} calculation is shown in the inset.

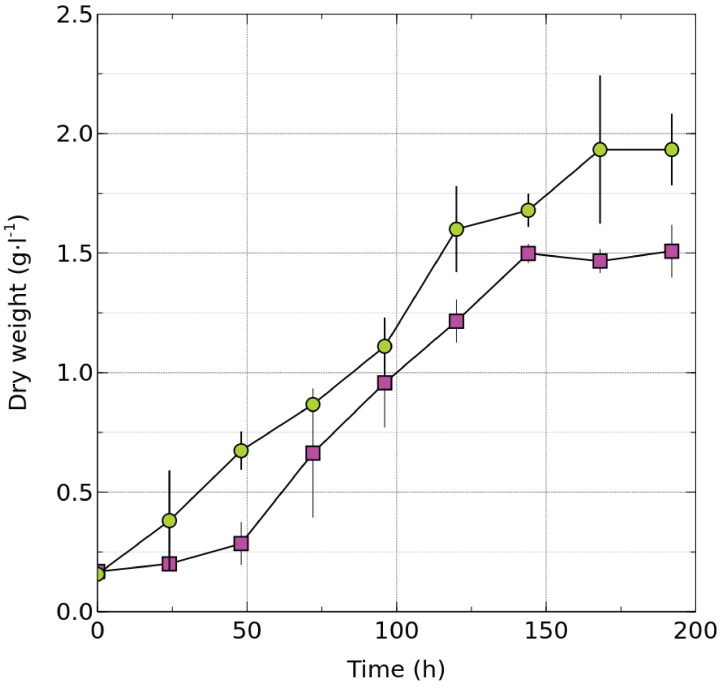

(b) Dry weight time course.

Figure 4.5.1: Comparison of *H. pluvialis* cultures in an ALR (◯) and a BCR (□): a) Cell number, b) Dry weight

conversion efficiency was calculated. For this reason, it is our opinion that increased productivities in ALRs can be almost completely addressed as the increased contribution of mixing induced flashing light to the overall reactor LCE.

4.5.2 BCR to ALR comparison: Cell number

By examining the cell number time course (Fig. 4.5.1a), further evidence corroborating this idea can be seen. Culture maximum growth rate (μ_{max}) calculated through the log base plot reported in the inset, reached 0.0288 h^{-1} in the ALR and 0.0239 h^{-1} in the BCR where a slightly lower slope of the curve results evident even to the naked eye. The increased LCE of the culture grown in the ALR allowed for the cells to duplicate faster thanks to the increased electron flow through the photosynthetic electron transport chain granted by a higher PQ pool oxidation state (Nedbal et al., 1996) than that in the BCR which represents the continuous light regime. While some confusion exists on the use of the growth rate as a parameter for comparison between flashing and continuous light conditions (Nedbal et al., 1996), in these experiments a 1.21-folds increase in the μ_{max} was recorded in the ALR which showed a good agreement between the LCE increase calculated with the CFD model and that measured in the PBR. It must also be noted that for long cultivation times, picking out the points for the calculation of the μ_{max} represents a difficult task as one tries to measure highly variable parameters. For this reason a 0.07 difference between the predicted and the recorded value may be considered still quite satisfying.

4.5.3 BCR to ALR comparison: Chlorophylls

Finally the Chlorophyll time course (Fig. 4.5.2a) shows that the total CHL concentration was always higher in the ALR than those in the BCR. These numbers, when compared with cell concentrations which are similar throughout the entire experi-

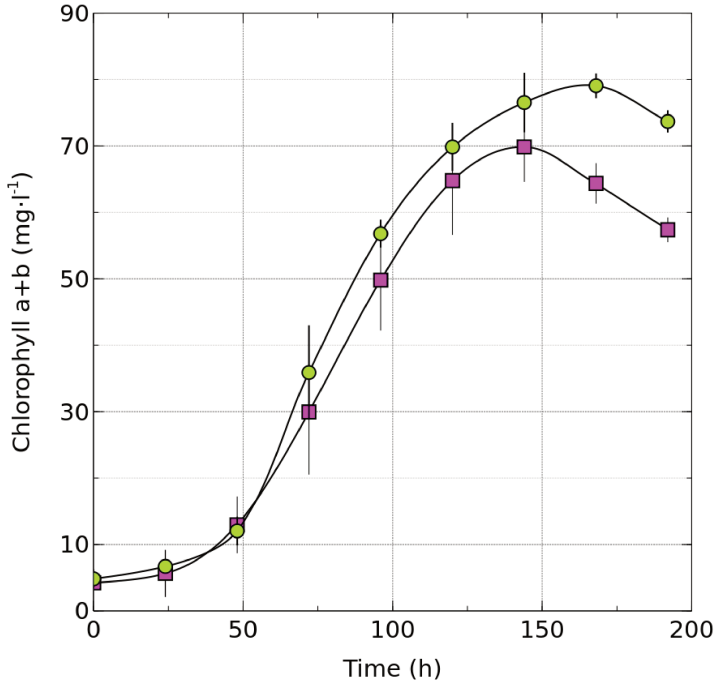

(a) CHL a+b time course.

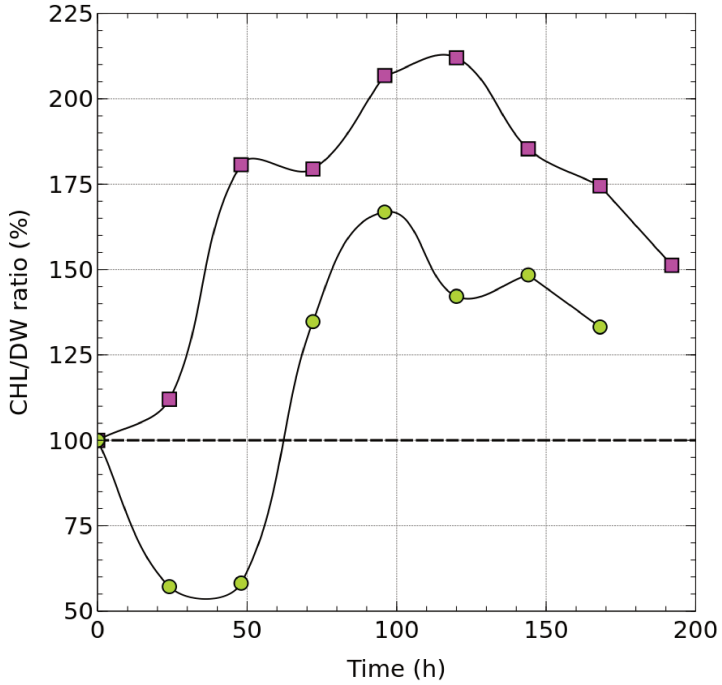

(b) CHL/DW ratio time course. The relative changes normalized to the initial CHL/DW ratio at $t = 0$ (100%) are shown.

Figure 4.5.2: Comparison of *H. pluvialis* cultures in an ALR (◯) and a BCR (□): a) Total chlorophyll , b) Chlorophyll content (CHL/DW ratio).

ment, show that cells grown in the ALR have a per-cell chlorophyll content higher than those grown in the BCR. Especially when the total CHL content is calculated (Fig. 4.5.2b), this becomes evident. The numbers shown in Fig. 4.5.2b are plotted as a percentage relative to the initial CHL/DW ratio; this is to highlight how the cells, when subjected to the very same cultivation conditions in different geometries behave differently revealing a different. It is well known that an high chlorophyll content is the first direct consequence of low light acclimation (Grobbelaar and Kurano, 2003) which means that algae over-produce CHL molecules to expand their light harvesting antenna in an effort to gather the higher amount of light in a dark environment. Despite the fact that the very same light intensity was used in both PBRs, according to CHL/DW data (Fig. 4.5.2b) the culture grown in the ALR appears to be slightly more high light acclimated than that in the BCR; this plays a tell tale role in this comparison as nothing more than the flow regime is changed between the two configurations. Nevertheless, the culture grown in the ALR is able to "see" more light than that in the BCR, which leads us to assert that mixing induced flashing light can be considered the main responsible for the differences shown by these two PBRs. In addiction, as a direct consequence of this evidence, higher PFDs together with higher CHL concentrations can reasonably lead to increased differences between the two configurations and should be further investigated, even though this was beyond the scope of this work.

4.6 Investigation of new geometries

With the positive correlation observed between the amount of mixing-induced flashing light effect and the increase in LCE, CFD simulation data can be used to foresee the best PBR configuration able to harness properly ordered fluid turbulence prior to actually building the reactor leading to a visible process development costs drop.

n	A_{DC}/A_R	$d_{i,n}\,(cm)$
0	1.10	4.8
1	1.89	4.1
2	3.21	3.4
3	6.23	2.6

Table 1.3: List of the draft tubes available for the PBR optimization.

4.6.1 Draft tube selection

According to what reported in literature, major ALR modifications able to significantly influence reactor productivity are those related to the draft tube size and positioning (Wu and Merchuk, 2004; Xu et al., 2012). Data reported in said studies show that a parameter especially linked to productivity variations is the ratio between the downcomer and riser cross section (A_{DC}/A_R) even if the conclusions in the two papers differ sharply. In the work from (Wu and Merchuk, 2004) an increase in the A_{DC}/A_R parameter reported a decrease in total PBR productivity, albeit a small one, while on the other hand Xu et al. (2012) recorded an opposite trend, with productivity peaking at $A_{DC}/A_R = 2.72$. While the former study was based on an entirely computational growth completely ignoring any potential flashing light contribution, the latter used real algal growth to validate the mathematical models presented. The result shown support our idea that mixing induced flashing light represents the major responsible of LCE variations correlated to the PBR geometry, even more than light distribution, at least if a properly dense culture is used. Under these hypothesis we then decided to select three different draft tube sizes from the glassware catalog with the proper A_{DC}/A_R as close as possible to that reported by Xu et al. (2012). The chosen d_i were: $d_{i,1} = 4.1\,cm$ ($A_{DC}/A_R = 1.89$), $d_{i,2} = 3.4\,cm$ ($A_{DC}/A_R = 3.21$) and $d_{i,3} = 2.6\,cm$ ($A_{DC}/A_R = 6.23$) (see Tab. 1.3). Among the three, $d_{i,2}$ was the closest to that used by Xu et al. (2012) available for purchase.

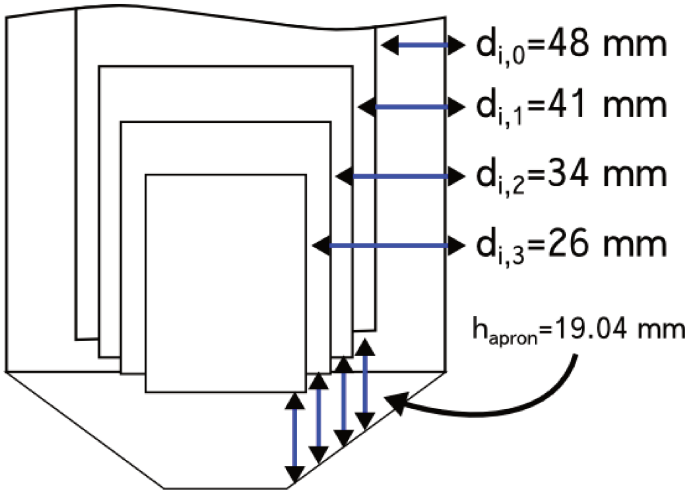

Figure 4.6.1: Arrangement of the various tubes in respect to the bottom clearance (h_{apron}) between the tube and the reactor base.

d_i	Riser			Downcomer			A_{PBR}	Total LCE
	t_f	$A_{F,riser}$	Local LCE	t_f	$A_{F,dc}$	Local LCE		
cm	s	px	—	s	px	—	px	—
2.6	-	-	-	0.0916	33970	2.239	91234	1.461
3.4	0.0945	23322	2.215	0.0945	12577	2.215	91234	1.616
4.1	0.1105	24369	2.154	-	-	-	91234	1.308
4.8	0.1269	23493	2.090	-	-	-	91234	1.280

Table 1.4: Comparison between different draft tube configurations. The mark (-) have been used for those PBR sections where no considerable mixing-induced flashing light effect was attained as a consequence of the lack of the high frequency whirling flows.

4.6.2 Improved LCE calculation

Using the same method explained in section 4.4, we aimed for the best draft-tube configuration to increase the ALR productivity. After setting up the proper mesh in the CFD software we thus applied the procedure reported in Fig. 4.4.1 to each new geometry and collected the needed data. The only precaution that proved to be necessary was to keep the clearance between the draft tube and the bottom part constant to prevent bubbles escaping from the riser, a phenomenon quite annoying especially for the thinnest draft tubes. Said clearance was kept constant and equal to 19 mm in all the simulations/experiments (Figure 4.6.1). The results of the LCE assessment can be seen in Table 1.4. As reported in Tab. 1.4, with smaller draft tube

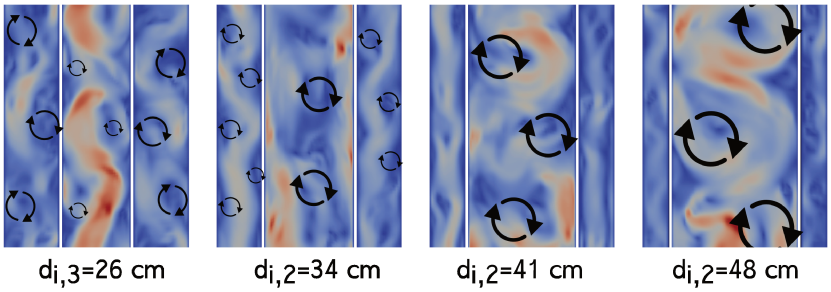

Figure 4.6.2: Schematic representation of the main location of the vortexes in the different ALRs. The size of the arrows simply represent the interested fluid volume and not the fluid velocity which is faster in the smaller ones. The location indicated by the arrows were not those used for the LCE determination and are used here only to represent the migration of the vortexes from the draft tube towards the downcomer.

diameters, we assisted to a migration of the whirling flows from the inside of the riser towards the downcomer; the increased downcomer section permitted the formation of small vortexes while the draft-tube inner part was progressively less affected by the S shaped fluid motion (Figure 4.6.2 for a schematic representation). Moreover, vortexes with a smaller diameter are characterized by faster frequencies and thus provide an even more beneficial effect albeit a lower culture portion is interested by the flashing light effect.. This new behavior prompted for a small correction in the calculation of the averaged LCE were a section-specific determination was carried out in the same fashion as in Eq. 4.4.3 but this time also taking into account the contribution of the downcomers. The resulting general equation is:

$$\eta_{PBR} = \frac{A_{F,riser}}{A_{PBR}} \cdot \eta_{F,riser} + \frac{A_{F,dc}}{A_{PBR}} \cdot \eta_{F,dc} + \frac{A_{PBR} - A_{F,riser} - A_{F,dc}}{A_{PBR}} \tag{4.6.1}$$

Among the chosen draft tubes, the faster t_f was achieved in the $d_{i,3}$ draft tube but the one closer to the A_{DC}/A_R ratio reported in Xu et al. (2012), i.e. $d_{i,2} = 3.4\,cm$, was that showing the higher LCE increase (1.616) when compared to a BCR configuration. The main reason for this is that high frequency light-dark cycles arise both inside the riser and the downcomer, effectively doubling the culture volume subjected to mixing induced flashing light. In this case, the effect of a slightly

slower t_f seems to be well balanced by the increase in the affected culture volume. For this reason, $d_{i,2}$ was chosen as the best replacement draft tube to be tested in order to asses model validity and its full scale applicability. Moreover, if the proposed model is correct, according to these calculated data, a further 26% increase in PBR productivity and in the growth rate have to be expected when algae are grown in an ALR optimized this way.

4.6.3 Culture growth

The new draft-tube configuration ($d_{i,2} = 3.4\,cm$) was tested as usual by using *H. pluvialis* cultures as a reference organism to measure the possible increase in productivity due to the augmented flashing light effect. The time course of the cell number, CHL concentration and DW recorded in the experiments are shown together in Figure 4.6.3. The behavior in the first 5 days was surprisingly similar to the growth curves attained for the standard draft tube (Fig. 4.5.1 and Fig. 4.5.2): the cell number and the total CHL showing a typical sigmoidal growth with the DW rising more or less steadily during the whole growth. By using the measured cell number data we calculated that μ_{max} reached 0.0377 h^{-1} for this configuration. The points used for the determination are the first three days of cultivation after the inoculum, the same time span that was used in the previous experiments for better comparison. The LCE increase when compared to the BCR ($\mu_{max} = 0.0239\,h^{-1}$) was 1.58-fold, and an effective increase in the culture μ_{max} was observed even in comparison with the standard ALR configuration ($\mu_{max} = 0.0288\,h^{-1}$). This partly confirms our expectations where, according to the flashing-light model, an 1.61-fold increase should be expected. We believe that the difference may be ascribable to the increased fluid dynamic stress conditions. In fact, a linear accumulation of culture biomass may be a sign of an increased stress in the ALR reactor probably due to

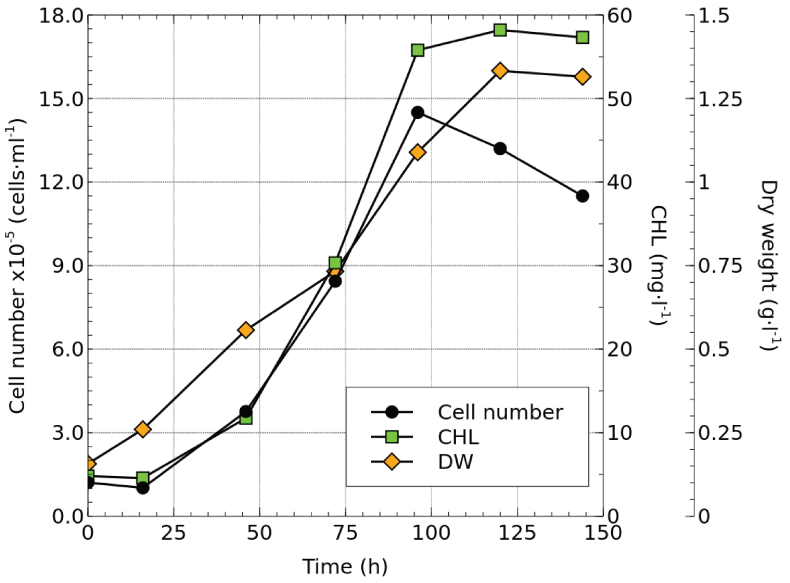

Figure 4.6.3: Growth in the ALR with the optimized draft tube: (◯) Cell number, (□) Total CHL, (◊) Dry weight.

the higher average local fluid velocity (i.e. the shear stress) when compared with the BCR.

Unfortunately, the growth after the fifth day did not live up to the expectations. In fact, the cell number abruptly decreased in just one day from $1.45 \cdot 10^6$ to $1.32 \cdot 10^6\, cells \cdot ml^{-1}$ (-9%) and the CHL accumulation showed a substantial decrease (only $2.42\, mg \cdot l^{-1}$ were accumulated). Only the biomass concentration rose with the same constant rate, indicating the upon the fifth day, a sudden increase in the cell weight was attained. Indeed, by calculating the DW/cell on the fifth and sixth days, we can see how the cells grown from 0.75 $ng \cdot cell^{-1}$ to 1.01 $ng \cdot cell^{-1}$ which represented a 35% weight increase. However, according to cell diameter measurements, cells were still normal in size ($D_{mean} = 16\,\mu m$) and microscope observations confirmed the presence of many non-motile small cells already starting to accumulate astaxanthin (shifting from green to pale orange). This findings likely confirmed two points:

- ➙ the increased DW/cell value was due to an initial stress-induced astaxanthin accumulation

- ➙ the loss of the flagella due to increased shear stress probably caused the cells to start accumulating astaxanthin (Vega-Estrada et al., 2005) and the loss of motility facilitated the precipitation under the increased weight to the (poorly mixed) bottom section of the reactor where in fact, an unprecedented quantity of sedimented cells was found at the end of the experiments (data not shown).

Considering this mixing-induced shear stress contribution, the culture proved to be subjected to an increased cell disruption rate during the whole cultivation, eventually reaching unbearable conditions on the fifth day when the cells practically "collapsed" towards the PBR bottom. Nonetheless, a strongly increased growth rate was measured by means of the μ_{max} parameter which showed a 1.58-fold increase in respect to the BCR, confirming that the LCE model can be used to predict the effect of the geometry on the culture growth performance. We believe that in this case the 0.04-fold discrepancy have to be attributed to the fragile nature of the used microalga which was not hardy enough to withstand the increased fluid dynamic stress or to a slight overestimation of the value attained with the CFD model. However, the correspondence between the measured data and the experiments was surprisingly accurate and we intend to proceed in the validation of the model by using a sturdy algal strain such as *Chlorella sorokiniana* which proved to be quite resilient, even in the presence of a mechanical stress generated by a centrifugal pump. In this way, a proper superposition of the model with the culture growth should be attained even in high stressful conditions.

4.6.4 Shear stress determination

As not all the algae of commercial interest are shear-stress tolerant like say, *Nannochloropsis* sp., *Chlorella* sp. or *Chlamydomonas* sp., we considered necessary to proceeded with a quantification of the shear stress in the various configuration condi-

tions to provide an additional tool to be used prior the definition of any "optimized" condition. The LCE model was used to compare different draft tube configurations by only taking into account the probable increase in the productivity or the culture growth but different algal strain may be subjected to different extent to the shear stress resulting from the mixing and an estimation of the expected average shear stress should be carried out. We measured the shear stress according to the Equation 2.4.1, reported in section 2.4.6:

$$\tau = -\mu\nabla\overline{U} = -\mu \cdot \begin{bmatrix} \dfrac{\partial U_x}{\partial x} & \dfrac{1}{2}\left(\dfrac{\partial U_x}{\partial y} + \dfrac{\partial U_y}{\partial x}\right) & \dfrac{1}{2}\left(\dfrac{\partial U_x}{\partial z} + \dfrac{\partial U_z}{\partial x}\right) \\ \dfrac{1}{2}\left(\dfrac{\partial U_y}{\partial x} + \dfrac{\partial U_x}{\partial y}\right) & \dfrac{\partial U_y}{\partial y} & \dfrac{1}{2}\left(\dfrac{\partial U_y}{\partial z} + \dfrac{\partial U_z}{\partial y}\right) \\ \dfrac{1}{2}\left(\dfrac{\partial U_z}{\partial x} + \dfrac{\partial U_x}{\partial z}\right) & \dfrac{1}{2}\left(\dfrac{\partial U_z}{\partial y} + \dfrac{\partial U_y}{\partial z}\right) & \dfrac{\partial U_z}{\partial z} \end{bmatrix} \tag{4.6.2}$$

and by using Paraview we obtained the magnitude of the shear stress tensor in each mesh cell (see Figure 4.6.4). The images of the various PBR geometries clearly show how the shear stress is quite evenly distributed inside the whole liquid domain with high share intensities localized on the free surface of the fluid where the bubbles explode when migrating to the gas phase. This is one of the zones which have always been indicated as a main source for the cell damage together with the area around the nozzles (Barbosa et al., 2004; Jobses et al., 1991). In our configuration, however, the inlet was characterized by shear stress values evidently lower than those recorded on the free culture surface showing that the sparging velocity and the quantity of nozzles were well balanced and did not have adverse effects on the culture. For this reason, the primary sources of shear stress were the culture surface and the fluid bulk where the bubbles obviously generate high shear stress regions visible as dark blue "streaks" in Fig. 4.6.4. The shear stress variation inside each configuration are quite limited and the color-map visualization is in logarithmic scale; for this reason it is very difficult to properly assess magnitude differences by the naked eye.

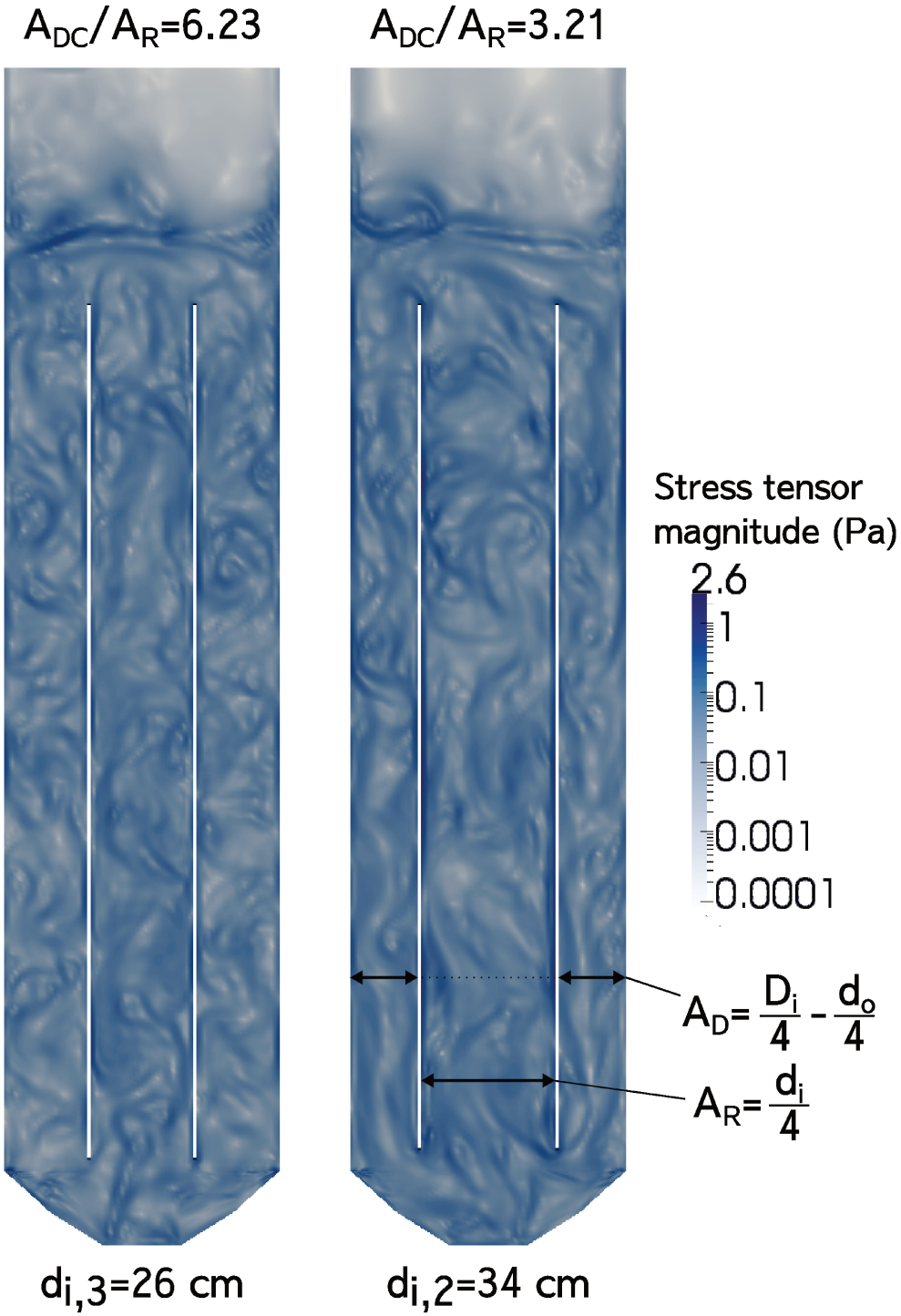

Figure 4.6.4: Shear stress magnitude distribution variation in ALR with different draft tube configurations, namely (form left to right): $d_{i,3} = 2.6\,cm$ ($A_{DC}/A_R = 6.23$), $d_{i,2} = 3.4\,cm$ ($A_{DC}/A_R = 3.21$), $d_{i,1} = 4.1\,cm$ ($A_{DC}/A_R = 1.89$) and $d_{i,0} = 4.8\,cm$ ($A_{DC}/A_R = 1.10$).

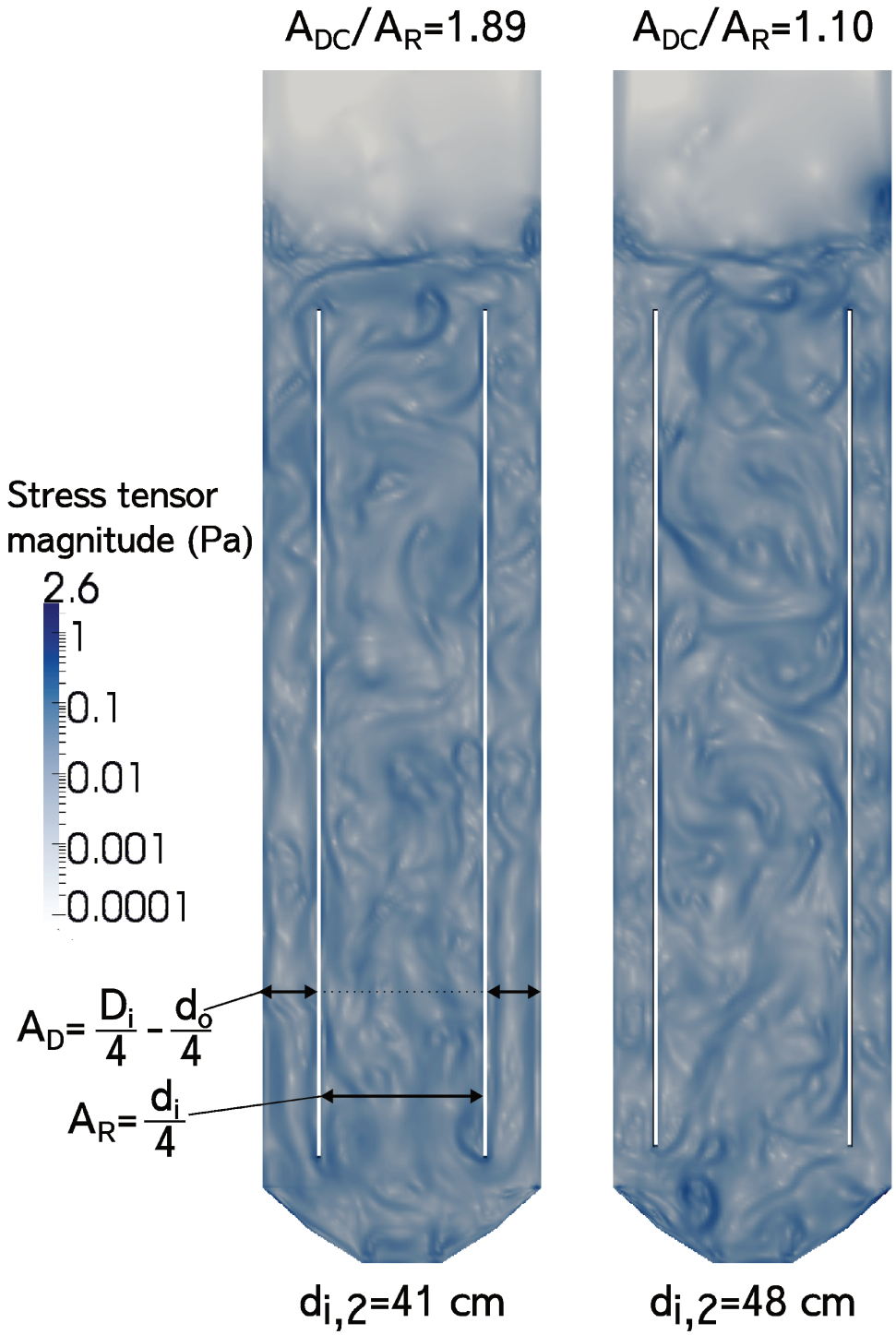
A_{DC}/A_R=1.89
A_{DC}/A_R=1.10
Stress tensor magnitude (Pa)
2.6
1
0.1
0.01
0.001
0.0001
$A_D = \frac{D_i}{4} - \frac{d_o}{4}$
$A_R = \frac{d_i}{4}$
$d_{i,2}$=41 cm
$d_{i,2}$=48 cm

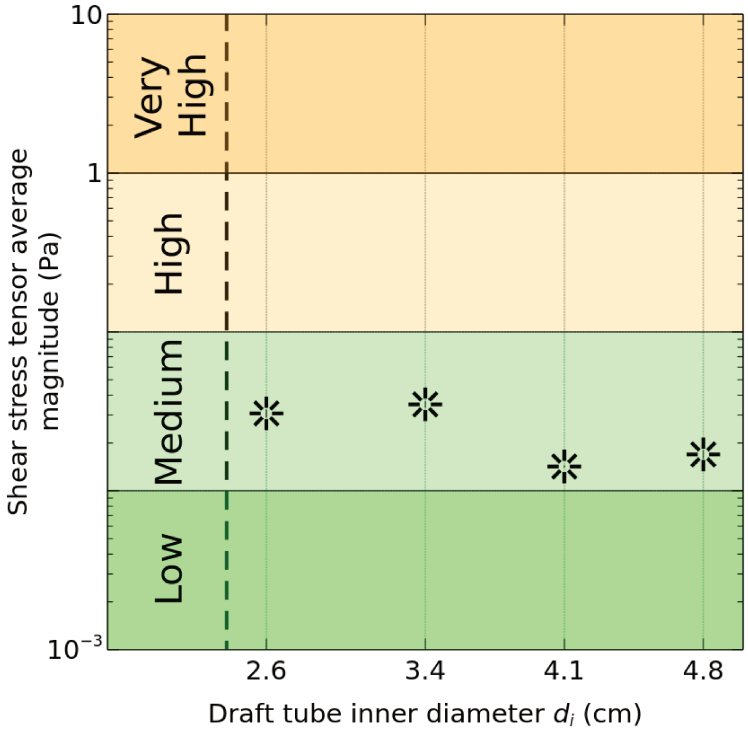

Figure 4.6.5: Average value of the shear stress tensor magnitude as a function of the different ALR draft tube configurations. The values of $\tau > 1\,Pa$ are reported here as "very high" however, very few points were falling in this category and we thus limited to those reported in the text.

It results however evident how, the smaller the value of d_i, the "darker" the image, hence the higher the shear stress magnitude. To better represent this fact, the 22000 local values were averaged by using Python to have a first direct comparison; the averaged shear stress values as a function of the draft tube diameter are shown in Figure 4.6.5. It is well known that shear stresses with a magnitude greater than 0.1 Pa generate negative effects on the growth of microorganisms (Elias et al., 1995) and for microalgae in particular, it has been found that stresses as low as 0.00016 Pa could create adverse effect on the growth in the dinoflagellate *Protoceratium reticulatum* (Garcìa Camacho et al., 2007). However, that alga could be considered a particularly fragile one as other species of commercial interest as *Spirulina platensis* demonstrated to be capable of withstanding shear stresses up to 0.3 Pa inside a *Couette* spinner without showing any negative effect on the photosynthetic activity

(Mitsuhashi et al., 1995). Moreover, the sturdy diatom *Chaetoceros muelleri* showed to be able to tolerate a shear stress up to 1 Pa (Michels et al., 2010) showing that this parameter is highly strain-dependent. For this reason we decided to consider the total average shear stress and the the distribution in the three categories shown in Fig. 4.6.5:

- Low: for the cells where $\tau < 0.01\,Pa$
- Medium: for the cells where $0.01\,Pa < \tau < 0.1\,Pa$
- High: for the cells where $\tau > 0.1\,Pa$

Looking at the results in Fig. 4.6.5 under the light of these considerations, we can notice how all the four configuration showed a mild environment with the optimal draft tube effectively showing the highest shear stress values but still lower than the acceptable limit of 0.1 Pa. These numbers are however the results of the averages over the whole PBR which do not take into account local higher values that may still occur. For this reason, the percentage of the reactor subjected to the different shear stress intensities have also been computed (Figure 4.6.6). As we can see, all the geometries actually have between the 60 and 80 % of the volume interested by medium shear stress values but the smaller draft tubes (2.6 cm and 3.4 cm) show that up to the 5% of the total volume is subjected to a high shear stress. Cell damage is interestingly time-independent (Michels et al., 2010) and we can thus conclude that the damage suffered by each culture is a proportion of the maximum shear stress values recorded in these high stress zones. Moreover, with a mixing time of 150 s compared with cultivation times of 200 hours (720000 s) we may infer that each cell will transit through these zones at least 4800 times. Of course this is an over-simplified analysis but it serves well for understanding why the culture in the improved geometry failed after five days of cultivation.

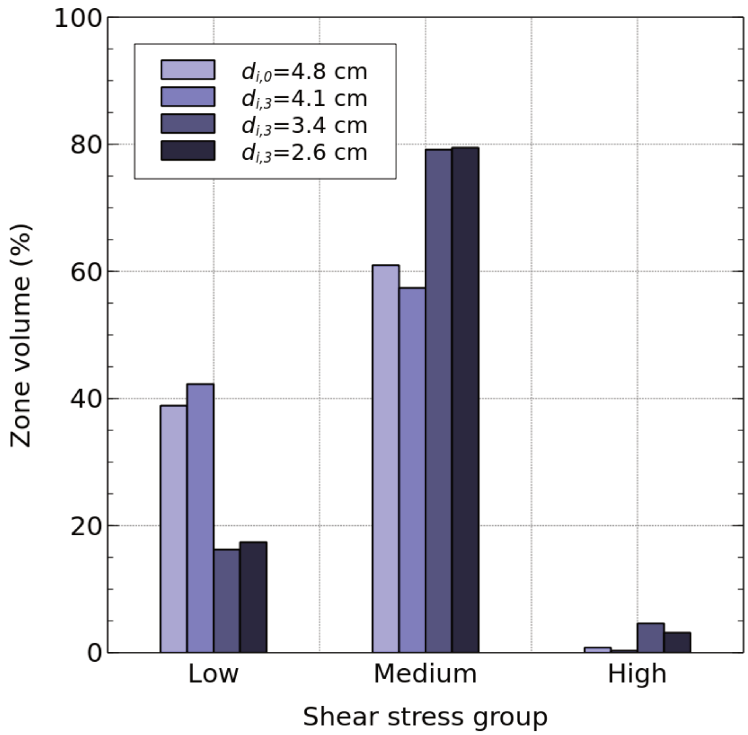

Figure 4.6.6: Subdivision of the total PBR volume in three shear stress magnitude areas.

We can therefore conclude that studying the effects of the mixing induced shear stress can provide further valuable information to be used together with the LCE model to foresee the effects of the PBR geometry on the culture growth.

4.7 Conclusions

In this section we tried to investigate on the reason why the ALRs have historically proven to be better than BCRs. We approached the problem from a CFD point of view by first analyzing the fluid velocity distribution and the streamlines in both configurations obtaining an highlight of the most probable fluid pattern arising in these PBRs. The discovery of a strong rising flow with an shape slightly resembling the letter "S" allowed us to hypothesize the arising of a strong set of swirling flows in the S pockets where, a sustained flashing-light effect could be the main responsible of the increased productivity in the ALR configuration. To verify this hypothesis, after properly the veridicity of the simulated data, we proceeded to determine the average flashing time attained in these vortex-like structures and to convert it in a LCE increase value to be used in the comparison to purely random flows. The resulting numbers when compared with those attained for algal growth experiments in the actual PBR shown a really good degree of agreement supporting entirely our hypothesis. We further validated these findings by establishing a full procedure to assess LCE increments in various PBR configurations, namely different draft-tube diameters and validating the model again under a different geometry, again with very promising results. Finally, given the increased stress conditions in the more dynamic condition of the improved ALR, we proceeded to add the measurement of the shear stress magnitude to the model protocol. With this addiction and by having in mind the shear stress resistance capabilities of the used algal strain, we believe that the model could be used to foresee the probable increase in LCE of new PBR geometries before actually proceeding to build them. This could save a lot of money during the new PBR design stage when, for example, preparing to build an outdoor PBR farm, proving to be an invaluable tool.

The next step on the road to a more effective PBR design stage should be the

automation of these procedures that, in the actual stage could be carried out only by operators highly skilled in the use of all the open source tools used (OpenFOAM, Paraview, Python, Bash, ImageJ, etc.). All these tools, being native of the same OS platform should be eventually mixed up in an easy-to-use GUI, maybe merged in the same Paraview as a plug-in component to also allow untrained people to repeat the design steps shown here without all the manual fiddling hassle. This goal however still lyes way too ahead along the path as more optimization work is needed and the hypothetic software eventually needed should be entirely coded from scratch and remains still the major aim of our future work.

Part 5

Results and Discussion II: Optimal temperature selection

5.1 Effects of temperature on culture growth

As a second step in the optimization of the cultivation conditions, we decided to dedicate some efforts on the investigation of the best culture conditions for the microalga *Haematococcus pluvialis*. Even if the optimization of the illumination conditions can be carried out with the proper design of the PBR inner structure, other culturing parameters directly affecting growth are present. In outdoor growing conditions, the parameter impacting the cultivation to the largest extent is the cultivation temperature therefore we investigated this parameter directly in laboratory scale PBRs.

5.1.1 Cell number

The growth curves of *H. pluvialis* under four different temperatures namely, $20°C$, $23.5°C$, $27°C$ and $30.5°C$ are shown in Figure 5.1.1. The culture cultivated at the lowest temperature ($20°C$) shown the highest growth in terms of cells number with a maximum cell concentration of about $1.7 \cdot 10^6\, cells \cdot ml^{-1}$. On the contrary, the other conditions were not able to reach the same final concentration with $23.5°C$ and $27°C$ reaching roughly the same concentration ($1.3 \cdot 10^6\, cells \cdot ml^{-1}$) and $30.5°C$ ending around $6 \cdot 10^5\, cells \cdot ml^{-1}$ which is about the 35% of the cell concentration attained by the culture grown at $20°C$ (Table 1.5). This behavior was not surprising as the optimum temperature for this strain is indicated as $20°C$ by the NIES but it was still interesting to note that *H. pluvialis* grown under temperature conditions as high as $27°C$ was still capable of sustained growth without showing any other counter-effect then a cell concentration loss. Again, this is not a surprising result as *Haematococcus* sp. strains isolated in different parts of the world show the ability to actively grow at these temperatures without any apparent problem (Imamoglu et al., 2009; Torzillo et al., 2003). Moreover, the same strain registered a similar growth performance

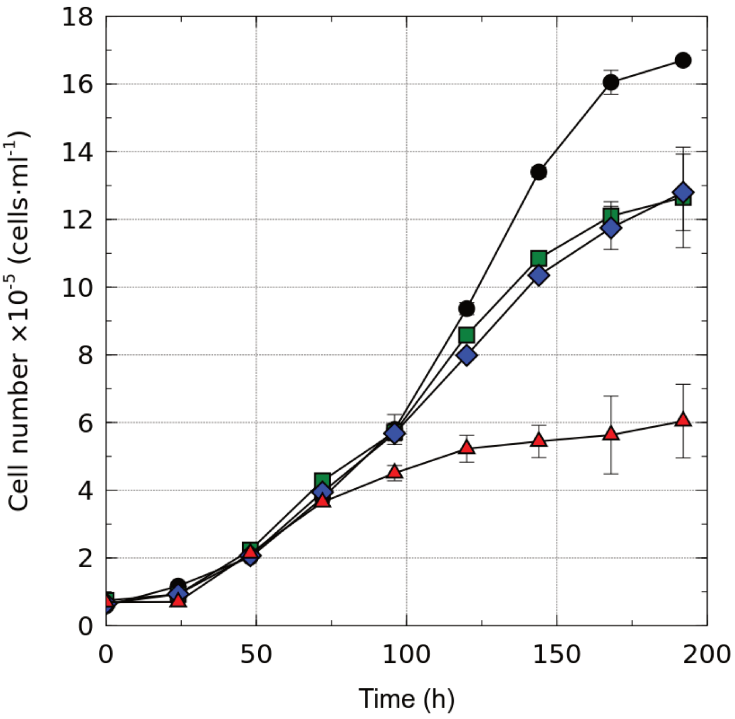

Figure 5.1.1: Growth curves of H. pluvialis cultures under different temperatures. Culture cell number time course at 20°C (•), 23.5°C (◆), 27°C (■) and 30.5°C (▲).

under analogous growth conditions where T=28°C (Dominguez Bocanegra et al., 2004).

Considering the maximum culture growth rate as a function of temperature as reported in Table 1.5, an opposite trend can be seen when compared with the maximum cell number. In fact, the higher the cultivation temperature, the higher the maximum growth rate attained by the culture in the first cultivation days, showing as expected a somehow increased metabolic activity (Goldman and Carpenter, 1974). In the presence of a temperature increase over the strain optimum temperature, a significant metabolic activity reduction is usually reported (Dominguez Bocanegra et al., 2004; Raven and Geider, 1988) mainly for the adverse effect that temperature have on the PSII (Yamamoto et al., 2008). On the contrary, in our cultivation conditions an increase of more than 10°C was needed to see a substantial decrease in the culture productivity. Furthermore, it is worth noting how, independently from the

Cultivation temperature ($^{\circ}C$)	Max. cell concentration ($cells \cdot ml^{-1}$)	Max. growth rate (h^{-1})
20	$1.67 \cdot 10^6$	0.0256
23.5	$1.28 \cdot 10^6$	0.0295
27	$1.27 \cdot 10^6$	0.0318
30.5	$6.04 \cdot 10^5$	0.0335

Table 1.5: Culture maximum cell concentration and maximum growth rate (μ_{max}) as a function of temperature.

cultivation conditions, the culture growth proceeded with the exact same behavior until the third day where all the cultures shown almost the same cell concentration. Starting from the fourth day the culture at $30.5^{\circ}C$ deviated from the others showing the inhibitory effects of the high temperature conditions and the same thing happened again at the fifth day when the growth rate of both the $23.5^{\circ}C$ and $27^{\circ}C$ cultures started to decline ending with a lower cell concentration. The concordance of this events is interesting as it shows how the effect of the temperature seems to be a cultivation time dependent parameter. Moreover, this gave us a first insight to better understand how the interplay between temperature and growth could be harnessed to achieve an overall increased productivity in outdoor cultivation conditions.

5.1.2 Dry weight

The same experiments show a rather different outline when the growth is displayed using the dry weight (DW) as a reference (Figure 5.1.2). From the point of view of the biomass concentration the culture at $20^{\circ}C$ shown the lowest overall productivity and a lower DW than the other conditions starting from the beginning of the experiments and differentiation further from the third day onward. Again, as for the previous section, an important change in the culture behavior was registered on the third day but this time it was registered only in the culture at $20^{\circ}C$. This change was not evident by looking at the plot in Fig. 5.1.1 where the culture seems to grow

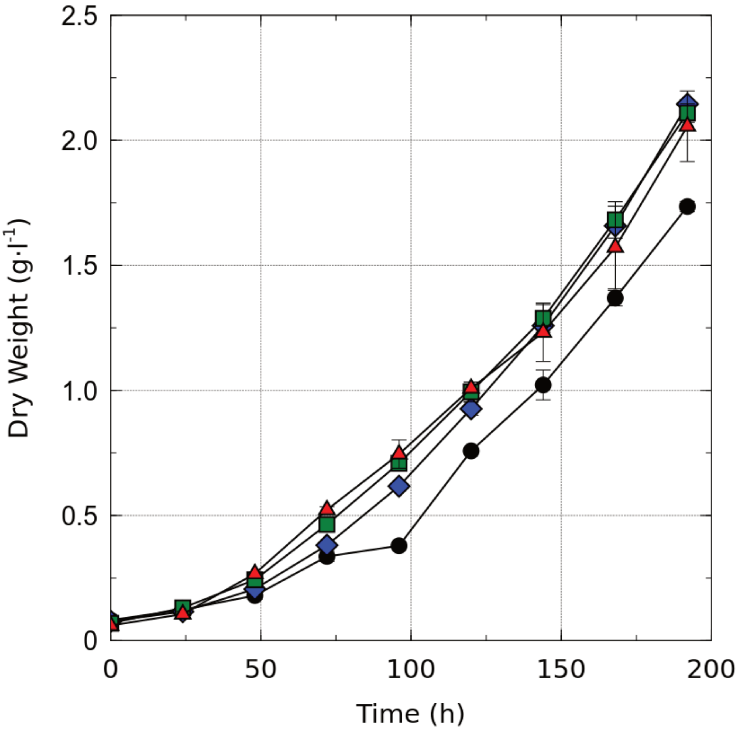

Figure 5.1.2: Growth curves of H. pluvialis cultures under different temperatures. Culture DW time course at $20°C$ (•), $23.5°C$ (⬥), $27°C$ (▪) and $30.5°C$ (▲).

without any major effect from the temperature. However, by looking at the growth from a different point of view we were able to realize that a culture growing at $20°C$ remains smaller than those in the other conditions showing an important effect of the temperature on the cell individual size and weight.

5.2 Pigment changes with temperature

To gather more insights on the effects of culture temperature on the algal culture we carried out an in-depth analysis of the algal pigments. As already pointed out in the introduction (1.2.3) accessory pigments play a major protecting role against external sources of stress (Falkowski and Raven, 2007; Kirk, 2011; Mimuro and Katoh, 1991) therefore representing an important indicator of environmental stress.

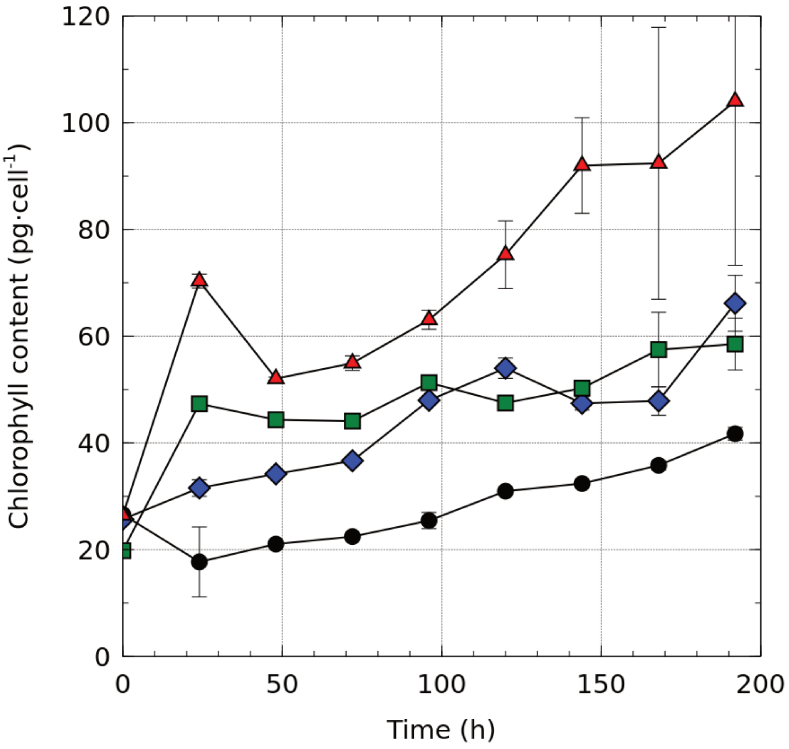

Figure 5.2.1: Time course of the total chlorophyll content expressed on a per-cell basis: $20°C$ (•), $23.5°C$ (◆), $27°C$ (■) and $30.5°C$ (▲).

5.2.1 Chlorophylls

The time course of the total chlorophyll content in growth experiments carried out under different temperature conditions is shown in Figure 5.2.1. Due to all the considerations in the previous section about size and number changes recorded under different temperature conditions, the total CHL content in Figure 5.2.1 is expressed as a per-cell basis. The CHL content varies in magnitude between the $20°C$ and $30.5°C$ conditions: the higher the cultivation temperature, the higher the final CHL content. Moreover, the accumulation process seems to sharply differ between the different conditions with the culture at $20°C$ accumulating CHL slowly and the culture at $30.5°C$ accumulating pigments really fast, especially on the first day. It was the first cultivation day in fact when an evident accumulation of CHL in the cells due to the temperature stress was recorded, with the sole exception of the culture

kept at $20°C$. The higher the temperature, the higher this accumulation rate, with a maximum CHL content of $70\,pg \cdot cell^{-1}$ in the case of the highest temperature, a rough three fold increase when compared with the inoculation conditions. This behavior was also shown by the cultures at $27°C$ and $23.5°C$ with a progressively lower impact and was not recorded at $20°C$ where, on the contrary, the culture lost CHLs on the first day to regain them on the following next 3 to 4 days.

Total chlorophylls are used by algae to absorb the light radiation to be converted in reducing power for the cell metabolism (see section 1.2in the introduction) therefore the behavior shown in Fig. 5.2.1 represents a powerful insight into the effect of temperature as it is perceived by the cells. The results shown in fact that the cells acclimated at higher temperatures were in fact in light limiting conditions. While the growth experiments were all carried out under different temperature conditions, the light was rigorously controlled and kept constant and thus such a result was quite puzzling. The only logical explanation to what reported in Fig. 5.2.1 was to think that the higher the temperature in the cultivation the lower the light perceived by the cells was. To demonstrate this intuition we proceeded to plot the CHL a/b ratio in the very same experiments as a function of time. The result is shown in Figure 5.2.2.

The ratio of CHL a to CHL b was indicated as a good bio-assay for assessing light limiting conditions (Dale and Causton, 1992; Gratani et al., 1998): lower values of this parameter (higher CHL b concentrations) are representative of highly photolimited plants while higher values (higher CHL a concentrations) represent plants subjected to photosaturating conditions. Using this criterion as a basis for the comparison, we observed that while all temperatures ended in a photolimited state (CHLa/b$<$ 0) due to the self shading phenomenon arising in the higher concentrations, the highest temperatures ($27°C$ and $30.5°C$) started in a photolimited state even on the first day. It took the first two days for the culture at $23.5°C$ to

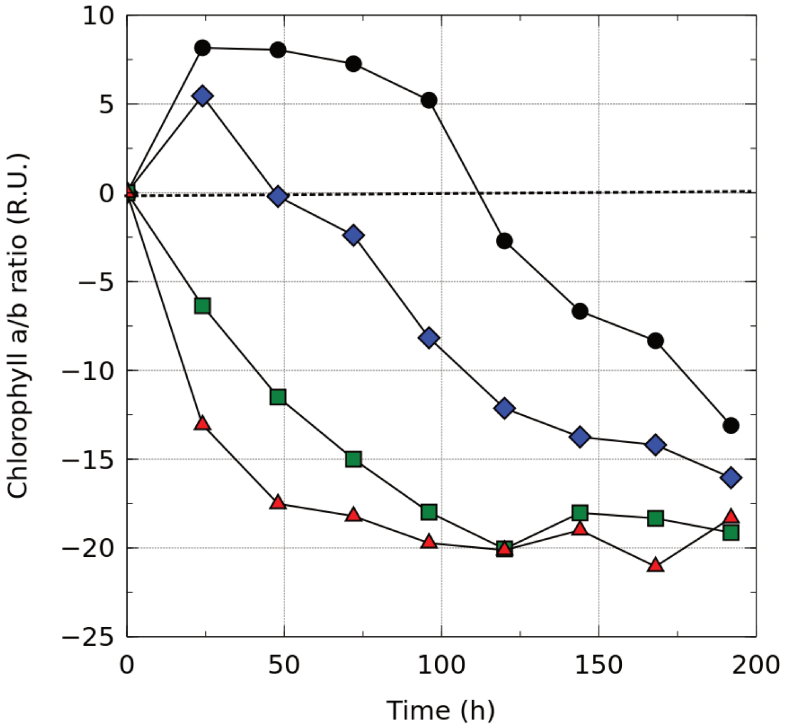

Figure 5.2.2: Time course of the chlorophyll a to b ratio: $20°C$ (•), $23.5°C$ (◆), $27°C$ (■) and $30.5°C$ (▲).

become photolimited (corresponding to a DW of about 0.2 $g \cdot l^{-1}$) and almost a full five days for the one at $20°C$ (DW=0.75).

We can then conclude that the first big effect of temperature changes on Haematococcus was to strongly limit the capability of the alga to harvest light leading the cultures subjected to progressively higher temperatures to progressively sever photolimiting conditions.

5.2.2 Accessory pigments

The accessory pigments (zeaxanthin, violaxanthin, etc.) are used as a protection against the ROS produced during the photosynthetic light reactions (see 1.2.3 for an explanation) and their (over)production is the synonym of the onset of light-induced oxidative stress, the so called xantophyll cycle induction (Demming Adams

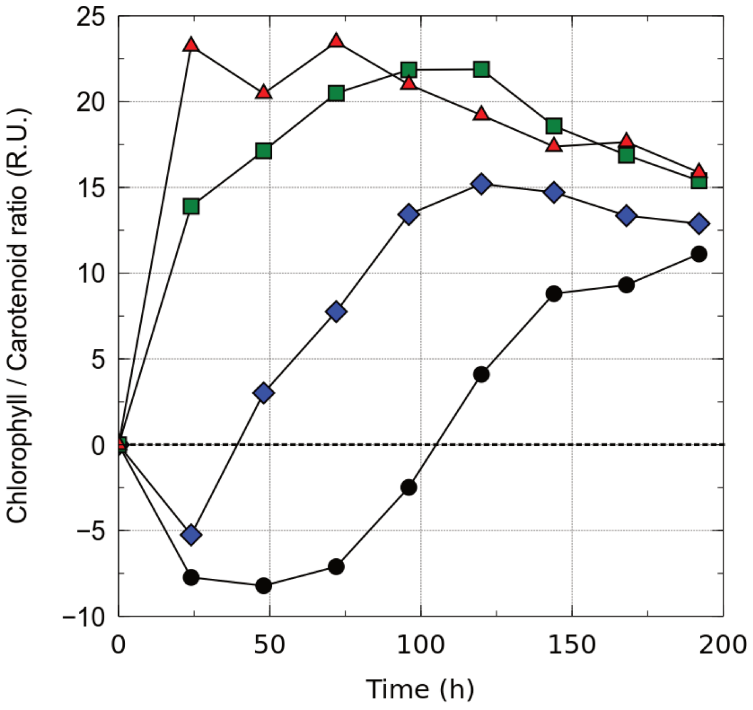

Figure 5.2.3: Time course of the total chlorophyll to carotenoid ratio: $20°C$ (•), $23.5°C$ (◆), $27°C$ (■) and $30.5°C$ (▲).

and Adams, 1996). They are therefore an indicator of the light-stress levels in the photosynthetic organisms and thus can be used to assess whether a culture is in light saturating conditions. According to Solovchenko et al. (2009), the ratio between CHL and total CAR is a better indicator for stress conditions than the absolute CAR concentration; we therefore plotted this parameter against time in Figure 5.2.3. The results in Fig. 5.2.3 are almost exactly specular with those representing the CHL a/b ratio further corroborating the hypothesis of a light limitation induced by the increased temperature conditions. It is in fact well known that light limited cultures are always characterized by high CHL and low CAR concentrations which is exactly the case of high temperature cultures ($27°C$ and $30.5°C$) while, on the contrary, the lowest culture temperature ($20°C$) is showing the typical behavior of a culture subjected to light stress conditions. This is an additional confirmation of the effect of temperature on the light harvesting capabilities of *H. pluvialis*.

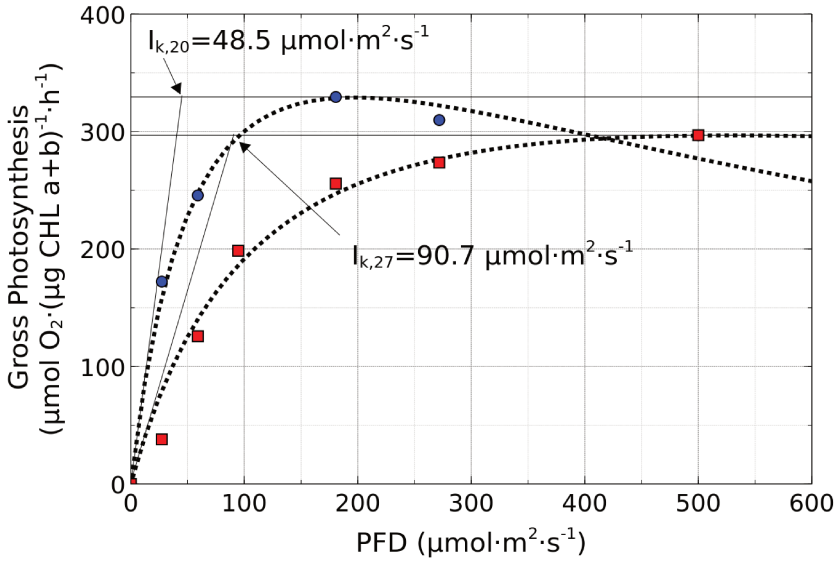

Figure 5.3.1: Photosynthesis/Intensity (PI) curve of Haematococcus pluvialis under different temperature conditions: $20°C$ (•) and $27°C$ (▪).

5.3 Light harvesting changes with temperature

5.3.1 PI curve determination

The correlation between an increased cultivation temperature and a decreased light harvesting capability in *H. pluvialis* as inferred in the previous section could be easily proved by using chlorophyll fluorescence, a well established procedure for this kind of experiments. The equipment needed by those measurements is really expensive and we were not able to get hold of a unit for carrying out the experiments so we had to resort to an alternative procedure to assess the differences. We selected the Photosynthesis-Intensity (PI) measurement as it represents an easy, consolidate and widely accepted method for comparing the photosynthetic characteristics of different organisms. The technique used to measure the OER is explained in detail in section 2.2.6. We only carried out the comparison between $20°C$ and $27°C$ as those were the temperatures selected for the final astaxanthin production stage: $23.5°C$ were

not enough impacting on the photosynthetic properties to be deemed economically feasible while conversely, $30.5°C$ where too high to be beneficial. Basing on other studies (Hata et al. (2001); Imamoglu et al. (2009); Torzillo et al. (2003)) where the temperature conditions were maintained around $25°C$, to obtain a cost sensible configuration, we thus selected $27°C$ as our reference "high temperature" condition.

The measurements results are shown in Table 1.6 as net photosynthetic rates and in Figure 5.3.1 as gross photosynthetic rats. The differences among the shapes of the PI curves attained under the two cultivation temperatures are evident. The PI curve at $20°C$ has a first steep portion followed by a saturation-inhibition curve with light intensities higher than 200 $\mu mol \cdot m^{-2} \cdot s^{-1}$ actually damaging photosynthesis. On the other hand, the PI curve at $27°C$ follows the typical saturation profile withstanding PFDs as high as those measured (500 $\mu mol \cdot m^{-2} \cdot s^{-1}$). The key difference between the two are the values of the I_k parameter which were 48.5 $\mu mol \cdot m^{-2} \cdot s^{-1}$ at $20°C$ and 90.7 $\mu mol \cdot m^{-2} \cdot s^{-1}$ at $27°C$. According to the literature (Vonshak and Torzillo, 2004) the I_k parameter can be used as an indicator of photoacclimation in microalgae: the higher the value of I_k, the more photoacclimated the culture. Using this consideration as the base of the comparison, the culture at $27°C$ was more photoacclimated than that at $20°C$ showing an almost double I_k value. This findings again confirm how higher temperatures influences the light harvesting capabilities of *H. pluvialis*. Moreover, according to (Vonshak and Torzillo, 2004), low I_k values in low temperature conditions represent a decrease in the high light utilization efficiency which means that cultures grown at $20°C$ do not only perceive an higher light intensity then those grown at higher temperature but are less efficient in its utilization. This confirms that the observation of the onset of light-mediated oxidative stress highlighted in Figs. 5.2.1, 5.2.2 and 5.2.3 was a direct consequence of the impaired light harvesting characteristics of the culture grown at $20°C$.

PFD	Photosynthesis	
	$20°C$	$27°C$
0	-159.4	-90.5
27	12.9	-52.5
60	86.3	35.3
95	—	108.1
180	170.1	165.3
271	150.4	183.2
500	137.5	206.4

Table 1.6: Net photosynthesis at $20°C$ and $27°C$

5.3.2 Metabolic effects

The effect of temperature on the the photosynthetic complex have been demonstrated both indirectly by measuring the pigment composition and directly by plotting the PI curves at two different temperatures. Cells cultivated at higher temperatures were still able to grow in cell number (with lower μ_{max}) but simultaneously accumulating biomass by increasing the DW more then the control ($20°C$). Hereafter we try to elucidate our explanation for this behavior.

It has been reported in literature that the effect of temperature on plants kept in dark can be detected primarily on the Plastoquinone Pool where an increased reduction is detected (Rumeau et al., 2007). For this reason, the plant becomes subject to a strong oxidative stress generated by the increased production of ROS around the plastoquinone pool itself even in the absence of light (Marutani et al., 2012). However, we noticed how the cultures grown at $23.5°C$, $27°C$ and $30.5°C$ did not show any sign of light induced stress which was instead recorded in the standard culture grown at $20°C$. To explain this difference, the I_k of the standard culture as recorded with the PI curve can be used. All the cultures were grown under medium light intensities of 100 $\mu mol \cdot m^{-2} \cdot s^{-1}$; this is approximately the double of the $I_{k,20°}$ and roughly equal to the $I_{k,27°}$. Under these consideration we may conclude that the cultures grown at $20°C$ were subjected to a light intensity

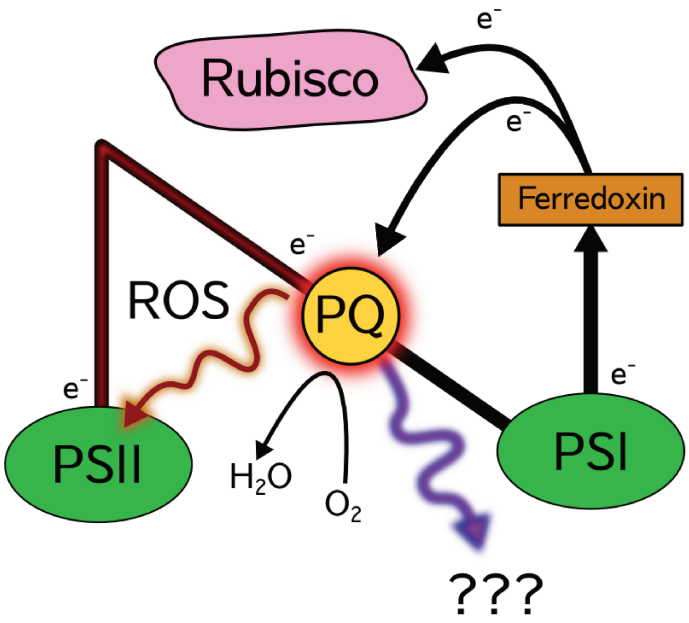

Figure 5.3.2: Ferredoxin mediated cyclic electron back-flow from PSI to the PQ pool. Electrons originating from the illuminated PSII and recirculating from the Ferredoxin exert a strong reducing pressure on the PQ pool (red halo). The high reducing pressure on the PQ is relieved by three different mechanisms: ROS formation, chloro-respiration and the NADH dehydrogenase pathway (an anabolic pathway).

which was almost double than the saturation intensity I_k and they suffered for the light stress up to biomass concentrations of 0.75 $g \cdot l^{-1}$ when the culture self shading finally lowered the average PFD below the stress levels. This can explain why the standard cultivation conditions showed an active xanthophyll cycle but does not explain why higher temperatures did not suffer from the increased ROS production and the xanthophyll cycle was never even present. This may be due to the cyclic electron back-flow originated from PSI and acting directly on the PQ through the mediation of the Ferredoxin (Fig. 5.3.2) reported in literature (Havaux et al., 1991; Marutani et al., 2012; Rumeau et al., 2007). This back-flow acting on the PQ pool together with the electrons coming from the PSII is thought to be responsible for the increased ROS production in the leaves under high temperature conditions. Stress conditions are also mitigated by the chloro-respiration (consuming the in-situ oxygen excess) and other anabolic pathways involving the activity of NADH dehydrogenase. We believe that the last is the main responsible of the increased DW growth of the

cultures which being effectively subjected to stress conditions slow down the cell duplication in favor of the accumulation of secondary metabolites like starch or lipids as an energy stock. This behavior is really common and has already been reported in literature (starch accumulation (Ball, 2002; Nakamura and Miyachi, 1982), lipid accumulation (Martìnez Roldàn et al., 2014; Rodolfi et al., 2009)) and we are convinced that *H. pluvialis* may be really good at discharging the overwhelming reducing power towards an increased lipid accumulation.

We are in the process of assessing whether in high temperature conditions an increased lipid productivity is recorded which, in turn, could be the reason of the increased astaxanthin accumulation at higher temperatures.

5.4 Astaxanthin accumulation under different temperatures

The correlation between high cultivation temperature and the light harvesting changes found in the previous part of this chapter can be used to facilitate the outdoor production of algal biomass both for lipid and astaxanthin production. The latter is the most interesting as the market for naturally grown astaxanthin is in a big expansion phase thanks to the heavy use of this substance as in supplements, nutraceuticals and cosmetics. We therefore concentrated further on the different astaxanthin accumulation capabilities shown by *H. pluvialis* under low and high temperature. The reference high temperature, namely $27°C$, has been chosen according to economic considerations which will be explained later.

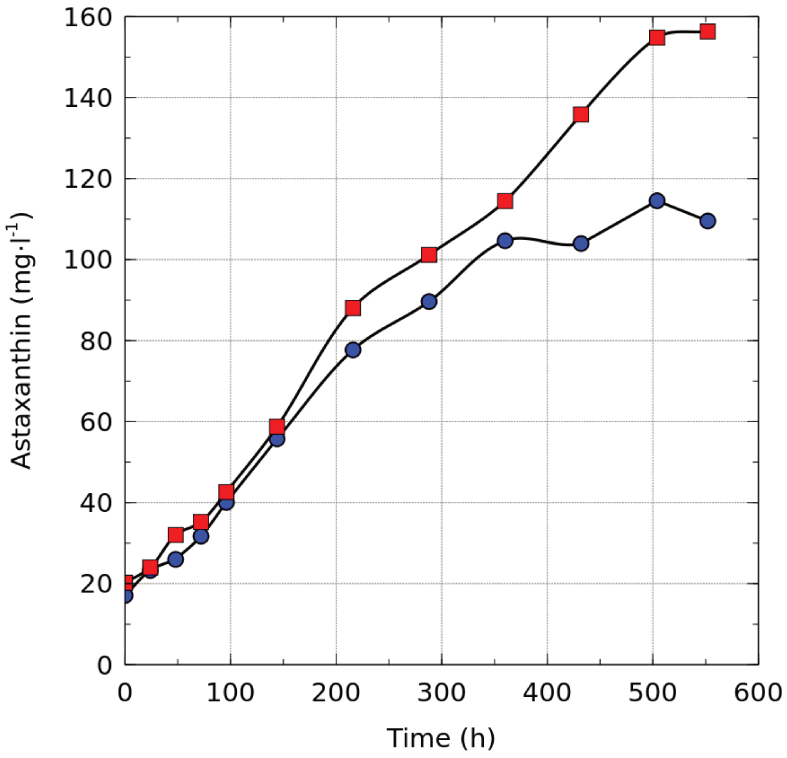

Figure 5.4.1: Astaxanthin accumulation in cultures kept at $20°C$ (•) and $27°C$ (▪).

5.4.1 Astaxanthin production evaluation

To initiate the accumulation of astaxanthin at $20°C$ and $27°C$, the same cells that underwent a normal growth (as explained explained in section 5.1) were centrifuged and resuspended in MSIM-N medium (Table 1.13) to a final concentration of $1 \cdot 10^6\, cells \cdot ml^{-1}$. This expedient was devised to reduce as possible the influence of light on the cultures: cultures with different light harvesting characteristics cannot be compared directly if the concentration is not kept at the very same value. In this way, the only effect of temperature could be expected and a proper comparison can be carried out. The results of the experiments are shown in Figure 5.4.1. For the first six days the cultures behaved similarly with the culture at $27°C$ accumulating a slightly higher amount then the control culture. Starting from the $7^{th}/8^{th}$ day of cultivation the two cultures differentiated and the high temperature culture ended up accumulating about 37% more astaxanthin then the control (156.33 $mg \cdot l^{-1}$

against 114.52 $mg \cdot l^{-1}$). As the starting cell concentration was the same for both cultures, this result should not depend on the overall cell number at the different temperatures. Indeed, the final total cell concentration was $9.82 \cdot 10^5\, cells \cdot ml^{-1}$ and $9.07 \cdot 10^5\, cell \cdot ml^{-1}$ for $27°C$ and $20°C$ respectively. As expected then, the increased temperature had a positive effect when combined with the nitrogen stress and allowed for an increased final astaxanthin production.

5.4.2 Economic assessment

As we demonstrated in the previous sections, an increased cultivation temperature exerts a physical stress on the culture which, in turn, gives place to at least three positive collateral effects:

- ➙ an increased lipid accumulation in the cell
- ➙ an increased resistance to high light conditions
- ➙ an increased astaxanthin accumulation in combination with the nitrogen starvation.

All these three new characteristics have a beneficial effect when seen in the frame of an outdoor cultivation condition. First of all, an increased lipid accumulation can be seen as an added value byproduct in the view of an integrate biofuel/astaxanthin producing plant. Moreover, outdoor cultivation conditions are rarely characterized by low PFDs, especially in summer where at noon on a clear day, up to 2000 $\mu mol \cdot m^{-2} \cdot s^{-1}$ can be reached. In these conditions, cells characterized by increased I_k values are more suitable due to their increased resistance to higher PFDs. Finally, an increased astaxanthin production can be seen as a beneficial effect even if the total green cell productivity is slightly lower than that at $20°C$. By taking into account this last point, together with the difference between the two temperature investi-

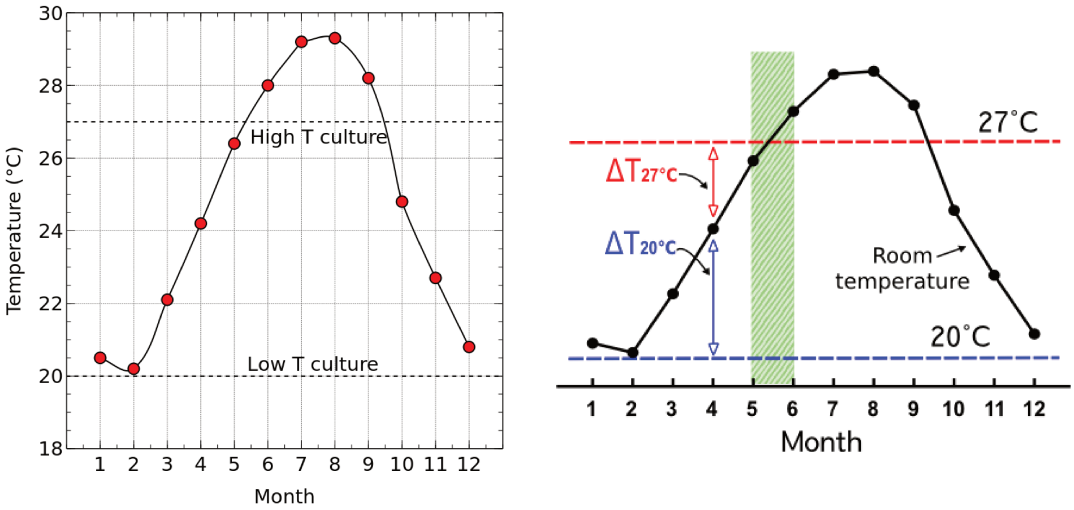

(a) Yearly temperature variation in the laboratory expressed as a monthly variation.

(b) Energy requirements calculation scheme.

Figure 5.4.2: Temperature variations used in the energy calculations.

gated we carried out an easy basic energetic comparison of the two reactors. First of all we wanted to compare two identical PBRs to avoid taking into account different materials, different productivities and all those parameters not strictly correlated to the temperature difference. To do this we just concentrated on the difference in the energy required to keep a constant temperature in the PBR throughout the year (Figure 5.4.2a). The aim was to give an indicative energy assessment for outdoor astaxanthin production basing on the lab scale productivities however it is well known that no easy comparison can be carried out *a priori* between indoor and outdoor conditions. We then restricted the comparison to the temperature changes we recorded in the laboratory where the cultivations were carried out. This comparison still remains significant even in a hypothetic outdoor comparison if we think that both reactors have to be heated up to a minimum temperature of $20°C$ even in outdoor conditions and the energy used this way despite being relevant towards the final product price it is not relevant in the direct comparison of the two different cultivation temperatures.

A second condition we imposed for the comparison was that the energy requirements to heat/refrigerate the cultures was easily calculable through the generic formula:

$$Q_i = m \cdot \hat{c}_p \cdot \Delta T_i \tag{5.4.1}$$

where Q_i is the energy required for the temperature i, $\hat{c}_p$ is the specific heat capacity of the culture and ΔT is the temperature difference between the room and the culture temperature. This is a bit simplistic approach as it does not take into account the power needed to heat/refrigerate the reactor but just the energy needed to heat the culture volume from the outer temperature to the reference cultivation temperature. Of course this calculation is largely overestimated as the only energy really needed to keep the temperature constant is that one lost by heat diffusion from/to the environment. As this lost energy is a function of the ΔT between the culture and the laboratory it was not easy to estimate and we opted for the overestimated albeit easier to carry out simplified formula (Eq. 5.4.1). It is thus easy to calculate the year-round energy requirement for each condition by integrating this equation under the temperature variations as reported in Figure 5.4.2b by using the formulas:

$$Q_{tot,20^\circ} = \int_1^{12} m \cdot \hat{c}_p \cdot dT_{20}(month) = 47.151\, kJ \cdot year^{-1} \tag{5.4.2}$$

$$Q_{tot,27^\circ} = \int_1^{12} m \cdot \hat{c}_p \cdot dT_{27}(month) = 34.276\, kJ \cdot year^{-1} \tag{5.4.3}$$

These are the values obtained for one reactor with a volume of 200 ml heated/refrigerated for one year, using the integral averaged room temperature. As we can see from Eqs. 5.4.2 and 5.4.3 with other conditions being equal, the lower temperature cultivation requires more energy than the higher temperature one. The difference becomes even more evident if we express the difference incorporating the

increased astaxanthin productivity. We can in fact calculate the energy required for the production of a μg of astaxanthin as:

$$\begin{aligned} UC_{asta} &= \frac{Q_{tot,i}}{Tot.\,Asta\,Prod.} \\ &= \frac{Q_{tot,i}}{[months] \cdot [Monthly\,prod.] \cdot [Reac.\,volume]} \end{aligned}$$

where UC_{asta} is the astaxanthin unitary energy cost expressed as $J \cdot \mu g^{-1}$. Using the required energies for each condition together with the productivities attained in the experiments of Fig. 5.4.1 we thus obtain:

$$\begin{aligned} UC_{asta,20} &= 172\,kJ \cdot g^{-1} \cdot year^{-1} \\ UC_{asta,27} &= 92\,kJ \cdot g^{-1} \cdot year^{-1} \end{aligned}$$

This means that the production of astaxanthin by means of a culture kept at $20°C$ is almost two times more expensive than the production of astaxanthin at $27°C$ as long as all the other conditions are equal. This halving in production costs just originated by rising the temperature by $7°C$ and seems to be quite an achievement especially when the comparison was carried out against the *optimum* temperature. There is definitely the need to better define in which regards a temperature should be defined "optimal".

Moreover, this result acquires even more relevancy if one thinks about Kobe climatic conditions: this is in fact what we may indicate a somewhat "cold" climate for algae cultivation. In fact, algal cultures are usually grown in temperate zones where longer day/night cycles are available and higher temperatures are recorded on a daily basis. Many cultivation plants are located in the Hawaii islands, California, South-East Asia etc. and therefore after this economic assessment we may conclude that to cultivate *H. pluvialis* for astaxanthin production in said regions a

culture temperature of $20°C$ is definitely counterproductive. Higher cultivation temperatures must be therefore investigated under real outdoor conditions to maximize productivities and simultaneously reduce the costs.

.

Part 6

Results and Discussion III: Implementing flashing light in cascade reactors

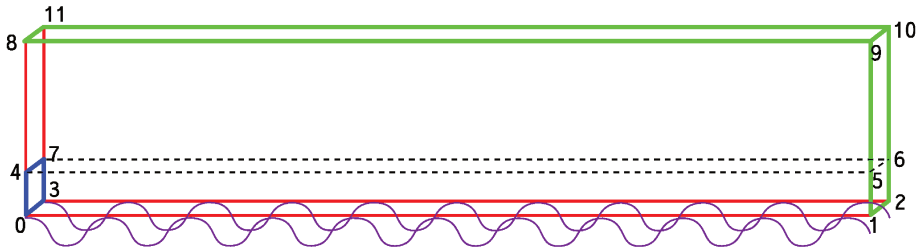

Figure 6.1.1: Cascade PBR mesh. The black lines only represent fictitious inner divisions in the reactor while colored lines represent the actual boundaries: red=Walls, blue=Inlet, green=Outlet. The violet line represents the wavy bottom.

6.1 Simulation setup

6.1.1 Mesh generation

This part of the work has been carried out by using the very same equations as in Part 4 with the sole difference being, obviously, the PBR mesh and the boundary conditions. The mesh for the flat cascade PBR has been easily created by using *blockMesh* and manually entering each point in the dictionary file. On the other hand, the creation of the wave bottom PBR mesh prompted for the creation of an *ad hoc* script able to map the points from the real wavy surface inside the dictionary file (details explained in Appendix II). For the definition of each boundary refer to Figure 6.1.1.

6.1.2 Boundary conditions

The boundary conditions were the same for both PBR designs, the only difference being the mesh used during the simulation. In the detail, the boundary conditions used for the cascade PBR simulation were the following:

- Fluid velocity - $\overline{U} = (U_x, U_y, U_z)$

  - Inlet:

    ```
    type fixedValue;
    ```

`value uniform (0 0 $U_x$);`

(the fluid velocity was changed according to the required culture flow rate and the inlet cross section)

⊖ Outlet:

```
type pressureInletOutletVelocity;
value uniform (0 0 0);
```

⊖ Walls:

```
type fixedValue;
value uniform (0 0 0);
```

(the fluid velocity on the walls is zero by definition)

➙ Pressure field - p

⊖ Inlet:

```
type buoyantPressure;
value uniform 0;
```

(the pressure is calculated by the Stevin Law)

⊖ Outlet:

type totalPressure;

p0 uniform 0;

U U;

phi phi;

rho rho;

psi none;

gamma 1;

value uniform 0;

⊖ Walls:

```
type buoyantPressure;
value uniform 0;
```

- Partition coefficient - $alpha1$
  - Inlet:

    ```
    type fixedValue;
    value uniform 1;
    ```

    (strictly equal to 1, meaning pure liquid is entering the domain)
  - Outlet:

    ```
    type inletOutlet;
    inletValue uniform 0;
    value uniform 0;
    ```

    (the outlet and the reactor upper part are left open for the mass to flow outward and/or inward)
  - Walls:

    ```
    type constantAlphaContactAngle;
    theta0 0;
    limit none;
    value uniform 0;
    ```

    (walls with perfect wettability)
  - At $t = 0$ no liquid is occupying the PBR therefore, no special $alpha1$ initialization was required.

The simulation of an open channel required the specification of an additional parameter of crucial importance: the universal gravitational constant g. This constant is in fact defined inside the proper file (stored in the $/constant/g$ file in the case directory) as the standard array:

$$g = (g_x, g_y, g_z)$$

In this kind of definition is pretty easy to define the reactor slope by modifying the direction towards which the gravitational force is acting. This is done by calculating (when the reactor slope is ϑ):

$$\begin{cases} g_x = g \cdot sin\vartheta \\ g_z = g \cdot cos\vartheta \end{cases}$$

The reactor slope was changed according to the modified cultivation conditions.

6.2 Modeling the flow over cascade PBRs

The cascade photobioreactors have been in use since the first one was deployed in *Třeboň* by Setlík et al. (1970). These reactors are known for being one of the most productive PBR design and are capable to reach biomass concentrations (DW) up to 40~50 $g \cdot l^{-1}$ and represent a good trade-off between the open pond (inefficient) design and the closed PBR (expensive). In this section we tried to investigate the fluid dynamics in a standard flat cascade PBR and to introduce in the design an additional component, the flashing light, by changing the PBR's bottom shape from flat to wavy. The increase in LCE was then investigated by using the very same model realized in to evaluate its usability in the presence of radically different PBR configurations.

6.2.1 Flat bottom cascade

Open channels are all those structures where a channel or an open conduit is used to displace water from an higher point to a lower one by only using gravitation as the driving force. With this definition, a cascade PBR clearly falls in the category

of said "open channels" and all the definitions of the characteristic parameters for this category of flows should be directly applicable to these reactors without any major change. Therefore, to analyze the fluid pattern in a cascade cultivation system consistent of a series of flat plates, it is necessary to refer to those parameters such as the culture layer thickness s, the fluid velocity $\overline{U}$ of the suspension, and the Reynolds number Re in the various situations. The model adopted for the system has been already described in depth in section 3.3 and we will therefore limit to the description of the model application to the reactor.

.

6.2.1.1 Laminar flow

As a first attempt to verify the applicability of the same simulation algorithm as that in Part 4 we proceeded to the analytical solution for the fluid layer thickness by means of Equation 3.3.4

$$U_{x,max} = \frac{\rho g}{\mu} \cdot \frac{s^2}{2} \cdot sin\theta$$

and compared the results with those attained by the numerical simulation with *interFoam* after creating the proper mesh for the reactor (Appendix II). At a given flow rate $Q = 0.0011\, m^3 \cdot s^{-1}$, we can easily verify that the flow regime is laminar ($Re < 1000$) and thus, using the notation in Figure 3.3.1, we can write:

$$\begin{aligned} Q &= A \cdot U_{x,max} \\ &= L \cdot s \cdot U_{x,max} \\ &= L \cdot \frac{\rho g}{\mu} \cdot \frac{s^3}{2} \cdot sin\theta \end{aligned}$$

where the only variables are the film thickness and the reactor slope; we could

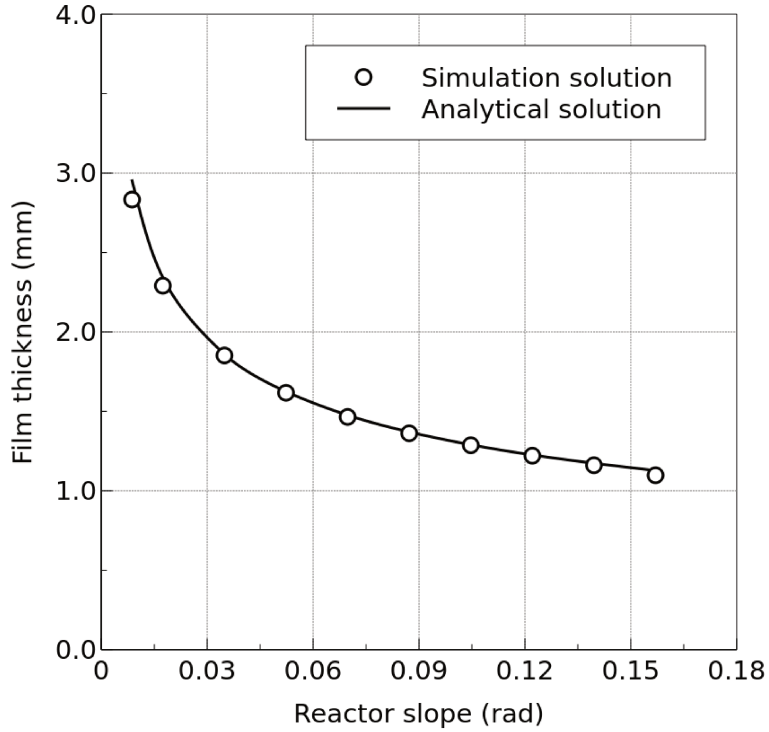

Figure 6.2.1: Culture film thickness as a function of the reactor slope: comparison between the simulation data (◯) and the analytical solution (line).

therefore calculate the film thickness as a function of the reactor slope and compare it to the results of the numerical simulation (Figure 6.2.1). The plot clearly shows an almost perfect matching between the analytical solution and the simulation results where only the thickest film conditions ($S_o = \vartheta = 0.0087$) showed a small difference, the simulation being slightly lower than the calculated value (2.83 mm and 2.95 mm respectively). Moreover, calculating the Reynolds number (Table 1.7) we verified that the fluid flow was indeed in the laminar regime where the Eq. 3.3.4 could be reliably applied. We thus concluded that the interFoam software could be used successfully to also predict the fluid behavior in the open channels.

In Tab. 1.7, another interesting phenomenon becomes evident: the flow in open channels, apart from small variations at low film thickness, evolves with a Re number which is constant with the slope. This is an indirect manifestation of the energy conservation in open channels. With a constant fluid flow and a changing slope, the

PBR slope (ϑ°)	Reynolds
0.5	552
1	537
2	533
3	538
4	536
5	530
6	527
7	516
8	503
9	501

Table 1.7: Reynolds number as a function of the reactor slope.

film thickness lowers progressively with the fluid velocity necessarily increasing with the same trend:

$$Q = 1 \cdot s \cdot \overline{U} = constant$$

which therefore directly influences the way Re is calculated (from Eq. 3.3.1):

$$\begin{aligned} Re &= \frac{\rho_L \cdot U_x \cdot \left(\frac{s}{1+2\cdot s}\right)}{\mu} = \frac{\rho_L \cdot U_x \cdot s}{\mu} = \frac{\rho_L \cdot Q}{\mu} \\ if &\quad s \ll 1 \end{aligned}$$

6.2.1.2 Manning equation

In the bench scale cascade model (Fig. 2.3.4) it was really easy to reproduce a perfectly laminar flow for experimental purposes but on the contrary, the full scale PBRs for culture productivity measurements were always operated in a fully turbulent regime ($Re \gg 1000$). For this reason we needed to verify if those reactors were well fit by analytical equations and if those equations were in turn well represented by the simulations.

The typical equation employed in the characterization of a turbulent channel

flow is the so called Manning equation (Eq. 3.3.6)

$$Q = A \cdot U = A \cdot \frac{R_h^{2/3} \cdot S_o^{1/2}}{n}$$

where R_h is the hydraulic radius, A the cross section area. S_o is the value of the slope percentage, calculated as the ratio between the heights reached at the initial section of the cultivation unit and its total length. As this value is usually very small (0.017 for the full scale PBR), we can simplify the calculations, avoiding the use of trigonometric functions (as $S_o = tan\vartheta = \vartheta$ for very small angles). The parameter n is called the Manning resistance coefficient, and it accounts for all frictional phenomena involved in the flow. Values for the Manning resistance coefficient can be obtained from the literature (Janna, 2010; Perry et al., 1999). Equation 3.3.6 correlates the volumetric fluid flux with the film thickness s, if acceptable values for the parameter n are known which is true for any "real" PBR but unfortunately not true for the simulation with OpenFOAM. The problem resides in the fact that interFoam solves the Navier-Stokes equations by imposing a "no slip" condition on the wall where the fluid velocity is, by definition, identically zero. The Manning equation with its semi-empirical nature relies on the quite simplistic assumption that the whole fluid body is flowing with a constant fluid velocity at each depth (Janna, 2010). In this conditions, the introduction of the resistance coefficient was mandatory and represented the correlation factor for adjusting the experimental results with those attained with the Chezy formula (3.3.5). This is a very big difference which required a further validation of the code.

First of all we quickly verified the assumption that a large scale PBR could be modeled by using the Manning equation. We used the 24 m cultivation unit in *Třeboň*, to measure the culture thickness obtained by the fixed flow rate of 0.0027 $m^3 \cdot s^{-1}$ and an approximate fluid speed to make the comparison. The results

Design parameter	Value
$Q\ (m^3 \cdot s^{-1})$	0.0027
S_o	0.017
$L\ (m)$	1
n	0.01

Parameter	Calculated	Measured
$s\ (m)$	0.0062	0.0060
$U_x\ (m \cdot s^{-1})$	0.44	0.50
Re	4485	4940

Table 1.8: Provisional calculations carried out to predict the behavior of the fluid flow prior to the first installation and subsequent validation by means of the Manning equation.

are shown in Table 1.8. The culture layer thickness calculated with the Manning equations showed a pretty good agreement with that measured in the reactor while the fluid velocity was slightly lower (0.44 and 0.5 $m \cdot s^{-1}$ respectively). The next step was to validate the simulation in the same way used for the laminar flow (Fig. 6.2.1) with the slight difference that, in this case, we did not even know a tentative value for the n parameter in the simulation. We thus used the simulation data with a "reverse interpolation" procedure where we calculated the value of n as a function of the slope to verify whether this value was constant or not. The Manning resistance coefficient is only dependent on the physical properties of the PBR materials and should be constant, independently from the changes in the PBR slope. As shown by the results in Figure 6.2.2, the correspondence between the numerical calculations and the simulation is interesting: the values of the n parameter are almost constant and the linear interpolation held an approximate value of 0.00435.

The major difference between the numerical solution of the flow analytical solution was in the fluid velocity distribution along the vertical axis, i.e. the fluid velocity attained at different depths. This is a parameter of fundamental importance, especially during the determination of the mass transfer coefficient where the concentration at a given PBR position have to be measured together with the fluid velocity in the same point. The fluid velocity profile attained in the simulation solution can be seen in Fig. 6.2.3. To use the simulated data together with the calculated one or even for making comparison of derived quantities (for example the

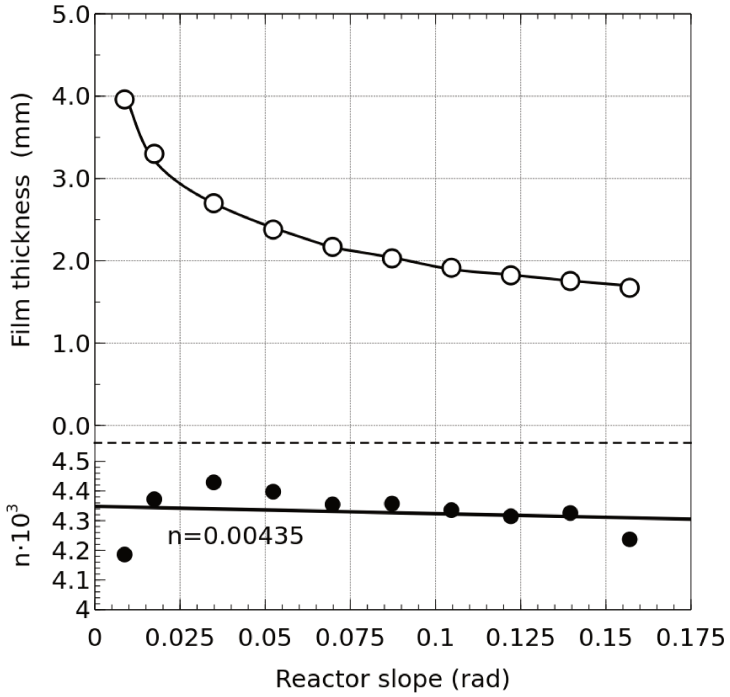

Figure 6.2.2: Culture film thickness as a function of the reactor slope for $Q = 0.0022\,m^3 \cdot s^{-1}$. Top: comparison between the simulation data (◯) and the Manning analytical solution (line); bottom: calculation of the n parameter used by the interFoam solver.

$k_L a$) the need of a proper alignment between the different results is evident. While the measurement of the film thickness s is quite straightforward, the measurement of the fluid velocity is not that easy, because of the waves that form on the top of the fluid layer. We therefore decided to acquire data from the simulation by measuring the fluid velocity at a predetermined fluid thickness amounting to the 80% of the total thickness. We were aware of the difference in the absolute value in the obtained values but we decided in the worst case, if needed, to introduce a correction factor for taking into account said differences.

6.3 Mass transfer coefficient determination

Comparing two different PBRs with completely different geometries is a quite difficult task: the illumination conditions, the fluid dynamics of the system, the mass

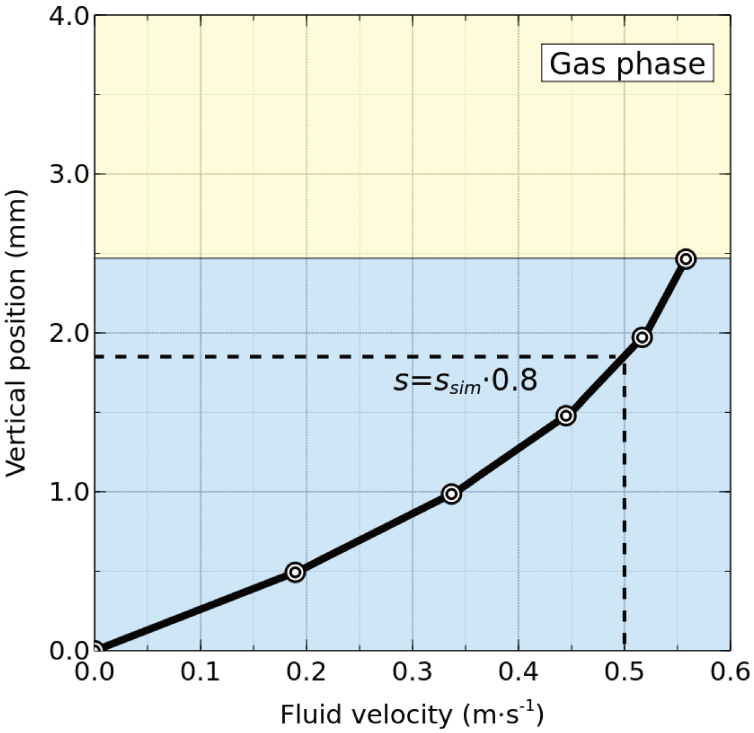

Figure 6.2.3: Fluid velocity distribution along the film thickness (z coordinate) in the case of $S_o = 1°$. Dashed lines identify the values used in the determination of $k_L a$ (see below).

transfer and all the most important parameters are likely to be completely different and not easy to compare. On the contrary, comparing two slightly different PBR is a much easier task as almost all the conditions will be the same. The most difficult point in this case is that, while a different PBR can be analyzed by assuming that "a comparison is not possible" in the case of two similar reactors, a proper comparison criterion have to be determined for each major condition. Failing to comply to this standard, will end up bearing completely non-consistent results which will eventually lead the researcher to blatantly wrong conclusions. Conclusions supported by verified and trusted data based on wrong comparison conditions.

For this reason we decided to properly establish the comparison conditions by using the small bench scale PBR together with the simulation software and then to proceed to the implementation of the findings in the wavy bottom PBR. The parameters we deemed to be the most important in this comparison were the mass transfer coefficient k_La and the light distribution.

6.3.1 k_La as a function of reactor slope

In the case of a flat bottom cascade, the conditions are ideal for the application of the Higbie penetration theory, which works well for stagnant or thin flowing films (Haroun et al., 2012) (see Fig. 6.3.1a for a calculation example). As the aim of this section was to confront the flat bottom reactor with a wavy bottomed equivalent reactor, we had to find a way to compare the geometries by using k_La values measured with different methods. It is in fact impossible to consider a wavy bottom cascade reactor either as stagnant or as a thin film. First of all we then compared two different data collecting methods. The best candidate for the measurement of the mass transfer coefficient in a wavy bottom PBR, is the gassing out method (Wise, 1951) which we simulated with the interFoam solver modified according to

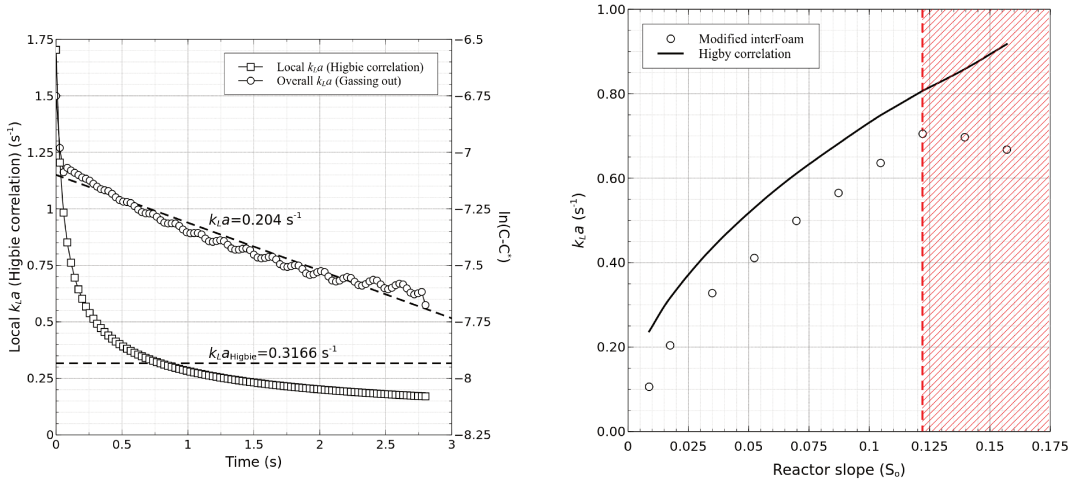

(a) Comparison of the Gassing out method and the Higbie correlation for a slope S_o=0.0174: (□) local k_La calculated using the Higbie correlation; (◯) simulated driving force for the gassing out method.

(b) Correlation between k_La values calculated by the Higbie correlation (straight line) and the modified interFoam solver (circles, sampling position at 80% of the film thickness).

Figure 6.3.1: Comparison of two different methods for measuring the k_La in cascade PBRs.

(Haroun et al., 2010) as already explained in section 3.4 (Fig 6.3.1a). The results of the comparison between the two methods are shown in Figure 6.3.1b. The trends of the two measuring methods shown a good degree of agreement even if the values of k_La measured according to the Higbie theory always shown a higher absolute value than those calculated through the simulation. Moreover, for slopes steeper than 0.125 the data obtained with the simulation evidently diverged showing the physical maximum slope limit beyond which the method should not be applied. The main reason for this difference resides in the more "realistic" behavior shown by the simulated flow when compared to that measured by the Higbie model: while the Higbie models tended to remove any inhomogeneity in the data, the simulation showed a flow pattern extremely similar to the real one with all the problems accompanying a real flow (surface waves, poor diffusion in shallow films etc). However, the difference between the two measurements was practically constant in all the points therefore we should further investigate on the origin of this difference. As for now we decided to use the k_La values from Higbie for their ease of calculation in various conditions

and the gassing out method for the wave PBR.

6.3.2 Laying down a new model

A flat bottom PBR showed a pretty regular flow and a quite simple dependence of said fluid regime on the PBR geometry and operational conditions. With this premise we decided to look for a correlation to use to fast assess the value of $k_L a$ by means of a mathematical method. The Higbie approach was a close candidate for this scope however, the fact that at least the residence time must be determined for its use was a bit of a deterrent. We then started to look for a more simple model.

In chemical engineering, one of the most important finding was the discovery of the mass transfer/heat exchange analogy: where the heat transfer is governed by the Nusselt number Nu, mass transfer is governed by its analogue, the Sherwood number Sh:

$$Sh = \frac{k_L \cdot L_{eq}}{\mathfrak{D}}$$

where the L_{eq} term represent the characteristic length of the system, like the diameter in a close conduit or, in the case of an open channel, the hydraulic radius. In a cascade PBR we have defined the hydraulic radius as

$$R_H = \frac{s}{1+2s} \cong s$$

because $s \ll 1$. We may therefore conclude that:

$$Sh = \frac{k_L \cdot R_H}{\mathfrak{D}} = \frac{k_L \cdot s}{\mathfrak{D}}$$

In addiction, we can easily express k_L as a function of the $k_L a$ when the expression

of a is used:

$$k_L = k_L \cdot \frac{a}{a} = k_L a \cdot \left(\frac{V_{PBR}}{S_{PBR}}\right) = k_L a \cdot \left(\frac{X \cdot L \cdot s}{X \cdot L}\right) = k_L a \cdot s$$

where the same notation of section 3.3 is used. With this final arrangement we can conclude that in cascade PBRs, the Sherwood number can be calculated as:

$$Sh = \frac{k_L a \cdot s^2}{\mathfrak{D}} \tag{6.3.1}$$

The correlation in Eq. 6.3.1 means that, if a simple correlation between the cultivation parameters and the Sh number could be provided, the calculation of the mass transfer coefficient would be trivial. Studying the $k_L a$ in open channels we faced then an interesting discovery: to the present day, no specific Sh correlation exists for the calculation in thin layer open channels. There indeed are various formulas describing the flow over a thick horizontal layer or in vertical films but the intermediate conditions seemed to be somewhat neglected by the literature. Moreover we found a common behavior for the various correlations that made us thinking we could arrange a new Sh correlation for the cascade PBRs. According to what is reported in (Barry, 2005), the Sherwood number for a fluid flowing on a flat plate can be calculated has:

$$Sh = A \cdot Re^{\frac{4}{5}} \cdot Sc^{\frac{1}{2}}$$

where A is a numerical constant and, of course, Sc is the Schmidt number:

$$Sc = \frac{\mu}{\rho \cdot \mathfrak{D}}$$

This equation is reportedly valid for open channels up to big scales like those used

for wastewater treatment[13] but does not incorporate any dependence on the slope of the channel itself, except for that in the Re number. On the other side of the applicability spectrum, another correlation widely used for falling films and droplets is that provided by Frössling (1938) where Sh is calculated by the empirical formula:

$$Sh = 2 + 0.552 \cdot Re^{\frac{1}{2}} \cdot Sc^{\frac{1}{3}}$$

This second correlation have an asymptote for Re approaching zero meaning that, for a stagnant fluid film, a constant Sh=2 have to be expected but again, no dependence of the slope of the film is provided.

As we already demonstrated by a mathematical approach, the Sherwood number should be strongly dependent on the PBR slope as it shows to be explicitly and implicitly depending on the reactor slope (in s^2 and k_La respectively). By rough data interpolation we found that both these correlations were more or less able to accurately predict Sh values starting from the simulated k_La data. Being the flat bottom cascade PBR half way between a falling film and an open channel, we thought that a combined equation between the two could be able to better fit the numerical data. We found in fact that the equation:

$$Sh = A \cdot Re^{\frac{4}{5}} \cdot Sc^{\frac{1}{2}} + B$$

was able to exactly predict k_La values starting from velocity data. The parameters A and B were just arbitrary constants[14] we introduced in the fitting procedure and to determine them we started by calculating A' from simulated data with the following formula (from Barry's formulation):

[13] Ambion and Ho, Unpublished data available online http://courses.washington.edu/microflo/Angelo_Ambion_Dan_Ho_Sp05.pdf

[14] To be precise, the term here denominated B represents the limit Sh number attained when pure diffusion represents the only mass transfer phenomenon in the system.

$$A' = A'(s) = \frac{Sh}{Re^{\frac{4}{5}} \cdot Sc^{\frac{1}{2}}}$$

As data for different slopes were used, we further noticed that the A' parameter was a function of the PBR slope with the same trend shown by the film thickness (lowering with S_o). In fact, interpolating A' against s held a perfectly linear fitting with the equation $A'(s) = 2.163 \cdot s + 0.00763$ (R^2=0.998). This equation was then used to calculate A and B while keeping in mind that the local Re is constant with S_o (as explained in section 6.2.1.1):

$$Sh = 2.163 \cdot s \cdot Re^{\frac{4}{5}} \cdot Sc^{\frac{1}{2}} + 0.00763 \cdot Re^{\frac{4}{5}} \cdot Sc^{\frac{1}{2}} = 2.53 + 2.163 \cdot s \cdot Re^{\frac{4}{5}} \cdot Sc^{\frac{1}{2}} \quad (6.3.2)$$

This represents a new correlation for shallow film open channel flows where Sh can be calculated as a function of the reactor slope just by velocity and s data, whether from analytical solutions or simulations.

6.3.2.1 Sherwood number and flow rate interactions

We tried to use the new formula under different flow rate conditions: the fluid flow in open channels appears to be "self regulating" due to the nature of the forces acting on the fluid (Figure 6.3.2). In fact, taking into account the variations caused by an increased flow rate of the fluid film thickness and the fluid velocity (due to mass conservation) we could reasonably expect that the culture flow rate could influence the measurement to a lesser extent. Moreover, looking at the film thickness variations caused by the reactor slope we were also expecting an increase in the mass transfer coefficient due to the increased mixing. We verified this hypothesis by using the Higbie correlation as a model. The results are shown in Figure 6.3.3. In agreement with what hypothesized, the Sh correlation showed to be quite independent

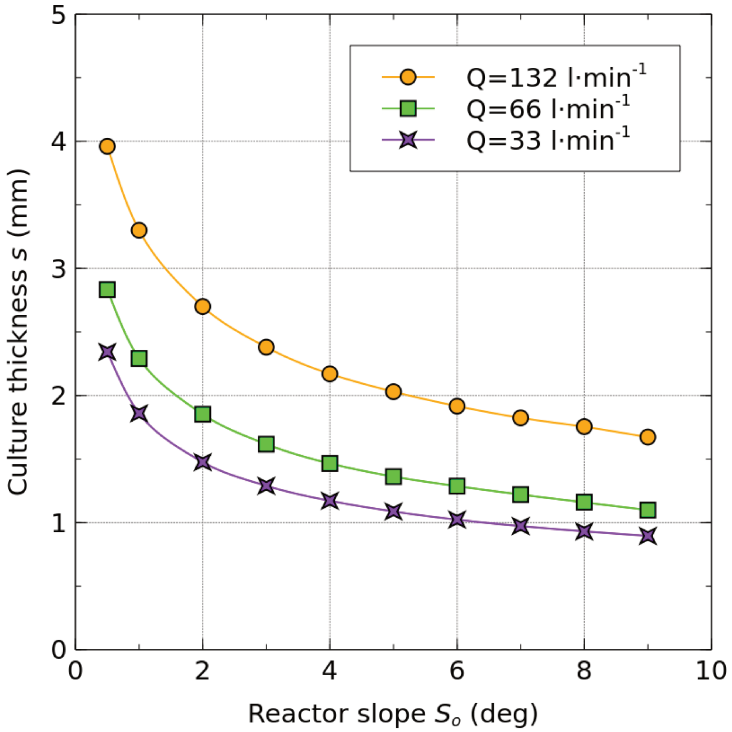

Figure 6.3.2: Culture thickness s as a function of the slope and the flow rate as obtained by with the OpenFOAM simulation.

from the flow rate while the mass transfer coefficient k_La was in fact rising together with the reactor slope. Results for the 132 $l \cdot min^{-1}$ show a perfect overlapping and 66 $l \cdot min^{-1}$ still show a good correspondence with an almost constant deviation between the two methods where our correlation was slightly underestimated. The k_La average deviation remained around an average of 4.29% for all the investigated slopes. The highest deviation was recorded in the central points where 5.6% was registered in correspondence of $S_o = 0.105$ (or $\vartheta = 6°$). We can therefore observe how an overall good fitting was attained by using our formula in Eq. 6.3.2 both for Q=66 and 132 $l \cdot min^{-1}$. Regarding the fitting at 33 $l \cdot min^{-1}$, however, the number calculated by the Sh formula and the Higbie theory were clearly different. It is our opinion that these deviations encountered at lower flow rates are originating from the different shape of the fluid velocity profile attained under the different conditions. At high flow rates, a thicker and faster film is attained even at the higher slopes;

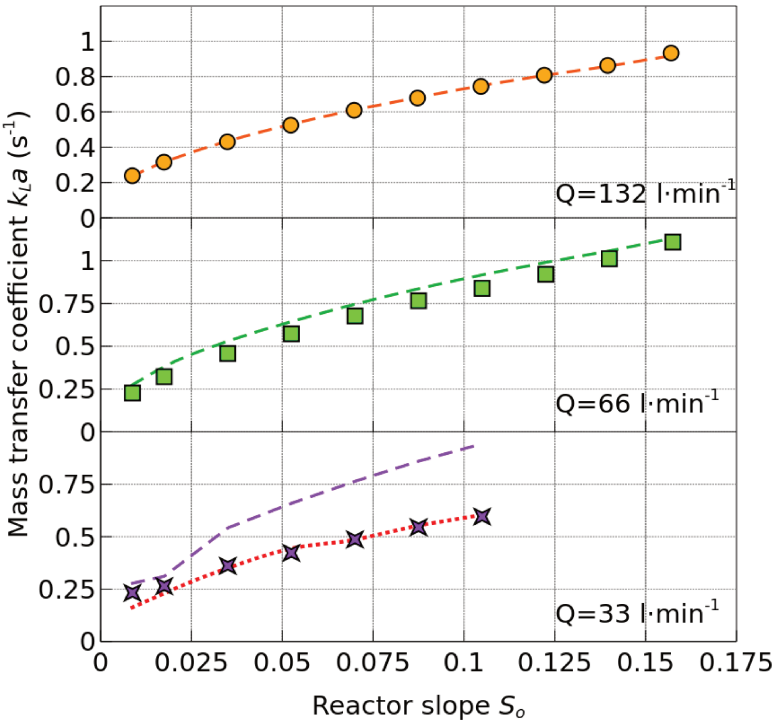

Figure 6.3.3: Application of the new Sh correlation to different flow rates. The symbols represent the results of Eq. 6.3.2 while the dashed lines represent the results of the calculation with the Higbie correlation. The velocity corrected k_La is only shown in the 33 $l \cdot min^{-1}$ conditions as it was not needed/calculated elsewhere.

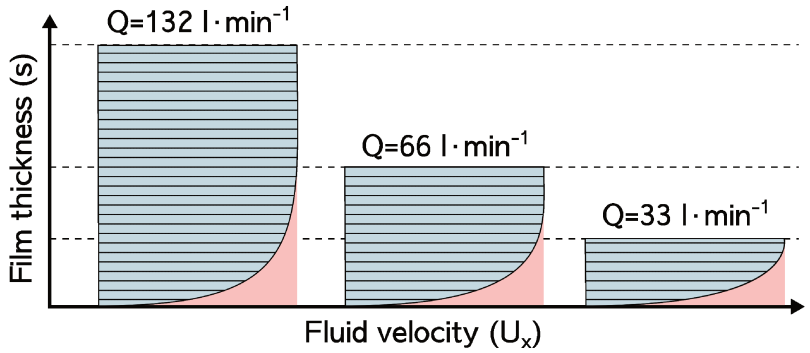

Figure 6.3.4: Representation of the three fluid velocity profiles attained with the three flow rates. Profiles are not derived from actual velocity data and are a mere representation.

within this film, the fluid velocity distribution along the z axis becomes closer to those constant distribution typically hypothesized in simplified equations (Chezy, Manning and even the laminar flow solution). With this closer correspondence, the Re number becomes more and more constant when the film thickness is increased, leading to more stable results. On the contrary, for shallower flows like that attained with the lowest flow rate (Q=33 $l \cdot min^{-1}$) the fluid velocity distribution is all but constant and closely follows the profile illustrated in Fig. 6.3.4. In a situation like this, the correspondence between the simplified Higbie correlation and the interpolation of numerical simulation data seems near to impossible. As a countermeasure for this phenomenon we tried to correct the k_La values obtained with the Higbie theory by using a velocity averaging approach: Higbie values are valid for thin fluids flowing with an uniform fluid velocity typical of the upper fluid layer while the data from the simulation are more close to a real fluid regime with a velocity U_x being a function of the fluid depth. We took the average fluid velocity and used it to correct Higbie values according to the formula:

$$k_La|_{Higbie,corr} = \frac{k_La|_{Higbie}}{U_x} \cdot \frac{1}{s}\int_0^s U_x(z)dz$$

The corrected values showed a very good agreement with the Sh formula (Fig. 6.3.3) we found thus confirming that the effect of the fluid velocity distribution is

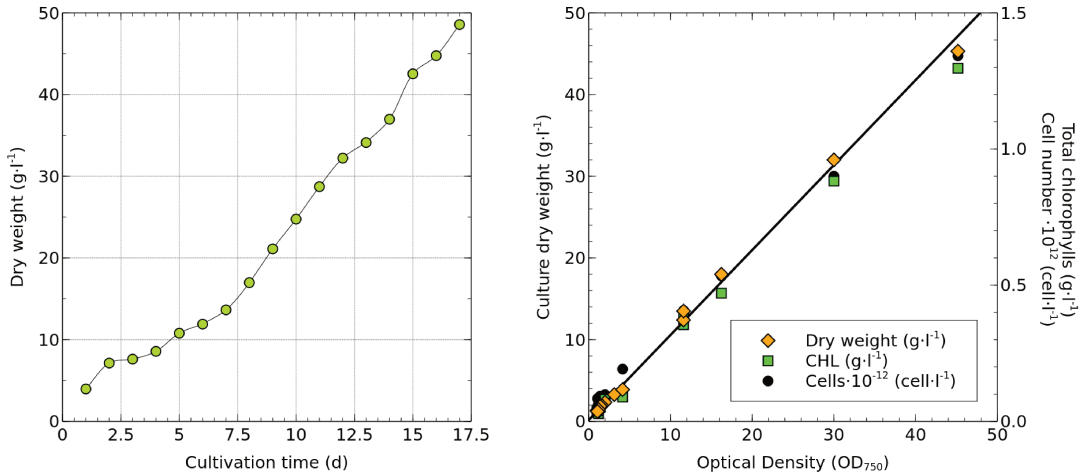

(a) Time course of the culture dry weight

(b) Interrelationship between the characteristic culture parameters and the culture OD_{750}: (◯) Cell number, (□) Total CHL, (◊) Dry weight.

Figure 6.4.1: *Chlorella* growth in a flat cascade PBR in outdoor conditions.

not negligible in very thin fluid layers. The new Sh correlation should be used only in high flow rate conditions which means that can be only applied under turbulent conditions. More investigation is however needed to ascertain whether by using different constants a "laminar version" of the equation could be also calculated.

In the case of thin layer PBRs like the cascade reactor, we ascertained that the culture thickness is always higher than 5 mm (see Tab. 1.8) and we believe that, for a fast k_La assessment with bare bone instruments like a pocket calculator, our equation could be a very useful tool.

6.4 *Chlorella* growth in flat bottom cascade PBRs

As the model for the growth of Chlorella inside a cascade PBR, the growth curves reported in Masojidek et al., 2011 were used. The 24 m growth unit is illustrated in section 2.3.3 and the result of the growth experiments are represented in Figure 6.4.1a. As expected, the PBR showed a very high overall productivity with a maximum biomass concentration of 48 $g \cdot l^{-1}$ attained after a cultivation period of 17

days. The daily productivity averaged thus around a value of $18.7 \pm 5.14\ g \cdot m^{-2} \cdot d^{-1}$ and peaked to $52.1 \pm 4.08\ g \cdot m^{-2} \cdot d^{-1}$ when only the effectively illuminated culture duration was taken into account. The LCE of such a culture, was therefore, incredibly high and close to the physiological limits highlighted in section 1.2.4. The increased productivity recorded in this kind of reactor have to be attributed to the ultra-high chlorophyll concentrations of the culture which actively shield the cells moving in the bottom part of the film that therefore can operate with relatively light and high efficiency. This was directly confirmed by the fluorescence measurements reported in Masojidek et al. (2011) where cultures with concentrations greater than $40\ g \cdot l^{-1}$ showed small negative effects even from the highest noon light intensities (about 1800 $\mu mol \cdot m^{-2} \cdot s^{-1}$ at 13.00). An in-depth dissertation on the consequences of the strong light conditions on the light harvesting system is beyond any doubt an interesting matter to discuss but we won't report it here to avoid digressing in a different major subject. The reader can further investigate on this matter by referring to Masojidek et al., 2011.

During these experiments we also verified how the culture parameters could be directly measured by means of the culture OD_{750} which was related to the DW, CHL and cell concentration values with a perfectly linear relationship (Figure 6.4.1b). The relationship between optical density and the three variables was linear according to regression equations:

$$\begin{aligned} DW &= 1.02879 \cdot OD \quad (R^2 = 0.997) \\ CHL &= 28.9 \cdot OD \quad (R^2 = 0.997) \\ Cells &= 0.0304 \cdot 10^{12} \cdot OD \quad (R^2 = 0.990) \end{aligned}$$

or, with a more elegant parametric equation:

$$\begin{cases} \underline{y = K_i \cdot 1.0071 \cdot OD} \\ K_{CHL} = 28.9\, mg \cdot l^{-1} \\ K_{DW} = 1.0287\, g \cdot l^{-1} \\ K_{cells} = 0.0302 \cdot 10^{12}\, cells \cdot l^{-1} \end{cases}$$

These equations were really useful to analyze the various parameters with a single measure. Moreover, in the laboratory conditions where the Coulter counter was unable to give a proper cell count for the small *C. sorokiniana* cells, we used these correlations to indirectly measure the cell numbers through the DW values.

6.4.1 Growth at different flow rates

The experiments reported hereafter were carried out in the small bench scale cascade PBR (Fig. 2.3.4) by using the same *C. sorokiniana* strain. Again, the same three different flow rates have been selected to investigate the effects of the previously measured mass transfer coefficients on the culture growth. The PBR slope was regulated to the lower possible value of $S_o = 0.0087$ or $\vartheta = 0.5^\circ$ and the light intensity was fixed and equal to 140 $\mu mol \cdot m^{-2} \cdot s^{-1}$ over the growth lane (the overflow tank was kept in the dark). The results are shown in Figure 6.4.2. All the three cultures, despite the different flow rates, behaved similarly in the first 3~4 days showing an almost perfect overlapping of each parameter plot, with deviations well inside the boundaries of the experimental error. This behavior showed how the cultures, in the diluted state were exposed to more or less the same PFD, independently from the effects of the different culture layer thickness. To be precise, only the low flow rate conditions (Q=33 $l \cdot min^{-1}$) due to the ultra-thin culture layer

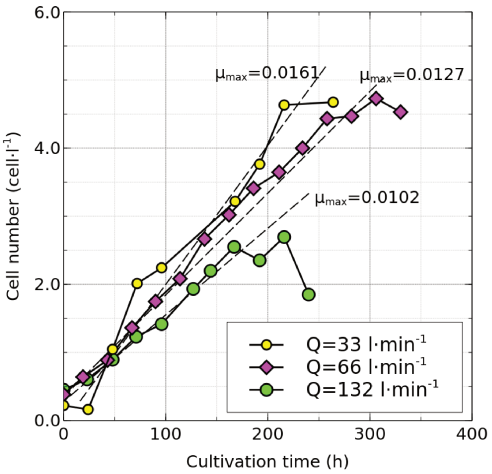

(a) Cell number time course

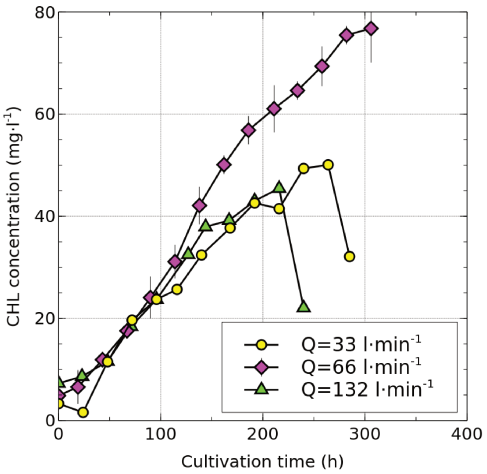

(b) Total chlorophylls time course

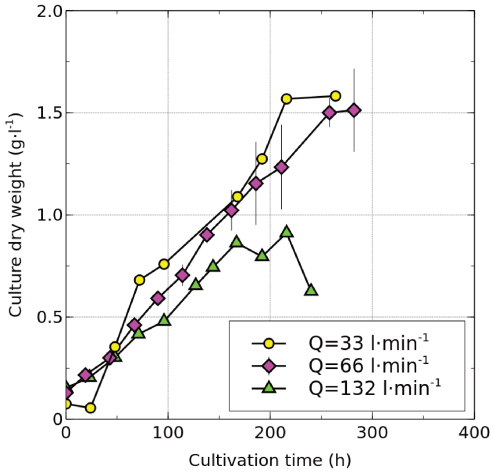

(c) Dry weight time course

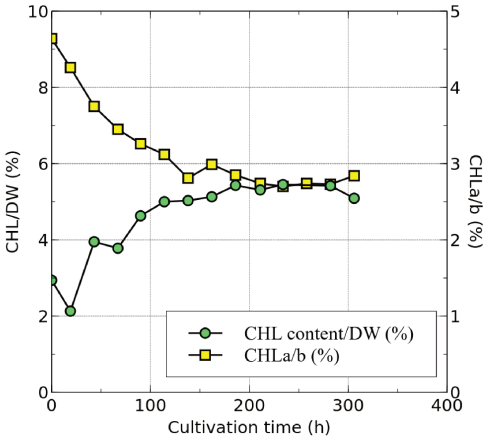

(d) Clorophyll content and CHL a/b ratio time course

Figure 6.4.2: Growth curves in flat bottom cascades with different flow rates

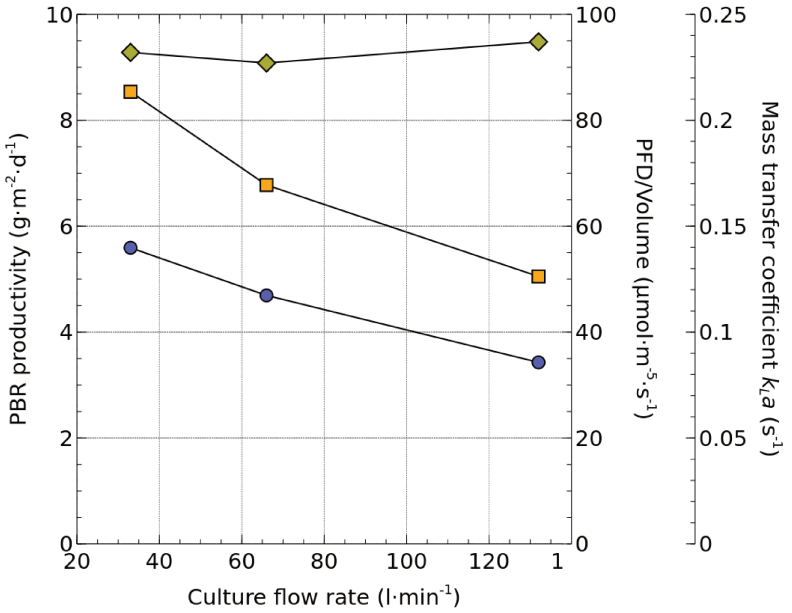

Figure 6.4.3: Reactor performance comparison: (◯) PBR productivity, (□) PFD per reactor volume, (◊) Mass transfer coefficient k_La.

showed a slight photo-inhibition on the first cultivation day. With the culture getting denser, the growth behavior obviously changed and the smaller flow rate conditions proved to be the most favorable for the culture growth. The total productivities, in fact where 5.6, 4.7 and 3.4 $g \cdot m^{-2} \cdot d^{-1}$ for the 33, 66 and 132 $l \cdot min^{-1}$ flow rates respectively (Fig. 6.4.3). This behavior denoted an evident photolimitation which was easy spotted when the characteristic indicator parameters, CHL a/b and CHL/DW were examined (Fig. 6.4.2d).

It is worth noting how the mass transfer coefficient k_La was almost constant in all conditions and thus its effects of on the growth were almost negligible. In these conditions we were able to ascertain that, at least in laboratory conditions, the most important factor limiting the algal growth was the light distribution. Looking at Fig. 6.4.3 we can in fact notice how the PBR productivity showed the same decreasing trend of the values of the volumetric PFD. The value of the PFD per cultivation volume was used to assess the effect of the different culture thickness derived from the different flow rates operated at the same slope and was carried out taking in

consideration only the illuminated portion of the reactor, the rest of the culture being kept in the dark in the overflow tank. The formula used was then:

$$\frac{PFD}{vol} = \frac{PFD}{X \cdot L \cdot s}$$

it appeared evident how the thinner culture layer received an higher PFD on an average, being the total impinging light constant in the three experiments. This was the biggest limit of the lab scale PBR that, as a consequence, showed overall productivities in the order of 1/10 when compared to the outdoor grown culture (5.6 and 52 $g \cdot m^{-2} \cdot d^{-1}$ respectively). The impinging light in the two growth conditions were, however, extremely different with the PFD attained outdoors being roughly ten times higher. This is an interesting observation which shows how *Chlorella* is able to utilize the incoming light with an almost constant LCE which, in cascade reactors, seemed not to be influenced by the impinging PFD or at least not to be influenced to a major extent. As a result, light limited cultures typical of indoor conditions can still be used as a comparison bench test between different configurations still expecting results scalable to outdoor conditions.

6.4.2 Growth at different slopes

The observations carried out in the experiments in the previous section highlighted how light limitation may be the main responsible for the productivity loss in the lab scale PBR. We considered this observation to be of primary interest to understand the growth kinetics of this *C. sorokiniana* strain. The culture, in fact, seemed to be influenced by the flow rate only as the result of the increased/decreased fluid thickness generated by the different slopes. It was thus really easy to use the simulated data for each flow rate to determine the $Q \mid S_o$ combinations where the $^{PFD}/_{vol}$ parameter was equivalent. Using the data reported in Fig. 6.3.2 we selected the

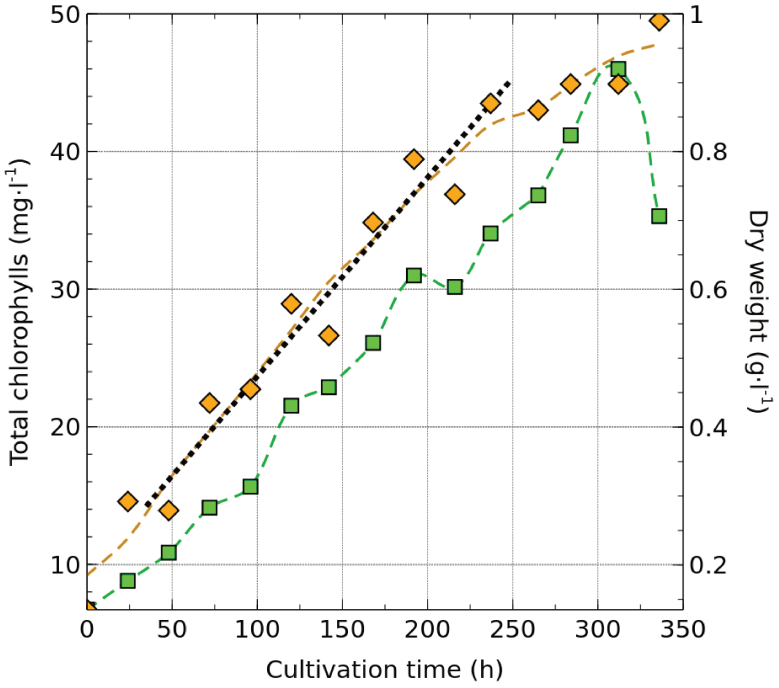

Figure 6.4.4: Growth rate with increased slope. (◊) Dry weight; (□) total chlorophyll concentration. The dotted line represents the maximum slope of the DW curve, i.e. the maximum productivity sustained during the experiments.

point $Q \mid S_o = 66 \mid 0.017$. In this point, in fact, the same $^{PFD}/_{vol}$ of the already tested $Q \mid S_o = 33 \mid 0.0087$ condition could be attained and it could be used to compare the results.

Chlorella was therefore grown under the selected conditions to verify the influence of the volumetric illumination value and aiming to the same productivities attained with $Q \mid S_o = 33 \mid 0.0087$. The results are shown in Figure 6.4.4. The first evident difference with the previous growth conditions (Fig. 6.4.2) was the lowered maximum chlorophyll concentration. As already thoroughly explained in this work, chlorophylls are connected to the average light intensity perceived by the culture and this result perfectly corresponds to the expected culture behavior under increased light conditions. Therefore it was not surprising that the maximum chlorophyll concentration was almost the same as that recorded by the $Q \mid S_o = 33 \mid 0.0087$ culture (Fig. 6.4.2). On the other hand, the DW shown a high degree of variability

	Shear stress (Pa)	
Flow rate ($l \cdot min^{-1}$)	$S_o = 0.0087$	$S_o = 0.017$
33	0.119	-
66	0.126	**0.153**
132	0.122	-

Table 1.9: Shear stress increase due to the increased slope and velocity.

throughout the whole culture and, more important, an overall lower value then the expected. The total produced biomass was 3.96 g (DW=0.99 $g \cdot l^{-1}$) which corresponded to an overall productivity of 2.493 $g \cdot m^{-2} \cdot d^{-1}$ which, compared to the productivity attained in the standard conditions (4.692 $g \cdot m^{-2} \cdot d^{-1}$) represented a rough 47% loss. While the increased illumination effectively inhibited the CHL production, the expected increase in productivity was absent and, on the contrary, the culture showed a relevant loss of productivity.

The very same behavior as seen in these experiments was already reported in Section 4.6.3 where the *H. pluvialis* cells were undergoing an increased shear stress generated by the improved fluid dynamic conditions. We therefore investigated in the same way as in Section 4.6.3 the average shear stress recorded under the different cultivation conditions to explain the productivity loss. The results of the calculations are shown in Table 1.9. All the investigated conditions showed average shear stress values really close to the upper limit of $\tau = 0.1\ Pa$ that is often reported as a dangerous value (Elias et al., 1995). The mildest environment resulted to be the $Q \mid S_o = 33 \mid 0.0087$ followed by $Q \mid S_o = 132 \mid 0.0087$ and $Q \mid S_o = 66 \mid 0.0087$. However, the culture cultivated with the highest slope reached 0.153 Pa which represented a 29% increase when compared to the best conditions. Despite the absolute values being still quite tolerable, an undeniable increase in the culture stress happened when a different slope was adopted and further investigation should be carried out to ascertain whether the productivity losses could be really related to this shear stress increase. This should be especially aimed at removing the border

effects that result evident inside the lab-scale cascade (borders, junctions, screws etc.) and can exacerbate the slightest difference between the real and the measured τ; difference that gets "diluted" when the same cultivation is carried out in the full scale PBRs.

6.5 Wavy bottom cascade

Microalgae productivity outdoors is strongly limited by the so called "light saturation effect". This phenomenon occurs because the growth of the microalgae saturates at a level of light intensity which is roughly 1/10 of the maximum recorded in summer days. The problem of light saturation may be greatly reduced if proper combinations between cell density, and mixing as those happening in the cascade PBRs could be achieved. Even if the flat bottomed cascade PBR is thought to be able to increase the light-dark cycles in the culture due to the high density coupled to the culture turbulence, we believe that a further increase in the reactor productivity could be attained if a proper sustained light-dark regimen could be implemented. We therefore investigated a wavy bottomed cascade PBR. First of all a rough estimation of the probable flashing-light regimen achieved in the reactor was carried out by a simple mathematical model and then a more accurate estimation was obtained by means of an in-depth CFD analysis.

6.5.1 Modeling the flow in the troughs

From the experimental observation of the laboratory scale cascade model, two main fluid flows can be individuated from a side inspection of the photobioreactor: one moving consistently to the typical one of a thin layer cascade, adherent to the PBR surface; the other is a swirling flow located in the bulk of the fluid hold-up inside each trough (Figure 6.5.1). As a first theoretical approach to the determination of

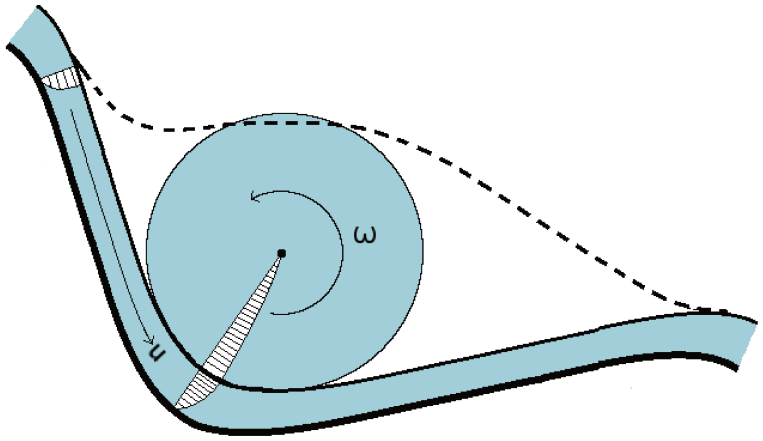

Figure 6.5.1: Schematic representation of fluid compartments with the relevant velocity vectors.

light/dark cycles frequencies, two hypothesis have been made: first, that the surface adherent flow has an homogeneous thickness along all the PBR length which is not disturbed by the rest of the fluid nor by the top part of the waves of the reactor's bottom. The second is that the swirling flow can be assumed to be steady revolving without friction at the interface liquid/air thus, after reaching a steady state, the speed can be assumed to be equal to the bottom surface flux. This second hypothesis doesn't take into account any frictional effect that arises inside the very rotating part of the swirling fluid that is equivalent to suppose a solid fluid cylinder rotating without friction and maintained at constant speed by the bottom surface-adherent flux. To simply calculate the value of the fluid velocity of this bottom flow we applied the Manning equation (Eq. 3.3.6), which was already successfully validated in section 6.2.1.2. For a cascade with a volumetric flow rate of $1.81 \cdot 10^{-3}\ m^3 \cdot s^{-1}$, a slope S_o of 0.0873, assuming a Manning factor n of 0.014, the film thickness s can be obtained directly from the solution of Eq. 3.3.6 and is equal to $3.64 \cdot 10^{-3}\ m$. The fluid velocity U is then easily obtained from the conservation equation, for a value of $0.498\ m \cdot s^{-1}$. This speed is the same speed of the fluid elements located on the boundary between the swirling flow and the bottom flow. It is therefore clearly related to the angular speed which can be calculated when the geometry of

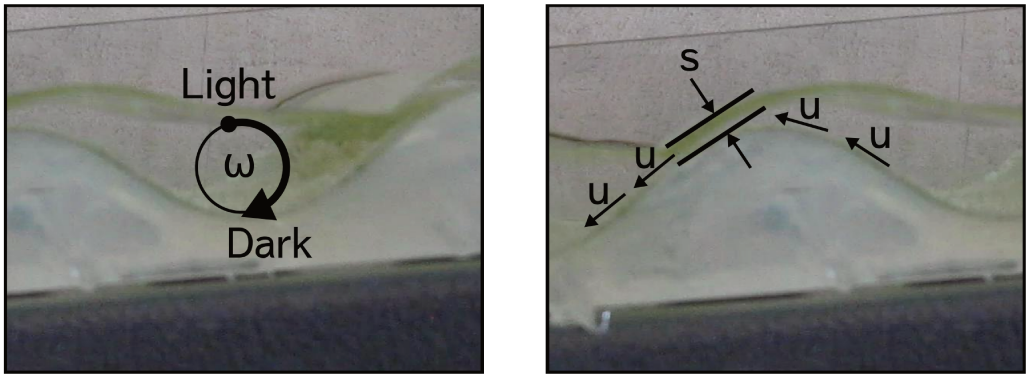

Figure 6.5.2: Screenshot from the video used for IA. Characteristic PBR dimensions are highlighted.

the system is known. In this case, the cylinder radius calculated experimentally by IA was 0.00945 m, while the calculated angular rotational speed is 52.5 $rad \cdot s^{-1}$ corresponded to a frequency of 8.4 rps (Figure 6.5.2). The flashing time t_f attained in these conditions could be easily calculated and amounted to 60 ms. At this point, bearing in mind the hypothesis of solid rotational flow for the fluid bulk, it is easy to imagine how different cells inside the swirling fluid cylinder are exposed to the same frequency of light/dark phases but to different light intensities. Plotting the results as a combination of position and received light radiation as function of time, we obtained the data depicted in Figure 6.5.3 which is clearly analogous to what already shown in Fig. 4.4.4 for a swirling flow in an ALR. The only difference is that in this case, the positions where not calculated by CFD calculations but through a simple mathematical model.

Finally, we analyzed the flow with the same consolidated high speed video technique already used extensively in this and previous works (Giannelli et al. 2009) to estimate the goodness of the simplified fluid dynamic model. Once again, the liquid flowing in the wavy cascade was inoculated by many small particles and their motion was recorded with a high speed camera. In this case, due to the shallow flow cross section and the elevated fluid velocity, the alginate particles were substituted by a fine red plastic particulate (irregular shape with an average particle size of

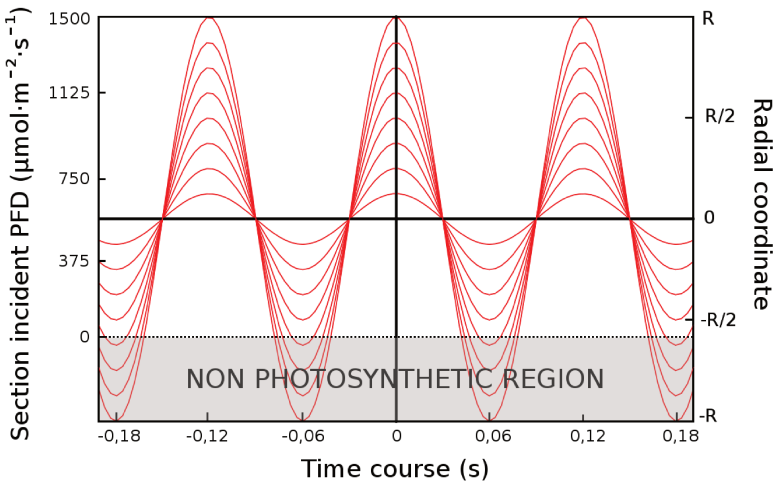

Figure 6.5.3: Light/dark cycles amplitude as a function of time and radial position from the centre of rotation using sinusoidal shaped curves. Incident light intensity is reported for an average 2009 August day at 11.00 UTC in Florence. Linear attenuation with depth is assumed linear owing to the highly concentrated cultures involved in the experiments.

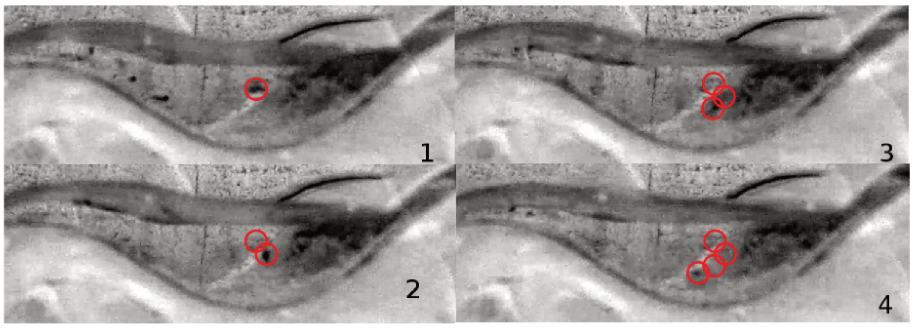

Figure 6.5.4: Temporal sequence of the colored particles tracking the fluid flow. The particles and their motion are highlighted in red.

0.5 mm). The flow pattern elucidated by this method showed a very high degree of similarity with that hypothesized in Fig. 6.5.1: roughly one half of the injected particles were washed out by the bottom flow while the remaining half was entrained in the swirling liquid bulk allowing us to measure the circulation frequency. Being the fluid velocity well above those showed by the BCR and the ALR, the maximum frame rate was barely sufficient to asses the frequency of the slowest particles. We concluded from the calculations that a flashing time $t_f \leqslant 100\ ms$ should be attained in these cultivation conditions. While the mathematical method represent a simplified approach to an "ideal" model, the image analysis was only able to measure

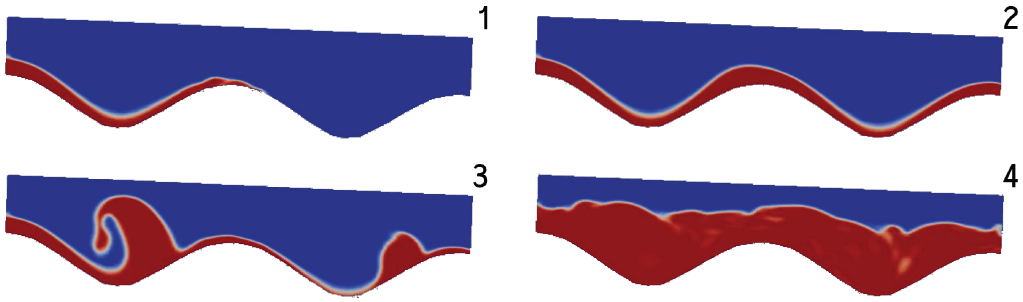

Figure 6.5.5: Initial fluid flow simulation for a cascade PBR. Consecutive 200, 400 and 600 ms time frames showing the fluid detachment (1,2 and 3) while the steady state solution is represented by the frame n° 4.

those particles fast enough to be smoothly recorded: we concluded therefore that the true t_f value experienced by the cells in the real PBR should lie between the two extremes dictated by these approaches, around 85 ms.

6.5.2 Comparison with CFD results

The numerical determination of the light/dark cycles and their relative duration in PBRs proved to be extremely accurate (see results in section 4.4 and following) despite being an extremely labor-intensive procedure. For this reason we preferred the aforementioned simplified approaches to have a grasp on the time scales involved in the flashing light in this reactor and only at a later stage the in-depth CFD analysis was carried out. Moreover, the analysis of both the indoor and outdoor wavy cascade reactors have been carried out because of the different size of the used wave board.

6.5.3 Outdoor wave reactor

According the the assumption explained in 6.5.1, the simulation result for the fluid flow inside the waves of the outdoor large scale PBR should be characterized by a fast, almost flat bottom stream and an entrained portion of fluid revolving on top of it (see Fig. 6.5.1 for the schematic representation). To verify this hypothesis we used

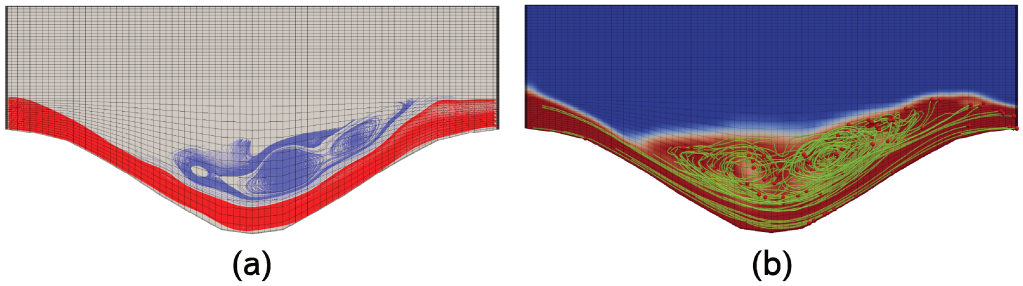

Figure 6.5.6: Fluid flow visualization inside the wave cascade PBR. Particle tracking (a) and Fluid velocity streamlines (b)

the OpenFOAM code by using as boundary conditions the very same flow rate (132 $l \cdot min^{-1}$) and slope (0.088) adopted in 6.5.1. The simulation was characterized by a first transient phase not present in the flat bottom cascade (Figure 6.5.5). The fluid sticking to the bottom of the reactor seemed to be initially flowing downwards with the same behavior of the flat bottom cascade (Fig. 6.5.5-1 and 6.5.5-2). However, the effects of the viscous strains and the centripetal acceleration impressed by the bottom profile to the fluid resulted in its detachment from the bottom, followed by the onset of the characteristic counter-revolving flow (Fig. 6.5.5-3 and 6.5.5-4). This behavior, despite not being representative for any valid measurement was interesting as it underlined how the theoretical model (Fig. 6.5.1) was well correlated with the reality. In particular, it was very interesting to notice the resemblance between Fig. 6.5.1 and Fig. 6.5.5-3, even if said resemblance was only maintained in the shown transient (10~20 ms).

To better verify the theoretical flashing time duration we further analyzed the simulation results by visualizing the fluid streamlines attained inside one trough isolated from the rest of the mesh (Figure 6.5.6-a). The picture shows, once again, an elevate degree of agreement with the theoretical approach. Moreover, it served as a base for two fundamental observations:

➙ the gravitational force acting on the fluids tend to flatten the swirling cylinder. The fluid revolution is therefore non perfectly circular. However, at least two

different fast swirling zones are highlighted: a faster, almost circular vortex and a flattened out "pancake" shaped swirling flow. These two different sections may be the responsible for the different t_f measured with the mathematical model and the high speed IA.

- The fluid fillets of the bottom flow tend to perfectly detach from the bottom plate realizing a small fluid pocket in the very bottom of the wave where the fluid velocity is almost zero. This could lead to culture and detritus sedimentation in the real PBR and should be taken into account.

The image attained by this filter was also used in the next step to assess the amount of culture volume interested by the swirling flow, to be used as the A_F for the LCE weighting process. Before those calculation were possible, the particle tracking was carried out in the isolated swirling flow as usual (see 4.4) and a representative image of the result is presented in Fig6.5.6-b. The particle trails show the unequivocal presence of a strong recirculation inside the trough and again highlight the presence of a double flashing light time scale, one generated by a wider and slower recirculation and the other generated by a fast circular swirling flow. Due to the high number of revolutions per second and the high degree of mixing registered in these fluid pockets we decided to calculate the t_f indifferently in the fast and in the slow swirling fluid portions and to average them. The determination was carried out as already explained in depth in section 4.4 and the result for 6 example particles have been reported in Table 1.10. The result of the calculations is well aligned with the provisional numbers attained by the simplified mathematical method and the high speed IA approaches where the t_f was determined to fall between 0.06 and 0.1 s. The average t_f calculated with the more accurate procedure was therefore used in the determination of the LCE increase derived by the increased flashing light effect according to Eq. 4.4.3:

Particle ID	Half time ($t_{1/2}$) (s)	Flash time (t_f) (s)
610	0.257	0.093
620	0.172	0.063
700	0.366	0.133
735	0.22	0.08
775	0.185	0.054
785	0.282	0.102
	0.241 ±0.079	0.087 ±0.028

Table 1.10: Flashing time determination for the outdoor wave cascade PBR

$$\eta_{PBR} = \frac{A_F}{A_{PBR}} \cdot \eta_F + \frac{A_C}{A_{PBR}} \cdot 1 = \frac{121075}{300277} \cdot 2.27 + \frac{179202}{300277} \cdot 1 = 1.51$$

The values for the A_F and A_C have been directly attained by a binary image file realized by using the fluid streamlines as outlined in Fig. 6.5.6-a while the LCE increase was calculated from the flashing light plot used in the *Haematococcus growth* (Fig. 4.3.2). While this last step may sound erroneous, the comparison between Fig. 4.3.2 and the plot from Kok (1953) showed how, for longer t_f (between 0.03 and 0.3) the increases in LCE were almost perfectly overlapping and for this reason Fig. 4.3.2 was preferred due to the availability of the raw data, not reported in Kok (1953).

As expected, the wave bottom cascade PBR looks really promising when the flashing light is taken into account as an astounding 51% increase in productivity have to be expected in comparison with a flat bottom cascade PBR according to the flashing light model.

6.6 *Chlorella* growth in wavy bottom cascade PBRs

Outdoor growth experiments have been carried out in Florence in the Istituto per lo Studio degli Ecosistemi (ISE) outdoor facility by comparing two cascade PBRS: a flat with the same characteristics as that described in 2.3.3.1 and the wave bottom cascade. Growth have been carried out simultaneously under direct solar light con-

Figure 6.6.1: Chlorella s. growing in the outdoor cascade photobioreactor in the ISE facility (Florence)

ditions to avoid the effect of adverse climate on the data acquisition and analysis. A picture of the Chlorella culture in the wave PBR can be seen in Fig. 6.6.1.

The cultivation was carried out by fixing two different dilution rates to assess the productivities under two different growth conditions: high and low concentrations. The adopted dilution rates were:

$$\begin{aligned} D_{high} &= \frac{\dot{V}_{sample}}{V_{reactor}} = 0.2\ d^{-1} \\ D_{low} &= 0.4\ d^{-1} \end{aligned}$$

This meaning that the cultivation was carried out in a fed-batch regime where the 20% and the 40% of the culture volumes were removed once a day and replaced with fresh media. By adopting this technique, the two cultures were forced to sit at two different average concentrations as the direct consequence of the dilution effect (Figure 6.6.2). It was evident how the two dilution rates affected the culture growth: when $D = 0.2\ d^{-1}$ the flat and the wave cascade reached an average biomass concentration of 14.4 $g \cdot l^{-1}$ and 9.7 $g \cdot l^{-1}$ respectively but with $D = 0.4\ d^{-1}$ the concentrations dropped to 4.35 and 3.9 $g \cdot l^{-1}$ respectively. The numbers reported

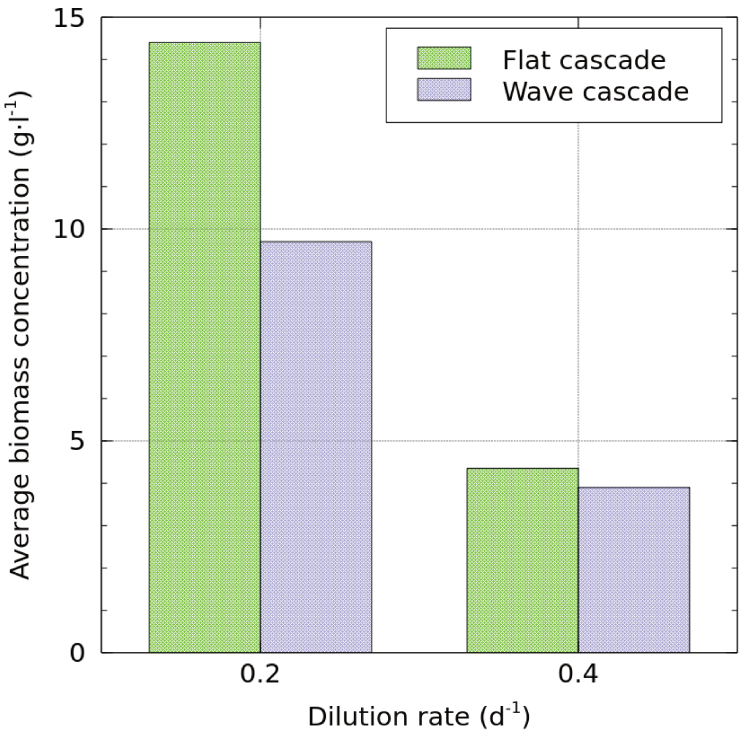

Figure 6.6.2: Average biomass concentration as a function of the dilution rate during the cultivation in the flat cascade and the wave cascade PBRs.

in Fig. 6.6.2 represent the biomass concentration, i.e. the DW of the culture which is not supposed to be affected by the dilution rate but a direct expression of the characteristic algal growth. It was quite puzzling to notice this behavior as it was indicating the the wave cascade PBR was operating at a lower growth rate. This was in complete disagreement with the LCE increase foreseen with the flashing light model and we therefore further analyzed the data by converting them to the areal productivity which is more closely correlated to the increase in LCE as it measures the direct output of the PBR that is, the direct product of the algal photosynthesis. The productivity data are shown in Figure 6.6.3. As expected, the implementation of the flashing light in the reactor resulted in a dramatic increase in the productivity of the cascade PBR: with a (low) dilution rate of 0.2 d^{-1} a +26% increase was attained while with a bigger dilution rate the difference was even bigger scoring at an amazing +81.7%. This result was very interesting as it pointed out towards two

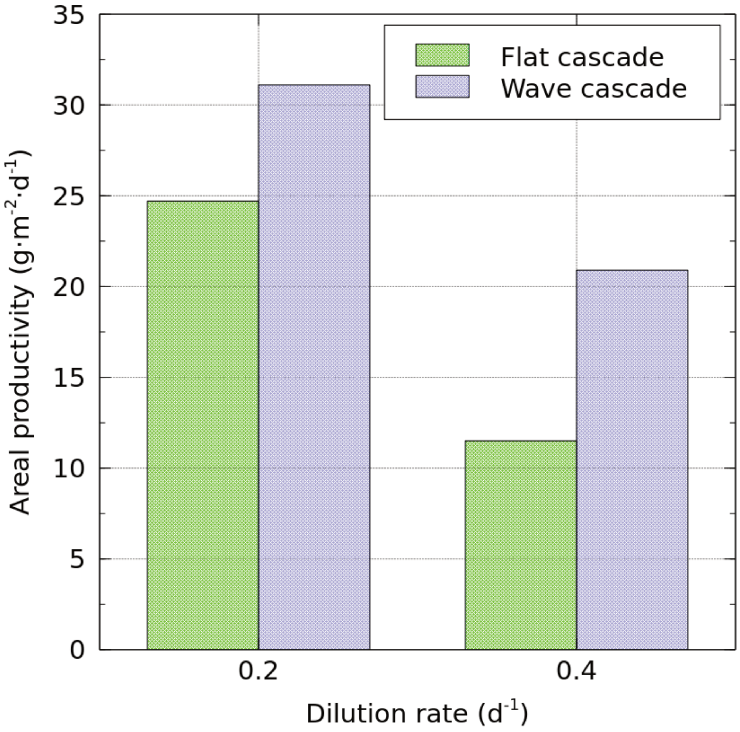

Figure 6.6.3: Areal biomass productivity as a function of the dilution rate during the cultivation in the flat cascade and the wave cascade PBRs.

evident phenomena:

1. the introduction of the flashing light in the cascade PBR apparently had an even greater impact than expected by using our model which was foreseeing a +51% increase.

2. even in low concentration conditions the wave cascade was able to get really close to the practical maximum areal productivity of 35 $g \cdot m^{-2} \cdot d^{-1}$.

6.6.1 Photobiochemical performance

The unpredictable behavior recorded in the outdoor cultures prompted for a detailed review of the designed flashing light model. The model itself proved to be reliable in small scale PBRs where low illumination intensities ensured that no photo-inhibition was acting on the photosynthetic electron transport chain. Under the light of the

new experiments this seemed to be a fundamental requirement for obtaining an acceptable representation for the reality. On the other hand, outdoor cultures were subjected to direct sunlight which, in Florence reaches up to 1900 $\mu mol \cdot m^{-2} \cdot s^{-1}$ an noon on an August day. This value is 10 to 20 times bigger than those applied in the laboratory and an high photo-inhibited culture have to be expected, at least in the 4~5 hours around noon. The flashing light model is based on the assumption that any absorbed photon can be utilized for the growth except for a small portion which is dissipated as heat (NPQ, see 1.2.2 for the detailed explanation). This assumption is obviously false for any outdoor grown culture where NPQ reaches values as high as 2.25 $r.u.$ in sufficiently diluted cultures (Masojidek et al., 2011; Vonshak and Torzillo, 2004) and must be therefore refined to be able to apply the model on outdoor PBRs.

It is common knowledge that the overall efficiency of the photosynthetic electron transport chain can be measured by using the F_v/F_m parameter (Baker, 2008); under low light conditions any trace of photo-damage is absent and the F_v/F_m reaches its highest values while under high light conditions F_v/F_m lowers proportionally to the light-induced damage in the photosynthetic apparatus. This parameter can be therefore used to assess the deviations from the ideal light-dark mode when outdoor cultures are considered. When said photo-damage is induced the LCE drops (sometimes dramatically) and the linear correspondence between LCE and productivity underlined in the laboratory scale experiments is lost. But still, a culture undergoing high frequency light dark cycles should be characterized by the very same increase in LCE when compared to a culture in continuous light in the very same conditions. The key point in this process is that under high light conditions any eventual increase in LCE can no longer be measured by means of a simple biomass productivity or growth rate but with a more physiological, low level measurement such the F_v/F_m.

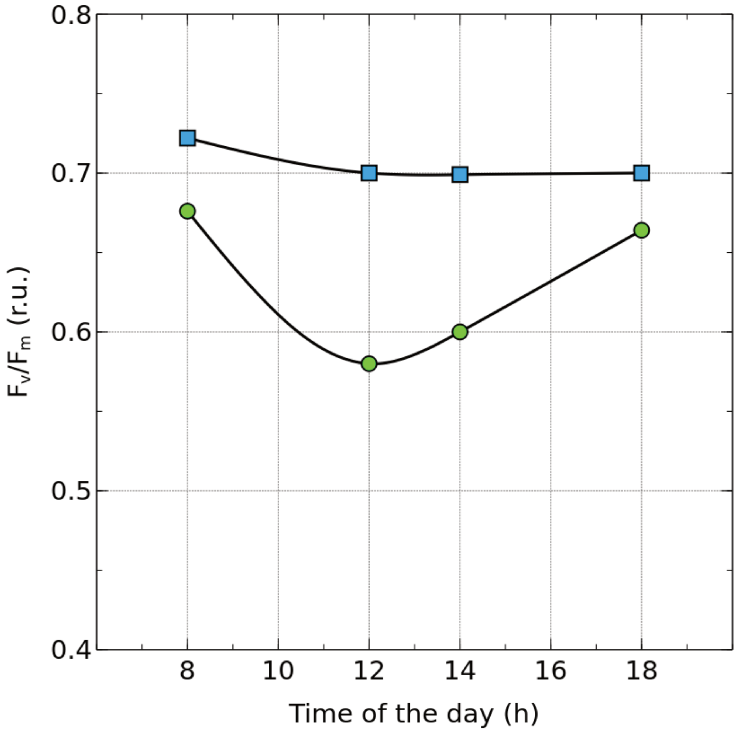

Figure 6.6.4: F_v/F_m daily variations in a flat (•) and a wave (▪) cascade PBR under direct solar light conditions.

For this reason we tried to recalculate and to quantify the evident LCE increase achieved by the wave cascade PBR and to compare it with that obtained through the CFD based flashing light method. The daily changes of the culture F_v/F_m are shown in Figure 6.6.4. The data shown in Fig. 6.6.4 were recorded under a 0.2 d^{-1} dilution rate and thus represent the highest concentration ranges adopted in the growth experiments. It can be noticed how, despite the high concentration, the flat cascade PBR already fell in a highly photo-inhibited state at 9.00/10.00 am and F_v/F_m kept lowering until midday. On the contrary, the wave cascade PBR was not apparently affected by the high light conditions and only a slight loss of F_v/F_m was recorded. This is in agreement with the observation that a sustained mixing-induced flashing light effect should contribute to an overall protection from increased illumination conditions. From the plot in Fig. 6.6.4 it appears evident why the flashing light model could not be directly applied to the outdoor conditions: the wave cascade is

only slightly affected by the increased light conditions while the flat cascade LCE is strongly hindered.

6.6.2 A proposed solution

The solution to the problem of the interferences in the model deriving by photochemical performance losses may be the introduction of an evaluation technique taking into account the $^{F_v}/_{F_m}$ variations. These variations, despite being difficult to assess without the proper instrument (Pulse Amplitude Modulated fluorometer) are strictly correlated to the photosynthetic efficiency and could represent a good point of comparison. On the other hand, microalgal cultures are notoriously able to adapt to any light intensity fluctuation by modifying their antenna size and therefore the linearity between the LCE and the productivity increases/decreases gets lost when the photosynthetic apparatus saturates. In other words, an arbitrary loss in LCE due to photo-saturation does not lead to an equivalent loss in productivity thanks to the adaptation mechanisms to the high light conditions. However, taking a look at Fig. 6.6.4, a first set of considerations may be used to extrapolate the new comparison parameter. Let's hypothesize that:

- ➙ the LCE of the wave PBR is affected by the increased light only to a minor extent (hypothesis supported by the $^{F_v}/_{F_m}$ data)

- ➙ the wave PBR productivity and its photosynthesis maintain a certain degree of linearity within the conditions reported in Fig. 6.6.4

- ➙ Both cultures are characterized by a dark-adapted $^{F_v}/_{F_m}$ value (in the morning) equal to 0.73 as shown by the data.

In these conditions, it results quite easy to calculate the photosynthetic performance losses in the flat PBR by means of the $^{F_v}/_{F_m}$ variations:

$$LCE_{flat,loss}(t) = 1 - \left(\frac{0.73 - {}^{F_v}/_{F_m}(t)}{0.73} \right)$$

This can be easily calculated as a point function and averaged on a daily basis. The averaged value attained by using the data in Fig. 6.6.4 is 0.849. This represents the new base over which the wave cascade PBR should be supposedly able to gain a 51% increase in LCE. This means that, by multiplying by 1.51 and keeping in mind the linearity between the LCE and the productivity, we should be able to calculate the biomass productivity increase in the wave PBR over that in the flat cascade:

$$LCE_{flat,loss} \cdot 1.51 = \frac{Prod_{wave}}{Prod_{flat}} = 0.849 \cdot 1.51 = 1.28$$

This number should represent the increase in productivity under the photo-inhibited conditions. The productivity increase effectively measured under these conditions have been reported in Fig. 6.6.3 and was equal to a +26% (that is 1.26).
These calculations demonstrated that, by using the same flashing light model verified in indoor conditions, coupled to a photo-inhibition model we could be able to foresee any increase/loss in productivity be means of a CFD simulation. In this case, the amount of photo-inhibition should be calculated apart by direct experimentation on the microalgae but still an enormous amount of time and money could be saved by using this approach over the old trial-and-error design techniques. Of course this approach is anything but rigorous and clearly represents the first corner-stone for the next work in this field: the adaptation of the indoor model to outdoor PBR by coupling the CFD calculations with the photochemical characteristics of the microalga and the environmental conditions.

Part 7

Conclusions

An innovative approach to the photobioreactor (PBR) design based on the use of computational fluid dynamics (CFD) was here deployed and thoroughly validated. The weakest point of the traditional PBR design techniques resides in the impossibility to properly assess the magnitude of the key parameters which, in turn, become limiting and hinder the algal growth. The most important parameters affecting algal growth are the light distribution and the mass transfer coefficient: both of them have been therefore explored in an effort to clarify the mechanisms which become determinant in the PBR design stage first and in the subsequent scale-up phase.

A special attention have been dedicated to the flashing-light effect realized by the so-called light/dark cycles and especially by those illumination fluctuations induced by the fluid motion inside the reactor. It was in fact well known how an enhanced mixing could help to sustain somewhat increased growth rates but, at the very best of our knowledge, no systematic method has ever been devised to take into account the extent to which the flashing light could get involved in the process. In an effort to answer to this question, we first uncoupled the "new geometry" against "improved productivity" binomial by adopting two highly investigated PBR geometries (air-lift and bubble column) and used the fluid dynamic differences between these to explain the productivity gains. In this scenario, the CFD simulation model was validated by using consolidated techniques to allow us to replicate exactly the fluid behavior inside the PBR and subsequently, the obtained data were used to predict the amount of culture subjected to fast flashing light. It appeared evident how the culture traveling through the ALR draft tube was subjected to high frequency swirling flows which positively influenced the algae light conversion efficiency (LCE) and ultimately, the overall productivity. By using a Lagrangian particle tracking approach we assessed the exact amount of culture interested by the flashing light and, coupling the results with the light/dark cycle frequency, we were able to model this increase. Experiments carried out with *H. pluvialis* cultures further confirmed

these results.

The innovative aspect of this CFD approach when compared with the traditional design techniques resides in the enormous decrease in the overall costs as only a PC with slightly-above-normal specs is needed to carry out the simulation and the subsequent calculation in a reasonable time span. Traditional techniques would require the construction of, at least: 1) a bench scale PBR to test the feasibility of the idea, 2) a small scale pilot (100~200 l) and finally 3) the large scale plant. Notwithstanding all the problems involved by the scale-up which could be objectively encountered with the CFD model as well, the total cost of this trial-and-error approach is almost always prohibitive. It is our opinion that this could be the main reason for the evident delay between the lab scale findings and their final application to outdoor, large scale conditions.

The gap between outdoor and laboratory conditions cannot be easily removed by simply using a numerical model, especially if this model was only validated under laboratory conditions. The most important parameters that need to be taken into account when scaling a PBR outside are the high intensity illumination and the culture temperature. As for the latter we provided in this study a detailed analysis which confirmed that any temperature-related issue is very likely the direct consequence of an increased (or impaired) LCE deriving from the photochemical effects of the temperature on the natural energy balances in the thylakoids' membranes. For this reason we tried to apply the model to an easily scalable system, the cascade PBR, after the implementation of high frequency flashing light by modifying the reactor bottom surface. Computational fluid dynamics allows for the full characterization of the PBR, especially in a case as simple as the cascade PBR where a thoroughly investigated flow is attained. By using this extended capabilities we were able to uncouple the influence of the mass transfer from the effects of the flashing light and to directly test the new model on the field. This means that two different

cascade PBRs were operated under controlled mass transfer conditions and the productivities were compared by means of the CFD approach hereby developed. The results showed how the model was able to predict a productivity increase but without the same degree of accuracy showed in the lab scale conditions. This behavior was studied by means of chlorophyll fluorescence measurements which demonstrated how the photo-inhibition phenomenon assumes a prominent role in outdoor conditions and suggesting that the model should be adjusted to further take into account this contribution.

What we finally obtained with this study was the firm conviction that the mixing-induced flashing light can be modeled by means of CFD calculations with very reasonable and provable results, at least in laboratory scale photobioreactors. On the other hand, outdoor conditions contemplate ultra-high light conditions coupled with high productivity requirements for the economical feasibility that were not taken into account for indoor PBRs. The model we obtained would therefore require a dedicated, in-depth study aimed at identifying the contribution of the photo-inhibition process and its synergy with the flashing light to provide an additional tool that is not required in bench scale PBRs but becomes of crucial importance outdoors. Being able to provide such an enhancement could result in a solid model for scaling-up reactors directly by computer simulations: the perfect toolbox for the earnest microalgal engineer. Unfortunately, a lot of work is still needed before this goal is achieved and this work is just the first step in the right direction.

Appendix I - Cultivation media

C medium

The C media is the standard inorganic substrate used by the japanese National Institute for Environmental Studies (NIES) from where the *Haematococcus* strain used in this work originated. It was therefore adopted as the standard storage media in our laboratory as well. The composition of the *C* media is shown in Table 1.11. For short term storage plates or slants used as a "live" cell stock, 1.2 $g \cdot l^{-1}$ of CH_3COONa were added as a carbon source to support mixotrophic growth.

C medium composition	
$Ca(NO_3)_2 \cdot 4\,H_2O$	150 mg
KNO_3	100 mg
β-Na_2glycerophosphate·5 H_2O	50 mg
$MgSO_4 \cdot 7\,H_2O$	40 mg
Vitamin B_{12}	0.1 μg
Biotin	0.1 μg
Thiamine HCl	1 μg
P-IV Metals	3 ml
TRIS	0.5 g
pH should be regulated to:	7.5

(a)

P-IV Metals stock solution	
$FeCl_3 \cdot 6\,H_2O$	0.196 g
$MnCl_2 \cdot 4\,H_2O$	36 mg
$ZnSO_4 \cdot 7\,H_2O$	22 mg
$CoCl_2 \cdot 6\,H_2O$	4 mg
$Na_2MoO_4 \cdot 2\,H_2O$	2.5 mg
$Na_2EDTA \cdot 2\,H_2O$	1 g

(b)

Table 1.11: C medium composition table: a) Nutrient stock solutions, b) Trace metals stock. All the amounts are based on a final media volume of 1 liter. Agarized media was realized by adding 15 g of Agar powder for each liter of media.

Kobayashi medium

Kobayashi medium has been extensively used in literature (Kobayashi et al., 1991) however we give here a detiled description of the full composition in Table XX. In this medium no trace metal is explicitly given as they are supplied through the yeast extract. This is a quite old and sub-optimal way of treating a crucial issue like trace metal nutrition (Juneau et al., 2002; Merchant et al., 2006) and should be subject of further studies to pin-point the optimal micro-nutrients concentrations for this alga. As any other organic media, Kobayashi medium is highly sensitive to contamination by exogenous bacteria or algae and should be treated accordingly.

Kobayashi medium composition	
Part I (make up to 200 ml)	
CH_3COONa	1.2 g

Part II (make up to 800 ml)	
Yeast extract	2 g
L-Asparagine	0.4 g
$MgCl_2 \cdot 6\,H_2O$	0.2 g
$FeSO_4 \cdot 7\,H_2O$	0.01 g
$CaCl_2 \cdot 2\,H_2O$	0.02 g
regulate pH to:	6.8

Table 1.12: Kobayashi medium composition table. Part I and II should be prepared and autoclaved separately to avoid precipitation. Once the autoclaved solutions are back to room temperature they can be mixed under the laminar flow hood to avoid contamination.

Molina medium

Molina standard inorganic medium (MSIM) was specifically optimized for *Haematococcus pluvialis* growth and widely used for that task (Katsuda et al., 2006; Ranjbar et al., 2008). Nitrate concentration is especially high to avoid astaxanthin accumulation in cysts during growth. Medium composition is given in Table 1.13.

MSIM medium composition	
$NaNO_3$	1.02 g
$Ca(NO_3)_2 \cdot 4\,H_2O$	40.1 mg
$CaCl_2 \cdot 2\,H_2O$	10 mg
K_2HPO_4	50.4 mg
$MgSO_4 \cdot 7\,H_2O$	49.3 mg
EDTAFeNa	4.74 mg
$EDTANa_2 \cdot 2\,H_2O$	4.5 mg
H_3BO_3	9.89 mg
$MnCl_2 \cdot 4\,H_2O$	2.8 mg
$ZnCl_2$	41 μg
$CoCl_2 \cdot 6\,H_2O$	22.1 μg
$(NH_4)_6Mo_7O_{24} \cdot 4\,H_2O$	19.2 μg
$CuSO_4 \cdot 5\,H_2O$	40 μg
Biotin	50 μg
Vitamin B_1	250 μg
Vitamin B_{12}	12.5 μg
regulate pH to:	6.8

(a) MSIM

MSIM-N medium composition	
NaCl	0.351 g
$CaCl_2 \cdot 2\,H_2O$	35 mg
K_2HPO_4	50.4 mg
$MgSO_4 \cdot 7\,H_2O$	49.3 mg
EDTAFeNa	4.74 mg
$EDTANa_2 \cdot 2\,H_2O$	4.5 mg
H_3BO_3	9.89 mg
$MnCl_2 \cdot 4\,H_2O$	2.8 mg
$ZnCl_2$	41 μg
$CoCl_2 \cdot 6\,H_2O$	22.1 μg
$(NH_4)_6Mo_7O_{24} \cdot 4\,H_2O$	19.2 μg
$CuSO_4 \cdot 5\,H_2O$	40 μg
Biotin	50 μg
Vitamin B_1	250 μg
Vitamin B_{12}	12.5 μg
regulate pH to:	6.8

(b) MSIM-N

Table 1.13: MSIM medium composition table. Nitrate salts have been substituted with their chloride analogue during astaxanthin accumulation esxperiments (MSIM-N); both concentrations are reported in the table while the other salts have the same concentration in both MSIM and MSIM-N. Composition is given for 1 l of culturing medium.

Trebon medium

We decided to name the medium used in the cascade PBR "Trebon medium" as a tribute to the city of *Třeboň* in the Czech Republic where the cascade PBR was invented by Setlik and coworkers back in the year 1970. This medium has been used in many studies and represents the most optimized medium for the growth of *Chlorella* strains in outdoor large-scale PBRs (Doucha and Livansky, 2006, 2009; Masojidek et al., 2011; Setlík et al., 1970; Šetlík et al., 1990). The composition is reported with minor changes in Table XX.

Trebon medium - Nutrients	
Nutrient Stock I (10 $ml \cdot l^{-1}$)	
Urea	30 g
NH_4SO_4	66.1 g
$NaNO_3$	42.5 g
Dilute to 1 l	
Nutrient Stock II (10 $ml \cdot l^{-1}$)	
$MgSO_4 \cdot 7\,H_2O$	50 g
$FeSO_4 \cdot 7\,H_2O$	1.4 g
Dilute to 1 l	
Phosphate Buffer (10 $ml \cdot l^{-1}$)	
KH_2PO_4	12.5 g
K_2HPO_4	27.5 g
Dilute to 1 l	

(a)

Trebon Medium - Metals	
Trace Metals I (0.5 $ml \cdot l^{-1}$)	
H_3BO_3	19.786 g
$MnCl_2 \cdot 4\,H_2O$	5.58 g
Trace Metals II	12 ml
Dilute to 1 l	
Trace Metals II	
$ZnCl_2$	0.818 g
$CoCl_2 \cdot 6\,H_2O$	0.441 g
$(NH_4)_6Mo_7O_{24} \cdot 4\,H_2O$	0.383 g
$CuSO_4 \cdot 5\,H_2O$	0.799 g
Dilute to 120 ml	

(b)

Table 1.14: Trebon medium composition table: a) Nutrient stock solutions, b) Trace Metals solutions. Stock solutions should be prepared dissolving the salts in the proper amount of water. The proper amount for each stock solution obtained this way must be used to prepare 1 liter of Trebon media.

Appendix II - OpenFOAM: mesh generation and case structure

In this appendix, all the general instructions needed to set up a functioning OpenFOAM (OF) case are given. The work flow is divided in different sub-sequential steps which need to be carried out one after the other to succeed. The order is not really that strict, however, having a mental image of the needed steps and to execute them properly will make the things way easier. Please keep in mind that this represents the most complicated task in the use of OF based simulations.

Mesh creation

All commercial softwares come with a proprietary 3D editor which perfectly interacts with the simulation software to easily create a functioning mesh, define its boundaries and the relative boundary conditions. This is not the case in OF. Except for the use of some external application[15], in OF meshes have to be created by using properly coded text files. Lets explore in depth the mesh creation by starting looking at an example of the mesh dictionary file (Code 1.1). The syntax written in the Code 1.1 must be written in the proper file which is located in the *./constant/polyMesh* directory in the OF case folder and must be named exactly *blockMeshDict* to be properly recognized by the system. Let's explore the dictionary file section by section.

- convertToMeters

  This parameter allows for the immediate scale-up/scale-down of the mesh just by simply changing the measuring units used in the dictionary file. If the file

[15]The Salome platform (www.salome-platform.org/) can be used to create 3D meshes suitable for use in OF. The creation/conversion task is well documented on the Internet and therefore no explanation will be given here.

```
/*--------------------------------*- C++ -*----------------------------------*\
| =========                 |                                                 |
| \\      / Field           | OpenFOAM: The Open Source CFD Toolbox           |
|  \\    /  Operation       | Version: 1.6                                    |
|   \\  /   And             | Web: http://www.OpenFOAM.org                    |
|    \\/    Manipulation    |                                                 |
\*---------------------------------------------------------------------------*/
FoamFile
{
version 2.0;
format ascii;
class dictionary;
object blockMeshDict;
}
// * * * * * * * * * * * * * * * * * * * * * * * * * * * * * * * * * * * * * * * * * * * //

convertToMeters 1;

vertices          // All the vertices constituting the mesh must be written here.
(                 //
(x0 y0 z0) //0    // The points are defined by using the absolute coordinates for
(x1 y1 z1) //1    // each point. The first point will be the number 0, the second
.....             // will be point 1, etc.
);


blocks
(
hex (0 1 2 3 4 5 6 7) (a b c) simpleGrading (1 1 1)       // A
hex (8 9 10 11 12 13 14 15) (a b c) simpleGrading (1 1 1) // B
.....             // Each block is a cube surrounded by 8 vertexes. For the
);                // exact instructions see the main text.

edges
(                 // To be left empty
);

patches           // Patches represent the reactor faces. They are made up
(                 // by 4 points
wall walls
(
(1 2 3 4) // Wall I  // Wall patches are self-explaining
.....
)

empty fake        // Empty patches represent symmetry and/or cut planes
(
(1 2 3 4) // Cut face I
.....
)

patch Inlet       // Patch patches are just ficticious walls used to define
(                 // inlet and outlets or even inner surfaces.
(1 2 3 4) // Inlet face I
.....
)

patch Outlet
(
(1 2 3 4) // Outlet face I
.....
)
);

mergePatchPairs
(                  // To be left empty
);
// ************************************************************************* //
```

Code 1.1: Example of an OpenFOAM mesh dictionary file. Lines starting with "//" are comments. They are not needed in the real files.

have been compiled by using SI units, the conversion to Anglo-Saxon units can be done by simply changing this parameter. Of course this is true for the conversion between every measuring units system. In this work, meters have been used so this field was left untouched.

➙ vertices

The vertices sub-dictionary is the first and most important section of the file. Here the absolute position of each point constituting the mesh is defined by using the three axial coordinates in the form of a space separated array:

$$(x_0\ y_0\ z_0)$$

This must be repeated for each point constituting the mesh. This part of the mesh creation represents the first topological definition of the points which receive a "number" to be able to later identify the easily. To further facilitate the subsequent operations, care should be used in adding the proper number as a comment after each point (see Code 1.1 for an example).

➙ blocks

This section is where the mesh starts to get a proper shape. Here are in fact defined all the inner volumes constituting the mesh itself. This means that eight adjacent points are needed to define each "cube". The proper definition is:

$$hex\ (Pt_1\ Pt_2\ Pt_3\ Pt_4\ Pt_5\ Pt_6\ Pt_7\ Pt_8)(a\ b\ c)simpleGrading(111)$$

Each point (Pt_i) must be represented with the proper number as assigned in the *vertices* section. Follow the common *right-hand rule* to assign the proper point sequence. The a, b and c parameters represents the number of subsec-

tions in which each of the corners in the three directions will be subdivided. For example (5 1 3) means that the cube should be constituted by 5 cell along the x axis, 1 along the y axis and 3 along the z axis. By using each segment length and the desired mesh density, the average cell size is defined by these three parameters. Using the same three numbers and considering a box with dimensions equal to 5x1x3 mm, the obtained cells will be a bunch of 1 mm^3 cubes.

The last very important point regarding this cell number definition is represented by the mesh thickness in the case of a purely bi-dimensional flow. In this case, the mesh cell number along the suppressed axis must be equal to 1. Using again the same example, we may imagine that the block represented is characterized by a x-z bi-dimensional section.

It is very important to keep in mind that every adjacent block must not be constituted by a different number of cells along the contact side, that is, each corner must contain the same number of cells of all the neighboring blocks. To have a multi-graded mesh, the last parameter triplet (1 1 1) (the cell expansion ratios) should be changed to accommodate for a progressive reduction on the grid size[16]. However, even in this case, every adjacent block must be multi-graded equally.

➞ patches

The patches are those sections of the reactor which represent the interfaces between the inner mesh domain and the outside. All the reactor walls must therefore be defined here as all the inner baffles/draft-tubes, etc. Walls are well identified by 4 points and the point order can be once again determined by using the *right hand rule*. In the OF mesh creation, the wall surface normal

[16]See the offcial BlockMesh tutorial for more information (http://www.openfoam.org/docs/user/blockMesh.php)

must be directed towards the outside of the mesh.

Every domain where in-bound or out-bound mass flows have to be taken into account must have a valid *inlet* or *outlet* patch defined. To be valid they shell not be defined by any word other then "patch". Further differentiations are applied through the boundary conditions definition but at this stage, the inlets and the outlets are practically the same thing: an open section of the mesh closed by a *patch*. No matter whether the accompanying flow will be directed inwards or outwards, the surface normal will need to be directed outside even in the inlet.

Once the mesh is properly defined and the dictionary is saved, the binary mesh must be calculated by running the command $blockMesh$ from inside the case folder. This will take care of compiling the mesh and to report any error encountered during the process. If the command is successfully executed, the mesh will be automatically saved locally. This means that, once a functioning mesh dictionary is created, this step must only be run once provided that no modifications have been done to the mesh file. To be completely sure the mesh represents the one we were designing, one could easily visualize the resulting domain by using Paraview; simply launch $paraFoam$ from the command line inside the case folder root.

Boundary conditions

In this section an explanation is given on how to set up the proper boundary conditions and not the actual values we applied to the simulations used in this study which are already reported in the main text.

To be able to properly define the boundary conditions required in a functioning case, OpenFOAM text file and directory structure must be explained. A simple schematic visualization of the most relevant files in the simulation folder is presented

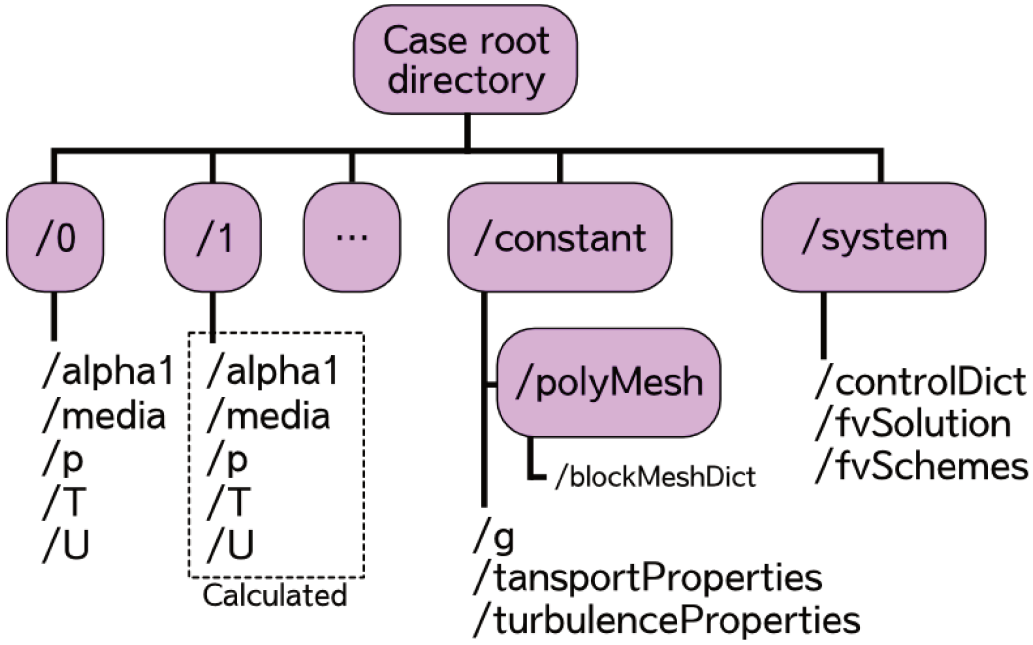

Figure 7.0.5: OpenFOAM case folder representation.

in Figure 7.0.5.

- The "0" folder

  This is the folder where the proper boundary conditions are stored as text files with a standard coded format. More accurate information will be given hereafter. All the folders with a numeric name are generated by the simulation itself and are characterized by calculated (not assigned) fields. Any folder at any given time t can be moved elsewhere (i.e. in a new case folder) to be used as an initialization step.

- The "constant" folder

  This folder contains all the files that describe peculiar aspects of the simulation. For example, the mesh file will be stored in the */polyMesh* sub-folder in this directory.

- The "system" folder

  As the name clearly suggests, this is the directory containing all the files

inherent to the simulation environment definition. The discretization schemes and other relevant simulation parameters are set by the text files in this folder.

The folder structure represented in Fig. 7.0.5 is quite simple and therefore, we will not go in bigger detail[17].

Definition files

The boundary condition definitions files in the /0 folder are all structured in subsequent sections and all in a similar way (Code 1.2): the definition of the file, the dimensions of the scalar/field, the initial internal field value and the boundary field section. While the first sections can be easily obtained by copying one of the example files in the OF tutorials, the *boundaryField* section is the one that needs to be modified case-by-case, i.e. the boundary conditions. In the example in Code 1.2 refers to the boundaries defined in the BCR/ALR system in Sec. 4 already listed in Code 1.1.

Each variable needs different parameters to be set so we will provide some detailed examples hereafter. We however urge the reader to critically adapt them to his typical case and we suggest again to make use of the very good documentation provided by the official OF on-line manual.

The "dimensions" section This is the place where the user defines the dimensions (in SI units) of the described variable. The section itself is characterized by an array of 7 components arranged as follows:

[17] See the official documentation available on-line http://www.openfoam.org/docs/user/case-file-structure.php

```
FoamFile
{
  version     2.0;
  format      ascii;
  class       volScalarField;
  location    "0";
  object      alpha1;
}
// * * * * * * * * * * * * * * * * * * * * * * * * * * * * * * * * * * * * * * * * * * * * //

dimensions      [0 0 0 0 0 0 0];

internalField   uniform 0;

boundaryField
{
    Walls
    {
    }
    Inlet
    {
    }
    Outlet
    {
    }
    fake
    {
    }
}
// ************************************************************************* //
```

Code 1.2: Example of an alpha1 definition file

$$\begin{bmatrix} Mass \\ Length \\ Time \\ Temperature \\ Quantity \\ Current \\ Light\ intensity \end{bmatrix} \longmapsto \begin{bmatrix} kg & m & s & K & mol & A & cd \end{bmatrix}$$

where the array on the left represents each physical quantity and that on the right its relative SI unit. The definition of the measuring unit with this system is carried out by populating the array with the exponent of each single fundamental dimension in the unit itself. Some examples are:

$$Velocity\ (m \cdot s^{-1}) \longmapsto \begin{bmatrix} 0 & 1 & -1 & 0 & 0 & 0 & 0 \end{bmatrix}$$
$$Pressure\ (N \cdot m^{-2}) \longmapsto \begin{bmatrix} 1 & -1 & -2 & 0 & 0 & 0 & 0 \end{bmatrix}$$
$$\mathfrak{D}\ (m^2 \cdot s^{-1}) \longmapsto \begin{bmatrix} 0 & 2 & -1 & 0 & 0 & 0 & 0 \end{bmatrix}$$

As the calculations automatically execute a check for unit homogeneity, the system units defined in the /0 folder must by dimensionally coherent. If the definitions mismatch, the simulation will fail complaining about this issue. This is especially important when new physical quantities are defined as for the case of the tracing solution in the modified interFoam (see Appendix III).

The "internalField" section The $internalField$ section describes the initial value of the scalar/field in the whole mesh domain. This section can be set to $uniform\ \Psi_i$; in the case of a constant and uniform initial value equal to Ψ_i. However, it is not always possible to set an uniform value for a given property if the space distribution is non-homogeneous. A clear example of this may be the boundary conditions associated to a mesh representing a liquid/gas filled dual phase domain as in the case of the ALR and BCR. In this scenario, OF comes with a tool called $setFields$ which is able to assign the proper variable value basing on a dictionary file. The dictionary file is located in the $/system/setFieldsDict$ and has the structure reported by Code 1.3. In this example, the alpha1 scalar field is defined in the way that: 1) the whole domain is first filled with air (alpha1=0) and 2) all the cells enclosed by the cube with extremes $P_1 = (x_1\ y_1\ z_1)$ and $P_2 = (x_2\ y_2\ z_2)$ are filled with liquid (alpha1=1). The mesh is then properly initialized by running $setFields$ in the case root directory and the results can be verified as usual by using Paraview.

The "boundaryField" section The last section in the dictionary file, it is usually subdivided in as many section as those defined in the mesh, which means that in our case, definitions for the inlet/outlet, walls and symmetry planes should be given (Code 1.1). A thorough definition of each variable for the simulation and its initialization syntax is given in Figure 7.0.6. Please notice how $alpha1$ and T most likely require a further initialization by the means of the $setFields$ command to

Variable	Walls	Inlet	Outlet	Fake (symmetry faces)
U fluid velocity	type fixedValue; value uniform (0 0 0);	type fixedValue; value uniform (0 0 U_z);	type pressureInletOutletVelocity; value uniform (0 0 0);	type empty;
p fluid pressure	type buoyantPressure; value uniform 0;	type buoyantPressure; value uniform 0;	type totalPressure; p0 uniform 0; U U; phi phi; rho rho; psi none; gamma 1; value uniform 0;	type empty;
alpha1* fluid partition coefficient	type constantAlpha ContactAngle; theta0 0; limit none; value uniform 0;	type fixedValue; value uniform 0;	type inletOutlet; inletValue uniform 0; value uniform 0;	type empty;
T** numerical tracer concentration or CO_2 concentration	type zeroGradient;	type fixedValue; value uniform $C_{tracer1}$;	type zeroGradient;	type empty;

* these represent the suggested inital conditions even though alpha1 mus be initizlized again with the setFields command.
** the tracer can be constantly injected through the inlet (as shown here) or initialized by the setField command onl for a limited fluidr region.

Figure 7.0.6: Boundary conditions definition example for a BCR/ALR reactor.

```
/*--------------------------------*- C++ -*----------------------------------*\
| =========                 |                                                 |
| \\      /  F ield         | OpenFOAM: The Open Source CFD Toolbox           |
|  \\    /   O peration     | Version:  1.6                                   |
|   \\  /    A nd           | Web:      www.OpenFOAM.org                      |
|    \\/     M anipulation  |                                                 |
\*---------------------------------------------------------------------------*/
FoamFile
{
version     2.0;
format      ascii;
class       dictionary;
location    "system";
object      setFieldsDict;
}
// * * * * * * * * * * * * * * * * * * * * * * * * * * * * * * * * * * * * * //
defaultFieldValues
(
     volScalarFieldValue alpha1 0 );

regions (
     boxToCell
    {          box (x1 y1 z1) (x2 y2 z2);
        fieldValues
         (
            volScalarFieldValue alpha1 1
         );
    }
);
// ************************************************************************* //
```

Code 1.3: SetFieldsDict dictionary file structure

work properly.

The constants folder

In this sub-folder, in addiction to the mesh files, the property dictionary files are stored. Said files are g, *transportProperties* and *turbulenceProperties*. While the g file is pretty self-explanatory, the most prominent of the three is represented by the *transportProperties* file where all the fluid properties are defined. The typical dictionary file for a modified interFoam simulation is shown in Code 1.4 (the header have been removed for brevity). In this file the density (ρ, rho) and the dynamic viscosity (ν, nu) of both the liquid and the gas phase can be described together with other relative coefficients. For a water/air system the proper values at $25°C$ are stored in the OF tutorial folders. On the bottom of the file, various system-wide properties are defined using the same symbol adopted in the equations. These

```
phase1
{
    transportModel  Newtonian;
    nu              nu [ 0 2 -1 0 0 0 0 ] 1e-06;
    rho             rho [ 1 -3 0 0 0 0 0 ] 1000;
    CrossPowerLawCoeffs
    {
        nu0             nu0 [ 0 2 -1 0 0 0 0 ] 1e-06;
        nuInf           nuInf [ 0 2 -1 0 0 0 0 ] 1e-06;
        m               m [ 0 0 1 0 0 0 0 ] 1;
        n               n [ 0 0 0 0 0 0 0 ] 0;
    }
    BirdCarreauCoeffs
    {
        nu0             nu0 [ 0 2 -1 0 0 0 0 ] 0.0142515;
        nuInf           nuInf [ 0 2 -1 0 0 0 0 ] 1e-06;
        k               k [ 0 0 1 0 0 0 0 ] 99.6;
        n               n [ 0 0 0 0 0 0 0 ] 0.1003;
    }
}
phase2
{
    transportModel  Newtonian;
    nu              nu [ 0 2 -1 0 0 0 0 ] 1.48e-05;
    rho             rho [ 1 -3 0 0 0 0 0 ] 1;
    CrossPowerLawCoeffs
    {
        nu0             nu0 [ 0 2 -1 0 0 0 0 ] 1e-06;
        nuInf           nuInf [ 0 2 -1 0 0 0 0 ] 1e-06;
        m               m [ 0 0 1 0 0 0 0 ] 1;
        n               n [ 0 0 0 0 0 0 0 ] 0;
    }
    BirdCarreauCoeffs
    {
        nu0             nu0 [ 0 2 -1 0 0 0 0 ] 0.0142515;
        nuInf           nuInf [ 0 2 -1 0 0 0 0 ] 1e-06;
        k               k [ 0 0 1 0 0 0 0 ] 99.6;
        n               n [ 0 0 0 0 0 0 0 ] 0.1003;
    }
}
sigma           sigma [ 1 0 -2 0 0 0 0 ] 0.07;
DT              DT [0 2 -1 0 0 0 0] 0.000000000181;
DC              DC [0 2 -1 1 0 0 0] 0.0000007;
Kappa                           Kappa [0 0 -1 1 0 0 0] 0.001052;
Acca                            Acca [0 0 0 0 0 0 0] 0.8317;
```

Code 1.4: Example of a *transportProperties* file

physical constants are:

- ➞ sigma: the surface tension of the liquid/gas system
- ➞ DT: the diffusivity of the solute in the liquid phase
- ➞ DC: A correction coefficient only used in the non-volatile case (namely, the product between DT and the interface equilibrium concentration as per Eq. 3.2.7).
- ➞ Kappa: Biological CO_2 uptake for a *Chlorella sorokiniana* culture (see 3.2.3). Can be safely set to zero in a non-reactive system.
- ➞ Acca: Henry's constant used to assess the phase change jump condition.

All the measuring units are set to SI standards.

The system files

The last file definitions we need to cover are those storing the global variables and the simulation inner setting and parameters. These files are kept in the */system* sub-folder of the OF case and the most important (must-edit) file is represented by the *controlDict* file (see Code 1.5. Header omitted.). This code should provide a fully working options set for any standard interFoam simulation and may not require editing. However, the key parameters are commented in Code 1.5 for simplicity.

```
application     interFoam;
startFrom       latestTime;   ** Resumable simulation
startTime       0;
stopAt          endTime;
endTime         20;           ** Desired simulation length (seconds)
deltaT          0.001;
writeControl    adjustableRunTime;
writeInterval   0.01;         ** Auto wirites data every 0.01 seconds
purgeWrite      0;
writeFormat     ascii;
writePrecision  6;
writeCompression uncompressed;
timeFormat      general;
timePrecision   6;
runTimeModifiable yes;
adjustTimeStep  yes;          ** Automatic time step length using the
maxCo           0.5;             maxCo value. Greately imporves stability.
maxDeltaT       1;
```

Code 1.5: Working *controlDict* file for a runtime-resumable interFoam simulation

Appendix III - Modify the interFoam solver

The instruction in this appendix are given as a reference in the case the need for a new equation should arise in any simulation using the interFoam solver. As already thoroughly explained in section 3.2 this was the case encountered in this work and therefore we decided to document the needed steps for the ease of reproducibility. Just in case.

Testing for the compilation capabilities of the OF install.

The steps involving the testing of the "standard" OpenFOAM supplied file are followed by substituting icoFoam with interFoam.

```
cd $FOAM_SOLVERS
cd multiphase
```

then proceed to creating a dedicated solver folder in the personal folder:

```
mkdir -p $WM_PROJECT_USER_DIR/applications/solvers
cp -r interFoam $WM_PROJECT_USER_DIR/applications/solvers/my_interFoam
cd $WM_PROJECT_USER_DIR/applications/solvers/my_interFoam
```

The next step consists in adapting the files to the new configuration by modifying the files as follows:

```
mv interFoam.C my_interFoam.C rm interFoam.dep
```

Using a text editor, make the file my_interFoam.C read like this:

```
my_interFoam.C

EXE = $(FOAM_USER_APPBIN)/my_interFoam
```

Modifying the parameter *$(FOAM_USER_APPBIN)*, the executable will be saved in the personal folder. The standard path can be left unaltered to have the file installed together with the others in the main folder.

These are the changes needed to recompile the file with the new name and have it installed; however, at least in the OpenFOAM 1.6.0 distribution together with Gcc 4.3.3 there are three additional steps that need to be done to avoid ending up with an incomplete compilation.

Options file correction

The options file located in the Make subdirectory needs to be edited to look like this:

```
EXE_INC = \
    -I$(LIB_SRC)/transportModels \
    -I$(LIB_SRC)/transportModels/incompressible/lnInclude \
    -I$(LIB_SRC)/transportModels/interfaceProperties/lnInclude \
    -I$(LIB_SRC)/turbulenceModels/incompressible/turbulenceModel \
    -I$(LIB_SRC)/finiteVolume/lnInclude

EXE_LIBS = \
    -linterfaceProperties \
    -lincompressibleTransportModels \
    -lincompressibleRASModels \
    -lincompressibleLESModels \
    -lfiniteVolume \
    -lincompressibleTurbulenceModel
```

This is needed only if the last library (lincompressibleTurbulenceModel) is not included in the list (probably a bug of the OpenFOAM pre-compiled code). If that is not present, the compiler will complain about that and end up with an error.

Automatically created options file TAB problem

Before launching the compilation using *wmake*, a clean is suggested. After launching *wclean* the options file stored in the CPU-specific folder will be removed and rewritten. In this step it seems that the TAB structure gets lost (probably due to a bug of the Gcc64 version). Copy the contents of the options file (the one in the previous step) and paste them in the broken one and the bug will be fixed.

Include MPI in the compiler string

The software won't compile if MPI (parallelization software) is installed but no specification to compile against its libraries is passed to the compiler. To avoid this problem modify the file "*/wmake/rules/linux64Gcc/general*" to include in the PROJECT_LIBS variable the line:

```
PROJECT_LIBS = -l$(WM_PROJECT) -liberty -ldl $(FOAM_MPI_LIBBIN)/libPstream.so
```

At this point, after complaining with these points and compiling the modified file should held a functioning executable. For this reason running my_interFoam should give the standard interFoam output (if executed in a valid case folder) and we can proceed to add the equation in the solver itself.

Include the equation in the interFoam solver

The equation must be now included in the *my_interFoam* solver source file. Following the steps in the official wiki[18], the variable T (standing for Tracer) is added: to ease things up with the dimensional analysis, the concentration have been represented as a temperature (K) even if the governing equation was properly expressed with that of the concentration. In the end, the dimensional analysis in OF just

[18] http://openfoamwiki.net/index.php/How_to_add_temperature_to_icoFoam

represents a sort of semantic check between the variables and the equations and if the two match, the result will be consistent.

The first step required is to create the T field in the *createFields.H* file in the new solver folder. As interFoam does not have a function for reading constant physical properties for single phases, it must be added in the head of the file:

```
IOdictionary transportProperties
     (
         IOobject
         (
             "transportProperties",
             runTime.constant(),
             mesh,
             IOobject::MUST_READ,
             IOobject::NO_WRITE
         )
     );

// Then add the T field where those for P
// and U are created by pasting this code:

    Info<< "Reading␣field␣T\n" <<endl;
     volScalarField T
     (
       IOobject
         (
              "T",
              runTime.timeName(),
              mesh,
              IOobject::MUST_READ,
              IOobject::AUTO_WRITE
         ),
       mesh
    );

    Info<< "Reading␣field␣media\n" << endl;
    volScalarField media
    (
        IOobject
```

```
        (
            "media",
            runTime.timeName(),
            mesh,
            IOobject::MUST_READ,
            IOobject::AUTO_WRITE
        ),
        mesh
    );

// Don't touch anything beyond this point until you find:

        ),
         rho1*phi
     );

// and add beyond this line:

    dimensionedScalar DT
     (
         transportProperties.lookup("DT")
     );
    dimensionedScalar DC
     (
         transportProperties.lookup("DC")
     );
    dimensionedScalar Kappa
     (
         transportProperties.lookup("Kappa")
     );
    dimensionedScalar Acca
     (
         transportProperties.lookup("Acca")
     );
```

The scalar DT, DC, Kappa and Acca are those explained in Appendix II. By looking up for them with the definition in this file, their definition in the *transportProperties* is therefore required. The scalar field *media* is just an accessory scalar used during

the calculation of the jump condition.

At this point the main source code in the *my_interFoam.C* file should be modified by adding the equation to be solved for. Open the file, look for the "*PISO loop*" and after that but before the time write, insert:

```
        // --- PISO loop
        for (int corr=0; corr<nCorr; corr++)
        {
            #include "pEqn.H"
        }


       #include "continuityErrs.H"


       turbulence->correct();
// Add all this (that represents the new equation):

       media = DT * ( (1 - Acca) / (Acca * alpha1 + (1 - alpha1)));


       fvScalarMatrix TEqn
        (
            fvm::ddt(T)
            + fvm::div(phi, T)
            + fvm::laplacian(DT, T)
            - Kappa * (1,1,0)
            - media * fvm::laplacian(alpha1, T)
        );


       TEqn.solve();

// ---------------------------


         runTime.write();
```

Here we can see how the *media* scalar is used in the calculation of the jump condition according to the equation

$$media = \mathfrak{D} \cdot \left(\frac{1 - acca}{acca \cdot alpha1 + (1 - alpha1)} \right)$$

which is just the ending section of Eq. 3.2.8 rewritten with the proper C++ variables. The *media* value is then used in the TEqn section to calculate the liquid/gas concentration jump.

When all these steps are terminated, the software can be compiled with wmake without errors. The executable file can be now accessed as usual by typing *my_interFoam* on the command line inside a valid OpenFOAM case folder. Of course, in this Appendix the name *my_interFoam* just for convenience while the name *alpha_tracer_interFoam_phase* have been used.

The last step before the execution of the simulation software is to modify the solution schemes for the newly added scalar field and equation. Open the $/system/fvSchemes$ file and add the preferred scheme to the div and laplacian operators for the equation. Do not adding anything will make the terms be solved by the default schemes:

```
divSchemes
 {
     div(rho*phi,U)  Gauss limitedLinearV 1;
     div(phi,alpha)  Gauss vanLeer;
     div(phirb,alpha) Gauss interfaceCompression;
     div(phi,T)      Gauss upwind;
 }
laplacianSchemes
 {
     default         Gauss linear corrected;
     laplacian(DT,T) Gauss linear corrected;
 }
```

Then open the $/system/fvSolution$ file and append the solver specifications for the T equation:

```
    T
    {
        solver            BICCG;
        preconditioner    DILU;
        tolerance         1e-7;
```

```
        relTol          0;
    };
```

This concludes the modifications needed. Defining a proper T file in the 0 folder (see Appendix II) and running the simulation will show the CO_2 diffusion in the liquid and gas domain.

Bibliography

Acién Fernandez, F. G., Garcìa Camacho, F., Sànchez Pérez, J. A., Fernàndez Sevilla, J. M., and Molina Grima, E. (1997). A model for light distribution and average solar irradiance inside outdoor tubular photobioreactors for the microalgal mass culture. *Biotechnology and Bioengineering*, 55(5):701–714.

Armstrong, F. A. J. (1963). Determination of nitrate in water by ultraviolet spectrophotometry. *Analytical Chemistry*, 35:1292–1294.

Baker, N. (2008). Chlorphyll fluorescence: a probe of photosynthesis in vivo. *Annual Review of Plant Biology*, 59:89–113.

Ball, S. G. (2002). The intricate pathway of starch biosynthesis and degradation in the monocellular alga *Chlamydomonas reinhardtii*. *Australian Journal of Chemistry*, 55:49–59.

Barbosa, M. J., Hadiyanto, and Wijffels, R. H. (2004). Overcoming shear stress of microalgae cultures in sparged photobioreactors. *Biotechnology and Bioengineering*, 85(1):78–85.

Barry, J. (2005). Estimating rates of spreading and evaporation of volatile liquids. *Chemical Engineering Professionals*, (January):32–39.

Becker, E. (1994). *Microalgae biotechnology and microbiology*. Cambridge University Press.

Belay, A. (2008). *Spirulina (Arthrospira): production and quality assurance*, chapter in: *Spirulina* in human nutrition and health, Gershwin M.E. and Belay A. editors. CRC Press, first edition.

Bitog, J. P., Lee, I. B., Lee, C. G., Kim, K. S., Hwang, H. S., Hong, S. W., Seo, I. H., Kwon, K. S., and Mostafa, E. (2011). Application of computational fluid dynamics for modeling and designing photobioreactors for microalgae production: A review. *Computers and Electronics in Agriculture*, 76:131–147.

Bonaventura, C. and Meyers, J. (1969). Fluorescence and oxygen evolution from *Chlorella pyrenoidosa*. *Biochimica and Biophysica Acta*, 189(3):366–383.

Borodin, V. (2008). Effect of red and blue light on acclimation of *Chlamydomonas reinhardtii* to CO_2-limiting conditions. *Russian Journal of Plant Physiology*, 55(4):441–448.

Borowitzka, M. (1999). Commercial production of microalgae: ponds, tanks, tubes and fermenters. *Journal of Biotechnology*, 70:313–321.

Boussiba, S. and Vonshak, A. (1991). Astaxanthin accumulation in the green alga *Haematococcus pluvialis*. *Plant Cell Physiology*, 32(7):1077–1082.

Brown, D. A. R., Jones, P. N., and Middleton, J. C. (2004). *Experimental methods, Part A: Measuring Tools and Techniques for Mixing and Flow Visualization Studies*, chapter in: Handbook of industrial mixing science and practice; Paul EL, Atiemo-Obeng VA and Kresta SM editors. John Wiley & Sons, first edition.

Carlozzi, P. and Torzillo, G. (1996). Productivity of spirulina in a strongly curved outdoor tubualr photobioreactor. *Applied Microbiology and Biotechnology*, 45:18–23.

Chisti, Y., Halard, B., and Moo-Young, M. (1988). Liquid circulation in airlift reactors. *Chemical Engineering Science*, 43(3):451–457.

Dale, M. and Causton, D. (1992). Use of the chlorophyll a/b ratio as a bioassay for the light environment of a plant. *Functional Ecology*, 6:190–196.

Demmig-Adams, B. and Adams, W. W. (2002). Antioxidants in photosynthesis and human nutrition. *Science*, 298(5601):2149–53.

Demming Adams, B. and Adams, W. W. (1996). The role of xanthophyll cycle carotenoids in the protection of photosynthesis. *Trends in Plant Science*, 1(1):21–26.

Dixon, J. M., Taniguchi, M., and Lindsey, J. S. (2005). PhotochemCAD 2: A refined program with accompanyng spectral databases for photochemical calculations. *Photochemistry and Photobiology*, 81:212–213.

Dominguez Bocanegra, A. R., Guerrero Legarreta, I., Martinez Jeronimo, F., and Tomasini Campocosio, A. (2004). Influence of environmental and nutritional factors in the production of astaxanthin from *Haematococcus pluvialis*. *Bioresource Technology*, 92:209–214.

Doucha, J. and Livansky, K. (2006). Productivity, CO_2/O_2 exchange and hydraulics in outdoor open high density microalgal (*Chlorella sp.*) photobioreactors operated in a middle and southern european climate. *Journal of Applied Phycology*, 18:811–826.

Doucha, J. and Livansky, K. (2009). Outdoor open thin-layer microalgal photobioreactor potential productivity. *Journal of Applied Phycology*, 21:111–117.

Eibl, H. and Lands, W. E. M. (1969). A new, sensitive determination of phosphate. *Analytical Biochemistry*, 30:51–57.

Elias, C. B., Desai, R. B., Patole, M. S., Joshi, J. B., and Mashelkar, R. A. (1995). Turbulent shear stress - effect on mammalian cell culture and measurement using laser doppler anemometer. *Chemical Engineering Science*, 50(15):2431–2440.

Emerson, R. and Arnold, W. (1932). The photochemical reaction in photosynthesis. *The Journal of General Physiology*, pages 191–205.

Emerson, R. and Lewis, C. (1941). Carbon dioxide exchange and the measurement of the quantum yeld of photosynthesis. *Americal Journal of Botany*, 28:789–804.

Falkowski, P. and Raven, J. (2007). *Aquatic Photosynthesis*. Princeton University Press, II° edition.

Frössling, N. (1938). über die verdunstung fallenden tropfen (evaporation of falling drops). *Gerlands Beitage Geophys.*, 52:170–216.

Garcìa Camacho, F., Gallardo Rodrìguez, J. J., Sànchez Miròn, A., Ceròn Garcìa, M. C., Belarbi, E. H., and Molina Grima, E. (2007). Determination of shear stress thresholds in toxic dinoflagellates cultured in shaken flasks. implications in bioprocess engineering. *Process Biochemistry*, 42:1506–1515.

Garcìa-Malea, M. C., Acién, F. G., Fenrnàndez, J. M., Ceròn, M. C., and Molina, E. (2006). Continuous production of green cells of *Haematococcus pluvialis*: Modeling of the irradiance effect. *Enzyme and Microbial Technology*, 38:981–989.

Giannelli, L., Scoma, A., and Torzillo, G. (2009). Interplay between light intensity, chlorophyll concentration and culture mixing on the hydrogen production in sulfur-deprived chlamydomonas reinhardtii cultures grown in laboratory photobioreactors. *Biotechnology and Bioengineering*, 104(1):76–90.

Giannelli, L. and Torzillo, G. (2012). Hydrogen production with the microalga *Chlamydomonas reinhardtii* grown in a compact tubular photobioreactor im-

mersed in a scattering light nanoparticle suspension. *International Journal of Hydrogen Energy*, 37:16951–16961.

Gobbelaar, J. U. (1994). Turbulence in mass algal cultures and the role of light/dark fluctuations. *Journal of Applied Phycology*, 6:331–335.

Goldman, J. (2000). Outdoor algal mass cultures i. applications. *Water Research*, 13:1–19.

Goldman, J. C. and Carpenter, E. J. (1974). A kinetic approach to the effect of temperature on algal growth. *Limnology and Oceanography*, 19(5):756–766.

Gratani, L., Pesoli, P., and Crescente, M. (1998). Relationship between photosynthetic activity and chlorophyll content in an isolated quercus ilex l. tree during the year. *Photosynthetica*, 35(3):445–451.

Grobbelaar, J., Kroon, B., Burger-Wiersma, T., and Mur, L. (1992). Influence of medium frequency light/dark cycles of equal duration on the photosynthesis and respiration of *Chlorella pyrenoidosa*. *Hydrobiologia*, 238:53–62.

Grobbelaar, J. and Kurano, N. (2003). Use of photoacclimation in the design of a novel photobioreactor to achieve high yields in algal mass cultivation. *Journal of Applied Phycology*, 15:121–126.

Grobbelaar, J. U. (1989). Do light/dark cycles of medium frequency enhance phytoplankton productivity? *Journal of Applied Phycology*, 1:333–340.

Grzebyk, D., Shofield, O., Vetriani, C., and Falkowski, P. (2003). The mesozoic radiation of eukaryotic algae: the portable plastid hypothesis. *Journal of Phycology*, 39:259–267.

Gudin, C. and Chaumont, D. (1991). Cell fragility - the key problem of microalgae mass production in closed photobioreactors. *Bioresource Technology*, 38:145–151.

Han, B., Virtanten, M., Koponen, J., and Straškraba, M. (2000). Effect of photoinhibition on algal photosynthesis: a dynamic model. *Journal of plankton research*, 22(5):865–885.

Harker, M., Tsavalos, A. J., and Young, A. J. (1996). Factors responsible for astaxanthin formation in the chlorophyte *Haematococcus pluvialis*. *Bioresource Technology*, 55:207–214.

Haroun, Y., Legendre, D., and Raynal, L. (2010). Volume of fluid method mor interfacial reactive mass transfer. *Chemical Engineering Science*, 65:2896–2909.

Haroun, Y., Raynal, L., and Legnedre, D. (2012). Mass transfer and liquid hold-up determination in structured packing by cfd. *Chemical Engineering Science*, 75:342 – 348.

Hata, N., Ogbonna, J. C., Hasegawa, Y., Taroda, H., and Tanaka, H. (2001). Production of astaxanthin by *Haematococcus pluvialis* in a sequential heterotrophic-photoautotrophic culture. *Journal of Applied Phycology*, 13:395–402.

Havaux, M., Greppin, H., and Strasser, R. J. (1991). Functioning of photosystems I and II in pea leaves exposed to heat stress in the presence or absence of light. *Planta*, 186:88–98.

Higbie, R. (1935). The rate of absorption of a pure gas into a still liquid during short periods of exposure. *Trans. A.I.Ch.E.*, 35:365.

Hill, D. P. (1998). *The Computer Simulation of Dispersed Two-phase Flows*. PhD thesis, Imperial College of Science, Technology and Medicine.

Hirt, C. W. and Nichols, B. D. (1981). Volume of fluid (vof) method for the dynamics of free boundaries. *Journal of Computational Physics*, 39:201–225.

Horvath, A., Jordan, C., Lukasser, M., Kuttner, C., Makaruk, A., and Harasek, M. (2009). Cfd simulation of bubble columns using the vof model: comparison of commercial and open source solver with experiment with VOF. *Chemical Engineering Transactions*, 18.

Imamoglu, E., Dalay, M. C., and Sukan, F. V. (2009). Influences of different stress media and high light intensities on accumulation of astaxanthin in the green alga haematococcus pluvialis. *N Biotechnol*, 26(3-4):199–204.

Ishii, M. and Hibiki, T. (2011). *Thermo-Fluid Dynamics of Two-Phase Flow*. Springer.

Janna, W. S. (2010). *Introduction to fluid mechanics*. CRC Press, fourth edition.

Janssen, M., de Bresser, L., Baijens, T., Tramper, J., Mur, L. R., Snel, J. F. H., and Wijffels, R. H. (2000). Scale-up aspects of photobioreactors: effects of mixing induced light/dark cycles. *Journal of Applied Phycology*, 12:225–237.

Jaouen, P., Vandanjon, L., and Quéméneur, F. (1999). The shear stress of microalgal cell suspensions (*Tetraselmis suecica*) in tangential flow filtration systems: the role of pumps. *Bioresource Technology*, 68:149–154.

Jobses, I., Martens, D., and Tramper, J. (1991). Lethal events during gas sparging in animal cell culture. *Biotechnology and Bioengineering*, 37:484–490.

Juneau, P., El Berdey, A., and Popovich, R. (2002). Pam fluorometry in the determination of the sensitivity of *Chlorella vulgaris*, *Selenastrum capricornutum*, and *Chlamydomonas reinhardtii* to copper. *Archives of Environmental Contamination and Toxicology*, 42:155–164.

Katsuda, T., Shimahara, K., Shiraishi, H., Yamagami, K., Ranjbar, R., and Katoh, S. (2006). Effect of flashing light from blue light emitting diodes on cell

growth and astaxanthin production of haematococcus pluvialis. *J. Biosci. Bioeng.*, 102(5):442–446.

Kirk, J. (2011). *Light and photosynthesis in aquatic environments*. Cambridge University Press, III° edition.

Knox, R. (2011). Forster's resonance excitation transfer theory: not just a formula. *Journal of Biomedical Optics*, 17(1):1–6.

Kobayashi, M., Kakizono, T., and Nagai, S. (1991). Astaxanthin production by a green alga, *Haematococcus pluvialis* accompanied with morphological changes in acetate media. *Journal of Fermentation and Bioengineering*, 71(5):335–339.

Kok, B. (1953). *Algal culture, from laboratory to pilot plant*, chapter Experiments On Photosynthesis By Chlorella In Flashing Light. Carnagie Institution of Washington Publication.

Krishna, R. and Van Baten, J. M. (2001). Scaling up bubble column reactors with the aid of cfd. *Transactions ICheme*, 79(Part A):283–309.

Leupold, M., Hindersin, S., Gust, G., Kerner, M., and Hanelt, D. (2013). Influence of mixing and shear stress on *Chlorella vulgaris*, *Scenedesmus obliquus*, and *Chlamydomonas reinhardtii*. *Journal of Applied Phycology*, 25:485–495.

Lichtenthaler, H. (1987). Chlorophylls and carotenoids: pigments of photosynthetic membranes. *Methods in Enzymology*, 148:349–382.

Lorenz, M., Friedl, T., and Day, J. (2005). *Perpetual mainteinance of actively metabolizing microalgal cultures*, chapter in: Algal Culturing Techniques; Andersen, RA ed. Elsevier, first edition.

Mandalam, R. and Palsson, B. (1998). Elemental balancing of biomass and medium composition enhances growth capacity in high-density *Chlorella vulgaris* cultures. *Biotechnology and Bioengineering*, 59(5):605–611.

Marden Marshall, E. and Bakker, A. (2004). *Computational Fluid Mixing*, chapter in: Handbook of industrial mixing science and practice; Paul EL, Atiemo-Obeng VA and Kresta SM editors. John Wiley & Sons, first edition.

Marek, M., Stroesser, T., Roberts, P. J. M., Witbrecht, V., and Jirka, G. H. (2006). CFD modeling of turbulent jet mixing in a water storage tank. In *Proceedings of* 32^{nd} *IAHR International Association for Hydraulic Research.*, Venice, Italy.

Martin, W. and Schnarrenberger, C. (1997). The evolution of the Calvin cycle from prokaryotic to eukaryotic chromosomes: a case study of functional redundancy in ancient pathways through endosymbiosis. *Current Genetics*, 32(1):1–18.

Martìnez Roldàn, A. J., Perales Vela, H. V., Canizares Villanueva, R. O., and Torzillo, G. (2014). Physiological response of *Nannochloropsis* sp. to saline stress in laboratory batch cultures. *Journal of Applied Phycology*, 26:115–121.

Marutani, Y., Yamauchi, Y., Kimura, Y., Mizutani, M., and Sugimoto, Y. (2012). Damage to photosystem ii due to heat stress without light-driven electron flow: involvement of enhanced introduction of reducing power into thylakoid membranes. *Planta*, 236(2):753–761.

Masojidek, J., Kopecky, J., Giannelli, L., and Torzillo, G. (2011). Productivity correlated to photobiochemical performance of chlorella mass cultures grown outdoors in thin-layer cascades. *Journal of Industrial Microbiology and Biotechnology*, 38(2):307–317.

Melis, A. (1999). Photosystem-II damage and repair cycle in chloroplasts: what

modulates the rate of photodamage in vivo? *Trends in Plant Science*, 4(4):130–135.

Merchant, S. S., Allen, M. D., Kropat, J., Moseley, J. L., Long, J. C., Tottey, S., and Terauchi, A. M. (2006). Between a rock and a hard place: trace element nutrition in chlamydomonas. *Biochim. Biophys. Acta*, 1763(7):578–94.

Merchuk, J. C., Garcia-Camacho, F., and Molina-Grima, E. (2007). Photobioreactor design and fluid dynamics. *Chemical and Biochemical Engineering Quarterly*, 21(4):345–355.

Michels, M. H. A., van der Goot, A. J., Norsker, N.-H., and Wijffels, R. H. (2010). Effects of shear stress on the microalgae chaetoceros muelleri. *Bioprocess and Biosystems Engineering*, 33(8):921–927.

Mimuro, M. and Katoh, T. (1991). Carotenoids in photosynthesis: absorption, transfer and dissipation of energy. *Pure and Applied Chemistry*, 63(1):123–130.

Mitsuhashi, S., Hosaka, K., Tomonaga, E., Muramatsu, H., and Tanishita, K. (1995). Effects of shear flow on photosynthesis in a dilute suspension of microalgae. *Applied Microbiology and Biotechnology*, 42:744–749.

Miyamoto, K. (1997). Renewable biological systems for alternative sustainable energy production. Fao agricultural services bulletin - 128, FAO - Food and Agriculture Organization of the United Nations, www.fao.org/docrep/w7241e/w7241e00.htm.

Molina-Grima, E., Acién Fernàndez, F. G., and Robles Medina, A. (2004). *Downstream Processing of Cell-mass and Products*, chapter in: Handbook of Microalgal Culture: Biotechnology and Applied Phycology, Richmond A. editor. Blackwell publishing, first edition.

Moreno-Garrido, I. (2008). Microalgae immobilization: current techniques and uses. *Bioresource Technology*, 99(10):3949–64.

Muller-Feuga, A., Pruvost, J., Le Guédes, R., Le Déan, L., Legentilhomme, P., and Legrand, J. (2003). Swirling flow implementation in a photobioreactor for batch and continuous culture of porphyridium cruentum. *Biotechnology and Bioengineering*, 84(5):544–551.

Nakamura, Y. and Miyachi, S. (1982). Change in starch photosynthesized at different temperatures in *Chlorella*. *Plant Science Letters*, 27:1–6.

Nedbal, L., Tichy, V., Xiong, F., and Grobbelaar, J. (1996). Microscopic green algae and cyanobacteria in high-frequency intermittent light. *Journal of Applied Phycology*, 8:325–333.

Nuffield Council on Bioethics (2011). Biofuels ethical issues. Technical report, http://www.nuffieldbioethics.org/publications.

Perry, R. H., Green, D. W., and Maloney, J. O., editors (1999). *Perry's chemical engineers' handbook*. McGraw-Hill, 7th edition.

Posten, C. (2009). Design principles of photo-bioreactors for cultivation of microalgae. *Engineering in Life Sciences*, 9(3):165–177.

Pruvost, J., Cornet, J. F., and Legarnd, J. (2008). Hydrodynamics influence on light conversion in photobioreactors: An energetically consistent analysis. *Chemical Engineering Science*, 63:3670–3694.

Pruvost, J., Pottier, L., and Legrand, J. (2006). Numerical investigation of hydrodynamic and mixing conditions in a torus photobioreactor. *Chemical Engineering Science*, 61(14):4476–4489.

Pulz, O. (2001). Photobioreactors: production systems for phototrophic microorganisms. *Applied Microbiology and Biotechnology*, 53:287–293.

Putri, E. V., Md Din, M. F., Ahmed, Z., Jamaluddin, H., and Chelliapan, S. (2011). Investigation of microalgae for high lipid content using palm oil mill effluent (pome) as a carbon source. http://www.ipcbee.com/vol12/17-C049.pdf.

Rabinowitch, E. and Govindjee (1969). *Photosynthesis*. John Wiley and sons, first edition.

Ranjbar, R., Inoue, R., Katsuda, T., Yamaji, H., and Katoh, S. (2008). High efficiency production of astaxanthin in an airlift photobioreactor. *J. Biosci. Bioeng.*, 106(2):204–207.

Rasmussen, B., Fletcher, I. R., Brocks, J. J., and Kilburn, M. R. (2008). Reassessing the first appearance of eukaryotes and cyanobacteria. *Nature*, 455(7216):1101–4.

Raven, J. A. and Geider, R. J. (1988). Temperature and algal growth. *New Phytologist*, 110:441–461.

Richmond, A. and Vonshak, A. (1978). Spirulina culture in israel. *Archiv für Hydrobiologie Beiheft Ergebnisse der Limnologie*, 11:274–280.

Richmond, A. and Zhang, C. W. (2001). Optimization of a flat plate glass reactor for mass production of *Nannochloropsis sp.* outdoors. *Journal of Biotechnology*, 85:259–269.

Rodolfi, L., Chini Zittelli, G., Bassi, N., Padovani, G., Biondi, N., Bonini, G., and Tredici, M. R. (2009). Microalgae for oil: strain selection, induction of lipid synthesis and outdoor mass cultivation in a low-cost photobioreactor. *Biotechnol. Bioeng.*, 102(1):100–112.

Rumeau, D., Peltier, G., and Cournac, L. (2007). Chlororespiration and cyclic electron flow around psi during photosynthesis and plant stress response. *Plant Cell Environ.*, 30(9):1041–51.

Rusche, H. (2002). *Computational Fluid Dynamics of Dispersed Two-Phase Flows at High Phase Fractions*. PhD thesis, Imperial College of Science, Technology & Medicine, Exhibition Road, London SW7 2BX.

Sanchez Miron, A., Ceron Garcia, M. C., Garcia Camacho, F., Molina Grima, E., and Chist, Y. (2004). Mixing in bubble column and airlift reactors. *Chemical Engineering Resesarch and Design*, 82(A10):1367–1374.

Šetlík, I., Allakhverdiev, S., Nedbal, L., Šetlíková, E., and Klimov, V. (1990). Three types of photosystem II photoinactivation. *Photosynthesis Research*, 23:39–48.

Setlík, I., Sust, V., and Málek, I. (1970). Dual purpose open circulation units for large scale culture of algae in temperate zones. i. basic design considerations and scheme of a pilot plant. *Algological Studies/Archiv für Hydrobiologie, Supplement Volumes*, 1:111–164.

Shen, G. (1994). *Bubble swarm velocities in a flotation column*. PhD thesis, McGill University, Montreal, Canada.

Solovchenko, A., Khozin-Goldberg, I., Cohen, Z., and Merzlyak, M. (2009). Carotenoid-to-chlorophyll ratio as a proxy for assay of total fatty acids and arachidonic acid acid content in the green microalga *Parietochloris incisa*. *Journal of Applied phycology*, 21:361–366.

Spolaore, P., Joannis-Cassan, C., Duran, E., and Isambert, A. (2006). Commercial applications of microalgae. *Journal of Bioscience and Bioengineering*, 101(2):87–96.

Thomas, W. and Gibson, C. (1990). Effects of small-scale turbulence on microalgae. *Journal of Applied Phycology*, 2:71–77.

Thorne, S. and Boardman, N. (1971). Formation of chlorophyll b, and the fluorescence properties and photochemical activities of isolated plastids from greening pee seedlings. *Plant Physiology*, 47:252–261.

Tolasa, S., Cakli, S., and Ostermeyer, U. (2005). Determination of astaxanthin and canthaxanthin in salmonid. *European Food Research and Technology*, 221:787–791.

Torzillo, G., Giannelli, L., Martìnez Roldàn, A. J., Verdone, N., De Filippis, P., Scarsella, M., and Bravi, M. (2010). Microalgae culturing in thin layer photobioreactors. *Chemical Engineering Transactions*, 20:265–270.

Torzillo, G., Goksan, T., Faraloni, C., Kopecky, J., and Masojidek, J. (2003). Interplay between photochemical activities and pigment composition in an outdoor culture of haematococcus pluvialis during the shift from the green to red stage. *Journal of Applied Phycology*, 15:127–136.

Tredici, M. (2004). *Mass Production of Microalgae: Photobioreactors*, chapter in: Handbook of Microalgal Culture: Biotechnology and Applied Phycology, Richmond A. editor. Blackwell Publishing, first edition.

Ugwu, C. and Aoyagi, H. (2011). Evaluation of the mass transfer capacity of a long tubular photobioreactor with static mixer and its outdoor performance with microalgal cultures. *Trends in Applied Sciences Research*, 6(10):1222–1229.

U.S. Energy Information Administration (2013). Annual energy outlook 2013, with projections to 2040. Technical report, http://www.eia.gov/forecasts/aeo.

Van Oorschot, J. (1955). *Conversion of light energy in algal culture*. H. Veenman & Zonen - Wageningen.

Vass, I., Styring, S., Hundal, T., Koivuniemi, A., Aro, E., and Andersson, B. (1992). Reversible and irreversible intermediates during photoinhibition of photosystem ii: Stable reduced qa species promote chlorophyll triplet formation. *Proceedings of the National Academy of Science*, 89:1408–1412.

Vega-Estrada, J., Montes-Horcasitas, M. C., Domínguez-Bocanegra, A. R., and Cañizares-Villanueva, R. O. (2005). Haematococcus pluvialis cultivation in split-cylinder internal-loop airlift photobioreactor under aeration conditions avoiding cell damage. *Applied Microbiology and Biotechnology*, 68(1):31–35.

Vonshak, A. and Torzillo, G. (2004). *Environmental Stress Physiology*, chapter in: Handbook of Microalgal Culture: Biotechnology and Applied Phycology, Richmond A. editor. Blackwell publishing, first edition.

Warburg, O. and Negelein, E. (1928). Über den Einfluß der Wellenlänge auf den Energieumsatz bei der Kohlensäureassimilation. *Über die Katalytischen Wirkungen der Lebendigen Substanz*, pages 444–469.

Wise, W. S. (1951). The measurement of the aeration of culture media. *Journal of General Microbiology*, 5:167–177.

Wu, L. B., Li, Z., and Song, Y. Z. (2009). Numerical investigation of flow characteristics and irradiance history in a novel photobioreactor. *African Journal of Biotechnology*, 8(18):4672–4679.

Wu, X. and Merchuk, J. C. (2004). Simulation of algae growth in a bench scale internal loop airlift reactor. *Chemical Engineering Science*, 59:2899–2912.

Xu, L., Liu, R., Wang, F., and Liu, C. Z. (2012). Development of a draft-tube airlift bioreactor for *Botryococcus braunii* with an optimized inner structure using computational fluid dynamics. *Bioresource Technology*, 119:300–305.

Yamamoto, Y., Aminaka, R., Yoshioka, M., Khatoon, M., Komayama, K., Takenaka, D., Yamashita, A., Nijo, N., Inagawa, K., Morita, N., Sasaki, T., and Yamamoto, Y. (2008). Quality control of photosystem ii: impact of light and heat stresses. *Photosyn. Res.*, 98(1-3):589–608.

Pubblication list

Part I

- Giannelli L., Yamaji H. and Katsuda, T. - A numerical model for the quantification of light/dark cycles in microalgal cultures: Air-lift and bubble-column photobioreactor analysis by means of computational fluid dynamics. *Journal of Chemical Engineering of Japan* (In press)
- Giannelli L., Yamaji H. and Katsuda, T. - Interplay between culture productivity and flashing light in *Haematococcus pluvialis* cultures. (to be submitted)

Part II

- Giannelli L., Yamada H., Yamaji H. and Katsuda, T. - Effects of cultivation temperature on the astaxanthin production efficiency of *Haematococcus pluvialis cultures*. (Under review)

Part III

- Masojidek J., Kopecky J., Giannelli L., and Torzillo, G. (2010). Productivity correlated to photobiochemical performance of *Chlorella* mass cultures grown outdoors in thin-layer cascades. *Journal of Industrial Microbiology & Biotechnology*, 38:307–317.
- Torzillo G., Giannelli L., Martìnez Roldàn A. J., Verdone N., De Filippis P., Scarsella M., and Bravi M. (2010) - Microalgae culturing in thin layer photobioreactors. *Chemical Engineering Transactions*, 20:265–270.
- Giannelli L, Watanabe Chihiro, Silva Benavides M., Yamaji H., Katsuda T., Torzillo G.: Predicting the productivity of a *Chlorella sorokiniana* culture grown outdoors on a corrugated thin layer cascade and subjected to fast light/-dark cycles. (in preparation).

Acknowledgements

First and foremost I would like to express my deep gratitude to the Government of Japan which directly supported this research by financing my stay in Japan by means of the MEXT scholarship. This allowed me to attend the doctoral course in Kobe University and to sustain the *numerous* and *onerous* expenses I incurred in. Of course, none of the research activity could have been carried out without the active help from my research directors, Prof. Yamaji Hideki and Prof. Katsuda Tomohisa to whom I wish to express my gratitude. They were not just my research reference but played an important role at making me feel "at home" even when being (actually) more than 10·000 km away from home. Of course, Prof. Ishida Kenji and Prof. Ohmura Naoto deserve a special mention for their active and highly constructive discussion during the final review of this thesis. I believe after the review I was able to deliver an even better work thanks to their suggestions. Just another confirmation for the importance of interdisciplinary studies. I also have to show my gratitude to the "foreign" part of the research group that helped my by granting me the possibility to work on innovative technologies even if not directly. First in this list is Dr. Torzillo Giuseppe. He was the first person to introduce me to the algal biotechnology field and I will be forever in debt with him for what I learned: and I'm talking of both scientific knowledge and human knowledge. I still have that piece of paper with his sign in my pocket and recur to it when I need a reminder. It was clearly thanks to his connections with the Czech republic that I was able to briefly collaborate with Prof. Jiri Masojidek on the outdoor photobioreactors. I wish I had more time to spend with him to enjoy his vast knowledge in chlorophyll fluorescence and his cheerful personality.

Finally I would like to thank all the young guys in my lab for the precious (invaluable) help they gave me to understand the Japanese society a little bit better.

I believe I was blessed with the most intelligent students of the whole lab and I wish to thank all of them. Wada-chan was the first student I got to know when I first came here: it took him 6 months to talk to me. Looking at how he turned out to be now... well, it was a surprise! After him came John (a.k.a. Yamada!). He's the kind of daunted genius you cannot refrain from admiring: catching up with all you tell him, elaborating, inventing. It was nice to teach to him some of my knowledge. I would love to see him working on a bigger scale.... I'm sure he will skyrocket after getting to work. And finally I want to thank Chi for her time spent working with me. She is a very rare kind of japanese and it was a pleasure to do research with her for this couple of years. She's the kind of person that doesn't get intimidated quite easily with a firm grip on her ideas and the determination to show how and why they are correct. I felt an affinity well beyond the research activity. I realized I'm not the only one with that mind frame! I just wish she won't be penalized for that in the future.... Last but not least, let me thank Tooru-chan for the long chats we had. I believe he's the personification of the concept of "devotion".

In this list there are still some names shouting for their absence. I deliberately omitted them as their meaning to me has risen well above these humble pages. You know who you are and moreover what you all mean to me. Guess I don't need to say more than this.